



HAL
open science

Precise predictions for top-quark observables at the LHC in the presence of Z' and W' bosons

Mohammad Mahdi Altakach

► **To cite this version:**

Mohammad Mahdi Altakach. Precise predictions for top-quark observables at the LHC in the presence of Z' and W' bosons. High Energy Physics - Phenomenology [hep-ph]. Université Grenoble Alpes [2020-..], 2021. English. NNT: 2021GRALY032 . tel-03499036

HAL Id: tel-03499036

<https://theses.hal.science/tel-03499036v1>

Submitted on 21 Dec 2021

HAL is a multi-disciplinary open access archive for the deposit and dissemination of scientific research documents, whether they are published or not. The documents may come from teaching and research institutions in France or abroad, or from public or private research centers.

L'archive ouverte pluridisciplinaire **HAL**, est destinée au dépôt et à la diffusion de documents scientifiques de niveau recherche, publiés ou non, émanant des établissements d'enseignement et de recherche français ou étrangers, des laboratoires publics ou privés.

THÈSE

Pour obtenir le grade de

DOCTEUR DE L'UNIVERSITÉ GRENOBLE ALPES

Spécialité : **Physique Subatomique et Astroparticules**

Arrêté ministériel : 25 mai 2016

Présentée par

Mohammad Mahdi ALTAKACH

Thèse dirigée par **Ingo SCHIENBEIN**, Université Grenoble Alpes,
et codirigée par **Tomás JEŽO**, et **Haitham ZARAKET**

préparée au sein du **Laboratoire de Physique Subatomique et
Cosmologie** dans l'École Doctorale Physique

**Prédictions précises pour les observables des
quarks top au LHC en présence de bosons Z' et W'**

**Precise predictions for top-quark observables at
the LHC in the presence of Z' and W' bosons**

Thèse soutenue publiquement le **12 mai 2021**,
devant le jury composé de :

Monsieur Johan COLLOT

Professeur des Universités, Université Grenoble-Alpes, Président

Monsieur Aldo DEANDREA

Professeur des Universités, Université Lyon 1, Rapporteur

Monsieur Benjamin Fuks

Professeur des Universités, Sorbonne Université, Rapporteur

Madame Gudrun HEINRICH

Professeur, Karlsruhe Institut für Technologie, Examinatrice

Madame Sabine KRAML

Directeur de recherche, CNRS, Examinatrice



Acknowledgements

First and foremost I would like to thank my supervisors, Haitham, Ingo, and Tomás. I am very grateful for the valuable guidance, support, and encouragement.

The work presented in this thesis has always been dependant on collaboration, I am also grateful for Jean-Nicolas, Jon, and Michael for their fruitful discussions and kind support.

I would like to thank the members of my jury, Gudrun, Johan, Sabine for their useful comments and in particular Aldo and Benjamin for referring my manuscript.

I also would like to express my most sincere gratitude to everyone that I have had the pleasure to interact with during this journey on the professional as well as personal level, especially to the members of the LPSC, the university of Münster, and the university college London.

Last but not least, I would like to thank my friends and my family, particularly my parents for their endless love, care, and support every moment.

Abstract

The Standard Model (SM) of particle physics, based on an $SU(3)_C \times SU(2)_L \times U(1)_Y$ gauge group, is an extremely successful theory that accounts for a wide range of high energy experiments at both the intensity and energy frontiers. Nevertheless it is widely believed to be incomplete, and manifestations of new physics are awaited to show up around the TeV scale. The unification of the SM gauge group in a larger, simple group, is theoretically very attractive. In this view, the SM is seen as an effective model valid at low energies. Thus, given the fact that the possible unification groups have a rank greater or equal than the SM, additional subgroups like a $U(1)$ or a second $SU(2)$ may appear at an intermediate stage when the unification group is broken down to the SM group. Interestingly, a new $U(1)$ group factor predicts one additional gauge boson generally denoted Z' in the literature. On the other hand, since $SU(2)$ is a non-Abelian group with three generators, an additional one leads to three gauge bosons of which one is neutral and two are charged and denoted W'^{\pm} .

In this thesis, we present precise predictions for top quark observables at the LHC in the presence of Z' and W' bosons. For this purpose, we extend and improve upon a previous calculation of electroweak top-quark pair hadroproduction in extensions of the SM with extra heavy neutral and charged spin-1 resonances. In particular, we allow for flavour-non-diagonal Z' couplings and take into account non-resonant production in the SM and beyond including the contributions with t-channel W^- and W'^- -bosons. All amplitudes are generated using the RecoLa2 package. We include NLO QCD corrections and consistently match to parton showers with the POWHEG method fully taking into account the interference effects between SM and new physics amplitudes. We consider the Sequential Standard Model, the lepto-phobic Topcolour model, the G_{221} class of models, as well as the Third Family Hypercharge Model featuring non-flavour-diagonal Z' couplings which has been proposed recently to explain the anomalies in B decays. For these models, we present numerical results for top-pair cross sections at hadron colliders with a centre-of-mass energy up to 100 TeV. Subsequently, we link our calculation to Contur (Constraints On New Theories Using Rivet), to obtain exclusion limits on the parameter space of models with extra heavy gauge bosons in the top-pair channel using real particle level data from the Large Hadron Collider.

Résumé

Basé sur le groupe de jauge $SU(3)_C \times SU(2)_L \times U(1)_Y$, le Modèle Standard (MS) de la physique des particules est une théorie fructueuse qui permet d'expliquer un grand nombre d'expériences jusqu'aux frontières d'intensités et d'énergies. Néanmoins, il est considéré comme incomplet et des manifestations de nouvelle physique sont attendues autour de l'échelle du TeV. L'unification du groupe de jauge du MS dans un groupe plus large et plus simple est théoriquement très intéressante. Dans cette optique, le MS est considéré comme une manifestation à basse énergie d'une théorie plus fondamentale. Ainsi, étant donné que les groupes d'unification possibles ont un rang supérieur ou égal à celui du MS, des sous-groupes supplémentaires tel que $U(1)$ ou un deuxième groupe $SU(2)$ peuvent entrer en jeu à un stade intermédiaire lors de la brisure de symétrie du groupe d'unification en groupe du MS. Il est intéressant de noter qu'un nouveau groupe facteur $U(1)$ permet de prédire l'existence d'un boson de jauge supplémentaire noté Z' dans la littérature. D'autre part, $SU(2)$ étant un groupe non-abélien ayant trois générateurs, il introduit alors trois bosons de jauge supplémentaires dont un est neutre et deux sont chargés et notés W'^{\pm} .

Dans cette thèse, nous présentons des prédictions précises pour les observables des quarks top au LHC en présence de bosons Z' et W' . À cet effet nous étendons et améliorons un précédent calcul d'hadroproduction électrofaible de paires de quarks top dans des extensions du MS avec des nouvelles résonances lourdes de spin-1, neutres et chargées. En particulier, nous autorisons les couplages non diagonaux du boson Z' dans la base des saveurs et prenons en compte la production non résonnante dans le MS et au-delà, y compris les contributions des bosons W et W' dans le canal t. Toutes les amplitudes sont calculées avec le programme RecoLa2. De plus, nous incluons les corrections QCD au deuxième ordre de la théorie des perturbations et les adaptons systématiquement aux cascades partoniques à travers la méthode POWHEG en tenant compte des effets d'interférences entre les amplitudes du MS et celles de la nouvelle physique. Nous considérons le Modèle Standard séquentiel, le modèle leptophobic Topcolour, la classe de modèles G_{221} , ainsi que le modèle d'hypercharge de la troisième famille avec des couplages Z' non diagonaux dans l'espace des saveurs qui a été proposé récemment pour expliquer les anomalies dans les désintégrations de mésons B. Nous présentons des résultats numériques pour les sections efficaces des paires de quark top dans des collisionneurs de hadrons avec une énergie dans le centre de masse allant jusqu'à 100 TeV. Par la suite, nous lions notre calcul à Contur (Constraints On New Theories Using Rivet), pour obtenir des limites d'exclusions sur l'espace des paramètres des différents modèles prédisant des bosons lourds supplémentaires pour le canal de production de paires de quarks top, en utilisant les données du grand collisionneur de hadrons.

Contents

Introduction and Survey	1
1 Extended Gauge Group Models: The G_{221} Class	5
1.1 G_{221} models general features	6
1.2 Two-step symmetry breaking and gauge boson masses	7
1.3 Neutral and charged fermionic currents	15
2 Z', W' Precision predictions at the HL- and the HE-LHC	21
2.1 Precision predictions for $pp \rightarrow Z' \rightarrow t\bar{t}$	22
2.1.1 Numerical results	23
2.1.2 Uncertainties	24
2.2 Precision predictions for $pp \rightarrow W' \rightarrow \ell\nu$	26
2.2.1 Numerical results	28
2.2.2 Uncertainties	30
3 QCD corrections to EW top-pair production beyond the Standard Model	33
3.1 Next-to-leading order QCD corrections to the electroweak top-pair production .	35
3.2 Parton level processes	39
3.2.1 Leading-order contributions	40
3.2.2 One-loop virtual corrections	41
3.2.3 Real emissions	42
3.3 RecoLa: Recursive Computation of 1-Loop Amplitudes	44
3.3.1 RecoLa model file: the Standard Model + $W' + Z'$	45
3.3.2 Power counting of couplings in RecoLa	45
3.3.3 Validation	46
3.4 POWHEG BOX: Matching NLO QCD computations with Parton Shower Monte Carlos	49
3.4.1 Monte Carlo integration	52
3.4.2 The subtraction method	54
3.4.3 Basics of QCD parton showers	56
3.4.4 The POWHEG method	59
3.5 POWHEG BOX implementation	61
3.6 EW top-pair production at NLO QCD accuracy at the LHC and beyond	73
3.6.1 Models	73
3.6.2 Numerical results	75

4	Constraining models with Z'-bosons using LHC fiducial measurements	83
4.1	The Contur method: workflow and philosophy	83
4.2	The Rivet analyses	85
4.3	Constraints on theories with extra heavy gauge bosons using Contur	86
	Summary and Outlook	93
A	G_{221} models	95
A.1	Derivation of the second stage SB mass matrices in BP-II	95
A.2	Neutral and charged currents in the NU model	96
B	RecoLa2	105
B.1	Amplitude structure in RecoLa	105
B.2	Input parameters of SMWZp	107
B.3	The anatomy of the SMWZp amplitudes within RecoLa2	107
B.4	Couplings in RecoLa2 vs couplings in old PBZp	119
B.5	Snippet codes to call an amplitude in Madgraph and in RecoLa2	119
B.6	The powheg .input file	122
C	Contur	127
C.1	Steering files	127
	Bibliography	149

Introduction and Survey

Developed in the early 1970s, the Standard Model (SM) of particle physics [1–9] is the most accurate theory known to describe the elementary particles of the universe and their interactions. It has been extremely successful in explaining a wealth of experimental data coming from highly-energetic colliders as well as low-energy precision experiments. Nevertheless, it is widely believed to be incomplete for different reasons. On the experimental side, the SM doesn't include gravity [10], it doesn't provide a candidate for a dark matter particle [11], the CP violation in the SM is not sufficient to explain the matter–anti-matter asymmetry observed in the universe [12–14], and massive neutrinos [15–17] are, a priori, not accounted for in the SM. Furthermore, the scalar sector of the SM suffers under naturalness problems: Why is the Higgs mass stable under quantum corrections? Why is CP-violation in the strong interaction absent or strongly suppressed? For this reason, in order to avoid fine-tuning in the scalar sector, the general expectation has been for a long time that new physics (NP) beyond the Standard Model (BSM) should be present close to the electroweak (EW) scale. On the aesthetical side, many of the 26 input parameters of the SM are quite peculiar (for example, the masses of the SM fermions span several orders of magnitude and there is no clear pattern in the CKM and PMNS mixing matrices), the SM gauge group is a direct product of three independent symmetry factors, and there is no clear relation between the three generations of the SM fermions (why are there three generations in the first place?).

For this reason, a large number of well-motivated extensions of the SM have been proposed in the literature which address one or several of the problems mentioned above. An elegant way to solve the naturalness problem is given by TeV-scale supersymmetry which would also provide a candidate for dark matter. Another attractive way to solve the naturalness problem and to better understand electroweak symmetry breaking is offered by theories postulating a new strong interaction at the TeV scale. Finally, models with large extra dimensions [18, 19] could explain why there is no large hierarchy between the EW scale and the fundamental Planck scale. On the other hand, Grand Unified Theories (GUT) [20–23] appeal to the old dream of unifying all interactions and matter. The strong, weak and electromagnetic interactions could then be understood as low energy manifestations of one fundamental interaction and also the quarks and leptons would just be low energy manifestations of the same fundamental particle multiplet. Many of such theories predict the existence of new resonances with properties similar to the W and Z gauge bosons of the SM. The new resonances, usually dubbed as Z' - and W' -bosons, are massive, neutral and electrically charged spin-1 particles, respectively and mediate the neutral and charged current interactions of the SM fermions. These interactions can be described in a completely model independent manner, however, it would be complicated to perform a phenomenological study in this way since the resulting Lagrangian will have a large

number of free parameters. Thus, one needs to restrict this freedom in practice. For instance, the couplings of the Z' - and W' -bosons in the Sequential Standard Model (SSM) [24] are defined to be identical to their SM counter parts with their mass being the only free parameter. Another approach is to collect together a group of models where the new resonances can be described by a minimal set of free parameters [25–29]. Furthermore, models can be grouped in a class based on their theoretical origin as can be seen in [30, 31].

In the first chapter of this thesis we study a class of models, following the latter approach, where the SM gauge group is supplemented by an additional $SU(2)$ gauge factor. Named as the G_{221} class, it contains six models, the Left-Right (LR) [32, 33], Lepto-Phobic (LP), Hadro-Phobic (HP), Fermio-Phobic (FP) [34, 35], Un-Unified (UU) [36, 37] and Non-Universal (NU) [38, 39] models. We describe the classification of these models in two groups based on their patterns of symmetry breaking (SB), and we show their particle content and their charge assignments. Subsequently, we discuss how the spontaneous symmetry breaking (SSB) is achieved and how the gauge bosons acquire their masses in the G_{221} class. We then summarise the couplings of the new resonances to SM fermions in the six models.

Although no new particles have been detected in the first two runs of the Large Hadron Collider (LHC) at CERN, there are still hopes that signals of new physics will appear in the future high-luminosity (HL) and possibly a high-energy (HE) mode of the LHC which has been proposed. In Chapter 2, we show numerical results for two different processes with $t\bar{t}$ and dilepton final states in the presence of Z' - and W' -bosons. The predictions for the $t\bar{t}$ production are at next-to-leading order (NLO) accuracy using the PBZp code developed in 2015 [40]. For the dilepton final state we use the Resummino package [41] which includes soft gluon resummation effects at next-to-leading logarithmic (NLL) accuracy matched to a NLO calculation. We present predictions for the SSM, NU, and UU models at a centre-of-mass energy of 14 TeV for the HL-LHC and 27 TeV for the proposed HE-LHC. The theoretical uncertainties due to the variation of the renormalisation and factorisation scales and, in some case, due to the uncertainties of the parton distribution functions (PDFs), are also presented.

In Chapter 3, we perform a completely new calculation of the NLO QCD corrections to electroweak top-pair hadroproduction in the presence of Z' - and W' -bosons and we describe how this calculation can be matched to parton shower (PS) algorithms following the Positive Weight Hardest Emission Generator (POWHEG) method [42]. This calculation includes several improvements with respect to the previous one performed in [40]: (i) We calculate our amplitudes using the REcursive Computation of 1-Loop Amplitudes (RecoLa2) package [43]. This package was created in order to automate the calculations of amplitudes in BSM theories including QCD and EW corrections at NLO. Our calculation and implementation into Monte Carlo event generators within the POWHEG BOX framework [44] is the first use case of RecoLa2 BSM

amplitudes in an NLO+PS matched calculation. (ii) The new code can handle flavour-non-diagonal and generation non-universal couplings in order to study Z' -models that aim to explain B-flavour anomalies. (iii) The calculation includes t-channel W and W' contributions. (iv) As in the old code, we take into account all interference terms as well as the photon induced channels for the SM, where the latter is needed to treat initial state QED singularities. This calculation represents a core part of this thesis. Compared to the previous calculation it is far more complex due to the additional amplitudes and more general coupling structure of the new gauge bosons to the SM fermions. It is also more subtle concerning various technical details as will be discussed in Chapter 3.

Measurements at particle collider experiments, even if primarily aimed at understanding SM processes, can have a high degree of model independence, and implicitly contain information about potential contributions from BSM physics. In Chapter 4, we briefly describe the Constraints On New Theories Using Rivet (Contur) method by explaining its workflow and philosophy. We then give some information about the Robust Independent Validation of Experiment and Theory (Rivet) repository, where the particle-level measurements, used subsequently by Contur to set limits on BSM theories, are preserved. In the last section of this chapter we show how our $t\bar{t}$ calculation of Chapter 3 is linked to Contur in order to set limits on models with additional heavy gauge bosons using LHC measurements. Additionally, we give an example to show how this tool chain can be used.

Finally, in the last chapter we summarise our work and give an outlook. Note that details on various calculations presented in this manuscript as well as extra material are relegated to the Appendices.

The material presented in this thesis has led to the following publications:

- A contribution to the CERN yellow report on the HL- and HE-LHC [45] where we contributed precision predictions for new dilepton and $t\bar{t}$ resonances (Chapter 2).
- The results of calculation of NLO QCD corrections to electroweak $t\bar{t}$ hadroproduction in the presence of Z' - and W' -bosons have been published in the regular article [46] and in an contribution to the proceedings of the ICHEP 2020 conference [47] (Chapter 3).
- The work on the implementation of our calculation in the Contur framework has led to a publication in [48]. A separate paper where we use the Contur framework to derive constraints on the leptophobic Topcolour (TC) model using LHC data on $t\bar{t}$ production is in preparation [49] (Chapter 4).

Chapter 1

Extended Gauge Group Models: The G_{221} Class

The Standard Model of particle physics, based on an $SU(3)_C \times SU(2)_L \times U(1)_Y$ gauge group, is an extremely successful theory that accounts for a wide range of high energy experiments at both the intensity and energy frontiers. Nevertheless, it is widely believed to be incomplete, and manifestations of new physics are expected to show up around the TeV scale.

The unification of the SM gauge group in a larger, simple group, e.g. $SU(5)$, $SO(10)$, or E_6 is theoretically very attractive. In this view, the SM is seen as an effective model valid at low energies $E \leq \Lambda_{NP}$, where $\Lambda_{NP} < m_{Planck}$ is the energy scale where new physics effects beyond the SM become large. Thus, given the fact that the possible unification groups have a rank larger than the SM, additional subgroups like a $U(1)$ or a second $SU(2)$ may appear at an intermediate stage when the unification group is broken down to the SM group. Interestingly, a new $U(1)$ group factor predicts one additional electrically neutral gauge boson denoted Z' in the literature [50, 51]. On the other hand, since $SU(2)$ is a non-Abelian group with three generators, an additional one predicts/leads to three gauge bosons of which one is electrically neutral and two are charged and denoted W'^{\pm} . Thus, named as G_{221} class, models with an extra $SU(2)$ gauge factor will be the main topic of this chapter. Moreover, despite sharing the same gauge group, various types of particle content, charge assignments and patterns of symmetry breaking can lead to different phenomenologies at the LHC [30]. We will present numerical results for two of the G_{221} models in Chapter 2 where we show cross section predictions for the future High Luminosity LHC as well as the proposed High Energy LHC.

This chapter is organised as follows. In Section 1.1 we present the models from the G_{221} class, their particle content, their charge assignments and we classify them according to different patterns of SB. The procedure of spontaneous symmetry breaking and the masses of the gauge bosons in the G_{221} class are illustrated with an example in Section 1.2. Finally, in Section 1.3 we describe the Lagrangian of the interaction between generic neutral and charged spin-1 gauge bosons and the fermions of the SM.

1.1 G_{221} models general features

The G_{221} class is a class of models based on a $SU(2)_1 \times SU(2)_2 \times U(1)_X$ gauge structure that ultimately breaks to $U(1)_{EM}$. It groups together the Left-Right [32, 33], Lepto-Phobic, Hadro-Phobic, Fermio-Phobic [34, 35], Un-Unified [36, 37] and Non-Universal [38, 39] models. Relative to the Standard Model, these models have three additional massive gauge bosons, and can be characterized in terms of their charge assignments and the specific patterns of SB. Following Ref. [52], the charge assignments to the SM quarks and leptons for the various models considered in this thesis are listed in Table 1.1 (This table/classifications comes from Ref. [52]).

BP	Model	$SU(2)_1$	$SU(2)_2$	$U(1)_X$
BP-II	Un-Unified (UU)	$\begin{pmatrix} u_L \\ d_L \end{pmatrix}$	$\begin{pmatrix} \nu_L \\ e_L \end{pmatrix}$	Y_{SM} for quarks, Y_{SM} for leptons
	Non-Universal (NU)	$\begin{pmatrix} u_L \\ d_L \end{pmatrix}_{1^{st}, 2^{nd}}$, $\begin{pmatrix} \nu_L \\ e_L \end{pmatrix}_{1^{st}, 2^{nd}}$	$\begin{pmatrix} u_L \\ d_L \end{pmatrix}_{3^{rd}}$, $\begin{pmatrix} \nu_L \\ e_L \end{pmatrix}_{3^{rd}}$	Y_{SM} for quarks, Y_{SM} for leptons
BP-I	Left-Right (LR)	$\begin{pmatrix} u_L \\ d_L \end{pmatrix}$, $\begin{pmatrix} \nu_L \\ e_L \end{pmatrix}$	$\begin{pmatrix} u_R \\ d_R \end{pmatrix}$, $\begin{pmatrix} \nu_R \\ e_R \end{pmatrix}$	$\frac{1}{6}$ for quarks, $-\frac{1}{2}$ for leptons
	Lepto-Phobic (LP)	$\begin{pmatrix} u_L \\ d_L \end{pmatrix}$, $\begin{pmatrix} \nu_L \\ e_L \end{pmatrix}$	$\begin{pmatrix} u_R \\ d_R \end{pmatrix}$	$\frac{1}{6}$ for quarks, $-Y_{SM}$ for leptons
	Hadro-Phobic (HP)	$\begin{pmatrix} u_L \\ d_L \end{pmatrix}$, $\begin{pmatrix} \nu_L \\ e_L \end{pmatrix}$	$\begin{pmatrix} \nu_R \\ e_R \end{pmatrix}$	Y_{SM} for quarks, $-\frac{1}{2}$ for leptons
	Fermio-Phobic (FP)	$\begin{pmatrix} u_L \\ d_L \end{pmatrix}$, $\begin{pmatrix} \nu_L \\ e_L \end{pmatrix}$		Y_{SM} for quarks, Y_{SM} for leptons

Table 1.1: The charge assignments of the different G_{221} models to the Standard Model fermions considered in this thesis. Fields that do not appear in a given column are transforming as singlets. Note that some models (LR, LP, HP) also require right-handed neutrinos ν_R . In the other cases, right-handed neutrinos may be present as SM singlets or just be absent.

The symmetry breaking is usually realised in two steps and at two energy scales. This is done, first, by breaking the $SU(2)_1 \times SU(2)_2 \times U(1)_X$ down to the Standard Model gauge group, which is, secondly, broken down to the $U(1)_{EM}$. The G_{221} models can be categorized by two patterns of SB, the breaking pattern-I (**BP-I**) and the breaking pattern-II (**BP-II**). In **BP-I**, the $SU(2)_1$ is identified as the $SU(2)_L$ of the Standard Model. The first stage of SB then is $SU(2)_2 \times U(1)_X$ to $U(1)_Y$ at a high scale¹. The second stage SB is the same as in the Standard

¹The high scale can in principle be anywhere between the electroweak and the Planck scale. However, for the heavy resonances to be accessible at the LHC the high scale has to be on the order of the TeV-scale.

Model, i.e. $SU(2)_L \times U(1)_Y$ to $U(1)_{EM}$ at the electroweak scale. This scheme applies not only to Left-Right, but also to Lepto-Phobic, Hadro-Phobic and to Fermio-Phobic models. In contrast, in **BP-II**, the $U(1)_X$ is identified with the $U(1)_Y$ of the Standard Model as in the Un-Unified and the Non-Universal models. Thus, the first stage of SB is $SU(2)_1 \times SU(2)_2$ to $SU(2)_L$ at the high scale. The second stage of SB is again the same as in the Standard Model. This classification is summarised in Table 1.2.

To complete the two stages of SB two multiplets of complex scalar fields are required. While experimental constraints on the electroweak gauge boson masses leave little freedom in the Higgs representation used for the electroweak SB, one has more freedom in the choice of the representation of the scalar used for the first stage SB. In **BP-I** we consider the two simplest

category	Identification	first stage	second stage
BP-I	$SU(2)_1 \equiv SU(2)_L$	$SU(2)_2 \times U(1)_X \rightarrow U(1)_Y$	$SU(2)_L \times U(1)_Y \rightarrow U(1)_{EM}$
BP-II	$U(1)_X \equiv U(1)_Y$	$SU(2)_1 \times SU(2)_2 \rightarrow SU(2)_L$	$SU(2)_L \times U(1)_Y \rightarrow U(1)_{EM}$

Table 1.2: The different patterns and stages of symmetry breaking in the considered G_{221} models.

cases for the first stage of SB: via a complex doublet scalar, or a complex triplet scalar. On the other hand, in **BP-II** we consider the simplest case of using a bi-doublet Higgs to achieve this SB. For the convenience of typesetting, we denote the **BP-I** models with first stage SB triggered by an $SU(2)$ -doublet(-triplet) as **BP-I-D** (**BP-I-T**)². The vacuum expectation value (VEV) of the various scalars and their quantum numbers are shown in Table 1.3.

1.2 Two-step symmetry breaking and gauge boson masses

The extra $SU(2)$ gauge factor in the G_{221} class will add three gauge bosons to the four predicted by the Standard Model. As a consequence of the Lagrangian gauge invariance, all those bosons are massless, and will be denoted as:

$$SU(2)_1 : W_{1\mu}^i, \quad SU(2)_2 : W_{2\mu}^i, \quad U(1)_X : X_\mu, \quad (i = 1, 2, 3). \quad (1.1)$$

²As usual, the components of the $SU(2)$ -triplet have been written as a 2×2 matrix using $\Phi \equiv \vec{\Phi} \cdot \vec{\sigma}$ where $\vec{\sigma}$ are the Pauli matrices. See, e.g., [Higgs Hunter's Guide, section 6.5]. Note that the index structure of the bi-doublet is $\Phi_{\alpha\dot{\alpha}}$ where the undotted index transforms according to the representation 2 of $SU(2)$ and the dotted index according to the representation $\bar{2}$ (in the same way as left- and right-handed Weyl spinors transform).

	Models	Rep.	Multiplet	VEV
First Stage SB	LR-D, LP-D, HP-D, FP-D	$\Phi \sim (1, 2, \frac{1}{2})$	$\Phi = \begin{pmatrix} \phi^+ \\ \phi^0 \end{pmatrix}$	$\langle \Phi \rangle = \frac{1}{\sqrt{2}} \begin{pmatrix} 0 \\ u_D \end{pmatrix}$
	LR-T, LP-T, HP-T, FP-T	$\Phi \sim (1, 3, 1)$	$\Phi = \frac{1}{\sqrt{2}} \begin{pmatrix} \phi^+ & \sqrt{2}\phi^{++} \\ \sqrt{2}\phi^0 & -\phi^+ \end{pmatrix}$	$\langle \Phi \rangle = \frac{1}{\sqrt{2}} \begin{pmatrix} 0 & 0 \\ u_T & 0 \end{pmatrix}$
	UU, NU	$\Phi \sim (2, \bar{2}, 0)$	$\Phi = \begin{pmatrix} \phi^0 + \pi^0 & \sqrt{2}\pi^+ \\ \sqrt{2}\pi^- & \phi^0 - \pi^0 \end{pmatrix}$	$\langle \Phi \rangle = \frac{1}{\sqrt{2}} \begin{pmatrix} u & 0 \\ 0 & u \end{pmatrix}$
Second Stage SB	LR-D, LP-D, HP-D, FP-D	$H \sim (2, \bar{2}, 0)$	$H = \begin{pmatrix} h_1^0 & h_1^+ \\ h_2^- & h_2^0 \end{pmatrix}$	$\langle H \rangle = \frac{v}{\sqrt{2}} \begin{pmatrix} c_\beta & 0 \\ 0 & s_\beta \end{pmatrix}$
	LR-T, LP-T, HP-T, FP-T	$H \sim (2, \bar{2}, 0)$	$H = \begin{pmatrix} h_1^0 & h_1^+ \\ h_2^- & h_2^0 \end{pmatrix}$	$\langle H \rangle = \frac{v}{\sqrt{2}} \begin{pmatrix} c_\beta & 0 \\ 0 & s_\beta \end{pmatrix}$
	UU, NU	$H \sim (1, 2, \frac{1}{2})$	$H = \begin{pmatrix} h^+ \\ h^0 \end{pmatrix}$	$\langle H \rangle = \frac{v}{\sqrt{2}} \begin{pmatrix} 0 \\ 1 \end{pmatrix}$

Table 1.3: The scalar fields representations and the VEV that achieve the symmetry breaking of the G_{221} models.

In order to derive the mass terms of the various physical gauge bosons, one has to go from the gauge eigenstates basis, in which we initially write the Lagrangian in the unbroken phase, to the physical basis in the broken phase in which all the mass terms are diagonal. As discussed earlier, the SSB of the G_{221} models will take place in two stages. After the first stage only \hat{Z}' and \hat{W}'^\pm acquire a mass ($m_{\hat{Z}'(\hat{W}')}^2$). Next, during the second stage, the Higgs VEV not only confers masses to \hat{Z} and \hat{W}^\pm ($m_{\hat{Z}(\hat{W})}^2$), but also induces mass mixing contributions ($\delta m_{\hat{Z}(\hat{W})}^2$) that lead to $\hat{Z}' - \hat{Z}$ and $\hat{W}' - \hat{W}$ mixing, and additional contributions to the mass of the \hat{Z}' and \hat{W}'^\pm ($\Delta m_{\hat{Z}'(\hat{W}')}^2$). This is summarised in Figure 1.1 for models that follow **BP-II**. Note that the states with the hats ($\hat{}$) are the intermediate step between the gauge and the physical mass eigenstates which will be denoted without the hats. In what follows, we will illustrate this procedure by the models following **BP-II**, then a summary for the models following **BP-I** with a doublet scalar field for the first stage SB (**BP-I-D**) is given.

BP-II:

Gauge boson masses are generated after SSB from the kinetic terms of the scalar fields. Before we proceed we note the following. For a square matrix $A = (a_{ij})$, we have $Tr(A^\dagger A) = \sum_{i,j} |a_{ij}|^2$.

That is, the outcome is the sum of the absolute value squared of all matrix elements. According to this note and the definitions of the Higgs bi-doublet Φ , see Table 1.3, it follows that if we take the kinetic Lagrangian of the scalars in the form

$$\mathcal{L}_{Scalar} = Tr[(D_\mu \Phi)^\dagger (D^\mu \Phi)],$$

we get the standard complex scalar field kinetic term (i.e. $(\partial_\mu \Phi)^\dagger (\partial^\mu \Phi)$) for the separate components of the matrix fields plus of course the interaction terms between the Higgs fields and the various gauge fields. Using the cyclic property of the trace operation, it is easily checked that this is indeed gauge invariant. Explicitly,

$$Tr[(D_\mu \Phi)^\dagger (D^\mu \Phi)] \rightarrow Tr[U_2 (D_\mu \Phi)^\dagger U_1^\dagger U_1 (D_\mu \Phi) U_2^\dagger],$$

where the different U_1 and U_2 matrices all combine to unity matrices. Thus, taking into account the second stage SB scalar field, the kinetic terms for the scalars in **BP-II** models take the following form

$$\mathcal{L}_{Scalar} \supset Tr[(D_\mu \Phi)^\dagger (D^\mu \Phi)] + (D_\mu H)^\dagger (D^\mu H),$$

where

$$\begin{aligned} D_\mu \Phi &= \partial_\mu \Phi - ig_1 \frac{1}{2} \vec{\sigma} \cdot \vec{W}_{1\mu} \Phi - ig_2 \Phi \frac{1}{2} \vec{\sigma}_{2^*} \cdot \vec{W}_{2\mu} \\ \text{using } \sigma_{2^*}^a &= -(\sigma_2^a)^* = -(\sigma_2^a)^T \equiv -(\sigma^a)^T \quad \text{one obtains} \\ D_\mu \Phi &= \partial_\mu \Phi - ig_1 \frac{1}{2} \vec{\sigma} \cdot \vec{W}_{1\mu} \Phi + ig_2 \Phi \frac{1}{2} \vec{\sigma} \cdot \vec{W}_{2\mu} \\ D_\mu H &= \partial_\mu H - ig_2 \frac{1}{2} \vec{\sigma} \cdot \vec{W}_{2\mu} H - i \frac{1}{2} g_X X_\mu H. \end{aligned} \tag{1.2}$$

For the sake of brevity, the μ index will be omitted in the rest of this section.

Step I:

At the first stage, the bi-doublet scalar field Φ takes its VEV and breaks the $SU(2)_1 \times SU(2)_2$ symmetry to $SU(2)_L$. Thus, after rotating the first and second components of the two $SU(2)$ s,

i.e. $W_{1(2)}^\pm = \frac{W_{1(2)}^1 \mp iW_{1(2)}^2}{\sqrt{2}}$, the charged gauge boson mass matrix can be written as

$$\begin{pmatrix} W_1^+ & W_2^+ \end{pmatrix} \frac{1}{4} u^2 \begin{pmatrix} g_1^2 & -g_1 g_2 \\ -g_1 g_2 & g_2^2 \end{pmatrix} \begin{pmatrix} W_1^- \\ W_2^- \end{pmatrix}. \tag{1.3}$$

Diagonalising this matrix leads to the masses of the charged gauge bosons, and to their compositions in terms of the gauge eigenstates. Here, we will obtain two massless gauge bosons called \hat{W}^\pm and two massive ones named \hat{W}'^\pm with $m_{\hat{W}'}^2 = \frac{1}{4}(g_1^2 + g_2^2)u^2$. These mass eigenstates are related to the non-physical gauge bosons by ³

$$\begin{pmatrix} \hat{W}^\pm \\ \hat{W}'^\pm \end{pmatrix} = \begin{pmatrix} c_\phi & s_\phi \\ -s_\phi & c_\phi \end{pmatrix} \begin{pmatrix} W_2^\pm \\ W_1^\pm \end{pmatrix}, \quad (1.4)$$

where ϕ is the mixing angle of the first stage SB and

$$c_\phi = \frac{g_1}{\sqrt{g_1^2 + g_2^2}}, \quad s_\phi = \frac{g_2}{\sqrt{g_1^2 + g_2^2}}. \quad (1.5)$$

On the other hand, spanned by the third components of the two $SU(2)$ gauge factors, the neutral mass matrix is written as

$$\frac{1}{2} \begin{pmatrix} W_1^3 & W_2^3 \end{pmatrix} \frac{1}{4} u^2 \begin{pmatrix} g_1^2 & -g_1 g_2 \\ -g_1 g_2 & g_2^2 \end{pmatrix} \begin{pmatrix} W_1^3 \\ W_2^3 \end{pmatrix}. \quad (1.6)$$

Again, by diagonalising this matrix we will obtain two states, \hat{W}^3 and \hat{Z}' of which the former is massless while the mass of the second reads $m_{\hat{Z}'}^2 = \frac{1}{4}(g_1^2 + g_2^2)u^2$, and the composition of the mass eigenstates at this stage is

$$\begin{pmatrix} \hat{W}^3 \\ \hat{Z}' \end{pmatrix} = \begin{pmatrix} c_\phi & s_\phi \\ -s_\phi & c_\phi \end{pmatrix} \begin{pmatrix} W_2^3 \\ W_1^3 \end{pmatrix}, \quad (1.7)$$

note that the mixing angle ϕ is the same as in (1.5). Thus, after the first stage of SB, there is still an unbroken $SU(2)_L \times U(1)_Y$ symmetry, which may be identified as the Standard Model gauge group. The gauge bosons $\hat{W}^{\pm,3}$ and $X \equiv \hat{B}$ are massless, and only \hat{Z}' and \hat{W}'^\pm are massive.

Step II:

At the electroweak scale, the second stage SB takes place and the second scalar field H acquire its VEV, which induces further mixing among the gauge bosons. Thus the charged gauge boson

³Note that in the following the sine, cosine and tangent trigonometric functions are shortened, e.g. $s_x \equiv \sin x$, $c_x \equiv \cos x$ and $t_x \equiv \tan x$ respectively.

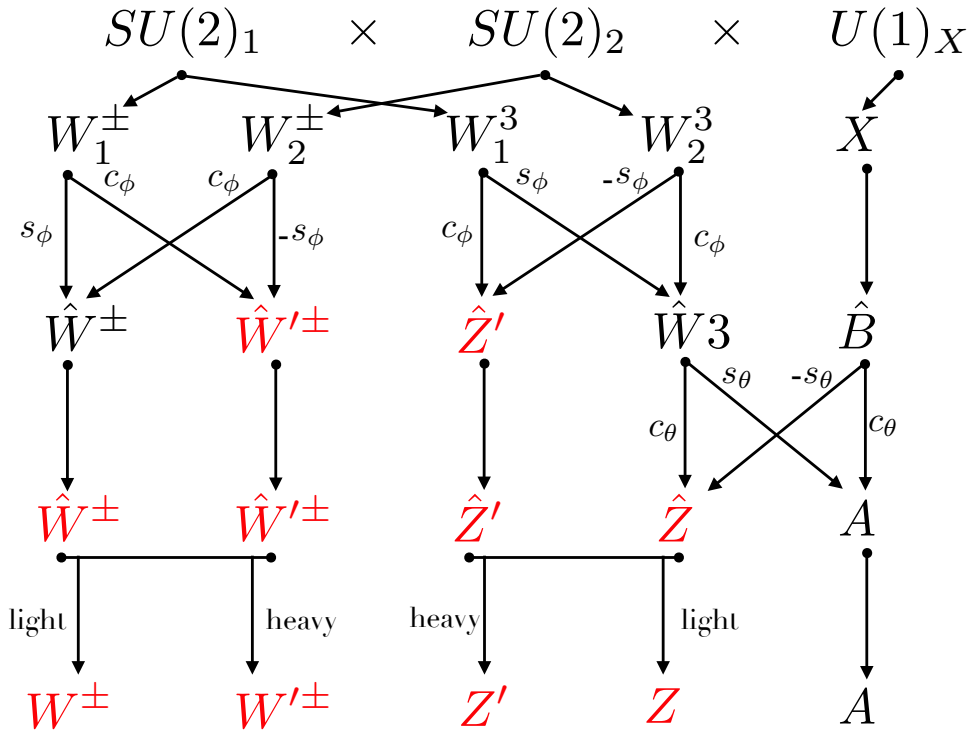


Figure 1.1: The mixing of the gauge bosons in **BP-II**. The gauge bosons colored in red are massive while bosons colored in black are massless.

mass matrix takes the following form

$$\begin{pmatrix} \hat{W}^+ & \hat{W}'^+ \end{pmatrix} \begin{pmatrix} m_{\hat{W}}^2 & \delta m_{\hat{W}}^2 \\ \delta m_{\hat{W}}^2 & m_{\hat{W}'}^2 + \Delta m_{\hat{W}'}^2 \end{pmatrix} \begin{pmatrix} \hat{W}^- \\ \hat{W}'^- \end{pmatrix}, \quad (1.8)$$

where for **BP-II**, one finds (see Appendix A.1)

$$\begin{pmatrix} m_{\hat{W}}^2 & \delta m_{\hat{W}}^2 \\ \delta m_{\hat{W}}^2 & m_{\hat{W}'}^2 + \Delta m_{\hat{W}'}^2 \end{pmatrix} = \frac{1}{4} \begin{pmatrix} g_2^2 c_\phi^2 v^2 & -g_1 g_2 s_\phi^2 v^2 \\ -g_1 g_2 s_\phi^2 v^2 & 4m_{\hat{W}'}^2 + g_2^2 s_\phi^2 v^2 \end{pmatrix}. \quad (1.9)$$

In the neutral sector and after rotating the fields similarly to the Standard Model, one obtains the gauge boson A, which turn out to be the photon, and \hat{Z} in terms of the massless gauge bosons \hat{W}^3 and \hat{B}

$$\begin{pmatrix} A \\ \hat{Z} \end{pmatrix} = \begin{pmatrix} c_\theta & s_\theta \\ -s_\theta & c_\theta \end{pmatrix} \begin{pmatrix} \hat{B} \\ \hat{W}^3 \end{pmatrix}, \quad (1.10)$$

where $\hat{\theta}$ is the second stage mixing angle and

$$c_{\hat{\theta}} = \frac{g_L}{\sqrt{g_L^2 + g_Y^2}}, \quad s_{\hat{\theta}} = \frac{g_Y}{\sqrt{g_L^2 + g_Y^2}}, \quad (1.11)$$

with $g_L = \left(\frac{1}{g_1^2} + \frac{1}{g_2^2}\right)^{-\frac{1}{2}}$ and $g_Y = g_X$ for the models following **BP-II**. This leads to the second stage SB neutral mass matrix

$$\frac{1}{2} \begin{pmatrix} \hat{Z} & \hat{Z}' \end{pmatrix} \begin{pmatrix} m_{\hat{Z}}^2 & \delta m_{\hat{Z}}^2 \\ \delta m_{\hat{Z}}^2 & m_{\hat{Z}'}^2 + \Delta m_{\hat{Z}'}^2 \end{pmatrix} \begin{pmatrix} \hat{Z} \\ \hat{Z}' \end{pmatrix}, \quad (1.12)$$

which reads for **BP-II** as (see Appendix A.1)

$$\begin{pmatrix} m_{\hat{Z}}^2 & \delta m_{\hat{Z}}^2 \\ \delta m_{\hat{Z}}^2 & m_{\hat{Z}'}^2 + \Delta m_{\hat{Z}'}^2 \end{pmatrix} = \frac{1}{4} \begin{pmatrix} (g_2 c_{\phi} c_{\theta} + g_X s_{\theta})^2 v^2 & -g_1 g_2 g_X \frac{s_{\phi}^2}{e} v^2 \\ -g_1 g_2 g_X \frac{s_{\phi}^2}{e} v^2 & 4m_{\hat{Z}'}^2 + g_2^2 s_{\phi}^2 v^2 \end{pmatrix}. \quad (1.13)$$

Finally, the diagonalisation of the matrices in Eqs. (1.8, 1.12), taking into account that the scale of the first stage SB is much larger than the electroweak scale, leads to the physical mass eigenstates denoted without the hats (similarly for the charged gauge bosons)

$$Z \equiv \hat{Z} - \frac{\delta m_{\hat{Z}}^2}{m_{\hat{Z}'}^2} \hat{Z}', \quad (1.14)$$

$$Z' \equiv \frac{\delta m_{\hat{Z}}^2}{m_{\hat{Z}'}^2} \hat{Z} + \hat{Z}', \quad (1.15)$$

and to their masses

$$m_{Z(W)}^2 = m_{\hat{Z}(\hat{W})}^2 - \frac{(\delta m_{\hat{Z}(\hat{W})}^2)^2}{m_{\hat{Z}'(\hat{W}')}^2 - m_{\hat{Z}(\hat{W})}^2 + \delta m_{\hat{Z}'(\hat{W}')}^2}, \quad (1.16)$$

$$m_{Z'(W')}^2 = m_{\hat{Z}'(\hat{W}')}^2 + \delta m_{\hat{Z}'(\hat{W}')}^2 + \frac{(\delta m_{\hat{Z}(\hat{W})}^2)^2}{m_{\hat{Z}'(\hat{W}')}^2 - m_{\hat{Z}(\hat{W})}^2 + \delta m_{\hat{Z}'(\hat{W}')}^2}. \quad (1.17)$$

Thus, using Eq. (1.17) one can write down the squared mass matrix of the physical gauge bosons in an expansion of powers of the vacuum expectation values for the various G_{221} models:

BP-II, $x = \frac{v}{u} \ll 1$:

$$m_{W'}^2 = \frac{1}{2}(g_1^2 + g_2^2)u^2 + \frac{g_2^2 s_\phi^2 u^2}{4} x^2 + \frac{s_\phi^6 g_1^2 u^2}{8} x^4 + \mathcal{O}(x^6), \quad (1.18)$$

$$m_{Z'}^2 = \frac{1}{2}(g_1^2 + g_2^2)u^2 + \frac{g_2^2 s_\phi^2 u^2}{4} x^2 + \frac{s_\phi^6 g_1^2 g_X^2 u^2}{8e^2} x^4 + \mathcal{O}(x^6), \quad (1.19)$$

where $e = \frac{g_1 g_2 g_X}{\sqrt{g_1^2 g_2^2 + g_1^2 g_X^2 + g_2^2 g_X^2}}$ is the electromagnetic charge. From Eqs. (1.18, 1.19) it is clear that in **BP-II**, the masses of W' and Z' are equal up to order x^2 included. Thus, one can assume that the new gauge bosons masses are identical in this breaking pattern.

BP-I-D:

We now summarise this procedure for the models following **BP-I-D**. The kinetic terms of the scalar fields in the model reads

$$\mathcal{L}_{Scalar} \supset (D_\mu \Phi)^\dagger (D^\mu \Phi) + Tr[(D_\mu H)^\dagger (D^\mu H)],$$

where

$$\begin{aligned} D_\mu \Phi &= \partial_\mu \Phi - ig_2 \frac{1}{2} \vec{\sigma} \cdot \vec{W}_{2\mu} \Phi - i \frac{1}{2} g_X X_\mu \Phi, \\ D_\mu H &= \partial_\mu H - ig_1 \frac{1}{2} \vec{\sigma} \cdot \vec{W}_{1\mu} H + ig_2 H \frac{1}{2} \vec{\sigma} \cdot \vec{W}_{2\mu}. \end{aligned} \quad (1.20)$$

Step I:

Once Φ has acquired its VEV one obtains the charged gauge bosons matrix

$$\left(\hat{W}^+ \quad \hat{W}'^+ \right) \frac{1}{4} u_D^2 \begin{pmatrix} 0 & 0 \\ 0 & g_2^2 \end{pmatrix} \begin{pmatrix} \hat{W}^- \\ \hat{W}'^- \end{pmatrix}, \quad (1.21)$$

where $\hat{W}^\pm \equiv W_1^\pm = \frac{W_1^1 \mp iW_1^2}{\sqrt{2}}$ and $\hat{W}'^\pm \equiv W_2^\pm = \frac{W_2^1 \mp iW_2^2}{\sqrt{2}}$. Thus only \hat{W}'^\pm becomes massive

($m_{\hat{W}'}^2 = \frac{1}{4} g_2^2 u_D^2$) after the first stage SB which of course is a consequence of the identification $SU(2)_1 \equiv SU(2)_L$.

In the neutral sector spanned by W_2^3 and X gauge bosons the mass matrix is read off the Lagrangian

$$\frac{1}{2} \begin{pmatrix} W_2^3 & X \end{pmatrix} \frac{1}{4} u_D^2 \begin{pmatrix} g_2^2 & -g_2 g_X \\ -g_2 g_X & g_X^2 \end{pmatrix} \begin{pmatrix} W_2^3 \\ X \end{pmatrix}. \quad (1.22)$$

Diagonalising this matrix leads to two states, \hat{B} and \hat{Z}' of which the former is massless, while the mass of the second reads $m_{\hat{Z}'}^2 = \frac{1}{4}(g_2^2 + g_X^2)u_D^2$, and to the relation between the mass eigenstates and the gauge eigenstates

$$\begin{pmatrix} \hat{B} \\ \hat{Z}' \end{pmatrix} = \begin{pmatrix} c_\phi & s_\phi \\ -s_\phi & c_\phi \end{pmatrix} \begin{pmatrix} X \\ W_2^3 \end{pmatrix}, \quad (1.23)$$

where ϕ is again the mixing angle of the first stage SB and

$$c_\phi = \frac{g_2}{\sqrt{g_2^2 + g_X^2}}, \quad s_\phi = \frac{g_X}{\sqrt{g_2^2 + g_X^2}}. \quad (1.24)$$

Hence, after rotating the fields according to ϕ we obtain after the first stage SB a massive \hat{W}'^\pm , a massive \hat{Z}' and three massless gauge bosons \hat{B} and \hat{W}^\pm .

Step II:

Below the electroweak scale the scalar field H acquires its VEV and the second stage SB occurs. Hence, The gauge bosons \hat{W}'^\pm and \hat{W}^\pm further mix and the second stage SB charged mass reads

$$\begin{pmatrix} \hat{W}^+ & \hat{W}'^+ \end{pmatrix} \frac{1}{4} \begin{pmatrix} g_1^2 v^2 & -g_1 g_2 s_2 \beta v^2 \\ -g_1 g_2 s_2 \beta v^2 & g_2^2 u_D^2 + g_2^2 v^2 \end{pmatrix} \begin{pmatrix} \hat{W}^- \\ \hat{W}'^- \end{pmatrix}. \quad (1.25)$$

In the neutral sector using Eqs. (1.10, 1.11), the second stage SB neutral mass reads

$$\frac{1}{2} \begin{pmatrix} \hat{Z} & \hat{Z}' \end{pmatrix} \frac{1}{4} \begin{pmatrix} \frac{g_1^2}{v^2} & -\frac{c_\phi^2}{e} g_1 g_2 g_X v^2 \\ -\frac{c_\phi^2}{e} g_1 g_2 g_X v^2 & 4m_{\hat{Z}'}^2 + g_2^2 c_\phi^2 v^2 \end{pmatrix} \begin{pmatrix} \hat{Z} \\ \hat{Z}' \end{pmatrix}, \quad (1.26)$$

note that $g_L = g_1$ and $g_Y = \left(\frac{1}{g_2^2} + \frac{1}{g_X^2}\right)^{-\frac{1}{2}}$. Finally, following Eq. (1.17), the squared masses for the physical gauge bosons in expansion of power of v over u_D are given by:

$$\mathbf{BP-I-D}, x = \frac{v}{u_D} \ll 1 :$$

$$m_{W'}^2 = \frac{1}{4}g_2^2 u_D^2 + \frac{1}{4}g_2^2 u_D^2 x^2 + g_1^2 c_\beta^2 s_\beta^2 u_D^2 x^4 + \mathcal{O}(x^6), \quad (1.27)$$

$$m_{Z'}^2 = \frac{1}{4}g_2^2 u_D^2 (1+t_\phi^2) + \frac{g_2^2 u_D^2}{4(1+t_\phi^2)} x^2 + \frac{(g_1^2 + g_1^2(1+t_\phi^2))u_D^2}{4g_2^2(1+t_\phi^2)^3} x^4 + \mathcal{O}(x^6), \quad (1.28)$$

Similarly, for the models following **BP-I** with a triplet scalar field for the first stage SB one finds

$$\mathbf{BP-I-T}, x = \frac{v}{u_T} \ll 1 :$$

$$m_{W'}^2 = \frac{1}{2}g_2^2 u_T^2 + \frac{1}{4}g_2^2 u_T^2 x^2 + \frac{g_1^2}{2}c_\beta^2 s_\beta^2 u_T^2 x^4 + \mathcal{O}(x^6), \quad (1.29)$$

$$m_{Z'}^2 = g_2^2 u_T^2 (1+t_\phi^2) + \frac{g_2^2 u_T^2}{4(1+t_\phi^2)} x^2 + \frac{(g_1^2 + g_1^2(1+t_\phi^2))u_T^2}{16g_2^2(1+t_\phi^2)^3} x^4 + \mathcal{O}(x^6). \quad (1.30)$$

From Eqs. (1.27)-(1.30) one can see that the new heavy gauge boson masses are not degenerated in **BP-I**, and that the mass dependency on β is negligible. Finally, for the expressions of the various mass matrices we refer the reader to Table VI of [52], which we have independently verified.

1.3 Neutral and charged fermionic currents

As in the SM, the W' - and Z' -boson interactions with leptons and quarks arise in the G_{221} models from the fermion kinetic Lagrangian

$$\mathcal{L}_{fermion} = \bar{f}_i i \gamma_\mu D^\mu f_i, \quad (1.31)$$

in which the sum runs over all the fermions in the model. The fermion fields are chosen to transform in specific representations under the G_{221} gauge group, leading to a different expression for the covariant derivative in each model. Although different breaking patterns and different group representations of the fermions will lead to different Lagrangians, one can write

the fermion kinetic Lagrangian in a general form

$$\begin{aligned} \mathcal{L}_{fermion} = & \widehat{W}_\mu^+ J^{+\mu} + \widehat{W}_\mu^- J^{-\mu} + \widehat{Z}_\mu J^{0\mu} + A_\mu J^\mu \\ & + \widehat{W}_\mu'^+ K^{+\mu} + \widehat{W}_\mu'^- K^{-\mu} + \widehat{Z}_\mu' K^{0\mu}, \end{aligned} \quad (1.32)$$

where the first line takes the same expression as in the SM and the second line is the new physics contribution. The SM-like currents have the familiar form

$$\begin{aligned} J_\mu &= e \sum_f Q^f \bar{f} \gamma_\mu f, \\ J_\mu^0 &= \sqrt{g_L^2 + g_Y^2} \sum_f [(T_L^{3,f} - s_\theta^2 Q^f) P_L - s_\theta^2 Q^f P_R] \bar{f} \gamma_\mu f, \\ J_\mu^+ &= \frac{g_L}{\sqrt{2}} \sum_f T_L^{+,f} P_L \bar{f} \gamma_\mu f, \end{aligned} \quad (1.33)$$

where the expressions for g_Y and g_L depend on the model. Furthermore Q^f is the charge of the fermion f , $T_L^{3,f}$ the third component of the isospin of $SU(2)_L$ ⁴ for the fermion f , and e plays the role of the electromagnetic charge. The expressions for the new currents K^0 and K^\pm are model dependent and can be read off Tables IV and V of [52].

Note that until now, the gauge bosons in $\mathcal{L}_{fermion}$ are not in the final physical state. In order to reach the interactions between the new heavy resonances and the fermionic fields, one has to rewrite $\mathcal{L}_{fermion}$ in terms of the mass eigenstates for both neutral and charged gauge bosons. This is done by first inverting Eqs. (1.14, 1.15) and then inserting the results in Eq. (1.32). Thus the fermion kinetic Lagrangian reads

$$\begin{aligned} \mathcal{L}_{fermion} = & W_\mu^+ \left(J^{+\mu} - \frac{\delta m_{\widehat{W}}^2}{m_{\widehat{W}'}^2} K^{+\mu} \right) + (+ \longleftrightarrow -) \\ & + W_\mu'^+ \left(K^{+\mu} + \frac{\delta m_{\widehat{W}}^2}{m_{\widehat{W}'}^2} J^{+\mu} \right) + (+ \longleftrightarrow -) \\ & + Z_\mu \left(J^{0\mu} - \frac{\delta m_{\widehat{Z}}^2}{m_{\widehat{Z}'}^2} K^{0\mu} \right) \\ & + Z_\mu \left(K^{0\mu} + \frac{\delta m_{\widehat{Z}}^2}{m_{\widehat{Z}'}^2} J^{0\mu} \right) \\ & + A_\mu J^\mu. \end{aligned} \quad (1.34)$$

⁴In **BP-I** the third component of isospin of the $SU(2)_L$ is identified with the third component of the isospin of $SU(2)_1$, while in **BP-II** it is identified with the sum of the third components of $SU(2)_1$ and $SU(2)_2$ isospin.

This procedure is exemplified in full detail for the NU model in Appendix A.2.

From another perspective, the most general Lorentz invariant Lagrangian describing the interaction of a neutral or a charged vector boson with the SM fermions⁵ can be written as

$$\begin{aligned} \mathcal{L}_{CC}^{W'} = \frac{g_W}{\sqrt{2}} & \left[\bar{u}_i \gamma^\mu \left((C_{q,L}^{W'})_{i,j} P_L + (C_{q,R}^{W'})_{i,j} P_R \right) d_j \right. \\ & \left. + \bar{v}_i \gamma^\mu \left((C_{\ell,L}^{W'})_{i,j} P_L + (C_{\ell,R}^{W'})_{i,j} P_R \right) e_j \right] W'_\mu + h.c., \end{aligned} \quad (1.35)$$

$$\begin{aligned} \mathcal{L}_{NC}^{Z'} = \frac{g_W}{c_{\theta_W}} & \left[\bar{q}_i \gamma^\mu \left((C_{q,L}^{Z'})_{i,j} P_L + (C_{q,R}^{Z'})_{i,j} P_R \right) q_j \right. \\ & \left. + \bar{\ell}_i \gamma^\mu \left((C_{\ell,L}^{Z'})_{i,j} P_L + (C_{\ell,R}^{Z'})_{i,j} P_R \right) \ell_j \right] Z'_\mu + h.c., \end{aligned} \quad (1.36)$$

where $q \in \{u_i, d_j\}$, $\ell \in \{v_i, e_j\}$ ($i, j = 1, 2, 3$). In addition, $P_{L,R} = (1 \pm \gamma_5)/2$, g_W is the $SU(2)_L$ gauge coupling, and θ_W is the Weinberg angle. Last but not least, the $C_{q,L(R)}$, $C_{\ell,L(R)}$ are arbitrary complex couplings that parametrise the interaction of the new resonances.

The expressions for the couplings for the different G_{221} models can be obtained by manipulating Eq. (1.34) so that it can be compared to Eqs. (1.35, 1.36). For **BP-II** models, we will use the symbol M to denote the mass of the new particle regardless of its nature since the masses of the new gauge bosons are degenerate, see Eqs. (1.18, 1.19), and t_ϕ the first stage SB tangent angle. In **BP-I**, we will use either $m_{W'}$ or $m_{Z'}$. Hence, the couplings will be expressed in terms of two new parameters compared to the SM for both **BP-I**⁶ and **BP-II** [53].

BP-I:

$$\begin{aligned} C_{q,L}^{W'} &= -\varepsilon^{W'}(t_\phi, m_{W'}, \beta) V_{CKM} \\ C_{\ell,L}^{W'} &= -\varepsilon^{W'}(t_\phi, m_{W'}, \beta) \\ C_{q(\ell),L}^{Z'} &= -s_\theta X^{q(\ell)} t_\phi + (T_L^{3,q(\ell)} + Q^{q(\ell)} s_\theta^2) \varepsilon^{Z'}(t_\phi, m_{Z'}) \\ C_{q(\ell),R}^{Z'} &= s_\theta (-X^{q(\ell)} t_\phi + T_L^{3,q(\ell)} \frac{1}{t_\phi}) + Q^{q(\ell)} s_\theta^2 \varepsilon^{Z'}(t_\phi, m_{Z'}) \end{aligned} \quad (1.37)$$

⁵This may also include a right-handed neutrino for each generation of SM fermions.

⁶In the case of **BP-I** the dependence on β can be neglected since it only enters via the $\varepsilon^{Z'(W')}$ functions which are strongly suppressed as will be further discussed below.

Left-Right

$$C_{q,R}^{W'} = -t_\theta \sqrt{\frac{1+t_\phi^2}{t_\phi^2}} V_R$$

$$C_{\ell,R}^{W'} = -t_\theta \sqrt{\frac{1+t_\phi^2}{t_\phi^2}}$$

Lepto-Phobic

$$C_{q,R}^{W'} = -t_\theta \sqrt{\frac{1+t_\phi^2}{t_\phi^2}} V_R \quad (1.38)$$

$$C_{\ell,R}^{W'} = 0$$

Hadro-Phobic

$$C_{q,R}^{W'} = 0$$

$$C_{\ell,R}^{W'} = -t_\theta \sqrt{\frac{1+t_\phi^2}{t_\phi^2}}$$

Fermio-Phobic

$$C_{q,R}^{W'} = 0 \quad (1.39)$$

$$C_{\ell,R}^{W'} = 0$$

BP-II:

Un-Unified

$$C_{q,L}^{W'} = \frac{1}{t_\phi} - c_\theta \mathcal{E}(t_\phi, m)$$

$$C_{\ell,L}^{W'} = -t_\phi - c_\theta \mathcal{E}(t_\phi, m)$$

$$C_{q,L}^{Z'} = T_L^{3,q} c_\theta \frac{1}{t_\phi} + (T_L^{3,q} + Q^q s_\theta^2) \mathcal{E}(t_\phi, m)$$

$$C_{\ell,L}^{Z'} = -T_L^{3,q} c_\theta t_\phi + (T_L^{3,q} + Q^q s_\theta^2) \mathcal{E}(t_\phi, m)$$

$$C_{q,R}^{W'} = 0$$

$$C_{\ell,R}^{W'} = 0$$

$$C_{q,R}^{Z'} = Q^q s_\theta^2 \mathcal{E}(t_\phi, m)$$

$$C_{\ell,R}^{Z'} = Q^q s_\theta^2 \mathcal{E}(t_\phi, m) \quad (1.40)$$

Non-Universal (see Appendix A.2)

$$C_{q^{(\ell)(1,2)},L}^{W'} = \frac{1}{t_\phi} - c_\theta \mathcal{E}(t_\phi, m)$$

$$C_{q^{(\ell)(3)},L}^{W'} = -t_\phi - c_\theta \mathcal{E}(t_\phi, m)$$

$$C_{q^{(\ell)(1,2)},L}^{Z'} = c_\theta \frac{1}{t_\phi} T_L^{3,q^{(\ell)}} + \mathcal{E}(t_\phi, m) (T_L^{3,q^{(\ell)}} + Q^{q^{(\ell)}} s_\theta^2)$$

$$C_{q^{(\ell)(3)},L}^{Z'} = -c_\theta t_\phi T_L^{3,q^{(\ell)}} + \mathcal{E}(t_\phi, m) (T_L^{3,q^{(\ell)}} + Q^{q^{(\ell)}} s_\theta^2)$$

$$C_{q^{(\ell)(1,2)},R}^{W'} = 0$$

$$C_{q^{(\ell)(3)},R}^{W'} = 0$$

$$C_{q^{(\ell)(1,2)},R}^{Z'} = \mathcal{E}(t_\phi, m) Q^{q^{(\ell)}} s_\theta^2$$

$$C_{q^{(\ell)(3)},R}^{Z'} = \mathcal{E}(t_\phi, m) Q^{q^{(\ell)}} s_\theta^2 \quad (1.41)$$

where q and ℓ denote the quarks and the leptons of the SM, while (1, 2) and (3) are the (first, second) and (third) generation of the SM fermions, respectively. Moreover, $T^{3,f}$ is, as in Eq. (1.33), the sum of the third components of $SU(2)_1$ and $SU(2)_2$, Q^f is the electric charge, X^f is, as given in Table 1.1, the $U(1)_X$ charge, V_R the right-handed analogue of the CKM mixing matrix, and V_{CKM} has been omitted in the NU model. The $\varepsilon^{W'}(t_\phi, m_{W'}, \beta)$, $\varepsilon^{Z'}(t_\phi, m_{Z'}, \beta)$ and $\varepsilon(t_\phi, m)$ collect terms proportional to $s_{2\beta}^2 \sqrt{1 + t_\phi^2/m_{W'}^2} t_\phi$, $1/m_{Z'}^2 t_\phi$ and t_ϕ/m^2 , respectively. In the allowed regions, under the constraints derived from low energy and precision data, the values of ε are strongly suppressed ($\sim \mathcal{O}(10^{-4})$), see Figure 1 of Ref. [54].

It is worth mentioning that the **BP-II** models are sometimes named left-handed models due to the fact that the W' -boson does not couple to right-handed fermions. On the other hand, models following **BP-I** are sometimes referred to as right-handed models for the reason that the W' couplings to the left-handed fermions are suppressed. It can also be mentioned that the W' -boson in the LP model does not couple to leptons at all, hence the name Lepto-Phobic. Similarly, the W' -boson in the HP and FP models does not couple to quarks and fermions respectively. Finally, one can also see that, within these assumptions, the couplings in **BP-I** do not depend on the representation of the first stage SB scalar field.

Chapter 2

Z' , W' Precision predictions at the HL- and the HE-LHC

After the discovery of the Higgs boson [55, 56], the LHC physics program can be considered one of the most successful experimental programs in Science. Built by the European Organization for Nuclear Research (CERN), it was first commissioned in 2010 for proton–proton collisions with a 7 TeV centre-of-mass energy, a new record at the time, which has been increased to reach 8 TeV from April 2012 until the end of the so called Run 1 in 2013. Following a long technical stop in 2013–2014, it operated in Run 2 with proton collisions at 13 TeV centre-of-mass energy from June 2015 to deliver to ATLAS and CMS a total integrated luminosity of about 189 fb^{-1} by the end of 2018. A two-year long shutdown is now in progress (2019–2020) and Run 3 is expected to start in 2021, potentially providing collisions at the nominal energy of 14 TeV and with nominal target integrated luminosities of 350 fb^{-1} .

Subsequently, and in order to fully profit from its potential, the high-luminosity phase of the LHC will commence then in the mid-2020s, after another long shutdown, with the aim of delivering an integrated luminosity of 3 ab^{-1} to each ATLAS and CMS, again at a centre-of-mass energy of 14 TeV. This is shown schematically in Figure 2.1 [57]. Moreover, in the perspective

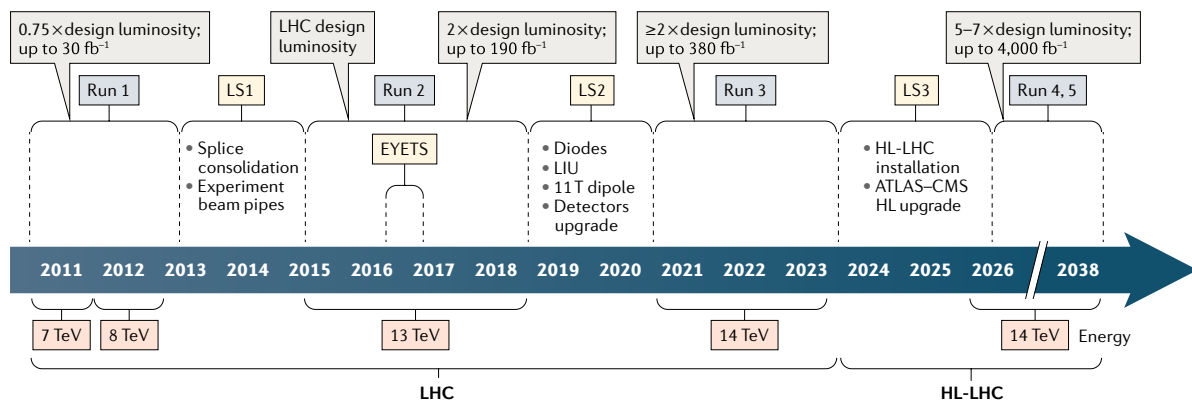


Figure 2.1: The LHC and the HL-LHC baseline plan for the next decade and beyond [57].

of pushing the LHC program even further, and relying on the future magnet technology, a high-energy LHC with a 27 TeV centre-of-mass energy that collects an integrated luminosity of 15 ab^{-1} could be installed.

The new heavy resonances that appear in G_{221} models have broad consequences. Indeed, because of their mixing with the SM W - and Z -bosons, all the SM processes involving the electroweak gauge bosons are sensitive to the new particles. In the previous chapter, we have

investigated this class of models, which are well motivated and simple to study since they can be described by two or three free parameters. Complementary to this study, in this chapter we focus on the HL- and HE-LHC phenomenology of these new resonances.

In Section 2.1 we present higher order predictions for top-quark pair production for models with Z' -bosons, while in Section 2.2 we study new physics contributions to the total cross section for the production of W' decaying into leptons. Besides the **BP-II** models, i.e, the NU and the UU models, we also consider the Sequential Standard Model [24], a toy model which copies the weak interactions of quarks and leptons by heavier versions W' and Z' of the W and Z boson, respectively. The only free parameters in this model are the masses of the new heavy gauge bosons. Due to its simplicity and convenience it is a widely used benchmark model in which LHC data are analysed.

2.1 Precision predictions for $pp \rightarrow Z' \rightarrow t\bar{t}$

Long after Makoto Kobayashi and Toshihide Maskawa explained the observed CP violations in kaon decay by the existence of a third generation of quarks [7], the top quark was discovered in 1995 at the $p\bar{p}$ collider (Tevatron) [58, 59], to be the heaviest elementary particle. Due to its short life-time, it decays before it hadronises, which offers a unique opportunity to study a bare quark through its decay products. Moreover, the processes with top quarks are very interesting since the 3rd generation plays a prominent role in the SM due to the Yukawa coupling of the top quark which is the only Yukawa coupling in the SM of order one. Therefore, it is quite conceivable that new physics (similar to the Higgs boson) couples predominantly to the top quark.

In the following we use the PBZp code [40] to obtain predictions for $t\bar{t}$ hadroproduction in the presence of a Z' resonance. This code contains the calculation of NLO QCD corrections to the electroweak $t\bar{t}$ production, properly accounting for the interference between SM (Z, γ) and new physics amplitudes, and implemented in the POWHEG BOX framework [42, 44, 60]. This framework allows to combine NLO QCD computations with parton shower Monte Carlos once the spin- and color-correlated Born amplitudes along with their virtual and real NLO QCD corrections are known.

Our results pertain to pp collisions at the HL- and HE-LHC and we present results for three models, the SSM and the UU- and NU models. As has been discussed in the previous chapter, in the UU model the quarks and leptons belong to different representations of the two $SU(2)$ gauge factors whereas in the NU model the first two generations transform differently than the third generation. Both models take two input parameters, the mixing angle of the first stage symmetry

breaking $t \equiv \tan \phi = g_2/g_1$ and the mass of the heavy resonance $m_{Z'}$. Exclusion limits on the parameters space for the G_{221} models have been derived in [52] by performing a global analysis of low-energy precision data. Improved limits for the W' and Z' masses were found in [54] using LHC data at $\sqrt{s} = 7$ and 8 TeV leading to $m_{W'} > 2.5$ TeV and 3.6 TeV in the UU and NU models, respectively. Accordingly, we choose the parameter $t = 0.465$ for the UU and $t = 0.438$ for the NU model. The top quark is assigned a mass of $m_t = 172.5$ GeV. The value of $\sin^2 \theta_W = 0.2312$ was taken from the Particle Data Group [61]. We vary the mass for total cross sections between 1 (2.5, 3.75) and 10 TeV for the SSM (UU, NU), respectively. The Z' width in all models is set to be the same as in the SSM, it has been calculated at leading order using PYTHIA 6 [62] with a running electro-magnetic coupling $\alpha(m_{Z'})$, such that $\Gamma_{Z'}^{SSM}/m_{Z'}$ slightly increases from 3.07% at $m_{Z'} = 1$ TeV to 3.19% at $m_{Z'} = 10$ TeV. For the parton distribution functions, we use the CT14nlo (ISET = 13100 in LHAPDF6) [63], and the renormalisation and factorisation scales μ_R and μ_F are identified with the invariant mass of the system. Opposed to our numerical results/studies in Chapter 3, no cut on the invariant mass of the $t\bar{t}$ pair has been applied.

2.1.1 Numerical results

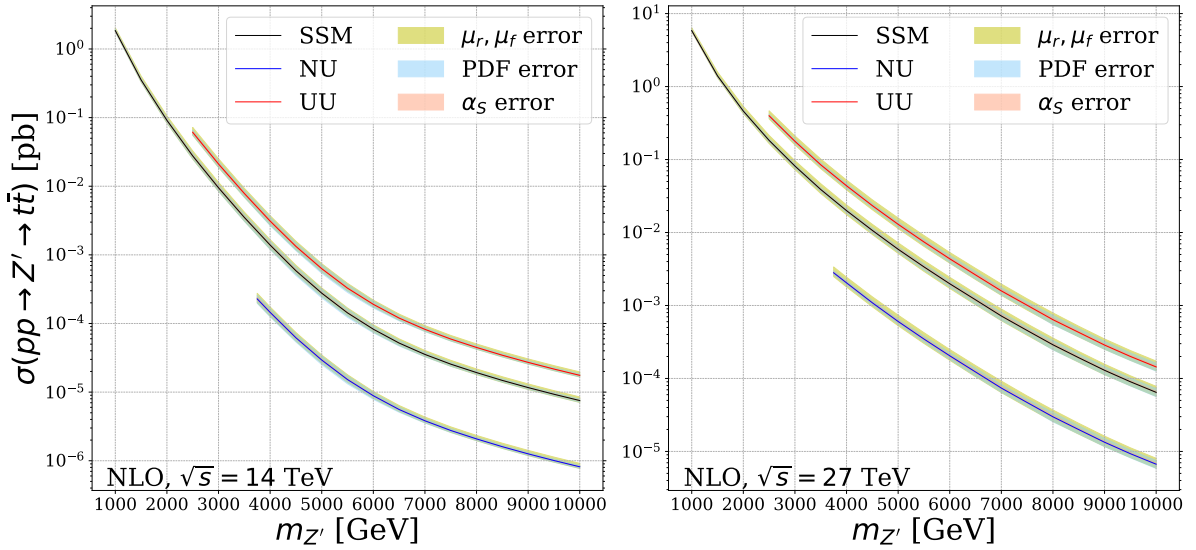


Figure 2.2: Left: NLO total cross section predictions in picobarns, with scale and α_s variation, and PDF uncertainties as a function of $m_{Z'}$, for $q\bar{q} \rightarrow Z' \rightarrow t\bar{t}[+g]$ in the NU, the UU, and the SSM, at a centre-of-mass energy $\sqrt{s} = 14$ TeV. Right: same as left but for a centre-of-mass energy $\sqrt{s} = 27$ TeV.

To illustrate the total number of events to be expected from resonant-only Z' -boson production at the LHC, we show on the left hand side of Figure 2.2 the total NLO cross sections at a centre-of-mass energy of $\sqrt{s} = 14$ TeV in the SSM (full black curve), the NU (full blue

curve), and the UU (full red curve) models, together with the associated renormalisation and factorization scale uncertainties (light khaki bands), the α_S uncertainties (light salmon bands), and the PDF uncertainties (light blue bands)¹. As one can see, in the case of the HL-LHC, with an integrated luminosity of 3 ab^{-1} , the number of expected events falls from almost 274×10^3 for $m_{Z'} = 2 \text{ TeV}$ to 23 for $m_{Z'} = 10 \text{ TeV}$ in the SSM and is about an order of magnitude smaller for the chosen parameters in the NU model, while for the chosen parameters in the UU model it ranges between almost 63×10^3 for $m_{Z'} = 3 \text{ TeV}$ and 53 for $m_{Z'} = 10 \text{ TeV}$. On the other hand, on the right hand side of Figure 2.2, we deal with the HE-LHC where $\sqrt{S} = 27 \text{ TeV}$ and the integrated luminosity is projected to be 15 ab^{-1} . Thus for the SSM we expect the number of events to fall from almost 7×10^6 at $m_{Z'} = 2 \text{ TeV}$ to almost 10^3 for $m_{Z'} = 10 \text{ TeV}$, and again less by about an order of magnitude in NU, while it ranges between 2.6×10^6 approximately for $m_{Z'} = 3 \text{ TeV}$ and 2×10^3 for $m_{Z'} = 10 \text{ TeV}$ in the UU model.

2.1.2 Uncertainties

Three different sources of uncertainty are presented in Figure 2.3, namely the renormalisation and factorization scale (light khaki bands), the strong coupling (light salmon bands), and the PFD (light blue bands) uncertainties. More specifically the ratio of the error bands to the central predictions is shown. On the left hand side we show the variations at $\sqrt{S} = 14 \text{ TeV}$ for SSM (top), UU model (centre), and NU model (bottom), and the same but for $\sqrt{S} = 27 \text{ TeV}$ is shown on the right hand side of Figure 2.3.

The renormalisation and the factorisation scale uncertainties have been estimated by varying their values in the range $[0.5, 2]$ times the nominal scale, with the constraint that $0.5 < \mu_F/\mu_R < 2$:² (i) $\mu_R = 0.5\mu_R^o$ and $\mu_F = 0.5\mu_F^o$, (ii) $\mu_R = 0.5\mu_R^o$ and $\mu_F = 1\mu_F^o$, (iii) $\mu_R = 1\mu_R^o$ and $\mu_F = 0.5\mu_F^o$, (iv) $\mu_R = 1\mu_R^o$ and $\mu_F = 2\mu_F^o$, (v) $\mu_R = 2\mu_R^o$ and $\mu_F = 1\mu_F^o$, (vi) $\mu_R = 2\mu_R^o$ and $\mu_F = 2\mu_F^o$, where μ_R^o and μ_F^o are the central renormalisation and factorisation scales, respectively. Then each one of the resulting 6 choices is divided by the central choice ($\mu_R = 1\mu_R^o$ and $\mu_F = 1\mu_F^o$), so that an envelope can be constructed by selecting the maximum and the minimum of the six ratios at each mass. As can be seen from Figure 2.3, the scale variations in the three models are of the order of 10 to 20 percent, which is relatively small and the typical size for NLO QCD predictions for an electroweak process. One reason might be that the renormalisation scale dependence only enters in one power of α_S which is also already quite small at $\mu_R \sim \mathcal{O}(\text{TeV})$ due to asymptotic freedom.

¹The PDF and α_S uncertainties are covered by the scale variation. They will be clearer in Figure 2.3.

²Note that this procedure is widely used in the literature. It is not fundamental but allows for reasonable comparisons as long as the same approach is used everywhere.

The uncertainties of the PDF extraction, due to uncertainties of the data, can be propagated into the theoretical prediction using for example the Hessian method [64, 65]. This method will typically lead to a best-fit or a central prediction. Additionally, modern PDFs will also provide the error pdfs. Here we use the CT14nlo PDF set [63], which, besides the PDF set with the value of $\alpha_S = 0.118$ (in this particular case, as well as in many other PDF fits, this represent the default choice), has 56 error pdfs that correspond to 28 eigenvectors of the Hessian matrix³. We estimate the uncertainty by applying the master formula of [66]:

$$\Delta\sigma = \frac{1}{2} \left(\sum_{i=1}^{N_p} [\sigma(S_i^+) - \sigma(S_i^-)]^2 \right)^{\frac{1}{2}} \quad (2.1)$$

where σ is the total cross section, and $\sigma(S_i^\pm)$ are the predictions for σ based on the PDF sets S_i^\pm from the eigenvector basis. What we show in Figure 2.3 is the envelope obtained through the ratio $(\sigma \pm \Delta\sigma)/\sigma$. As can be seen, the PDF uncertainties are generally slightly smaller than the scale uncertainties. In the case of the HL-LHC they increase with $m_{Z'}$ and reach $\pm 15\%$ at $m_{Z'} \sim 5 \dots 6$ TeV. For even larger Z' masses the uncertainty band then shrinks again to $\pm 5\%$. This behaviour may be understood as follows: due to the large resonance masses the PDFs are probed at high x -values where the PDF uncertainties become increasingly large. Assuming leading order kinematics and central rapidities one has $x_1 = x_2 = m_{Z'}\sqrt{S}$ at the s -channel resonance. For example, at $\sqrt{S} = 14$ TeV (HL-LHC) and $m_{Z'} = 6$ TeV the typical x -values are $x \sim 0.4$. Following this logic one might expect even higher x -values and hence larger PDF uncertainties for $m_{Z'} > 6$ TeV. However, at these high x values the sea quark PDFs are steeply falling overcompensating the enhancement due to the s -channel (Breit-Wigner) resonance at $\hat{s} = x_1 x_2 s = m_{Z'}^2$, such that eventually off-shell production of the Z' boson will dominate and the x -values probed do not further increase. At the HE-LHC with $\sqrt{S} = 27$ TeV, $x \sim 0.37$ for $m_{Z'} = 10$ TeV and we stay in the regime where on-shell production of the Z' resonance dominates for the entire $m_{Z'}$ range shown.

Finally, we present the uncertainty arising from the variation of the strong coupling constant which turns out to be the smallest one. Besides the PDF set with the value of $\alpha_S = 0.118$, which in many PDF fits represent the default choice, CT14nlo provides a series of NLO sets with different strong coupling constants $\alpha_S = 0.111\text{--}0.123$. Here we treat the α_S variations in the same way as in the case of the scale variations, i.e. by dividing each one of the 12 choices by the central cross section and then creating an envelope by choosing the maximum and the minimum for each mass of the heavy gauge-boson. As can be seen from Figure 2.3, the α_S variations are

³Note that there are two error PDFs associated to each eigenvector, one for the positive and one for the negative direction.

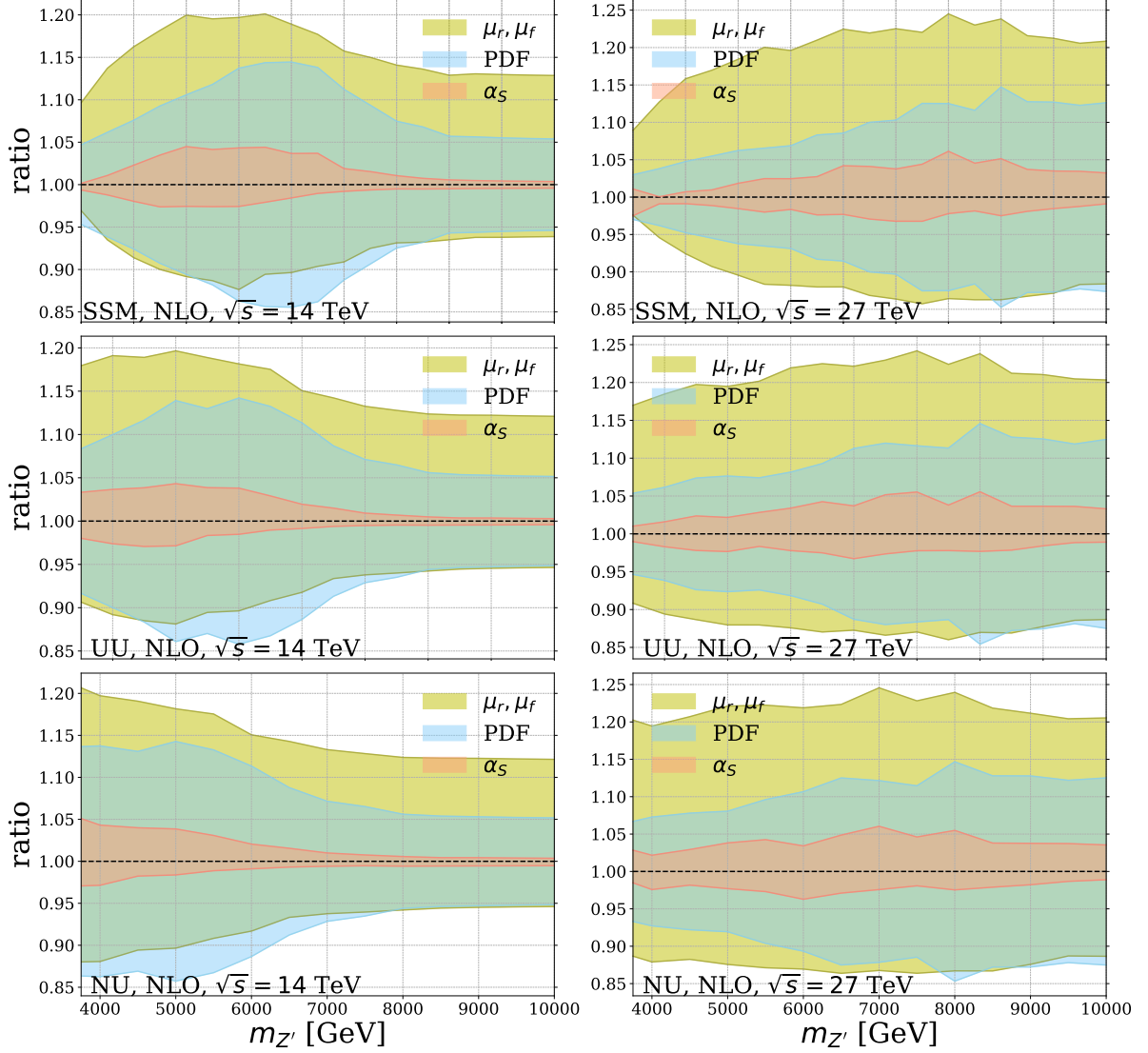


Figure 2.3: The fractional uncertainty due to the scale and the α_s variation, as well as the PDF uncertainty as a function of $m_{Z'}$, for $q\bar{q} \rightarrow Z' \rightarrow t\bar{t}[+g]$ in the SSM (top row), the UU model (centre row), and the NU model (bottom row), at the HL-LHC (left) and the HE-LHC (right).

the smallest ones. This may be because the available range of α_s values is relatively small. Also note that the α_s dependence only enters at the NLO level.

2.2 Precision predictions for $pp \rightarrow W' \rightarrow \ell\nu$

In this section we present the total cross section describing the production of a W' -boson decaying into a lepton and a neutrino, where the interference with SM W -boson is taken into account. This is done using the NLO+NLL code Resummino [41] which matches a soft-gluon

resummation at NLL accuracy to a fixed order NLO calculation. But first let us briefly explain the concept of resummation.

Despite the fact that NLO fixed order calculations are finite for well defined observables, logarithmic terms are usually present in the perturbation series. For example, such terms arise as finite remainders after the cancellations of soft singularities. There may also be logarithmic terms resulting from collinear particle emission off massive quarks (such as the top quark). These collinear logarithms are finite but can become large in certain regions of phase space. Beside the fact that such terms are large, the problem is that they appear systematically to all orders in the perturbative expansion. For instance, let us consider the following perturbative expansion for an observable O :

$$O = O^{(0)} + \alpha_S (a_1 \log(s) + \dots) + \alpha_S^2 (a_2 \log^2(s) + b_1 \log(s) + \dots) + \mathcal{O}(\alpha_S^3), \quad (2.2)$$

where s is a small ($\ll 1$) but positive parameter. We obtain, in this particular example, for each power of α_S^n , terms like:

- $\alpha_S^n \log^n(s)$ (Leading Logs, or LL),
- $\alpha_S^n \log^{n-1}(s)$ (Next-to-Leading Logs or NLL),
- $\alpha_S^n \log^{n-2}(s)$ (Next-to-Next-to-Leading Logs or NNLL), etc.

This means that what we call LL is a series of terms to all orders in α_S . These terms are multiplied by coefficients: $a_1 \alpha_S \log(s) + a_2 (\alpha_S \log(s))^2 + a_3 (\alpha_S \log(s))^3 + \dots$, this and the fact that $\alpha_S \log(s)$ can be of order one or larger implies that O is not convergent at all, i.e., the perturbation series with α_S as expansion parameter fails. In order to restore the predictivity of the theory one has to resum the leading logarithmic terms $\sim (\alpha_S \log(s))^n$ to all orders in α_S . Once this is done, the NLL terms could to be resummed, too. And so on and so forth.

Resumming effectively resums to all orders in α_S the large logarithmic terms arising in large invariant mass (Q) and/or small transverse momentum (p_T) regions, i.e. regions that are close to the edge of the phase space, by performing a Mellin transform.

In other words, it treats two different regions of phase space where the perturbation theory is spoiled:

- Regions close to the partonic production threshold, where $z = Q^2/s \rightarrow 1$ or equivalently in Mellin space $N \rightarrow \infty$, which include terms

$$\sim \left(\frac{\alpha_S}{2\pi}\right)^n \left(\frac{\ln^m(1-z)}{1-z}\right)_+ \rightarrow \left(\frac{\alpha_S}{2\pi}\right)^n \ln^{m+1} \bar{N} + \dots,$$

with $m \leq 2n - 1$ and $\bar{N} = Ne^{\gamma_E}$ [67, 68].

• Small- p_T , or equivalently in Mellin conjugate space (after applying a Fourier transform to the partonic cross section), large- b region, which induces large logarithms of the form

$$\alpha_S^n \left(\frac{1}{p_T^2} \ln^m \left(\frac{Q^2}{p_T^2} \right) \right)_+ \rightarrow \alpha_S^n \ln^{m+1} \bar{b}^2 + \dots,$$

with $m \leq 2n - 1$ and $\bar{b} = \frac{1}{2}bQe^{\gamma_E}$ [69, 70].

This treatment accounts only partially for the full perturbative cross section away from these regions. In order to obtain a valid cross section at all values of z and p_T , the fixed-order (f.o.) and the resummed (res.) calculations must be matched consistently by subtracting from their sum their overlap i.e. the perturbatively expanded (exp.) resummed component,

$$\sigma_{q\bar{q}} = \sigma_{q\bar{q}}^{(f.o.)} + \sigma_{q\bar{q}}^{(res.)} - \sigma_{q\bar{q}}^{(exp.)}. \quad (2.3)$$

Then after the resummation of the partonic cross section has been performed in N - and b -space, Resummino multiplies the resummed cross section and its perturbative expansion with the corresponding parton distribution functions where also a Mellin transform has been applied, and transforms the hadronic cross section obtained in this way back to the physical z - and p_T -spaces. More details can be found in [54].

Keeping the same values for the Weinberg angle as in the previous section, we have chosen benchmark points such that the width $\Gamma_{W'}$ in all models is the same as in the SSM. We have calculated the width in the SSM ($\Gamma_{W'}^{SSM}$) at leading order using PYTHIA 6 [62] with a running electro-magnetic coupling, $\alpha(m_{W'})$, such that $\Gamma_{W'}^{SSM}/m_{W'}$ slightly increases from 3.49% at $m_{W'} = 1$ TeV to 3.60% at $m_{W'} = 9$ TeV. This is achieved by setting the parameter $t = 1$ in the UU and NU models. As a consequence, the W' couplings to the SM fermions are the same in the SSM and NU cases. Again we use CT14nlo for the PDFs and we identify μ_R and μ_F with the invariant mass of the system. And finally, in order to enhance the contribution from the new gauge boson and limit the one from the SM W -boson as well as interference effects, we have implemented a cut on the invariant mass of the lepton pair: $m_{ll} > \frac{3}{4}M_{W'}$.

2.2.1 Numerical results

In Figure 2.4 we show the W' production cross sections at a centre-of-mass energy $\sqrt{S} = 14$ TeV at LO (dashed black), NLO (solid red), and NLO+NLL (solid green), along with the associated renormalisation and factorisation scale uncertainties (light khaki bands), in the SSM as a function

of the heavy gauge boson mass (top left). The ratios of the total cross sections at the HL-LHC at NLO (solid red) and NLO+NLL (solid green) over the LO cross section as a function of the W' mass is also presented (bottom left). Similarly, on the right hand side of Figure 2.4, we show the same but for a centre-of-mass energy $\sqrt{S} = 27$ TeV. Interference terms between W^- and W' -gauge bosons are included. As one can see, in the case of the HL-LHC, with an integrated luminosity of 3 ab^{-1} , the number of expected events falls from almost 40×10^3 (42×10^3) for $m_{W'} = 3$ TeV to 9 (11) for $m_{W'} = 7$ TeV in the SSM at NLO (NLO+NLL). On the other hand, when dealing with the HE-LHC where $\sqrt{S} = 27$ TeV and the integrated luminosity is of 15 ab^{-1} , the expected number of events falls from almost 1.6×10^6 (1.66×10^6) at $m_{W'} = 3$ TeV to almost 1.4×10^3 (1.5×10^3) for $m_{W'} = 9$ TeV at NLO (NLO+NLL). Furthermore, by looking at the bottom parts of Figure 2.4, one can see that with increasing mass, the threshold effects become more and more important leading to almost a 16% (6%) increase of the cross section at $M_{W'} = 8$ TeV for $\sqrt{S} = 14$ (27) TeV. On the same footing, in Figure 2.5 we show the results in the UU model. Here the total cross sections are slightly above the ones in the SSM, and as in the SSM case, the threshold effects increase with increasing mass to reach 14% (5,8%) at $m_{W'} = 8$ TeV for HL(HE)-LHC.

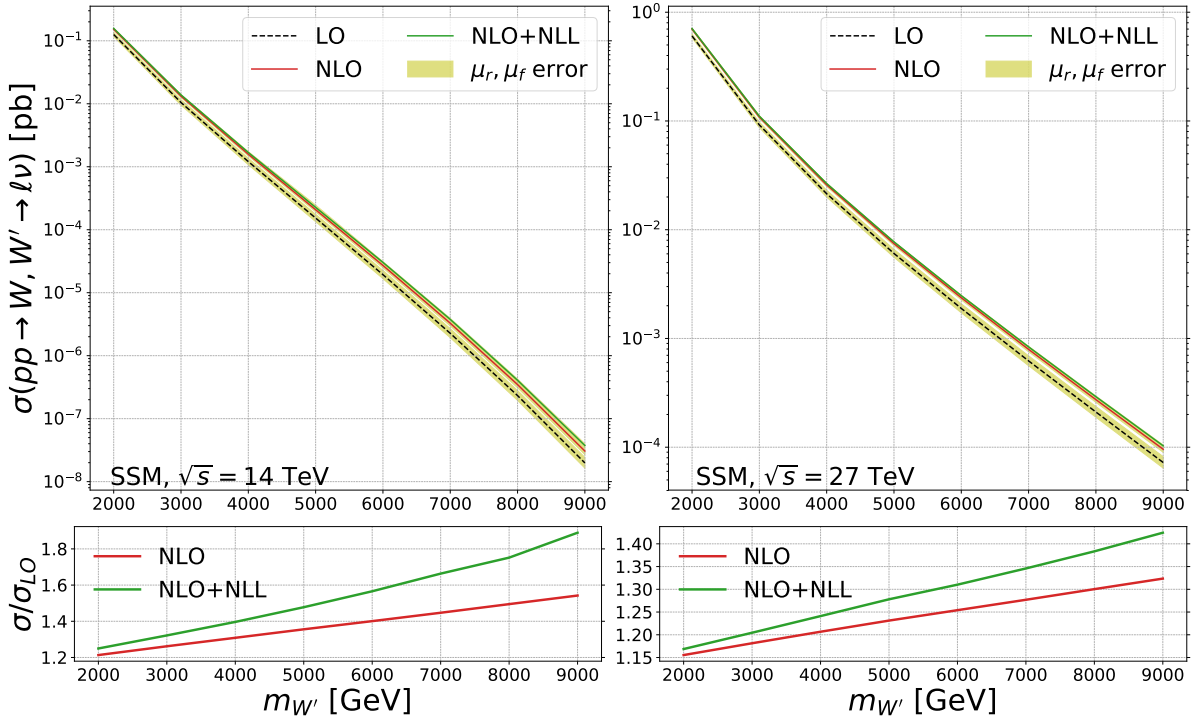


Figure 2.4: Left: LO, NLO, and NLO+NLL total cross section predictions in picobarns, with scale variation, as a function of $m_{W'}$, for $q\bar{q} \rightarrow W, W' \rightarrow l\nu$ in the SSM (top), and the corresponding NLO/LO and the NLO+NLL/LO K-factors (bottom), at a centre-of-mass energy $\sqrt{S} = 14$ TeV. Right: same as left but for a centre-of-mass energy $\sqrt{S} = 27$ TeV.

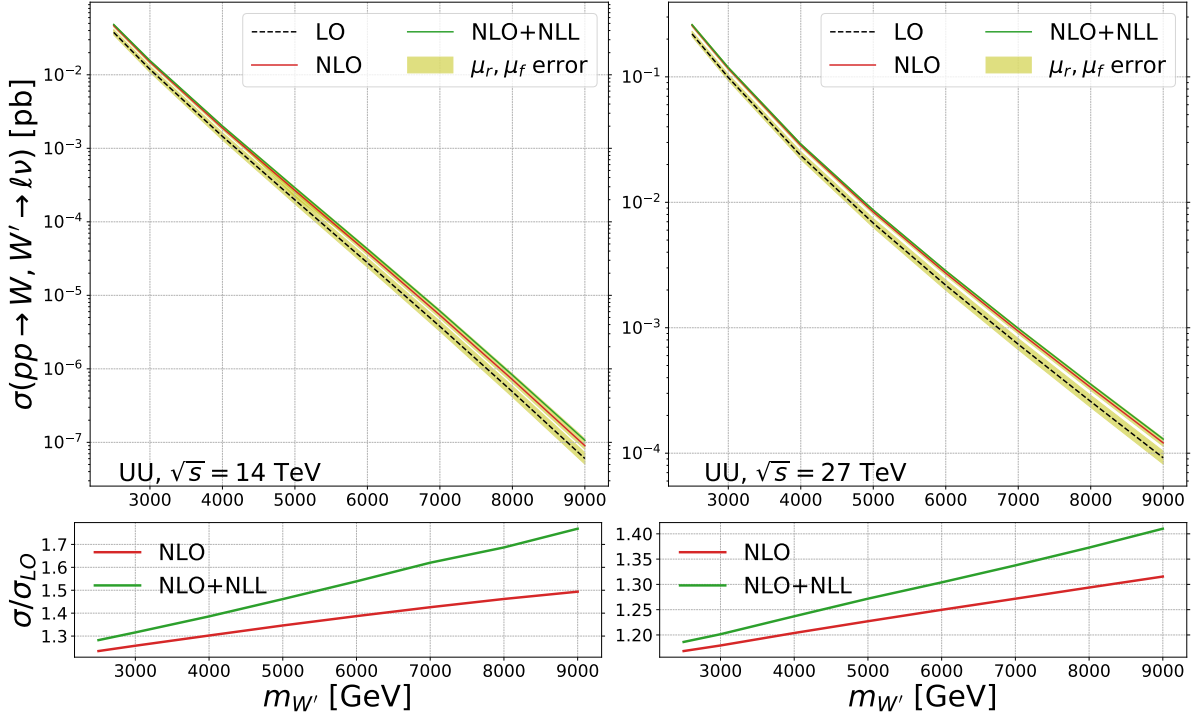


Figure 2.5: Same as Figure 2.4 but for the UU model.

2.2.2 Uncertainties

By convention, the theory uncertainty, i.e. from missing higher orders, is estimated by change of cross section when varying the renormalisation and factorization scales around the central value as discussed in Section 2.1. In Figure 2.6 we show the fractional uncertainty at different orders in perturbation theory due to the scale variation, in particular the LO (light khaki bands), the NLO (light blue bands), and the NLO+NLL (light salmon bands). This is done at $\sqrt{S} = 14$ TeV (right) and at $\sqrt{S} = 27$ TeV (left) in the SSM (top) and in the UU model (bottom). As is naively expected, for all the models and at different energies, the higher we go in perturbation theory the smaller the errors are. In fact, the LO result has no dependence on the renormalisation scale because it has no dependence on α_S .

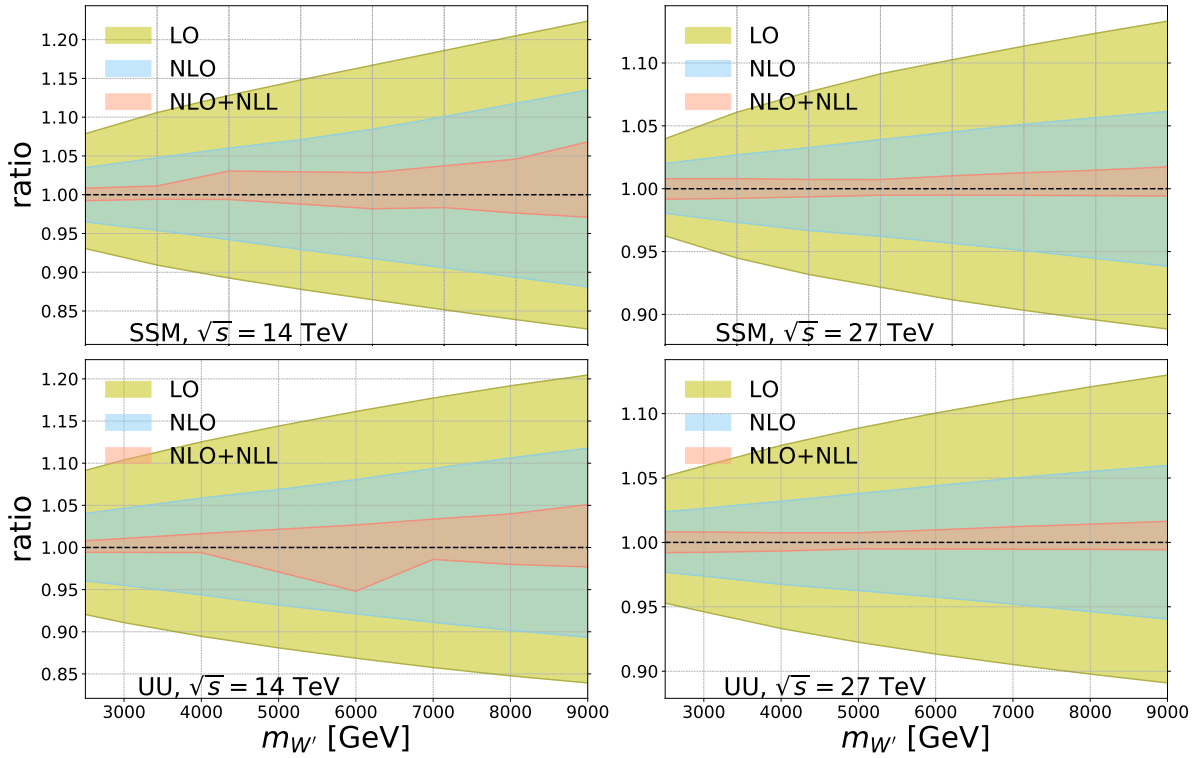


Figure 2.6: The fractional uncertainty at LO, NLO, and NLO+NLL due to the scale variation as a function of $m_{W'}$, for $q\bar{q} \rightarrow W, W' \rightarrow l\nu$ in the SSM (top row), and in the UU model (bottom row), at the HL-LHC (left) and the HE-LHC (right).

Chapter 3

QCD corrections to EW top-pair production beyond the Standard Model

Despite the fact that no signals of new physics have been found in the first and the second runs of the LHC at CERN, there are still high hopes that new particles will show up in the future high-luminosity runs. It is also clear that such signals will likely appear as small deviations from the SM predictions and that they will critically depend on the size of the theory uncertainties which makes precision predictions of both the SM background and the new physics signals an essential ingredient for a correct and reliable comparison between experimental data and theories describing the fundamental interactions of Nature.

The focus of this chapter is, again, on the W'^{\pm} and the Z' -bosons. As discussed in the previous chapters, such resonances are predicted by several well-motivated extensions of the SM and are extensively sought after by three of the experimental collaborations (ATLAS, CMS, and LHCb) at the LHC. In this context it is noteworthy that Z' models with a non-universal flavor structure [71, 72], where the Z' couples differently to the fermions of the three SM families, are viable candidates to explain the current B-flavour anomalies [73–81].

The strongest constraints on the parameter space of models with Z' and W' resonances come, in many cases, from searches with dilepton final states. In this case, precise predictions at NLO accuracy including a resummation of soft gluon terms at NLL accuracy can be obtained with the Resumino code [41] which has been used previously to derive limits on Z' and W' masses using data for dilepton final states [54] and to provide predictions for the High Energy/High Luminosity options of the LHC [45].

However, also top quark observables are very interesting since the 3rd generation plays a prominent role in the SM due to the Yukawa coupling of the top quark which is the only Yukawa coupling in the SM which is of order one. Therefore, it is quite conceivable that new physics (similar to the Higgs boson) couples predominantly to the top quark. In 2015, a calculation of next-to-leading order QCD corrections to the electroweak $t\bar{t}$ production in the presence of a Z' resonance [40] was performed. It properly accounted for the interference between SM and new physics amplitudes in a semi-automated fashion. The calculation was implemented in the POWHEG BOX framework [42, 44, 60] performing a consistent matching of the fixed NLO calculation with shower Monte Carlo (SMC). The results obtained with this tool, dubbed PBZp, are useful since they bridge the gap between first-principles higher order calculations and the complex detector signatures and data from the experiments.

In this chapter, we perform a complete re-calculation of the processes implemented in the PBZp including a number of improvements:

- The amplitudes have been calculated using the RecoLa2 package [43]. This package has been designed to automatize the calculations of amplitudes in theories beyond the SM including QCD and electroweak corrections at NLO. Our calculation is the first to use (and validate) this tool for a BSM calculation. Implementing the amplitudes obtained with RecoLa2 into Monte Carlo event generators (within the POWHEG BOX framework) is an important aspect which makes the tool more useful for LHC experiments.
- The new code can now deal with flavour non-diagonal/generation non-universal couplings such that the Z' -models mentioned above explaining the B -flavour anomalies can be implemented.
- Another new feature is that the calculation now includes t -channel W and W' contributions.
- As before, all interference terms are fully taken into account and the photon induced channels for the SM are included, properly matched with POWHEG. As discussed in [40] they give a large/sizable contribution to the cross section.

This chapter is organised as follows: In Section 3.1 we define the production of top-quark pairs at hadron colliders including new electroweak gauge bosons, focusing on the perturbative organisation of the cross section and its contributions at leading and next- to-leading order in the strong and electroweak coupling constants. In Section 3.2 we describe the Born, virtual, and real processes that contribute to our calculation. In Section 3.3 we give a brief description of the RecoLa2 package, provide some details on the UFO [82] model file that need to be linked to it in order to calculate our amplitudes, and validate the resulting amplitudes against the old calculation. Section 3.4 and Section 3.5 present a discussion of the POWHEG method and a detailed description of the implementation of our NLO calculation in a Monte Carlo generator within the POWHEG BOX framework. To conclude, we summarise in Section 3.6 the models for which we present numerical results as a function of both the new gauge bosons masses and the collider energy and propose useful kinematic cuts to disentangle the different contributions.

3.1 Next-to-leading order QCD corrections to the electroweak top-pair production

The cross section of the top-pair production in hadronic collisions can be calculated using a property of QCD called factorisation¹ which permits us to divide the calculation of the observables into two independent factors that encompass the underlying physics at different scales: a low-momentum non-perturbative hadronic part and a high-momentum part that describes what happens at short distance, see Figure 3.1.

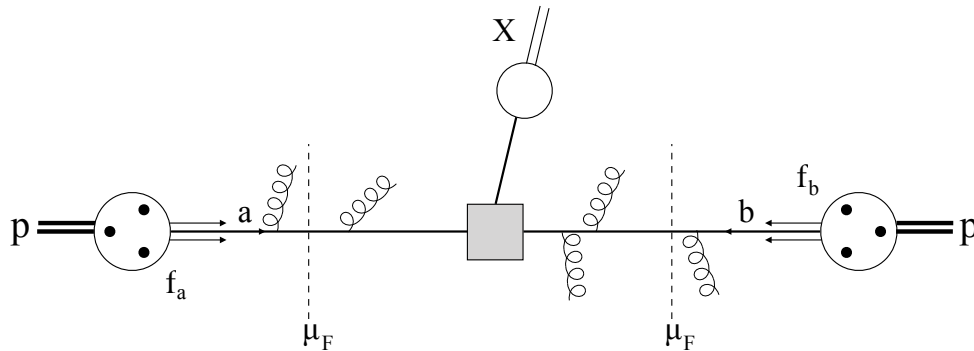


Figure 3.1: A pictorial representation of the factorisation formula in Eq. (3.2). The central part between the dashed vertical lines, describes the high-momentum transfer part represented by the short distance cross section $\hat{\sigma}_{ab}$ where X denotes any hadronic final state. The remaining parts on the left and right sides of the dashed vertical lines, describe the low-momentum transfer part of the hadronic collision represented by the parton distribution functions. The dashed lines represent the scale of the factorisation μ_F , the separation between the high-momentum and low-momentum parts of the hadronic collision.

At the LHC, when two protons collide at a centre-of-mass energy of 13 TeV, each one carries a momentum $p = 6.5$ TeV in the centre-of-mass frame. If we give the partons coming from the first proton the index a , and the ones of the second proton an index b , then the interacting constituents of these protons will each carry a portion of the momentum of the parent proton, p'_a and p'_b respectively, where

$$p'_a = x_a p_a, \quad p'_b = x_b p_b, \quad x_a, x_b \in [0, 1]. \quad (3.1)$$

Using this notation, the hadronic cross section can be written as

$$\sigma = \sum_{a,b} \int_0^1 dx_a f_a(x_a, \mu_F) \int_0^1 dx_b f_b(x_b, \mu_F) \hat{\sigma}_{ab}(x_a p_a, x_b p_b; \mu_F). \quad (3.2)$$

¹The factorisation has been proven in so-called QCD factorisation theorems [83]. For deep inelastic scattering (DIS) it is also a consequence of the operator product expansion.

Here, a sum over all the constituents of the protons a and b is performed in order to take into account all relevant partonic channels. Moreover, one has to integrate over all possible momentum fractions x_a and x_b of the two partons. In our case, this integration ranges extend from the threshold at which two top quarks t with mass m_t can be produced up to the collider hadronic centre-of-mass energy. The high-momentum transfer part, the hard scattering of the partons a and in b is described by the parton level short distance cross section $\hat{\sigma}_{ab}$. On the other, the structure of the protons is encoded in terms of parton distributions functions $f_i(x, \mu_F)$. The PDFs are non-perturbative objects describing the probability of finding a parton of type "i" carrying a longitudinal momentum fraction x of the parent proton momentum. It is important to note that the PDFs are universal, i.e., they are independent of hard scattering process which gives the formalism predictive power. Finally, both the hadronic and the partonic parts of the cross section depend on the factorisation scale μ_F which fixes the energy scale at which the factorisation is realised. The final result of any computation should not depend on this unphysical, and essentially arbitrary scale. However, in practice, this is not the case due to missing higher orders in the perturbative expansion and as seen in Section 2.1.2 one can vary the scales to estimate the theoretical uncertainty due to these missing terms.

Since the PDFs are universal objects and since their scale dependence is well known we will focus on the high scale object i.e. on the partonic cross section which is usually obtained by performing a perturbative calculation and one can achieve higher formal accuracy by including higher-order effects. At the lowest or leading order of perturbation theory, in powers of the two parameters α_S and α_W , where the former parametrises strong interactions and its value is roughly 0.1 at the TeV scale and the latter parametrises the strength of the electroweak interactions and its value is around 0.01, the top-pair production partonic cross section, $\hat{\sigma}_{ab}^{LO}$, can be written as

$$\hat{\sigma}^{LO} = \hat{\sigma}_S^{LO}(\alpha_S^2) + \hat{\sigma}_{SW}^{LO}(\alpha_S\alpha_W) + \hat{\sigma}_W^{LO}(\alpha_W^2), \quad (3.3)$$

where we drop the indices a and b of the contributing partons and we concentrate on the dependence of the coupling constants. The first component on the right hand side of Eq. (3.3) represents the gluon mediated subprocesses in the gg channel as can be seen in Figure 3.2 (a)–(c), and in the $q\bar{q}$ channel, as in Figure 3.2 (d). The first obvious amplitude that contributes to $\hat{\sigma}_{SW}^{LO}$ would be the one including diagrams (d) and (e) of Figure 3.2, however this choice is equal to zero since it will lead to a closed fermionic loop with one gluon vertex. Instead, $\hat{\sigma}_{SW}^{LO}$ includes the interference of diagrams (d) and (f) of Figure 3.2 as well as the photon-induced diagrams as depicted in Figure 3.3. Finally, the last term, $\hat{\sigma}_W^{LO}$ denotes the partonic cross section of the subprocesses mediated by the electroweak gauge bosons, photon γ , neutral Z -boson, and charged W -bosons initiated by $q\bar{q}$, as shown in Figure 3.2 (e) and (f) respectively.

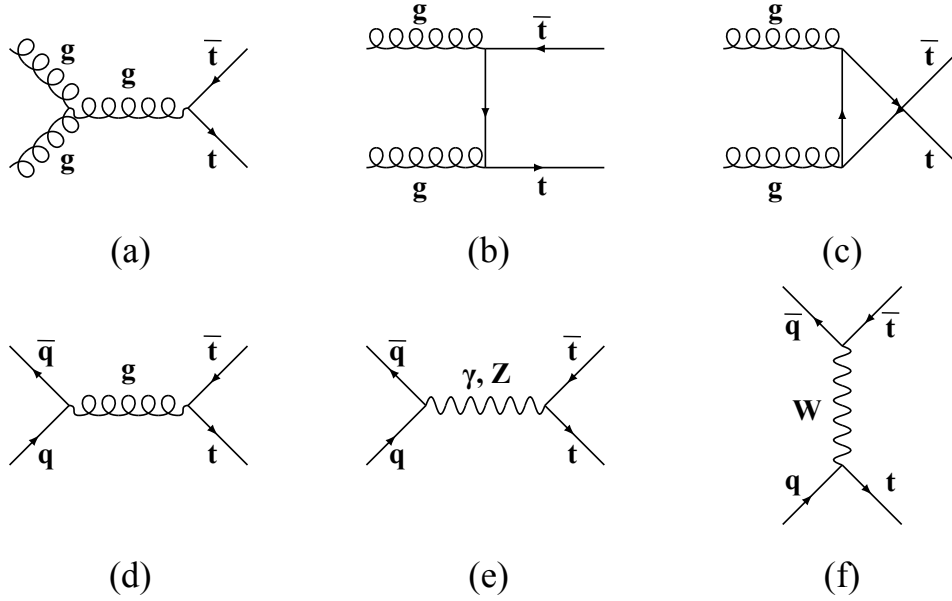


Figure 3.2: LO Feynman diagrams for $t\bar{t}$ production. gg -channel of $\mathcal{O}(\alpha_S^2)$ (a)–(c), $q\bar{q}$ -channel at the order $\mathcal{O}(\alpha_S^2)$ (d) and $q\bar{q}$ -channel at the order $\mathcal{O}(\alpha_W^2)$ (e)–(f).

LO accuracy is not sufficiently precise in some case, and higher order corrections are needed. The next-to-leading corrections to the top-pair production, collect, in addition to the three components of Eq. (3.3), terms with one additional power of one of the coupling constants α_S or α_W . Up to NLO, the cross section of the partonic top-pair production has the following perturbative expansion

$$\hat{\sigma}^{NLO} = \hat{\sigma}_{2;0}(\alpha_S^2) + \hat{\sigma}_{1;1}(\alpha_S\alpha_W) + \hat{\sigma}_{0;2}(\alpha_W^2) + \hat{\sigma}_{3;0}(\alpha_S^3) + \hat{\sigma}_{2;1}(\alpha_S^2\alpha_W) + \hat{\sigma}_{1;2}(\alpha_S\alpha_W^2) + \hat{\sigma}_{0;3}(\alpha_W^3), \quad (3.4)$$

where the indices $m;n$ represent the powers of α_S and α_W respectively. Throughout this manuscript we would refer sometimes to the term $\hat{\sigma}_{m;n}$ in the perturbative expansion as the partonic cross section at order $\mathcal{O}(\alpha_S^m\alpha_W^n)$, for example, $\hat{\sigma}_{1;2}$ could be referred to as the partonic cross section at order $\mathcal{O}(\alpha_S\alpha_W^2)$. The first three components of Eq. (3.4) correspond to the LO partonic cross sections $\hat{\sigma}_S^{LO}$, $\hat{\sigma}_{SW}^{LO}$, and $\hat{\sigma}_W^{LO}$ from Eq. (3.3) respectively. At NLO, these terms can receive QCD corrections through an interaction with an extra QCD particle or EW corrections through an interaction with an extra EW particle, as represented in the last four terms of Eq. (3.4). In that sense, $\hat{\sigma}_{2;0}$ and $\hat{\sigma}_{3;0}$ are the LO SM QCD contribution and the NLO corrections to it, they have been calculated in the late 1980 [84–87]. Moreover, NLO calculations for heavy quark correlations [88] and $t\bar{t}$ spin correlations [89, 90] are available too. $\hat{\sigma}_{2;1}$ represents the EW corrections to the QCD backgrounds. In this case, a gauge-invariant subset was first investigated neglecting the interferences between QCD and EW interactions arising from box-diagram topologies and pure photonic contributions [91] and later including also

additional Higgs boson contributions arising in 2-Higgs doublet models (2HDMs) [92]. The rest of the electroweak corrections was subsequently calculated in a series of papers and included also Z -gluon interference effects and QED corrections with real and virtual photons [93–97]. In principle, $\hat{\sigma}_{2;1}$ would also receive contributions from new Z' and W' resonances. However, these contributions are expected to give a small correction to $\hat{\sigma}_{2;1}$ and since they are highly model-dependent due to the rich structure of the scalar sector in many models we don't include them in our calculation.

In our calculation we focus on the tree-level EW top-quark pair production and the NLO QCD corrections to it, i.e. $\hat{\sigma}_{0;2}$ and $\hat{\sigma}_{1;2}$ respectively. $\hat{\sigma}_{0;2}$ receives contributions from the s -channel amplitudes $q\bar{q} \rightarrow (Z', Z, \gamma) \rightarrow t\bar{t}$ including the Z' signal and its interference with the photon and SM Z -boson. Due to the resonance of the Z' -boson, we expect these terms to be the most relevant for new physics searches. In addition, we include new contributions from diagrams with non-resonant t -channel exchange of W^- , W' - and Z' -bosons that were not considered in Ref. [40]. Note that out of these, the first two take into account CKM mixing and the last one is only allowed in models with flavour non-diagonal couplings due to the absence of a top quark PDF in a 5FNS. A particular advantage of the $\hat{\sigma}_{0;2}$ contribution is that the calculation of higher order QCD corrections to it, $\hat{\sigma}_{1;2}$, can be carried out in a model-independent way as long as the couplings of Z' and W' are kept general. We also include $\hat{\sigma}_{1;1}$ which receives contributions from the photon induced subprocess $\gamma g \rightarrow t\bar{t}$ and the interference of the s -channel QCD and the t -channel electroweak top-pair production. Note that the photon induced subprocess is numerically relevant and needed for a consistent treatment of the mass singularities in the process $gq \rightarrow t\bar{t}q$ when the t -channel photon is collinear to the quark q . Finally, the purely electroweak term $\hat{\sigma}_{0;3}$ would also receive contributions from new Z' and W' resonances. However, It is of order $\mathcal{O}(\alpha_W^3)$ and parametrically suppressed compared to the other terms. We therefore do not include it in our calculation.²

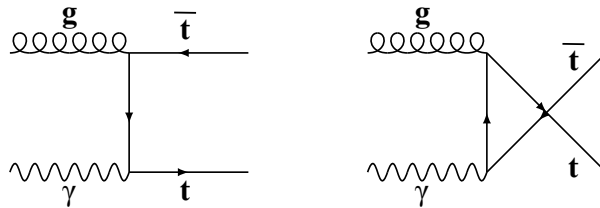


Figure 3.3: Photon-induced top-pair production of $\mathcal{O}(\alpha_S\alpha_W)$

²Note, however, that despite the parametric suppression they have been shown to be important in the SM in a region with large top transverse momentum [98, 99].

3.2 Parton level processes

The perturbative partonic cross section of Eq. (3.2) can be written as

$$\hat{\sigma}_{ab} = \frac{1}{2\hat{s}} \int d\phi(x_a p_a, x_b p_b; p_1, \dots, p_n) |\mathcal{A}(x_a p_a, x_b p_b; p_1, \dots, p_n)|^2 \quad (3.5)$$

where $2\hat{s}$ is the (inverse) flux factor and $\hat{s} = Q^2$ is the squared (partonic) centre-of-mass energy. $|\mathcal{A}(x_a p_a, x_b p_b; p_1, \dots, p_n)|^2$ is the (squared) matrix element or (squared) amplitude, it depends on all final state momenta p_1, \dots, p_n as well as the initial state momenta $x_a p_a$ and $x_b p_b$. In what follows we will refer to $|\mathcal{A}(p_a, p_b; p_1, \dots, p_n)|^2$ as $|\mathcal{A}|^2$ for compactness.

A coherent calculation in perturbation theory requires taking into account all the diagrams at a given order, as well as all those of lower order. For instance, to calculate $\hat{\sigma}_{1;2}$, again we drop the indices a and b of the contributing partons and we concentrate on the dependence of the coupling constants, one needs to include all the squared amplitudes of order $\mathcal{O}(\alpha_S \alpha_W^2)$ and lower. In other words, $\hat{\sigma}_{1;2}$ is proportional to the squared amplitude $|\mathcal{A}|^2$, where

$$|\mathcal{A}|^2 = |\mathcal{A}_{0;1}|^2 + 2\Re[\mathcal{A}_{0;1} \mathcal{A}_{1;1}^*] + |\mathcal{A}_{\frac{1}{2};1}|^2, \quad (3.6)$$

the first term on the right side of Eq. (3.6) has the lowest order ($\sim |\mathcal{O}(\alpha_W)|^2$) and is called the Born term, the second one is of order $\mathcal{O}(\alpha_S \alpha_W^2)$ it represents the amplitudes with an emitted and re-absorbed field within the same diagram and is known as the virtual contribution, and the last component is also of order $\mathcal{O}(\alpha_S \alpha_W^2)$, it describes the amplitudes with one additional emitted particle with respect to the Born amplitudes and dubbed as the real component. It is worth mentioning that the Born and virtual contributions live in the same phase space ($2 \rightarrow 2$ in this particular case), while the real contribution has a different number of particles in the final state ($2 \rightarrow 3$ in our example), and thus can not be combined with the Born nor with the virtual amplitudes.

Taking into account the virtual and real contributions will lead to many difficulties because of the appearance of divergences. In general, these divergences could be one of the three different types: (i) the ultraviolet (UV) divergences which reflect the behavior at short distances or large momenta of the theory and only appear in virtual terms with very large loop momenta, (ii) the soft divergences that arise when the momentum of a massless particle tends to zero, it reflects the behavior of the theory at small energies or large distances and can appear in both real and virtual contributions, and (iii) the collinear divergences, also known as mass singularities, that happen when the momenta of two massless particles become parallel can also appear in both real and virtual amplitudes.

The UV divergences are treated by the so-called renormalisation procedure where all the parameters of the Lagrangian are redefined in a renormalisation scheme and acquire a renormalisation scale dependence (running couplings) and thus need to be measured at one scale. The running parameters can then be calculated at a different scale using a set of differential equations known as the renormalisation group equations. The soft singularities must cancel in the sum of real and virtual terms for infrared (IR) safe observables³. Last but not least, the initial state collinear divergences are treated by the so-called mass factorisation procedure, where, in the same spirit as in the renormalisation procedure, the PDFs and fragmentation functions are redefined in a factorisation scheme and acquire a factorisation scale dependence and thus need to be measured at one scale. The evolution for the measured scaled to a different one can then be obtained with the set of differential equations called DGLAP equations. More details about how we treat these singularities in our calculation will be given in the next sections.

In this section, we describe the amplitudes that contribute to $\hat{\sigma}_{1;1}$, $\hat{\sigma}_{0;2}$, and $\hat{\sigma}_{1;2}$ in more detail. We work in a 5-Flavour Number Scheme (5-FNS), meaning that only the top-quark mass is different than zero, and that all relevant contributions with u, d, s, c, b (anti-)quarks, gluons and photons are included in the initial state. Furthermore, we allow for a completely general flavour structure for the coupling of the Z' - and W' -bosons to the Standard Model fermions.

3.2.1 Leading-order contributions

The lowest order diagrams, also known as the Born amplitudes $\mathcal{A}_{0;1}$ contributing to the electroweak top-pair production cross-section $\hat{\sigma}_{0;2} \sim |\mathcal{A}_{0;1}|^2$ are shown in Figure 3.4. Figure 3.4a) depicts in a compact form the contribution with an s -channel vector boson V_1 which can be a photon, a SM Z -boson, or a new heavy Z' -boson. In the previous version of PBZp only flavour-diagonal Z' couplings with $q' = q \in \{u, d, s, c, b\}$ were allowed.

In this calculation we include contributions with flavour-changing couplings of the Z' -boson to the quarks in the initial state ($q'\bar{q} \in \{u\bar{u}, c\bar{u}, d\bar{d}, s\bar{d}, b\bar{d}, d\bar{s}, s\bar{s}, b\bar{s}, u\bar{c}, c\bar{c}, d\bar{b}, s\bar{b}, b\bar{b}\}$). Note that the corresponding amplitudes with a charge-conjugated initial state are not shown. In the new calculation, we now also take into account the t -channel diagrams in Figure 3.4b) where the exchange boson V_2 can be a W^- , W'^- , or Z' -boson. Needless to say that those amplitudes in Figure 3.4a) and b) having the same initial (and final) states are added coherently.

As was discussed in [40], the diagrams in Figure 3.4a) have zero interference with the QCD amplitude $q\bar{q} \rightarrow g^* \rightarrow t\bar{t}$ since such interference terms are proportional to the vanishing colour

³An IR safe observable is an observable that does not depend on long distance physics and is therefore calculable in perturbative QCD

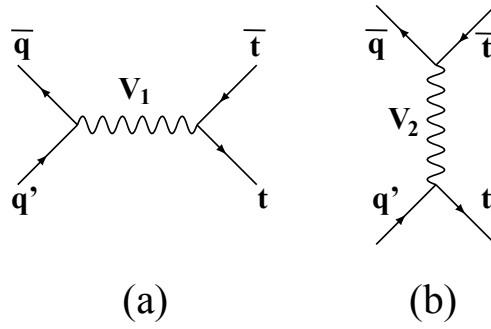


Figure 3.4: Born amplitudes $\mathcal{A}_{0;1}$ contributing to the electroweak top-pair production cross section $\hat{\sigma}_{0;2}$. a) s -channel contribution where $V_1 \in \{\gamma, Z, Z'\}$ and $q, q' \in \{u, d, s, c, b\}$. In the case of Z' exchange we allow for flavour-changing amplitudes with $q' \neq q$ and we don't show the corresponding amplitudes with a charge-conjugated initial state. b) t -channel contributions where $V_2 \in \{W, W', Z'\}$. All allowed amplitudes with the same initial (and final) state are added coherently.

trace $\text{Tr}(T^a)$. On the other hand, the t -channel diagrams in Figure 3.4b) with $q' = q$ do interfere with the QCD amplitude $q\bar{q} \rightarrow g^* \rightarrow t\bar{t}$. Thus they contribute to $\hat{\sigma}_{1;1}$ and we take them into account.

3.2.2 One-loop virtual corrections

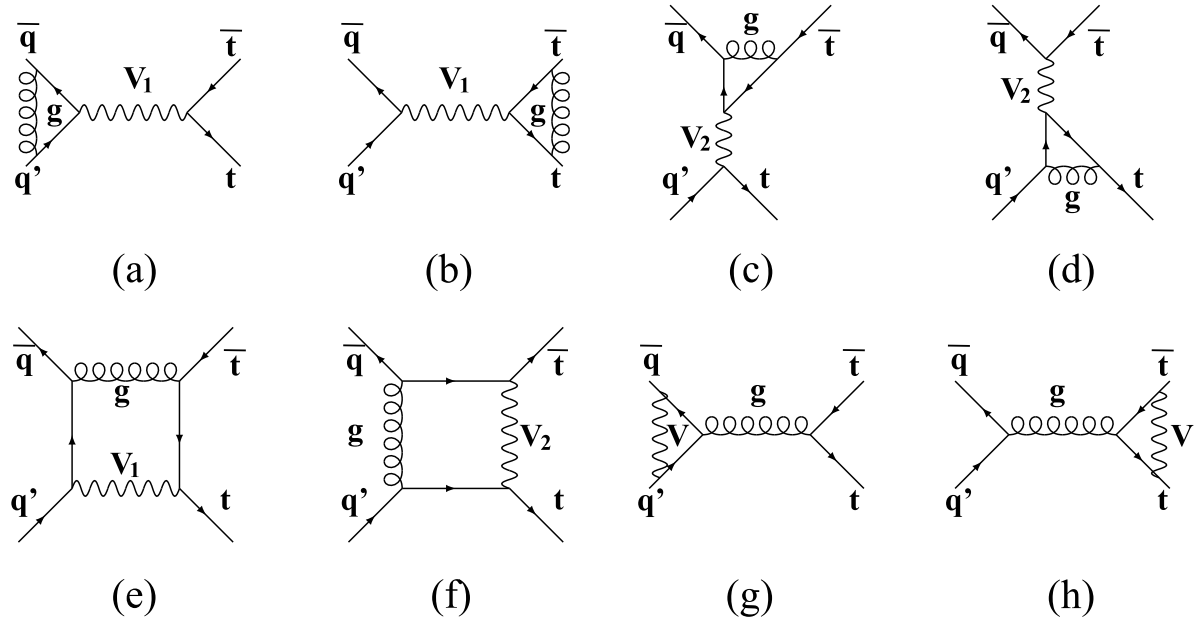


Figure 3.5: One-loop QCD corrections, $\mathcal{A}_{1;1}$, to the diagrams in Figure 3.4. As before, $V_1 \in \{\gamma, Z, Z'\}$, $V_2 \in \{W, W', Z'\}$, and $V = V_1 \cup V_2$ denotes the union of V_1 and V_2 .

In Figure 3.5 we show the one-loop QCD corrections, $\mathcal{A}_{1;1}$, to the diagrams in Figure 3.4. They contribute to the EW top-pair production at $\mathcal{O}(\alpha_s \alpha_W^2)$ due to the interference of these diagrams with the Born amplitudes in Figure 3.4: $\hat{\sigma}_{1;2}^V \sim 2\Re[\mathcal{A}_{0;1} \mathcal{A}_{1;1}^*]$.

Note again, that there is no interference of the diagrams in Figures 3.5a) and b) with the Born level QCD amplitude $q\bar{q} \rightarrow g^* \rightarrow t\bar{t}$, whereas the diagrams in Figures 3.5c) and d) will interfere with it contributing to $\hat{\sigma}_{2;1}$. As discussed in Section 3.1, we don't consider the effect of heavy new resonances on $\hat{\sigma}_{2;1}$ in this work.

In our re-calculation we define the virtual corrections as the set of diagrams with no vector bosons inside the loops, effectively treating them as background-fields in RecoLa2 [100, 101]. The resulting QCD loop corrections constitute a gauge-invariant subset which can be seen by realising that if either of the quark lines is replaced by an auxiliary non colour-charged conserved current (e.g. a lepton-lepton vector interaction), the so-defined virtual corrections represent not only the full QCD corrections and are thus gauge-independent, but, moreover, they do not depend on the specific form of the auxiliary conserved current. Therefore, the statement holds true for the EW production if one vetoes diagrams with a gluon exchange between the two different quark lines, i.e. excluding box corrections. In summary, we therefore include diagrams such as Figures 3.5c) and d), but we omit amplitudes in the second row of Figure 3.5. In principle one could compute all corrections, but the renormalisation of the amplitudes in Figures 3.5g) and h) requires to account for quark mixing self-energy diagrams with transitions between different flavors due to W^- , W'^- , or Z' -bosons in the loop. Such quark mixing in the renormalisation is currently not implemented in RecoLa2/Rept11. In the limit of a diagonal CKM matrix and including only diagonal W' and Z' couplings, we investigated in our calculation the impact of the diagrams in Figure 3.5e)-h) and it turns out that in this case, their contribution is negligibly small. Since any deviation from this ‘‘diagonal’’ setup is additionally suppressed by the small off-diagonal couplings we expect the contributions from Figure 3.5e)-h) to remain negligible also in this general ‘‘non-diagonal’’ case.

3.2.3 Real emissions

The following $2 \rightarrow 3$ tree-level amplitudes, $\mathcal{A}_{\frac{1}{2};1}$, contribute to electroweak top-pair production at $\mathcal{O}(\alpha_s \alpha_W^2)$: (i) $q'\bar{q} \rightarrow t\bar{t}g$ (and the charge conjugated process) and (ii) $gq \rightarrow t\bar{t}q'$ (and the charge conjugated process). The corresponding Feynman diagrams are shown in Figures 3.6 and 3.7 respectively.

For comparison, the real emission diagrams in Figures 4 and 5 in the previous calculation [40] are a (small) subset of the diagrams depicted in Figures 3.6 and 3.7 in a rather compact manner.

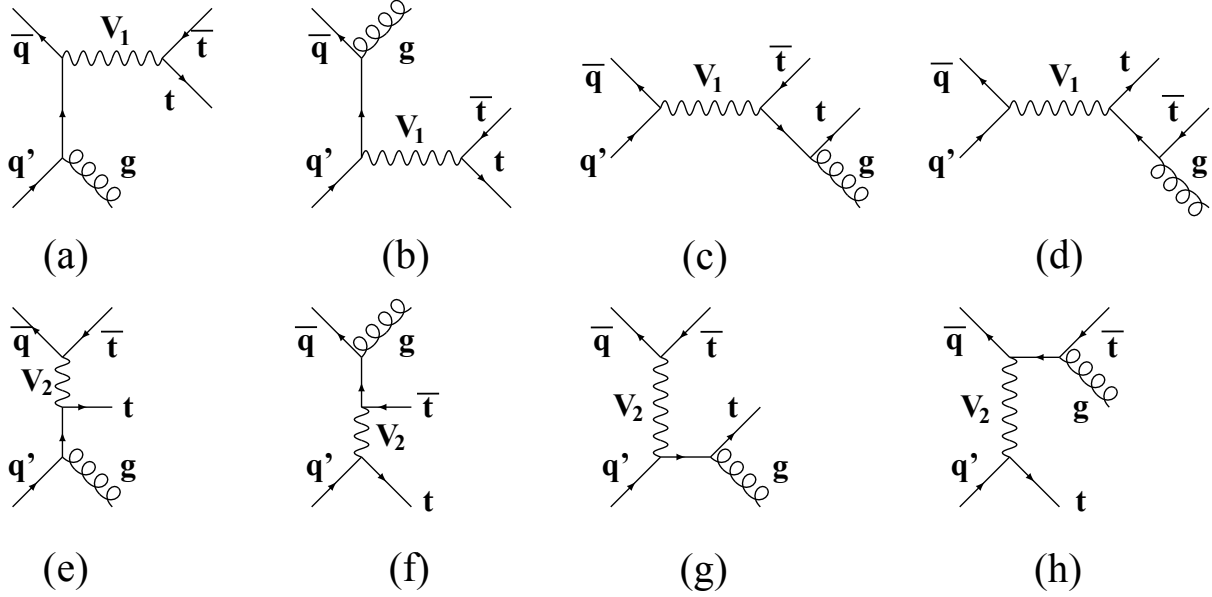


Figure 3.6: Diagrams contributing to the $q'\bar{q} \rightarrow t\bar{t}g$ subprocesses at order $\mathcal{O}(\alpha_s\alpha_W^2)$. As in Figure 3.4, $V_1 \in \{\gamma, Z, Z'\}$, $V_2 \in \{W, W', Z'\}$, and $q, q' \in \{u, d, s, c, b\}$. All allowed amplitudes with the same initial (and final) state are added coherently.

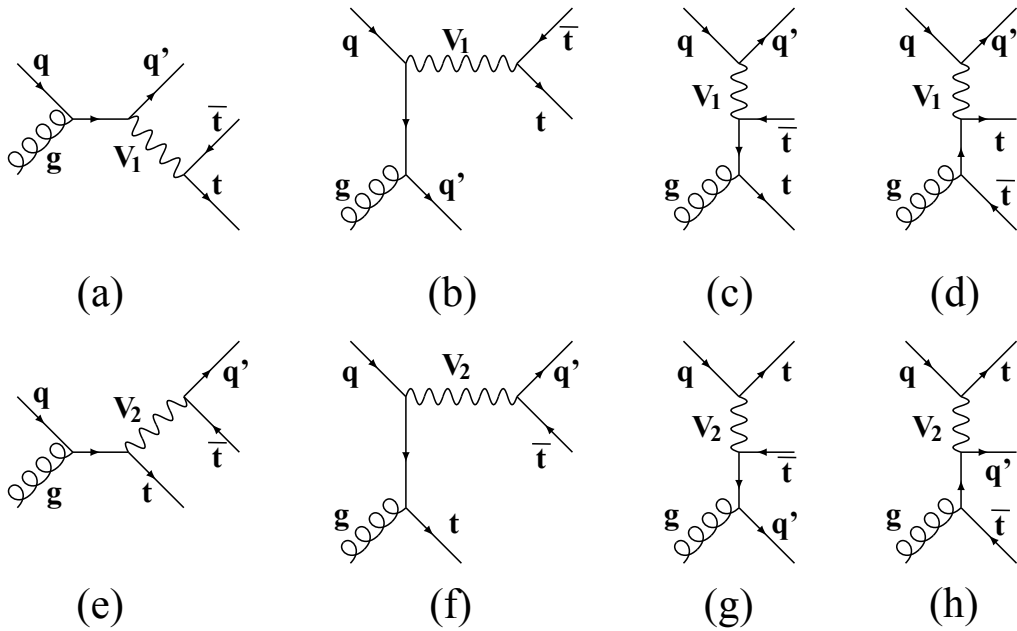


Figure 3.7: Similar as in Figure 3.6 but for the subprocesses $gq \rightarrow t\bar{t}q'$.

The $q'\bar{q}$ subprocesses in Figures 3.6 contain soft and collinear divergences, which cancel in the sum of real and virtual cross sections as a consequence of the KLN theorem. Within

POWHEG they are treated using the Frixione-Kunszt-Signer subtraction [102, 103]. Collinear divergences are present in Figures 3.6(a), b), e), and f). On the other hand, collinear gluon emission from a top quark line leads to a finite logarithm of the top quark mass which we keep in $\hat{\sigma}$ in fixed order perturbation theory.

The gq and $g\bar{q}$ channels can only have collinear singularities. While the diagrams in Figures 3.7(a), e), f), and h) are completely finite the other diagrams in Figure 3.7 contain configurations where a light quark propagator [b),g)] or a photon propagator [c),d)] can be close to its mass shell. As already discussed in [40], the fact that the collinear divergences appearing in Figures 3.7 c) and d) involve a photon propagator has two consequences: (i) we have to introduce a PDF for the photon inside the proton, and (ii) the corresponding underlying Born process shown in Figure 3.3, $g\gamma \rightarrow t\bar{t}$, must be included in the calculation.

3.3 RecoLa: Recursive Computation of 1-Loop Amplitudes

The amplitudes that contribute to our calculation, see Section 3.2, were calculated using the RecoLa2 package.

RecoLa2 is an extension of RecoLa [104] for the computation of tree and one-loop amplitudes in the Standard Model and beyond. In RecoLa, one-loop amplitudes are decomposed in terms of tensor coefficients and tensor integrals, the latter being model independent and evaluated with the help of the COLLIER tensor integral library [105]. Thus, the model-dependent part only concerns the tensor coefficients and rational parts of type R_2 [106] that are being constructed with the help of a RecoLa2 model file in a recursive and numerical way. The model file used in our study has been generated using the toolchain FeynRules [107] and Rept11 [101] and is publicly available.⁴ RecoLa regularises amplitudes in dimensional regularisation with space-time dimension $D = 4 - 2\epsilon$ adopting by default the COLLIER normalisation for 1-loop integrals [105]. More precisely, conventional dimensional regularisation is used which treats all particles and momenta in D dimensions. Similarly, the Lorentz algebra is upgraded to D -dimensions with a special treatment of γ_5 , known as naive dimensional regularisation (NDR) [108]. As the treatment of γ_5 is delicate in $D \neq 4$ dimensions, it can be formulated as a problem of determining the correct rational term of type R_2 which may not have a γ_5 scheme dependence or would otherwise prohibit defining (chiral) gauge symmetry of the theory in a consistent way. In NDR, rational terms for amplitudes with closed fermion loops and external vector bosons are evaluated using a reading point prescription, giving up on the cyclicity of the trace. This procedure guarantees that no symmetries of the theory are being broken, at least to one-loop order. The

⁴The model file can be found on the official website <https://recola.hepforge.org/> under model files.

UV renormalisation is carried out in the complete on-shell scheme for all particles [109]. Since in this work we start from electroweak production including QCD corrections, no further renormalisation of couplings is required.

3.3.1 RecoLa model file: the Standard Model + W' + Z'

In this section we provide more details about the model file that, as discussed in Section 3.3, is linked to RecoLa2 in order to calculate the amplitudes at LO and NLO. Dubbed as “The Standard Model + W' + Z' ” or “SMWZp”, this model implements the SM at NLO QCD supplemented by interaction terms with a W' and Z' based on the following Lagrangian

$$\begin{aligned} \mathcal{L}_{W'Z'} = & k_{W,\pm} \frac{e}{\sqrt{2}s_W} W'_\mu \left(C_{W,\pm}^l \bar{\nu}^i \gamma^\mu w^\pm l^j + C_{W,\pm}^q \bar{u}^i \gamma^\mu w^\pm d^j \right) + h.c. + \\ & k_{Z,\pm} \frac{e}{s_W c_W} Z'_\mu \left(C_{Z,\pm}^l \bar{l}^i \gamma^\mu w^\pm l^j + C_{Z,\pm}^u \bar{u}^i \gamma^\mu w^\pm u^j + C_{Z,\pm}^d \bar{d}^i \gamma^\mu w^\pm d^j \right) + h.c., \end{aligned} \quad (3.7)$$

where $q \in \{u^i, d^j\}$, and $\ell \in \{v^i, e^j\}$ ($i, j = 1, 2, 3$) are the SM fermions in the mass eigenstate basis. Furthermore, $w_\pm = (1 \pm \gamma^5)/2$, $k_{W(Z),+}$ and $k_{W(Z),-}$ are free parameters that affect the couplings between the W' (Z') boson and the right-handed and left-handed SM fermions respectively, $e = 2\sqrt{\pi\alpha_W}$ is the electromagnetic charge, and s_W and c_W are the sine and the cosine of the Weinberg angle respectively. Finally, $C_{W,\pm}^l$, $C_{W,\pm}^q$, $C_{Z,\pm}^l$, $C_{Z,\pm}^u$, and $C_{Z,\pm}^d$ are CKM-like coupling matrices. For instance, $C_{Z,-}^u$ would have 9 free parameters, CZ1L1x1, CZ1L1x2, CZ1L1x3, CZ1L2x1, CZ1L2x2, CZ1L2x3, CZ1L3x1, CZ1L3x2, and CZ1L3x3 controlling the couplings between Z' and left-handed $\bar{u}u$, $\bar{u}c$, $\bar{u}t$, $\bar{c}u$, $\bar{c}c$, $\bar{c}t$, $\bar{t}u$, $\bar{t}c$, and $\bar{t}t$ respectively. It is worth mentioning that the SM CKM matrix is also a free parameter in this model and can be fixed by setting the 9 input parameters CKM1x1, CKM1x2, CKM1x3, CKM2x1, CKM2x2, CKM2x3, CKM3x1, CKM3x2, and, CKM3x3. For the complete set of the external parameters of SMWZp and how to edit their values see Appendix B.2.

3.3.2 Power counting of couplings in RecoLa

The orders associated to couplings for a given theory define a power-counting in RecoLa. As a result, the amplitudes are ordered and computed according to the power-counting of the model in consideration. In the SM the amplitudes are proportional to $(\sqrt{\alpha_S})^{n_S} (\sqrt{\alpha_W})^{n-n_S}$ where n is the total number of vertices and n_S is the number of QCD vertices. For instance, the squared amplitude for the electroweak $u\bar{u} \rightarrow t\bar{t}$ will have a total of 4 vertices of which 0 are of QCD nature and 4 are of EW type. Thus, in this particular case one has two amplitudes that are

proportional to $(\sqrt{\alpha_S})^0(\sqrt{\alpha_W})^2$. Now going back to the SMWZp model where each vertex is proportional to either $\sqrt{\alpha_S}$ or $\sqrt{\alpha_W}$ with the latter describing, not only the EW SM vertices, but also the couplings to the BSM Z' - and W' -bosons. Thus, in order to allow for the selection of pure BSM contributions, The model has been implemented with, in addition to the SM power counting, a power counting for the BSM vertices. Again if one takes the same example as before, i.e., the squared amplitude of the electroweak $u\bar{u} \rightarrow t\bar{t}$, but this time in the SMWZp model, one will have two possibilities, either a SM EW production via a Z -boson or a BSM EW production mediated by a Z' -boson. The squared amplitude in the former case would have 0 QCD vertices and 4 EW vertices of which none are of BSM type, in RecoLa's power-counting language this means: "0 QCD 4 QED 0 WZP", where QED means SM EW and WZP is the identifier for BSM EW. On the other hand, in the latter case, the squared amplitude has: "0 QCD 4 QED 4 WZP". More details about the power-counting and the anatomy of the SMWZp amplitudes within RecoLa that we include in our calculation can be found in the Appendix B.3.

3.3.3 Validation

The SSM amplitudes calculated with RecoLa were validated at the Born level against the ones in Madgraph (MG5) and the old PBZp package, and at the real and virtual levels to the old PBZp package only. This was done by sampling the full phase space. To this aim, we generated the phase space points using POWHEG BOX where the Born (and virtual) phase space is described by three vectors of random variables, X_{born1} , X_{born2} , and X_{born3} , and the real phase space has, in addition to the X_{born} vectors, three variables in the unit cube $X_{\text{rad}} = \{X_{\text{rad1}}, X_{\text{rad2}}, X_{\text{rad3}}\}$ that set the radiation kinematics. Note that the RecoLa and the old PBZp packages use a different notation for couplings of gauge bosons to SM fermions, for more details see Appendix B.4.

Born

In Figure 3.8 we compare the tree level amplitudes calculated in RecoLa2 for $u\bar{u} \rightarrow Z' \rightarrow t\bar{t}$ and $d\bar{d} \rightarrow Z' \rightarrow t\bar{t}$ against the ones calculated with MG5 (purple) and the old PBZp (blue) finding a very good agreement. The list of parameters that enter in this comparison can be read from Listing B.1 of Appendix B.5. Note that while sinus of the Weinberg angle is an external parameter in the old PBZp, this is not the case in RecoLa where it is an internal parameter depending on the masses of Z - and W -bosons. More precisely $s_W^2 = 1 - (m_W^2/m_Z^2)$.

We also show the ratio of the photon induced amplitudes calculated in RecoLa2 over the ones calculated in the old PBZp where we find a perfect agreement as can be seen from Figure 3.9.

The only new parameter that affect this amplitudes with respect to the ones in Figure 3.8 is the strong coupling constant.

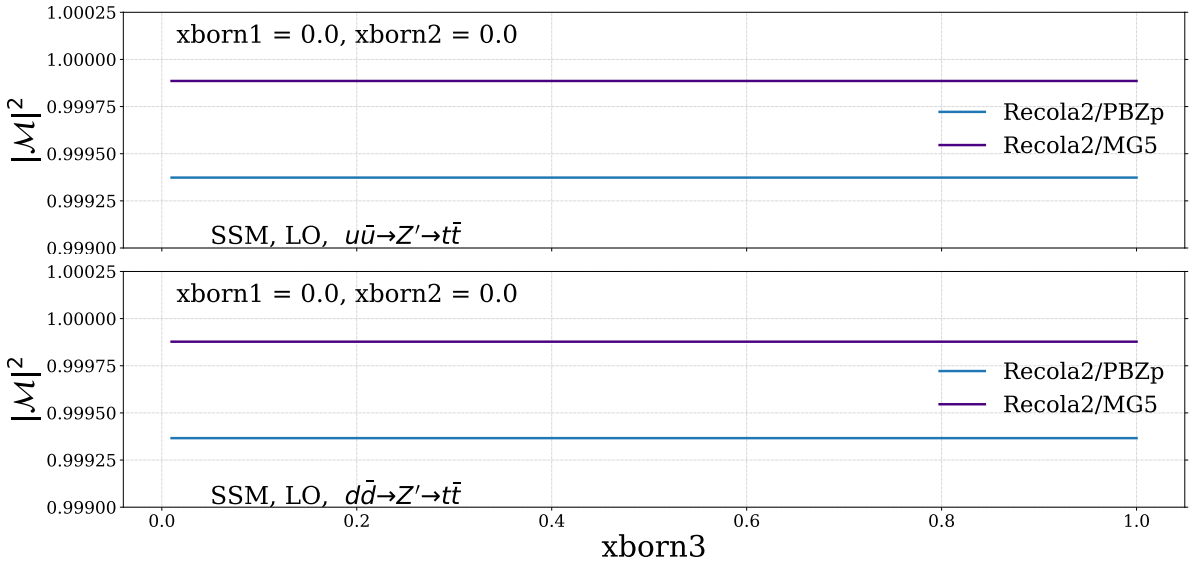


Figure 3.8: The ratio of the Born amplitude in Recola2 vs PBZp and MG5 in the SSM for $u\bar{u} \rightarrow Z' \rightarrow t\bar{t}$ (top). Bottom: same but for $d\bar{d} \rightarrow Z' \rightarrow t\bar{t}$.

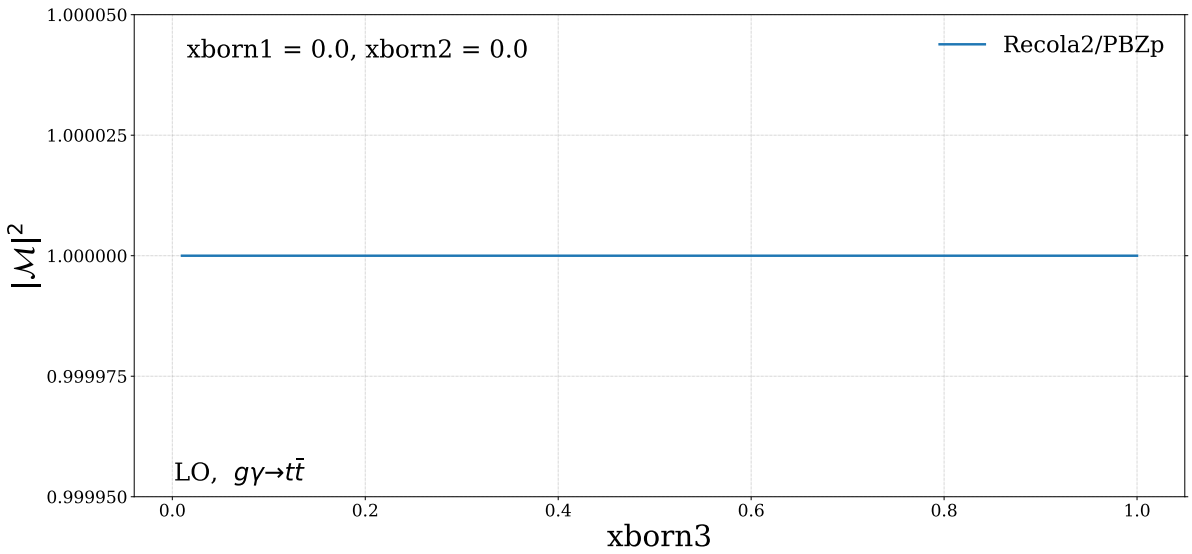


Figure 3.9: The ratio of the Born amplitude for Recola2 over PBZp in the SSM for $g\gamma \rightarrow t\bar{t}$.

Real

The real amplitudes for Z' mediated processes have been also validated against the old calculation. In Figure 3.10 we show the $u\bar{u} \rightarrow Z' \rightarrow t\bar{t}g$ and the $d\bar{d} \rightarrow Z' \rightarrow t\bar{t}g$ squared amplitudes of

the SSM calculated in RecoLa2 over the ones obtained using the old PBZp package. In both cases we find a very good agreement after multiplying RecoLa2's amplitudes by a factor of $2\pi/\alpha_S$. In addition, we compare, in the SSM, the sum of the squared amplitudes of $g\bar{q} \rightarrow Z' \rightarrow t\bar{t}\bar{u}$

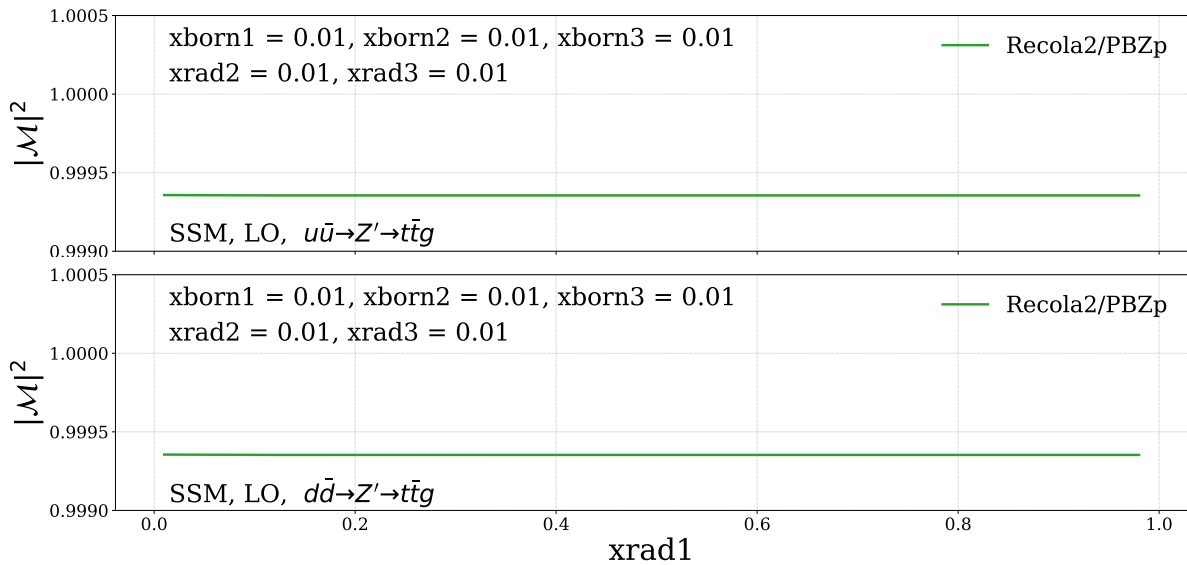


Figure 3.10: The ratio of the real amplitude for RecoLa2 over PBZp in the SSM at for $u\bar{u} \rightarrow Z' \rightarrow t\bar{t}g$ (top). Bottom: same but for $d\bar{d} \rightarrow Z' \rightarrow t\bar{t}g$.

and $gq \rightarrow Z' \rightarrow t\bar{t}q$, where q can be an up type or a down type quark, in both RecoLa2 (times $2\pi/\alpha_S$) and PBZp and we find again a very good agreement as can be seen from Figure 3.11.

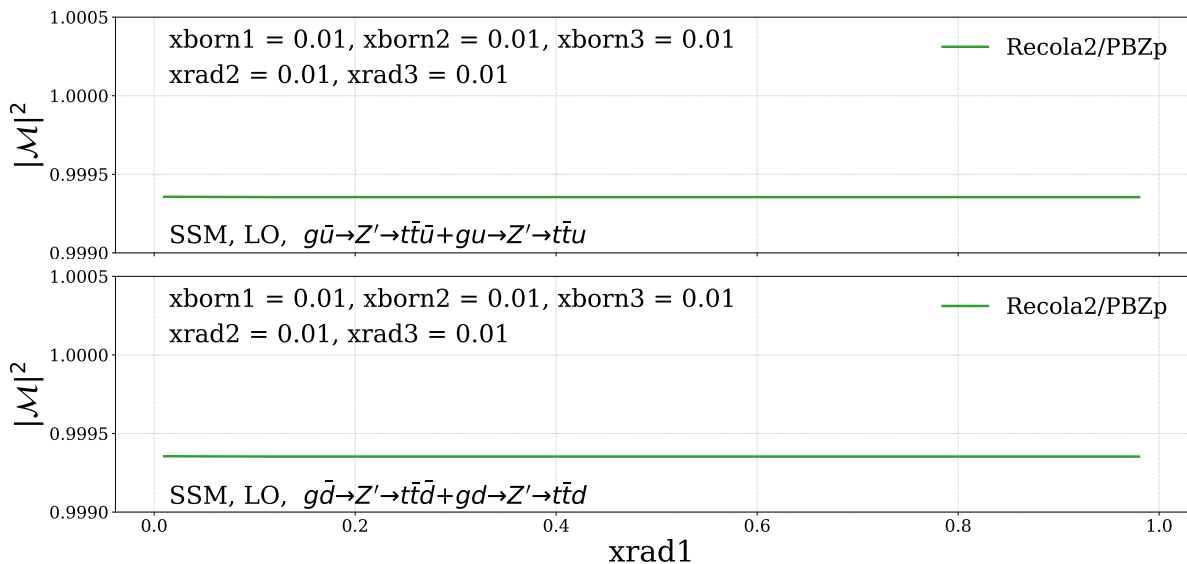


Figure 3.11: The ratio of the real amplitude for RecoLa2 over PBZp in the SSM for $g\bar{u} \rightarrow Z' \rightarrow t\bar{t}\bar{u} + g\bar{u} \rightarrow Z' \rightarrow t\bar{t}u$ (top). Bottom: same but for $g\bar{d} \rightarrow Z' \rightarrow t\bar{t}\bar{d} + g\bar{d} \rightarrow Z' \rightarrow t\bar{t}d$.

Virtual

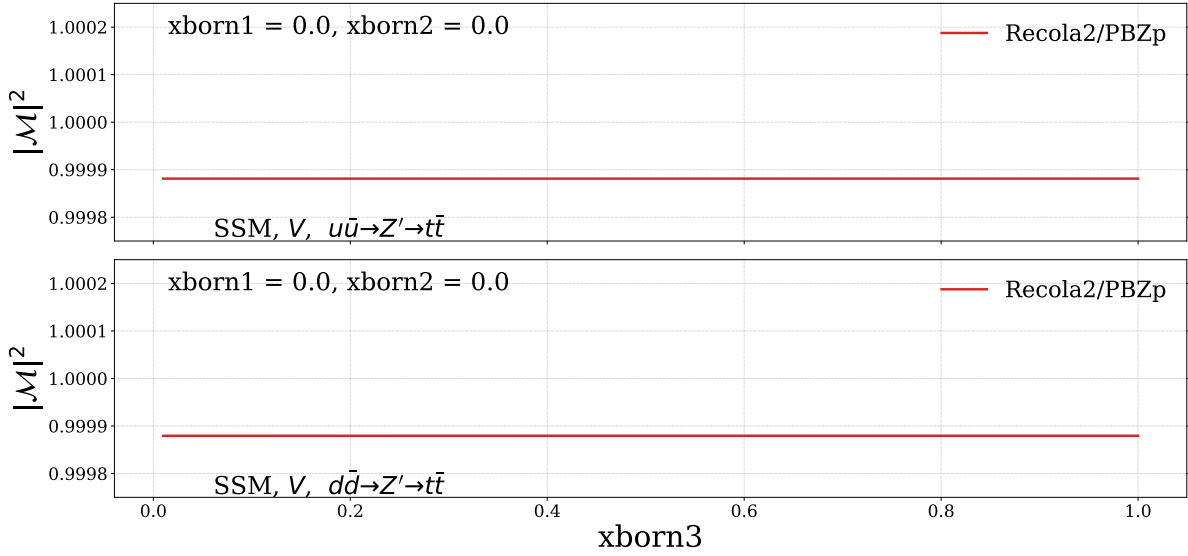


Figure 3.12: The ratio of the virtual amplitude for RecoLa2 over PBZp in the SSM for $u\bar{u} \rightarrow Z' \rightarrow t\bar{t}[+g]$ (top). Bottom: same but for $d\bar{d} \rightarrow Z' \rightarrow t\bar{t}[+g]$.

Last but not least, as shown in Figure 3.12, we also validate the virtual squared amplitudes of RecoLa2 against the old PBZp calculation for both $u\bar{u} \rightarrow Z' \rightarrow t\bar{t}[+g]$ and $d\bar{d} \rightarrow Z' \rightarrow t\bar{t}[+g]$ finding a very good agreement. To this end, in addition to the parameters used to calculate the Born amplitudes, we also needed to set the renormalisation scale of the strong coupling constant to be equal to the infrared renormalisation scale in RecoLa2, because these two parameters can not have different values in PBZp, moreover we had to fix one additional parameter of RecoLa2 that contributes to the infrared regularisation (Δ_{IR2}) to $\pi^2/6$. To see how these parameters can be called in RecoLa2 see Listing B.3 of Appendix B.5. Note that the resulting RecoLa2 squared amplitudes have to be multiplied by $2\pi/\alpha_S$ to match the squared amplitudes in PBZp.

3.4 POWHEG BOX: Matching NLO QCD computations with Parton Shower Monte Carlos

We implemented the squared amplitudes for the EW top pair hadroproduction at LO and NLO QCD accuracy calculated with RecoLa2 in the computer framework POWHEG BOX [44] in order to obtain numerical results for hadron colliders. The Positive Weight Hardest Emission Generator method, used in the POWHEG BOX, aims to attain a NLO precision for an inclusive observable while sustaining at least leading logarithmic accuracy for exclusive ones obtained through

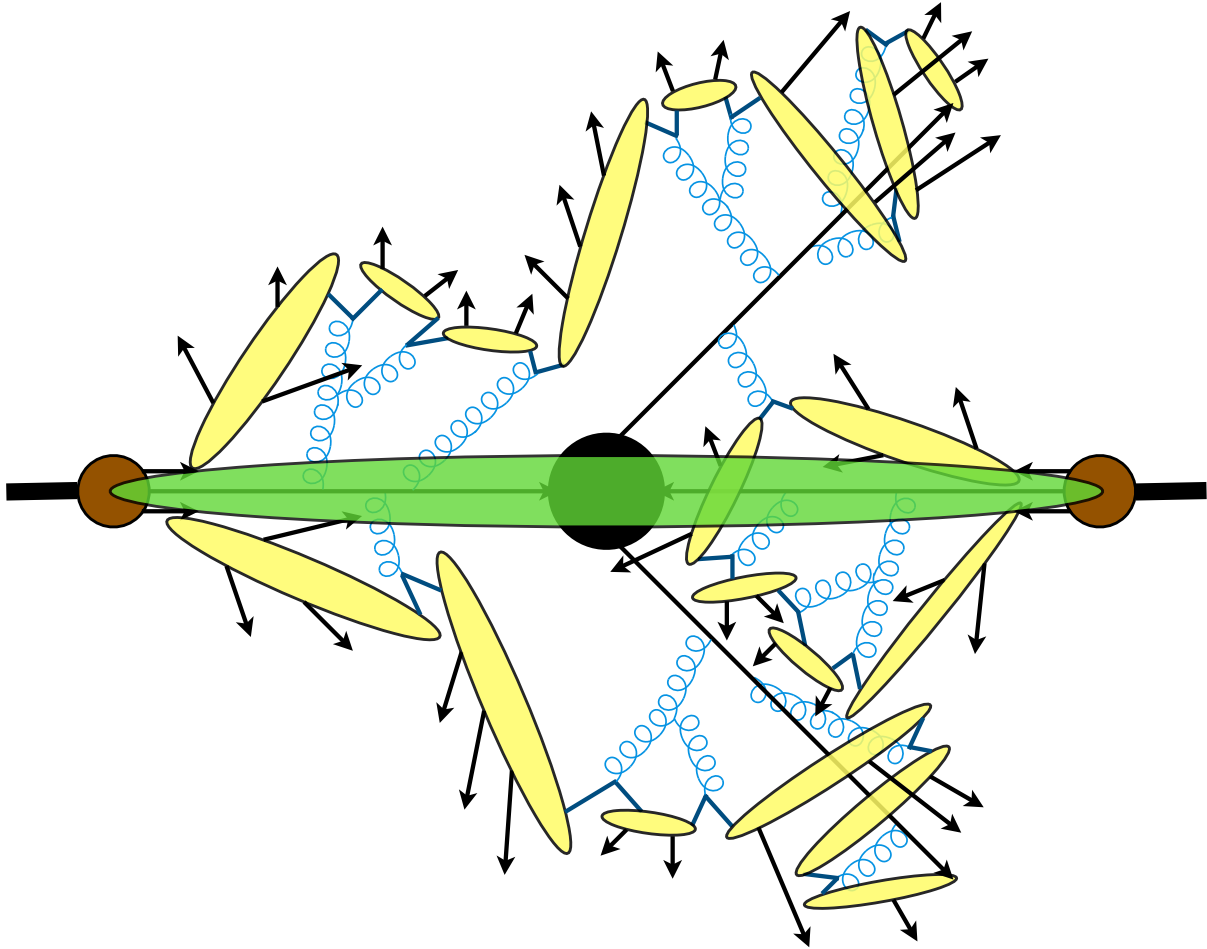


Figure 3.13: The structure of a proton proton collision at the LHC as described by event generators.

parton shower algorithms implemented in various publicly available Shower Monte Carlo event generators such as PYTHIA [62, 110] or Herwig [111].

The SMC event generators aim to simulate particle collisions in full detail starting from the high-energy perturbative domain down to the detector level⁵, which is, basically, what is observed by experiments. They can be seen as virtual colliders with the ultimate goal of producing unweighted events, that is events with the same probability as they occur in nature, each consisting of a list of final-state particles and their momenta. The structure of a proton-proton collision at the LHC as built up by event generators can be described as follows. The simulation starts by calculating the hard subprocess, described by a black blob in Figure 3.13, which is the highest momentum transfer process in the event. The incoming and outgoing partons (quarks and gluons) involved in the hard scattering, together with any coloured particles, can emit virtual gluons, which can produce quark-antiquark pairs or even radiate further gluons, resulting

⁵This does not include the detector effects which can be obtained through detector simulation tools like DELPHES [112] for example.

in a cascade of partons known as the parton showers, this is shown in blue in Figure 3.13. The parton shower evolution starts from the hard process and falls down to lower and lower momentum scales reaching the non-perturbative regime, where the strong coupling constant is not small anymore. At this point, the process of hadronisation (yellow in Figure 3.13), in which the partons are confined into colourless hadrons, begins. The fact that the colliding protons contain other coloured partons in addition to the ones involved in the hard scattering implies that these additional constituents will undergo multiple interactions, this is known as the underlying event and is shown in green in Figure 3.13. Many of the resulted hadrons are not stable, thus, the last stage of event generation is the simulation of the decay of those hadrons.

The LO matrix element at fixed order description have very few partons in the final state and is only valid with partons that are hard and well separated, however, it includes the correct quantum interference effects. On the other hand, a shower MC is a resumming procedure which has no limits on parton multiplicity, but is only valid in the soft and collinear regions of the phase space and only account for a partial interference. Thus, these two approaches are complementary. Combining fixed-order tree-level matrix elements and parton showers can be done in Monte Carlo simulations with methods like MLM [113] and CKKW [114, 115] where, using a cut-off, one truncates the phase space in two parts, the hard well separated part and the soft and/or collinear part. Nevertheless, LO accuracy is insufficient and more precision is needed.

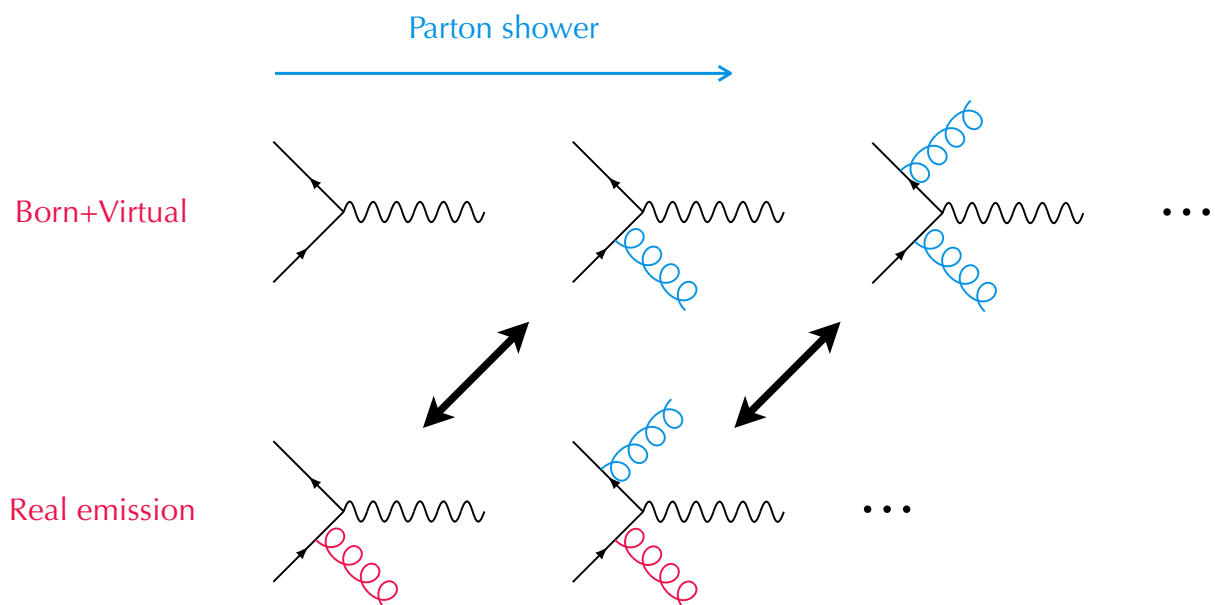


Figure 3.14: A pictorial representation of the double counting problem at NLO. The first line consists of the Born and virtual amplitudes. The second line contain the real amplitudes. The blue radiations come from the parton shower while the red emission comes from the matrix element.

Matching NLO fixed order calculations with parton showers is beyond the ability of SMC event generators. In contrast to the tree level matrix elements, the partons of the hard scattering at NLO are not always hard and well separated, they can go soft or collinear. Thus, requiring a cut-off as in the LO case is not infrared safe, since at NLO, one has to integrate the real radiation over the complete phase space of the one particle that can be soft or collinear to obtain the IR poles that cancel against the virtual corrections. Furthermore, as seen in Figure 3.14, an overlap between the extra radiation of the real emission matrix element and the one coming from the parton shower can occur, this is known as the double counting problem.

In this section we describe the POWHEG method that can circumvent the previously mentioned problems by consistently matching the NLO matrix elements with the parton shower. We start by briefly discussing the concepts of the Monte Carlo integration and the subtraction method, that are used in POWHEG to perform the integration over the phase space and to deal with the IR singularities. We then review the basics of the parton shower algorithm. Finally, we briefly discuss the POWHEG method.

3.4.1 Monte Carlo integration

The amplitudes obtained with RecoLa2 need to be integrated over the complex multidimensional phase space $d\phi$. This task is done in POWHEG using Monte Carlo integration along with an optimization called VEGAS.

The idea of the Monte Carlo method is to estimate the numerical integration using random numbers⁶. To illustrate this, let us take the following integral

$$I = \int_{[0,1]^d} d^d y f(y_1, \dots, y_d), \quad (3.8)$$

where I is the integral of the function $f(y_1, \dots, y_d)$ which is square-integrable⁷ and depends on d variables y_1, \dots, y_d over the unit hypercube $[0, 1]^d$. For brevity, we will denote a point in the unit hypercube by $x = (y_1, \dots, y_d)$ and the function evaluated at this point by $f(x) = f(y_1, \dots, y_d)$. Hence, the integral I can read as follows

$$I = \int dx f(x). \quad (3.9)$$

⁶In practice, computers can not deliver random numbers since they are deterministic machines, instead, they can produce pseudo random numbers which can approximate the properties of random numbers to a very good accuracy.

⁷A square-integrable function is a real- or complex-valued measurable function for which the integral of the square of the absolute value is finite.

Given N uniform samples, or in other words N uniformly distributed and continuous random points $\{x_n, n = 1, \dots, N\}$ in the integration domain, the integral on $f(x)$ can be estimated by

$$E = \frac{1}{N} \sum_{n=1}^N f(x_n). \quad (3.10)$$

E is the so-called Monte Carlo estimate. Using the law of large numbers we find

$$\lim_{N \rightarrow \infty} \frac{1}{N} \sum_{n=1}^N f(x_n) = I. \quad (3.11)$$

In words, this means that the Monte Carlo estimate converges to the true value of the integral for large samples. Since we are talking about an estimation, we need to provide information about its error. To this aim, let us first introduce the variance S^2 of the function f

$$S^2[f] = \int dx (f(x) - I)^2. \quad (3.12)$$

Using Eq. (3.12), it can be shown that the variance of our Monte Carlo estimate E is

$$S^2[E] = \frac{S^2[f]}{N}, \quad (3.13)$$

meaning that the error in our Monte Carlo integration decreases as $1/\sqrt{N}$ which independent of the dimension d of the integral. In practice, Eq. (3.13) can not be used easily since we do not know the result of the integral I . Alternatively, we can use the Monte Carlo estimate that we have computed

$$S^2[E] = \frac{1}{N-1} \sum_{n=1}^N (f(x_n) - E)^2 = \frac{1}{N} \sum_{n=1}^N (f(x_n))^2 - E^2. \quad (3.14)$$

As we have seen, the convergence of the Monte Carlo integration is relatively slow ($1/\sqrt{N}$). In order to ameliorate this, the so-called variance reduction techniques [116] can be used. One of these techniques is importance sampling where, instead of sampling from an uniform distribution, one uses a distribution that is suited for the integrand. Schematically, this is equivalent to a change of variables

$$\int dx f(x) = \int dx g(x) \frac{f(x)}{g(x)} = \int dG(x) \frac{f(x)}{g(x)}, \quad (3.15)$$

where $dG(x) = g(x)dx$. In case $g(x)$ is not uniformly distributed, the definition of the Monte Carlo estimate and variance become

$$E = \frac{1}{N} \sum_{n=1}^N \frac{f(x)}{g(x)}, \quad (3.16)$$

$$S^2(E) = \frac{1}{N} \sum_{n=1}^N \left(\frac{f(x)}{g(x)} \right)^2 - E^2. \quad (3.17)$$

The optimal case is when $g(x) \rightarrow f(x)/I$ which yields a vanishing variance $S^2 = 0$, but this would require preliminary knowledge about the integrand. As a solution, an adaptive algorithm that learns about the function to be integrated as it proceeds can be used. It realises importance sampling without requiring advance knowledge about the integrand. This algorithm is called VEGAS and was suggested in 1977 by G. Peter Lepage, for a detailed description of this optimisation we refer the reader to [117, 118].

3.4.2 The subtraction method

As we have seen in Section 3.2, NLO calculations involve 3 different types of amplitudes in perturbation theory, namely the Born, the virtual and the real amplitudes. Schematically the integration over the phase spaces of these 3 contributions in a $2 \rightarrow n$ NLO process can be described as follows

$$\sigma^{NLO} = \int_n d\sigma^B + \int_n d\sigma^V + \int_{n+1} d\sigma^R, \quad (3.18)$$

where the subscripts B , V , and R stands for Born, virtual, and real respectively. Furthermore, in the Born and virtual cases, the integral is over the n -particle phase space, whereas in the real case it is over the $(n+1)$ -particle phase space.

Even though the virtual amplitudes obtained with RecoLa2 are UV finite, they still suffer, together with the real amplitudes, from IR divergences when integrated over the phase space. However, for infrared safe observables, the sum of the real and the virtual contributions is finite after integration. In practice, this is done by the mean of dimensional regularization where one shifts the dimension of the integral from 4 to $4+2\epsilon$, where ϵ is a very small number. After integration the divergences appear as explicit poles in both virtual and real terms but with opposite signs resulting in their cancellation. This can only be done analytically and, as we saw in the previous section, we use Monte Carlo integration in POWHEG where an integral with a non-integer number of dimensions can not be estimated.

An alternative solution that suits numerical techniques is the subtraction method. The basic idea of the subtraction method is to modify Eq. (3.18) by including a term that matches the singularity structure of the real contribution but with an opposite sign. This cancels the IR divergences in the real phase space integral. The subtraction term needs to be added back to guarantee that Eq. (3.18) remains unchanged. In addition, it needs to be simple enough in order to ensure that its integral over the momenta of the unresolved parton can be done analytically in dimensional regularization. Once this analytic integral is performed, we obtain an object that shares the same phase space as the Born and the virtual terms. Additionally, ensured by the KLN theorem and the definition of the subtraction term, this integrated subtraction term will have an explicit pole structure that cancels the one from the virtual contribution. As a result, the integrated subtraction term and the virtual term can then be merged into one non-divergent term, which is integrated over the same phase space. Thus, we obtain an equation with three finite integrals

$$\sigma^{NLO} = \int_n d\sigma^B + \int_n \left[d\sigma^V + \int_1 d\sigma^S \right] \int_{n+1} \left[d\sigma^R - d\sigma^S \right], \quad (3.19)$$

where S stands for subtraction. While different methods can be used to construct these subtraction terms, we will only briefly describe the FKS subtraction method by Frixione, Kunszt and Signer [102, 103] used in the POWHEG BOX.

To elaborate on the FKS method let us go back to the real part of Eq. (3.18) which can be written in terms of the real matrix element and the $n + 1$ phase space as follows

$$d\sigma^R = |\mathcal{A}_{n+1}|^2 d\phi_{n+1}, \quad (3.20)$$

where the squared amplitude $|\mathcal{A}_{n+1}|^2$ diverges⁸ as $\frac{1}{\xi_i(1-y_{ij})}$, with ξ_i representing the ratio of the energy of the final state leg i over the total partonic energy, and y_{ij} describing the cosine of the angle between the two legs i and j . The FKS subtraction method relies on the partition of the $n + 1$ phase space into distinct zones that contain at most one collinear and/or one soft singularity. This can be attained schematically by editing Eq. (3.20) as follows

$$d\sigma^R = \sum_{i,j} S_{ij} |\mathcal{A}_{n+1}|^2 d\phi_{n+1}, \quad (3.21)$$

where the partitioning function S_{ij} is a function of the momenta of the particles i and j . It is defined such that it vanishes for all singular regions that are not associated with parton i

⁸Here we suppose that the ξ_i factor in the phase space already cancels with one of $\frac{1}{\xi_i}$ in the squared amplitude.

going soft or partons i and j becoming collinear and that the full phase space is recovered when summing over all possible pairs

$$\sum_{i,j} S_{ij} = 1. \quad (3.22)$$

As a result, every term in Eq. (3.21) is convergent everywhere over the phase space except for the ones where the energy of the parton i approaches zero or the partons i and j are very close to one another. Thus, these remaining divergences can be regularised, which, using the fact that

$$\int dx \left(\frac{1}{x} \right) f(x) = \int dx \frac{f(x) - f(0) \Theta(x_{cut} - x)}{x}, \quad (3.23)$$

leads to changing every term in the sum of Eq. (3.21) to

$$\left(\frac{1}{\xi_i} \right)_{\xi_{cut}} \left(\frac{1}{1-y_{ij}} \right)_{\delta_0} \xi_i (1-y_{ij}) |\mathcal{A}_{n+1}|^2 d\phi_{n+1}. \quad (3.24)$$

Even though the cancellation between ξ_i and $(1-y_{ij})$ of Eq. (3.24) and the divergent poles of the squared amplitude has to be performed analytically, this does not cause a problem since the real amplitude factorises to the Born times the Altarelli-Parisi splitting functions in the collinear limit and to the Born times the eikonals in the soft limit. Furthermore, as mentioned previously, the integrated subtraction terms have to be added back to the virtual corrections. This leads to terms proportional to the colour correlated Born amplitudes when integrated over the one particle phase space. For a more complete explanation on how to construct the subtraction terms in the FKS framework we refer the reader to Ref [119].

3.4.3 Basics of QCD parton showers

A parton shower transforms the inclusive partonic prediction into an exclusive quantity. This is done by dressing the external legs of the matrix element with radiations. By doing so, it selects one possible history, in case of a final state parton, or prehistory, in case of an initial state parton, of all possible histories of the hard event. Furthermore, a parton shower is unitary, it does not change the probability of the hard event. In other words, the inclusive cross section should not change when the extra radiation is added.

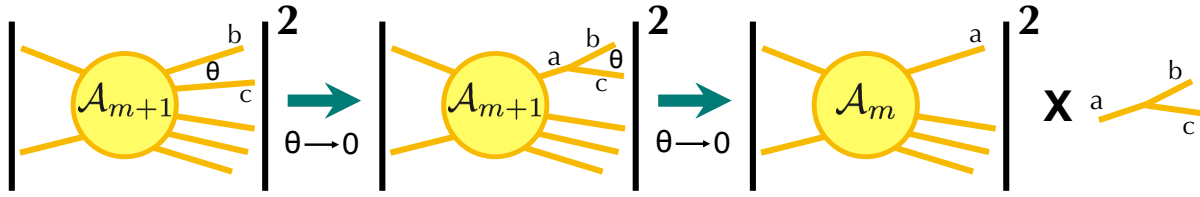


Figure 3.15: Pictorial representation of the collinear factorisation in QCD.

A general property of QCD, which goes under the name of collinear factorisation or universality of amplitudes, is that the squared amplitudes near the collinear limit factorise. This means, as can be seen in Figure 3.15, that if we consider an amplitude with $m + 1$ partons in the final state and we square it, then if two of the final state partons are close enough in the phase space (their angle goes to zero), they can be seen as coming from the same particle, and the value of the full square amplitude factorises into the probability of m partons times a universal object known as the splitting function. This is universal in the sense that the physics of the splitting does not interfere with the rest of the amplitudes. This can be formulated mathematically as

$$|\mathcal{A}_{m+1}|^2 d\phi_{m+1} \rightarrow |\mathcal{A}_m|^2 d\phi_m \times \frac{\alpha_S}{2\pi} \frac{dt}{t} dz \frac{d\varphi}{2\pi} \hat{P}_{a \rightarrow bc}(z), \quad (3.25)$$

where \mathcal{A}_{m+1} and \mathcal{A}_m are the amplitudes for the $m + 1$ and m particle processes respectively, $\hat{P}_{a \rightarrow bc}$ is the Altarelli-Parisi splitting function with a, b , and $c \in \{q, g\}$, t represents the hardness of the branching and tends to zero in the collinear limit, it can be the virtuality, the transverse momentum, or the angular variable, φ is the azimuthal angle, it can be chosen to be the angle between the polarisation of the particle a and the plan of the branching, and z is the energy variable, it represents the energy fraction taken by parton b from parton a .

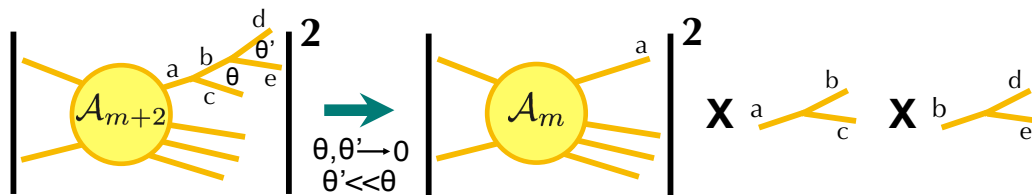


Figure 3.16: Pictorial representation of the recursive application of the collinear factorisation formula in Eq. (3.26).

The previous picture can be applied many times in a parton shower program. For instance, as shown in Figure 3.16, if, instead of one branching, we start with two branchings, then in the limit

where both angles are very small and strongly ordered⁹ Eq. (3.25) can be applied recursively

$$|\mathcal{A}_{m+2}|^2 d\phi_{m+2} \rightarrow |\mathcal{A}_m|^2 d\phi_m \times \frac{\alpha_S}{2\pi} \frac{dt}{t} dz \frac{d\varphi}{2\pi} \hat{P}_{a \rightarrow bc}(z) \times \frac{\alpha_S}{2\pi} \frac{dt'}{t'} dz' \frac{d\varphi'}{2\pi} \hat{P}_{b \rightarrow de}(z'). \quad (3.26)$$

This procedure is called the recursive collinear factorisation and can be done for an arbitrary number of emissions. It is also known as the leading-log approximation where leading-log refers to a single power of logarithmic enhancement for every power of α_S . This can be seen explicitly in the case of a real emission cross section with k qg splittings for example

$$\sigma_0 \alpha_S^k \int \frac{dt_1}{t_1} \dots \frac{dt_k}{t_k} \theta(Q^2 > t_1 > \dots > t_k > Q_0^2) = \sigma_0 \frac{1}{k!} \alpha_S^k \log^k \frac{Q^2}{Q_0^2} \quad (3.27)$$

where σ_0 is the lowest-order cross section for the process at hand, Q is a typical hard scale, Q_0 is a small infrared cut-off that separates perturbative from non-perturbative regimes, and the function θ is equal to 1 if its argument is true and zero otherwise.

Although Eq. (3.27) involves a lower cut-off, the fact that it would blow up as t approaches 0 means that the real emission cross section is susceptible to low energy phenomena that cannot be interpreted by perturbative QCD. As we have seen before, for IR safe observables, this can be dealt with by including the virtual corrections as stated by the KLN theorem. This is guaranteed in parton shower programs by means of the so-called Sudakov form factors.

The Sudakov form factor is the probability that a parton leaves a high scale to actually show up at a lower scale without having emitted any resolvable radiation. If we describe the differential probability for the splitting $a \rightarrow bc$ in the phase space element $[t, t + dt]$ knowing that no emission occurred before as

$$dp(t) = \sum_{bc} \frac{dt}{t} \int dz \frac{d\varphi}{2\pi} \frac{\alpha_S}{2\pi} \hat{P}_{a \rightarrow bc}(z) \quad (3.28)$$

then the probability of no splitting between the scales t and $t + dt$ is $1 - dp(t)$. This can be generalised to

$$\Delta(Q^2, t) = \prod_k \left[1 - \sum_{bc} \frac{dt}{t} \int dz \frac{d\varphi}{2\pi} \frac{\alpha_S}{2\pi} \hat{P}_{a \rightarrow bc}(z) \right] \quad (3.29)$$

$$= \exp \left[- \sum_b \int_t^{Q^2} \frac{dt'}{t'} \int dz \frac{d\varphi}{2\pi} \frac{\alpha_S}{2\pi} \hat{P}_{a \rightarrow bc}(z) \right] \quad (3.30)$$

⁹Strongly ordered means that the angle of the second branching is smaller than the angle of the first one. It also means that the virtuality of the first branching is higher than the one of the second splitting.

where $\Delta(Q^2, t)$ is the Sudakov form factor describing that the parton a does not emit in the scale interval $[Q^2, t]$. The nice property about the Sudakov form factor is the fact that it is multiplicative. For instance, for a parton, the probability of no emission from one scale A down to another scale B times the probability of no emission from B to a lower scale C is equal to the probability of no emission from A to C .

Using the fact that (i) the splitting functions are universal and (ii) the Sudakov form factor is multiplicative, the probability for k ordered splittings from a leg at a given scale can be defined in a parton shower algorithm as

$$dP_k(t_1, \dots, t_k) = \Delta(Q^2, Q_0^2) \prod_{l=1}^k dp(t_l) \theta(t_{l-1} - t_l) \quad (3.31)$$

where Q_0 is the hadronisation scale below of which the description for parton splitting cannot be trusted anymore.

So far, we limited our discussion to the parton shower in the collinear regions and did not consider the issues related to soft IR divergences. Indeed, in regions of the phase space where the energy fraction z goes to either zero or one the QCD amplitudes manifest singularities. This is properly treated in public SMC tools; for the sake of brevity we do not describe it here and we refer the reader to [120] for a detailed description.

3.4.4 The POWHEG method

The POWHEG method is a procedure for matching NLO calculations with parton shower generators. The idea behind it was first proposed in [60], and then discussed at great length in [42]. What distinguishes the positive weight hardest emission generator method from other interfacing procedures is that, as suggested by its name, it is capable of generating positive weighted events only, and it does not depend on the SMC program used for subsequent showering.

To overcome the problem of double counting, POWHEG produces the hardest emission¹⁰ first separately from the subsequent ones. Schematically¹¹, the POWHEG cross section for the generation of the hardest event is

$$d\sigma = \bar{B}(\phi_B) d\phi_B \left[\Delta_R(p_T^{min}) + \frac{R(\phi_R)}{B(\phi_B)} \Delta_R(k_T(\phi_R)) d\phi_{rad} \right] \quad (3.32)$$

¹⁰By hardest we mean the emission that has the highest transverse momentum, either with regard to the beam for initial state radiation (ISR), or as compared to another particle for final state radiation (FSR).

¹¹Here we do not go into the details about the radiation regions and the correct treatment of the associated flavour configurations, for a complete discussion we refer to [42, 60]

where $B(\phi_B)$ and $R(\phi_R)$ are the Born and real amplitudes respectively. $k_T(\phi_R)$ is the transverse momentum of the radiation relative to the beam or to another parton, depending on the singular region. The p_T^{min} parameter is introduced as a lower cut-off on the transverse momentum, it is needed in order to prevent the strong coupling constant from reaching unphysical values. $\bar{B}(\phi_B)$ is the NLO differential cross section at fixed underlying Born kinematics and integrated over the radiation variables, it can be expressed as

$$\bar{B}(\phi_B) = B(\phi_B) + \left[V(\phi_B) + \int d\phi_{rad} R(\phi_R) \right] \quad (3.33)$$

where $V(\phi_B)$ is the virtual contribution and the square bracket reflect the fact that a subtraction procedure, as described in Section 3.4.2, has been used. Finally, Δ_R is the POWHEG Sudakov form factor, and can be expressed as follows

$$\Delta_R(p_T) = \exp \left[- \int d\phi_{rad} \frac{R(\phi_R)}{B(\phi_B)} \theta(k_T(\phi_R) - p_T) \right] \quad (3.34)$$

where θ is the usual step function rendering values $k_T(\phi_R) < p_T$ prohibited. Thus, the POWHEG method is a kind of a multiplicative approach that uses the old k factor¹² thinking to improve the original SMC equation. This is achieved, as can be seen from Eq. (3.32), by replacing the Born cross section by $\bar{B}(\phi_B)$ which is normalized to NLO by construction. At low transverse momenta the POWHEG Sudakov form factor turns into a standard one as in the SMC programs. Nevertheless, for inclusive quantities, the NLO precision of Eq. (3.32) is preserved. Furthermore, due to the fact that $\Delta_R \approx 1$ and $\bar{B}/B \approx 1 + \mathcal{O}(\alpha_S)$ in the high transverse momentum regions of the phase space, the high- p_T regions of the radiation is properly described by the real contributions

$$d\sigma \approx \bar{B}(\phi_B) d\phi_B \frac{R(\phi_R)}{B(\phi_B)} d\phi_{rad} \approx R(\phi_R) d\phi_B d\phi_{rad}. \quad (3.35)$$

In reality, a collision process involve multiple coloured massless particles in the initial or in the final state. Hence, the procedure described previously need to be repeated whenever one of these massless coloured partons goes soft or becomes parallel to another leg resulting in a divergence. For this to be possible, the real emission cross section is divided, as discussed in 3.4.2, into a sum of terms having at most one collinear and one soft singularities. Subsequently, for every term of the sum, a radiation is produced independently and only the one with the highest p_T is maintained. Finally, the event is generated with respect to the flavour and kinematics associated to hardest emission.

¹²When we didn't have a fully exclusive prediction at NLO we were using a k factor to normalise the cross section.

Once generated, the hardest event can be then interfaced with any SMC program which can then create the rest of the shower. One important condition required by POWHEG in order to avoid the over-counting problem is that the SMC need to be either p_T -ordered or can veto radiations that have a transverse momentum higher than the first emission.

3.5 POWHEG BOX implementation

The POWHEG method described in the previous section has been implemented in a computer framework dubbed the POWHEG BOX [44]. This framework collects a set of formulae and algorithms in Fortran 77 in order to facilitate the POWHEG implementation of a QCD NLO process in a semi-automated fashion. This is achieved given the following ingredients

- The list of all flavour structures of the Born processes.
- The list of all flavour structures of the real processes.
- The Born phase space.
- The Born squared amplitudes B , the colour correlated ones B_{ij} and the spin correlated ones $B_{\mu\nu}$.
- The real matrix elements squared for all relevant partonic processes.
- The finite part of the renormalised virtual corrections, calculated in D-dimensions.
- The Born colour structures in the limit of a large number of colours.

Once these ingredients have been specified, the POWHEG BOX can automatically identify the singular regions, build the soft and collinear counter terms, construct the collinear remnants which are the left-over of the PDFs redefinition, produce the event with Born kinematics including virtual corrections, and then generates the hardest additional radiation according to the POWHEG Sudakov form factor. Many processes are already implemented in the POWHEG BOX including, but not limited to, single-top and single-top W associated production, Higgs boson production in gluon fusion etc [121–126].

In what follows, we review the previously listed elements that need to be provided by the user. This is done in the context of electroweak top-pair production using the RecoLa2 package. We then compare some cross sections obtained with our new implementation against the old calculation in [40].

Process specification

The first step of a POWHEG implementation is to provide the code with the lists of all possible flavour structures¹³ for both Born and real processes that can contribute to the NLO calculation we want to implement. Dubbed `flst_born` and `flst_real`, the two lists are declared in the header file `pwhg_flst.h` as `flst_born(nlegborn, maxprocborn)` and `flst_real(nlegreal, maxprocreal)` respectively, where `nlegborn` set the number of external legs of the Born (or virtual) processes whereas `nlegreal` set the number of external particles of the real processes, and both need to be specified by the user in the `nlegborn.h` file¹⁴, furthermore the variables `maxprocborn` and `maxprocreal` specify the maximal number of inequivalent Born and real flavour configurations respectively. The two arrays have then to be filled in a subroutine called `init_processes`. The elements of these arrays consist of the list of initial and final state particles of the Born and real process represented by their PDG codes [127] except for the gluon which, instead of 21, has the code 0. For instance, the entry `[2, -2, 6, -6]` represent the process $u\bar{u} \rightarrow t\bar{t}$. The index of the first light parton in those arrays must be specified in `init_processes` by setting the variable `flst_lightpart`. Finally, and also in `init_processes`, one need to fill the array `kn_masses`¹⁵ with the masses of the external particles of the process and to fix the lower limit on the mass of the final state by setting the variable `kn_minmass`.

In our particular case, we implement the EW top-pair hadroproduction and its NLO QCD corrections, and since the produced tops are on-shell, we deal with $2 \rightarrow 2$ processes at the Born and virtual level. Thus, our `nlegborn` and `nlegreal` are equal to 4 and 5 respectively. Additionally we set the variables `maxprocborn` and `maxprocreal` to 30 and 100 respectively. As seen in 3.2.1, the tree level processes that contribute to our calculation are $q'\bar{q} \rightarrow t\bar{t}$ with $q'\bar{q} \in \{u\bar{u}, c\bar{c}, d\bar{d}, s\bar{s}, b\bar{b}, d\bar{s}, s\bar{d}, b\bar{c}, c\bar{b}, d\bar{b}, s\bar{b}, b\bar{b}\}$, and due to QED singularities, we also include the photon induced processes. Thus, our Born flavour configuration array `flst_born` contains the following 28 entries

$$\begin{aligned} \text{flst_born} = & [[-5, 5, 6, -6], [-5, 3, 6, -6], \dots, [-1, 3, 6, -6], [-1, 1, 6, -6], \\ & [0, 22, 6, -6], [1, -1, 6, -6], \dots, [5, -5, 6, -6], [22, 0, 6, -6]]. \end{aligned}$$

The real processes have one additional parton and can have either two quarks or one gluon and one quark in the initial state. Our real flavour configuration array `flst_real` consists of the

¹³Here we mean by flavour structure of a process the type of all its incoming and outgoing particles.

¹⁴Note that in `nlegborn.h`, `nlegreal` is set to `nlegborn+1` automatically.

¹⁵All variables with the `kn` prefix are defined in the header file `pwhg_kn.h`.

following 78 entries

```
flst_real = [[-5,5,6,-6,0], [-5,3,6,-6,0], ..., [-1,3,6,-6,0],
             [-1,1,6,-6,0], [1,-1,6,-6,0], ..., [5,-5,6,-6,0],
             [0,-5,6,-6,-5], [0,-5,6,-6,-3], ..., [0,-1,6,-6,-3],
             [0,-1,6,-6,-1], [0,1,6,-6,1], ..., [0,5,6,-6,5],
             [-5,0,6,-6,-5], [-5,0,6,-6,-3], ..., [-1,0,6,-6,-3],
             [-1,0,6,-6,-1], [1,0,6,-6,1], ..., [5,0,6,-6,5]].
```

As we can see from `flst_real`, the variable `flst_lightpart` need to be given the value 5 in our case. Finally we set `kn_masses` and `kn_minmass` as follows

```
kn_masses = [0,0,mt,mt,0]
kn_minmass = 2*mt,
```

where `mt` is the mass of the top quark and can be chosen in the POWHEG input file `powheg.input`. Additional information about the input file will be given in the following subsections.

The Born and Born-correlated squared amplitudes

Even though the Born phase space needs to be provided by the user, we skip the explanation on how this was done for our implementation since we used the same `born_phsp`¹⁶ file as in the `hvg`¹⁷ POWHEG package [128]. For more details about the Born phase space in POWHEG we refer the reader to [44, 53].

We now move on to the implementation of the Born and Born-correlated squared amplitudes. In POWHEG BOX this is done through the routine

```
setborn(p(0:3,1:nlegborn),bflav(1:nlegborn),born,
        bornjk(1:nlegborn,1:nlegborn),bmunu(0:3,0:3,1:nlegborn)).
```

where `setborn` should return the Born squared amplitude in `born`¹⁸, the colour-correlated one in `bornjk`, and the spin-correlated one in `bmunu`, according to the choice of the 4-momenta

¹⁶This file contains the `born_phsp(xborn)` subroutine that fills the four-momenta of Born-process particles (both in the laboratory and in the centre-of-mass frame), the Bjorken x of the two incoming partons, the minimal mass of the Born system and the phase space volume.

¹⁷A POWHEG package to calculate the heavy flavour production in hadronic collisions at NLO.

¹⁸The Born amplitude should not contain the flux factor $1/(2s_b)$ (where s_b is the centre-of-mass energy squared of the Born process) since it is provided by the POWHEG BOX.

p and the flavour structure `bflav`. Both the colour- and spin-correlated Born amplitudes are needed for the treatment of soft and collinear singularities in the FKS subtraction method and are defined in POWHEG, respectively, as follows

$$2s_b B_{jk} = -N \sum_{\substack{\text{spins} \\ \text{colours}}} \mathcal{A}_{\{c_i\}} \left(\mathcal{A}_{\{c_i\}}^\dagger \right)_{c_j \rightarrow c'_j, c_k \rightarrow c'_k} T_{c_j, c'_j}^a T_{c_k, c'_k}^a \quad (3.36)$$

$$B_k^{\mu\nu} = N \sum_{\{j\}, s_k, s'_k} \mathcal{A}(\{j\}, s_k) \mathcal{A}^\dagger(\{j\}, s'_k) (\varepsilon_{s_k}^\mu)^* \varepsilon_{s'_k}^\nu \quad (3.37)$$

where in Eq. (3.36), $\mathcal{A}_{\{c_i\}}$ is the Born matrix element with $\{c_i\}$ representing the colour indices of all the external coloured legs. The suffix in the Hermition conjugate indicates that the colour indices of particles j and k are replaced with primed indices. N is the appropriate normalization factor including averages over initial spin and colour and symmetry factors. The $SU(3)$ generator $T_{c,b}^a$ is equal to the $SU(3)$ structure constant if_{cab} for gluons, while it is equal to the colour matrix in the fundamental representation t_{bc}^a for incoming quarks (outgoing anti-quarks), and to $-t_{bc}^a$ for incoming anti-quarks (outgoing quarks). In Eq. (3.37), the spin-correlated amplitude $B_k^{\mu\nu}$ vanishes if particle k is not a gluon, it is obtained by leaving un-contracted the indices of the k^{th} particle. The parameter s_k of the Born amplitude describe the spin of the k^{th} leg, while $\{j\}$ represents collectively all the remaining spins and colours of the incoming and outgoing particles. Finally, $\varepsilon_{s_k}^\mu$ and $\varepsilon_{s'_k}^\nu$ are the polarisation vectors. For more information about the formula of colour- and spin-correlated amplitude in POWHEG see section 2.3 of [44].

Typically, a calculation of a squared amplitude with RecoLa involves the following steps: (i) Setting the input parameters, (ii) defining the processes, (iii) generating the processes, (iv) and computing them. This should be done following the same order, except for the first step which could be alternatively carried out after defining the processes. On the other hand, the calculation of a tree level cross section in POWHEG starts with the previously mentioned `init_processes` file, then goes through the `init_couplings` routine where all the parameters are defined and then through the `born` file where the routine `setborn` is constructed.

We start by defining the processes for RecoLa in `init_processes` by calling RecoLa's subroutine

$$\text{define_process_rcl}(\text{npr}, \text{processIn}, \text{order}) \quad (3.38)$$

this defines the `process(es)` we want to compute. The argument `npr` of type integer is an identifier to the process we want to define. The argument `processIn` of type character specifies the external particles involved in the process. For instance, if we wish to define a process with $u\bar{u}$ in the initial state and $t\bar{t}$ in the final state, `processIn` should be formulated as 'u

$u \rightarrow t \bar{t}$. It is possible to define multiple processes with `define_process_rcl`, in this case each process should be given a different identifier. The argument `order` of type `character(*)` takes only two values, 'LO' or 'NLO'. In the former case `RecoLa` can only evaluate tree level amplitudes whereas in the latter case it can evaluate both LO and NLO amplitudes. For our calculation, we set `npr` to `flst_nborn`, with the latter being a POWHEG variable of type integer that changes with each inequivalent Born flavour structure. Furthermore, for each entry of the list `flst_born`, which we discussed in the previous subsection, we fill a variable that we called `process` with the particles involved in the entry in the format of `processIN`, and we set the argument `processIN` to our variable `process`. Last but not least, we set the argument `order` to 'NLO' in order to avoid doing the definition step twice, one for Born and one for virtual, since both amplitudes share the same phase space ($2 \rightarrow 2$ in our case).

In order to have the choice between calculating only SM amplitudes, only BSM amplitudes, or SM and BSM together (which will include the interference effects between the two), we call, directly after `define_process_rcl`, the subroutine `setpowerBornLoopRecoLa(prid)` and set `prid` to `flst_nborn`. The building blocks of this subroutine, which we created, can be seen in Listing 3.1. Here we create a new variable `channel` and we add it as an element of `powhe.input`. This variable can take three values only, 3, 4, or 7. Each value will then call a combination of the following `RecoLa`'s subroutines

$$\text{select_power_BornAmpl_rcl}(npr, cid, power) \quad (3.39)$$

$$\text{unselect_power_BornAmpl_rcl}(npr, cid, power) \quad (3.40)$$

$$\text{unselect_all_powers_BornAmpl_rcl}(npr) \quad (3.41)$$

$$\text{select_power_LoopAmpl_rcl}(npr, cid, power) \quad (3.42)$$

$$\text{unselect_power_LoopAmpl_rcl}(npr, cid, power) \quad (3.43)$$

$$\text{unselect_all_powers_LoopAmpl_rcl}(npr) \quad (3.44)$$

where `npr` is the same as in 3.38, `cid` is of type `character` and defines the type of the vertex, and `power` is of type `integer` and specify how many vertices of type `cid` are considered (or not considered), for more information about the values that `cid` and `power` can take in our calculation see subsection 3.3.2. The subroutines (3.39, 3.40) allow to select/unselect the contribution to the Born amplitude according to the choice of `cid` and `power` while the subroutine (3.41) unselect all contributions to the Born amplitude (with any power and any coupling type) for the process with identifier `npr`. The subroutines (3.42, 3.43, 3.44) are the same as the subroutines (3.39, 3.40, 3.41) respectively, but for Loop amplitudes. Thus, according to our choices for the arguments `cid` and `power`, channel 7 would select SM and BSM contributions, channel 4 only SM contributions, and channel 3 only BSM ones, this is done for both the Born and the virtual

amplitudes. However, since we want to include the amplitudes involving one s-channel gluon mediated diagram and one t-channel EW diagram, see subsection 3.2.1, which would affect channels 4 and 7, and since with RecoLa, using the previous subroutines, it is not possible to

Listing 3.1: The subroutine `setpowerBornLoopRecola(prid)`

```

subroutine setpowerBornLoopRecola(prid)
  use recola
  implicit none
  real*8 powheginput_default, channel
  external powheginput_default
  integer prid
  channel = powheginput_default('channel',7d0)
  if (channel.eq.7) then
    call unselect_power_LoopAmpl_rcl(prid, 'QCD', 4)
    call unselect_power_LoopAmpl_rcl(prid, 'QED', 4)
    call unselect_power_LoopAmpl_rcl(prid, 'WZP', 4)
  elseif (channel.eq.4) then
    call unselect_power_BornAmpl_rcl(prid, 'WZP', 2)
    call unselect_all_powers_LoopAmpl_rcl(prid)
    call select_power_LoopAmpl_rcl(prid, 'QCD', 2)
    call select_power_LoopAmpl_rcl(prid, 'QED', 2)
    call select_power_LoopAmpl_rcl(prid, 'WZP', 0)
  elseif (channel.eq.3) then
    call unselect_all_powers_BornAmpl_rcl(prid)
    call select_power_BornAmpl_rcl(prid, 'QCD', 0)
    call select_power_BornAmpl_rcl(prid, 'QED', 2)
    call select_power_BornAmpl_rcl(prid, 'WZP', 2)
    call unselect_all_powers_LoopAmpl_rcl(prid)
    call select_power_LoopAmpl_rcl(prid, 'QCD', 2)
    call select_power_LoopAmpl_rcl(prid, 'QED', 2)
    call select_power_LoopAmpl_rcl(prid, 'WZP', 2)
  endif

```

select these contributions without including the pure QCD amplitudes, additional work will be needed. This can be explained in the language of subsection 3.3.2 and Appendix B.3 as follows, at the Born level we want channel 7 to include the squared amplitudes 040, 042, 044, 220, and 222 and channel 4 to involve only 040 and 220. However, with the previous subroutines we are not able to select 222 and 220 or only 220 without including the squared amplitude 400 in both channel 7 and 4 respectively. we will address how we treat this later on.

The parameters needed by RecoLa in order to compute the squared amplitudes are set in the file `init_couplings`. This will be explained in more details in the following subsections. We now continue in `init_couplings` but addressing other information. Since we include the photon induced diagrams which involve one power in $\sqrt{\alpha_S}$ at the Born level, and since POWHEG

will evaluate these amplitudes at different phase space points, we need to use the subroutine

$$\text{set_dynamic_settings_rcl}(n) \quad (3.45)$$

this regulates which input parameters can be set dynamically. The integer n can take the values 0 or 1, in the former case only α_S can be reset after generating the process while in the latter case additional parameters needed when calculating Loop amplitudes can be reset as well. Since we aim to implement a NLO calculation, we set n to 1. Then, after calling all the input parameters, in order to generate our processes we call the subroutine

$$\text{generate_processes_rcl} \quad (3.46)$$

this constructs the skeleton of the recursive procedure for all previously defined processes, and stores it in global variables that later on are used by RecoLa for the computation of amplitudes. At this stage, RecoLa can compute the amplitudes, however setting any of the already defined processes to zero would lead to an error, this can occur for example in case some of the couplings were set to zero. In order to overcome this problem, and allow the couplings to be set to zero whenever desired, we do, once the processes are generated, the following:

- We check whether the process exists or not using the subroutine `process_exists_rcl(npr, exists)` where the integer `npr` is the process identifier and the argument `exists` is of type logical.
- Then only if `exists` is true we take the process into account and we fill its external particles as an entry in the list `flst_born`.
- After that we call `reset_recola_rcl()` which will free the memory and allow for the definition of a new set of processes in the same run of the program without changing the values of the input parameters.
- Then we call again the subroutine (3.45) since it was reset by the previous step.
- Finally, we define the existing processes and we select their powers as done before.

During these steps we set the `npr` argument in the subroutines `process_exists_rcl`, `define_process_rcl`, and `setpowerBornLoopRecola` to `prid`, with the latter chosen according to a routine that we created to be able to assign the identifiers of the processes independently for each channel¹⁹. This routine is dubbed `bflavToPrid(bflav, channel)` where the previously mentioned argument `bflav` is a list of four integers that defines the flavour structure of the pro-

¹⁹Remember the channel will define whether we will calculate SM amplitudes only, BSM amplitudes only, or both SM and BSM amplitudes together.

cess and channel is the variable that we introduced previously and specifies which amplitudes will be calculated.

Remember that the goal was to create the subroutine `setborn` where the Born and Born-correlated squared amplitudes can be calculated for each flavour configuration. This can now be done with `Recola`. To this aim we created in the file `born.f` a subroutine called `computeBornRecola(prid,bflav,p,born,bornjk,bmunu)` which, given the identifier of the process `prid`, its flavour structure `bflav` and its 4-momenta `p`, returns the Born squared amplitudes in `born`, the colour-correlated ones in `bornjk`, and the the spin-correlated ones in `bmunu`. We start by calling `Recola`'s subroutine `set_alphas_rcl` that sets the value of the strong coupling constant which can now have different values for different scales since we used the subroutine `set_dynamic_settings_rcl`. This is needed since we include the LO photon induced processes in our calculation. Then in order to calculate the Born amplitude we call the subroutine

$$\text{compute_process_rcl}(npr,p,order,A) \quad (3.47)$$

where `A` is a real vector with 2 entries, `A(1)` where the value of the Born squared amplitude will be saved and `A(2)` where the virtual squared amplitude will be saved. Since we want to only calculate tree level amplitudes we set `order` to `'LO'`. Now in order to get the Born squared amplitude in `born`, one has just to set `born = A(1)`. However, since, as we discussed earlier, our SM and SM+BSM amplitudes still contain the pure QCD contribution `400`, in order to only choose the amplitudes `220` and `040` for channel 4 and `220`, `222`, `040`, `042`, and `044` for channel 7 we need to use the subroutine

$$\text{get_squared_amplitude_rcl}(npr,pow,order,B) \quad (3.48)$$

where `B` is one of the entries of `A`. The argument `pow` specify the powers of all the vertices involved in the squared amplitude. For instance, for an amplitude with 2 QCD vertices and 2 EW vertices, `pow = [2,2,0]`. To exemplify how this can be done let us take the case of channel 4 (SM only), after calling the subroutine (3.47) we do the following

```
get_squared_amplitude_rcl(prid,[2,2,0],'LO',B1(1))
get_squared_amplitude_rcl(prid,[0,4,0],'LO',B2(1))
```


and then we set `born` to `B1(1)+B2(1)`. The same can be done for channel 7. Once the Born amplitude is calculated, the colour-correlated one can be obtained with `Recola` by calling

$$\text{rescale_colour_correlation_rcl}(\text{npr}, \text{i1}, \text{i2}, \text{A2cc}) \quad (3.49)$$

The integer arguments `i1` and `i2` denote the position identifiers of the respective external particles (ordered as in the process definition). The argument `A2cc` of type `real(dp)` delivers the output of the subroutine. As in the Born case, we can't yet set `bornjk` to `A2cc` since we do not want to include the pure QCD contributions, thus similarly to the previous case we have to call the subroutine

$$\text{get_colour_correlation_rcl}(\text{npr}, \text{pow}, \text{i1}, \text{i2}, \text{B2cc}) \quad (3.50)$$

and thus the `bornjk` can be set to the sum of the `B2ccs` for all the desired powers. However, it turns out that, since the definition of the colour-correlated amplitudes in `Recola` is different than the one in `POWHEG`, one should multiply the amplitude obtained with `Recola` by $-C_A$ if `i1` is a quark or an anti-quark and by $-C_F$ if it is a gluon, with C_A and C_F being the Casimir operators in the adjoint and fundamental representations respectively. Last but not least, `Recola` can provide the spin-correlated squared amplitudes through the subroutine `rescale_spin_correlation_matrix_rcl(npr, j, order, A2sc)`. This is only non zero when `j` is a gluon, it is thus straightforward to implement it in our particular case because the only diagrams that involve a gluon are the photon induced ones, and they only have one external gluon each.

The last piece related to the Born amplitudes that need to be including is the Born colour structure. This is done in `born.f` through the subroutine `born_colour_lh` which sets up the colours for our 28 Born flavour configurations.

The virtual and real amplitudes

When it comes to the virtual amplitudes, the user needs to create the routine

$$\text{setvirtual}(\text{p}(0:3, 1:\text{nlegborn}), \text{vflav}(1:\text{nlegborn}), \text{virtual})$$

which should return the regularised part of the virtual amplitude in `virtual` given the flavour structure `vflav` of the process and its 4-momenta `p`. As we already know by now, `Recola` needs to go through different steps in order to be able to compute the amplitudes. Since the virtual contributions share the same phase space as for the Born ones, many of the steps were already

achieved when calculating the tree level amplitudes, this was attained by simply setting the argument order to 'NLO' in the subroutine `define_process_rcl` whenever called. Thus we will mainly concentrate on the computation step which will be done in the file `virtual.f`. But first let us briefly explain what needs to be added in the `init_processes` and `init_couplings` files.

The routine `setpowerBornLoopRecola(prid)` of `init_processes` in Listing 3.1 selects the amplitudes that contribute to each channel, not only at the Born level, but at the Loop level as well. As in the tree level case, for channels 4 and 7, some unwanted amplitudes will still be involved in our calculation. More precisely channel 4 would involve the unwanted 4_{20} amplitude and channel 7, in addition to that, will also include the squared amplitude 4_{22} . This is surpassed in the same fashion as in the Born routine. We will elaborate on the solution when discussing the computation step. In the `init_couplings` file, whenever the `set_dynamic_setting_rcl` is called, one should also add the subroutines `set_on_shell_scheme_rcl` and `set_delta_ir_rcl(d,d2)` of which the former will select the on-shell scheme for the mass renormalisation of unstable particles and the latter will set the variables `DeltaIR` and `DeltaIR2` parametrizing the IR poles to `d` and to `d2`, respectively (`d` and `d2` are of type `real(dp)`), see Listing B.3 for our choice of these 2 arguments.

The computation of the virtual amplitudes is evaluated in `virtual.f` through the subroutine `computeVirtualRecola(prid,vflav,p,virtual)`. It returns in `virtual` the regularised virtual amplitude calculated with `Recola` for the process with an identifier `prid`, which as in the Born case should be obtained through `bflavToPrid`, its flavour structure `vflav`, and its 4-momenta `p`. We first start by setting the factorisation and renormalisation scales (`set_fac_ren_scales`), the \overline{MS} scale (`set_mu_ms_rcl`), the IR scale (`set_mu_ir_rcl`), and the strong coupling constant value (`set_alphas_rcl`). Then using the subroutine (3.47) and setting its argument order to 'NLO', the virtual amplitudes are calculated. However, as stated earlier, the amplitudes still involve some unwanted diagrams. Similarly to the Born case, this is overcome using the subroutine (3.48) but setting the argument order to 'NLO' this time. Finally, due to the difference in the definition of the virtual amplitudes between POWHEG and `Recola`, we multiply the resulted amplitudes with $(2\pi)/\alpha_S$.

The real contribution is expected to be implemented by the user in the file `real.f` through the subroutine

```
setreal(p(0:3,1:nlegborn),rflav(1:nlegborn),amp2)
```

which computes, according to the momenta \mathbf{p} of the external legs, the squared amplitude²⁰ for the real process specified by the flavours `rflav`, stripped off by a factor $\alpha_S/(2\pi)$ as in the virtual case. This is done using `RecoLa` exactly as in the Born case. The only difference is that the order argument needs to be set to 'L0' when defining the processes. Of course one should do that for the real configurations of the list `flst_real` in this case. Finally, the resulted amplitudes should be multiplied by the factor $(2\pi)/\alpha_S$.

Input parameters

The handling of the (new) external parameters of the SMWZp model (see Section 3.3.1), the contributions to the calculation, and some other parameters needed by POWHEG in order to perform the integration, can be specified in the file `powheg.input`. The new parameters are defined in the subroutine `init_couplings`. Their default values can then be edited through `powheg.input`. For instance, the Z' couplings to the SM fermions can be manipulated by setting the variables `lzpu1x1`, `lzpu1x2`, ..., `lzpu3x3` for left-handed up-type quarks, `rzpu1x1`, `rzpu1x2`, ..., `rzpu3x3` for right-handed up-type quarks, `lzpd1x1`, `lzpd1x2`, ..., `lzpd3x3` for left-handed down-type quarks, and `rzpd1x1`, `rzpd1x2`, ..., `rzpd3x3` for right-handed down-type quarks. For an example of `powheg.input` including the complete list of parameters see Appendix B.6.

Our implementation of EW top-pair hadroproduction can be compiled using a provided `Makefile`. Executing `make` will create the binary `pwhg_main`. Since we use `RecoLa` to calculate the amplitudes, its libraries should be added to the main path by the user. A typical run would then be executed in a new directory containing the input file `powheg.input` together with the binary `pwhg_main`. In the input file, the hadronic CM energy can be set for each beam separately in variables `ebeam1` and `ebeam2` and the PDFs for the two beams can be specified in the variables `lhans1` and `lhans2`. Events will be generated if the variable `numevts` specifying the number of events to generate is set to a value larger than 0. Note that it is also possible to simulate only the Born contribution and this is achieved by setting the variable `bornonly = 1`²¹. For more settings, we refer the reader to the POWHEG BOX manual [129] or the comments in the `powheg.input` file in Listing B.4. During the initialization, the consistency between the real and the Born contributions is checked and the result is stored in `pwhg_checklimits`. This is followed by the integration and event generation. The result of the integration is printed on screen as well as

²⁰Averaged over spin and colours; Similar to the Born and the virtual cases, the real contributions should not contain the flux factor.

²¹Furthermore, if LO events are required the variable `L0events` should be set to 1 as well, otherwise POWHEG BOX will attach POWHEG radiation.

saved in the file `pwgstat.dat` and the events in the Les Houches Event format [130] are stored in the file `pwgevents.lhe`.

Validation

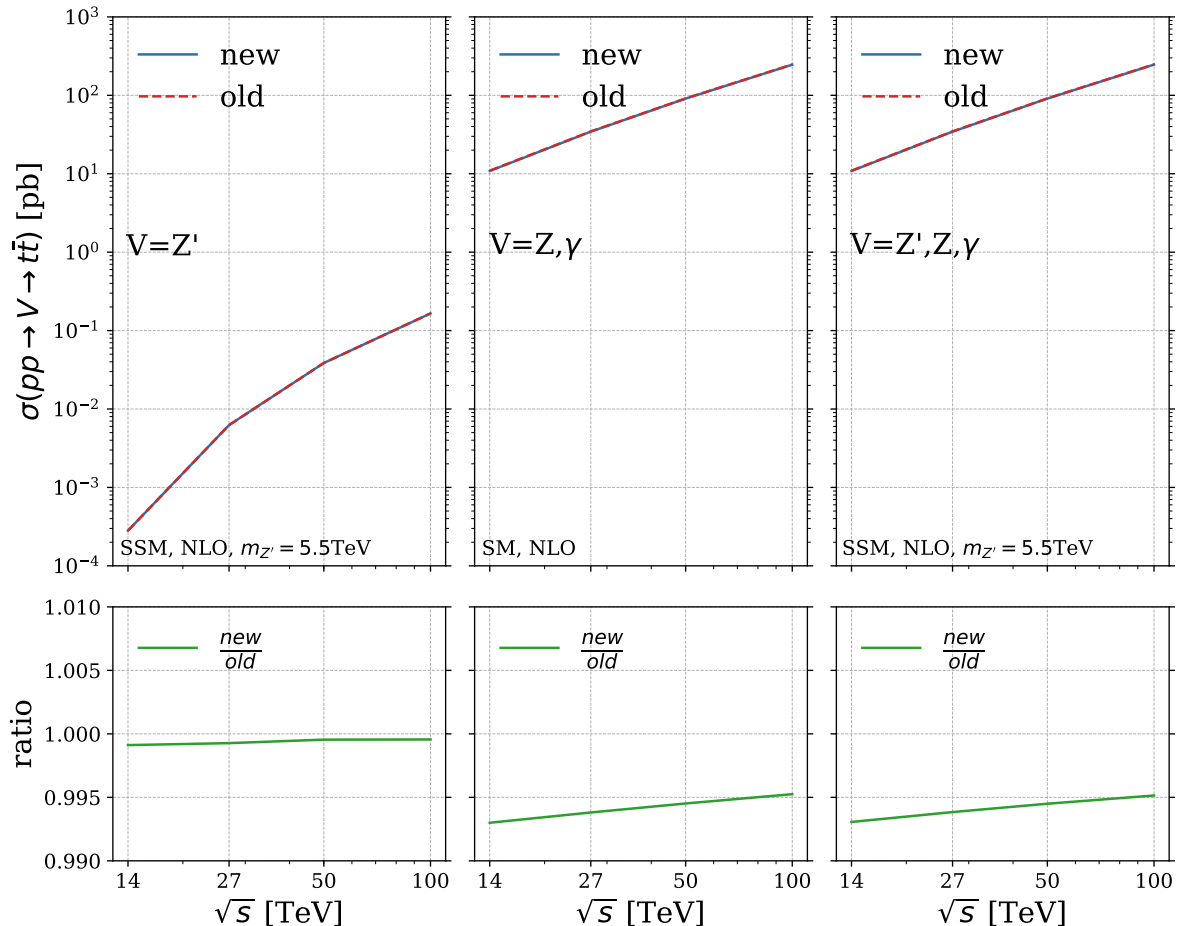


Figure 3.17: Top: The SSM NLO total cross section predictions in picobarns for $pp \rightarrow Z' \rightarrow t\bar{t}$ (left), $pp \rightarrow Z, \gamma \rightarrow t\bar{t}$ (central), and $pp \rightarrow Z', Z, \gamma \rightarrow t\bar{t}$ (right) at $\sqrt{s} = \{14, 27, 50, 100\}$ TeV for the new- and the old-PBZp. Bottom: their ratios in the same order at a centre-of-mass energy $\sqrt{s} \in \{14, 27, 50, 100\}$ TeV.

Our implementation was validated against the old PBZp calculation by comparing some NLO cross sections for channels 3, 4, and 7 between the two. Since the old package only allow for diagonal Z' couplings and does not include the t-channel W and W' contributions, we set, in the new package, the non-diagonal couplings of Z' together with the CKM parameters and the couplings of W' to zero. The comparison was performed in the SSM for channels 3 and 7, and in the SM for channel 4. We assume a Z' of 5.5 TeV mass and we vary the centre-of-mass energy to take the values 14, 27, 50, and 100 TeV. This can be seen in Figure 3.17 where the

cross sections calculated with the new PBZp are represented in blue while the ones obtained with the old package are plotted in dashed red. The upper part of the Figure shows the cross sections in channel 3 (Z' only) on the left, the NLO production in channel 4 (Z and γ) in the middle, and the NLO cross sections of channel 7 (Z' , Z , and γ) on the right. The lower panels of Figure 3.17 shows, in the same order of the upper ones, the ratio of the total cross sections of the new calculation over the ones obtained from the old PBZp. As can be seen from the plots, we get a very good agreement in the three cases.

3.6 EW top-pair production at NLO QCD accuracy at the LHC and beyond

We have calculated the QCD corrections to the EW top-pair production in theories with extra Z' - and W' -boson using the RecoLa2 package and linked them to POWHEG in order to be able to produce results at NLO+PS accuracy. The implementation together with the validation was discussed in the previous section. In this section we present some models with additional new heavy resonances for which we produce numerical results using the new PBZp package.

3.6.1 Models

With the intention of presenting the different aspects of the new calculation we introduce, in addition to the SSM, two new models. It is worth mentioning that the most stringent limits on W' and Z' masses in the SSM are derived from searches with dilepton final states. Assuming $\Gamma_{Z'}/m_{Z'} = 3\%$, a mass below 5.1 TeV is excluded by the ATLAS Z' search for high-mass dilepton resonances at the LHC run II with $\sqrt{S} = 13$ TeV and 139 fb^{-1} integrated luminosity (see Figure 3 and Table 3 of [131]). The CMS search for a narrow resonance in high mass dilepton final states using data from LHC run II at $\sqrt{S} = 13$ TeV with 140 fb^{-1} integrated luminosity leads to a lower mass limit of $m_{Z'} \geq 5.15$ TeV assuming a signal width $\Gamma_{Z'}/m_{Z'} = 3\%$ (see Table 4 of [132]). For W' gauge bosons in the SSM, masses below 6.0 TeV are excluded by the ATLAS W' search with charged lepton plus missing transverse momentum final states using data from LHC run II with $\sqrt{S} = 13$ TeV and an integrated luminosity of 139 fb^{-1} [133], where $\Gamma_{W'}/m_{W'}$ varies between 2.7% at $m_{W'}' = 150$ GeV and 3.5% above the $t\bar{b}$ threshold. The CMS W' search using LHC Run II data from 2016 (not the complete Run II data set) at 35.9 fb^{-1} integrated luminosity set the lower limit on the mass of W' to 5.2 TeV [134].

Topcolour model

The Topcolour model [135, 136] can generate a large top-quark mass through the formation of a top-quark condensate. This is achieved by introducing a second strong $SU(3)$ gauge group which couples preferentially to the third generation, while the original $SU(3)$ gauge group couples only to the first and second generations. To block the formation of a bottom-quark condensate, a new $U(1)$ gauge group and associated Z' -boson are introduced. Different couplings of the Z' -boson to the three fermion generations then define different variants of the model [137]. A popular choice with the LHC collaborations is the leptophobic TC model (also called Model IV in the reference cited above) [138], where the Z' couples only to the first and third generations of quarks and has no significant couplings to leptons. This particular choice has three parameters: the ratio of the two $U(1)$ coupling constants, $\cot\theta_H$, which should be large to enhance the condensation of top quarks, but not bottom quarks, as well as the relative strengths f_1 and f_2 of the couplings of right-handed up- and down-type quarks with respect to those of the left-handed quarks. This model is excluded by the ATLAS search for $t\bar{t}$ resonances in fully hadronic final states in pp collisions at $\sqrt{S} = 13$ TeV and an integrated luminosity of 139 fb^{-1} for Z' masses below 3.9 and 4.7 TeV and for the decay widths of 1 and 3%, respectively [139]. At $\sqrt{S} = 13$ TeV and with an integrated luminosity of 35.9 fb^{-1} , the CMS search for resonant $t\bar{t}$ production in proton-proton collisions excludes masses up to 3.80, 5.25, and 6.65 TeV for Z' decay widths of 1, 10, and 30%, respectively [140].

Third Family Hypercharge Model

The Third Family Hypercharge Model (TFHM) [71] is a minimal extension of the SM by an anomaly-free, spontaneously broken $U(1)_F$ gauge symmetry. Apart from the new gauge boson (X) and a SM singlet, complex scalar field ($\Theta(x)$), needed for the spontaneous symmetry breaking of the $U(1)_F$ symmetry, no new particles are introduced. The model has flavour-dependent couplings designed to explain various measurements of B meson decays ($R_K^{(*)}$ [73, 141], $BR(B_s \rightarrow \mu^+ \mu^-)$ [76–79], angular distributions in $B \rightarrow K^{(*)} \mu^+ \mu^-$ decays [74, 75, 142, 143]) which are currently in tension with SM predictions. In addition, it provides an explanation of the heaviness of the third generation of SM particles and the smallness of the quark mixing. An update of the allowed parameter space (post Moriond 2019) can be found in Ref. [144]. Recently, the TFHM has been slightly modified to make it more natural in the charged lepton sector [72]. In the following we will use the original TFHMeg model from Ref. [71]. The collider phenomenology of the TFHMeg has also been studied in [145]. This model has three free parameters, the extra $U(1)$ coupling, g_F , the angle controlling the mixing of the second and third family quarks, θ_{sb} and the Z' -boson mass. The width of Z' in the TFHMeg is $\Gamma_{Z'} = \frac{5g_F^2 m_{Z'}}{36\pi}$.

The Z' couplings to the quarks depend on g_F and θ_{sb} (see Eq. (2.15) in [71]):

$$-\mathcal{L}_{X\psi} = g_F \left(\frac{1}{6} \bar{\mathbf{u}}_{\mathbf{L}} \Lambda^{(u_L)} \boldsymbol{\gamma}^\rho \mathbf{u}_{\mathbf{L}} + \frac{1}{6} \bar{\mathbf{d}}_{\mathbf{L}} \Lambda^{(d_L)} \boldsymbol{\gamma}^\rho \mathbf{d}_{\mathbf{L}} + \frac{2}{3} \bar{t}_R \boldsymbol{\gamma}^\rho t_R - \frac{1}{3} \bar{b}_R \boldsymbol{\gamma}^\rho b_R \right) Z'_\rho, \quad (3.51)$$

where all quark fields are in the mass eigenbasis and $\mathbf{u}_{\mathbf{L}} = (u_L, c_L, t_L)^T$ and $\mathbf{d}_{\mathbf{L}} = (d_L, s_L, b_L)^T$. The matrix $\Lambda^{(d_L)}$ can be found in Eq. (2.16) of Ref. [71]. It depends on θ_{sb} :

$$\Lambda^{(d_L)} = \begin{pmatrix} 0 & 0 & 0 \\ 0 & \sin^2(\theta_{sb}) & \frac{1}{2} \sin(2\theta_{sb}) \\ 0 & \frac{1}{2} \sin(2\theta_{sb}) & \cos^2(\theta_{sb}) \end{pmatrix}. \quad (3.52)$$

Moreover, $\Lambda^{(u_L)} = V \Lambda^{(d_L)} V^\dagger$, where V is the CKM matrix.

3.6.2 Numerical results

We now use our next-to-leading order calculation to obtain predictions for top-quark-pair production for the three models introduced in the preceding section: the Sequential Standard Model, the Topcolour model, and the Third Family Hypercharge Model. Here, our goal is not an exhaustive study of the collider phenomenology for each of these models scanning over the entire allowed parameter space, but rather to exemplify our calculation by showing results for a number of benchmark points. We will present results for the LHC at $\sqrt{S} = 14$ TeV but also for pp collisions at higher centre-of-mass energies.

We will first discuss the general setup of our calculations and event selection in Section 3.6.2 and 3.6.2 before showing predictions for fiducial cross sections and NLO K-factors in Section 3.6.2. The impact of the newly included contributions is discussed in Section 3.6.2, and finally the impact of the interference of the BSM signal and the SM background is studied in Section 3.6.2.

Setup and input

The theoretical description of our calculation and of the models we consider here can be found in the preceding sections. Here we describe the additional input required for the numerical computations for which the results are presented in the next few sections. This general setup and the input parameters are used by default if not stated otherwise.

We employ a top quark pole mass $m_t = 172.5$ GeV. Furthermore, the masses and widths of the weak gauge bosons are given by $m_Z = 91.1876$ GeV, $\Gamma_Z = 2.4952$ GeV, $m_W = 80.385$ GeV, $\Gamma_W = 2.085$ GeV [146]. The weak mixing angle is fixed by $\sin^2 \theta_W = 1 - m_W^2/m_Z^2 = 0.222897$ and the fine-structure constant is set to $\alpha(2m_t) = 1/126.89$. We neglect the running of this coupling to higher scales. We consider quark mixing between all three families and use a unitary CKM matrix constructed using Wolfenstein parameters as in Ref. [127].

For the proton parton distribution functions (PDFs), we use the NLO *luxQED* set of NNPDF3.1 [147–149] as implemented in the *LHAPDF* library (ID = 324900) [150, 151]. This set provides, in addition to the gluon and quark PDFs, a precise determination of the photon PDF inside the proton which we need for our cross section predictions. The running strong coupling $\alpha_s(\mu_R)$ is evaluated at NLO in the $\overline{\text{MS}}$ scheme and is provided together with the PDF set²².

For our numerical predictions in the following sections, we choose equal values for the factorisation and renormalisation scales, μ_F and μ_R respectively, which we identify with the partonic centre-of-mass energy: $\mu_F = \mu_R = \sqrt{s}$. Additionally we vary μ_F and μ_R by independently multiplying the scales by factors of $\xi_R, \xi_F \in \{0.5, 1, 2\}$ discarding combinations with $\xi_F/\xi_R = 4$ or $1/4$. We combine such seven-point variations into an uncertainty band by taking the envelope of all the predictions.

We present (N)LO+PS predictions for a pp collider with a range of energies $\sqrt{s} \in \{14, 27, 50, 100\}$ TeV. We consider the SSM, TC and TFHM models and a range of Z' masses $m_{Z'} \in [2, 8]$ TeV. In the SSM we set the mass of W' equal to the mass of Z' and its mixing matrix to that of the SM W . The widths of Z' - and W' -bosons must then be $\Gamma_{Z'}/m_{Z'} = 3\%$, $\Gamma_{W'}/m_{W'} = 3.3\%$. The parameters of the TC model are chosen as follows: we set $f_1 = 1$ and $f_2 = 0$ and calculate $\cot \theta_H$ such that $\Gamma_{Z'}/m_{Z'} = 3.1\text{--}3.2\%$. In the TFHM we set $\theta_{sb} = 0.095$, $g_F/m_{Z'}' = 0.265$ where $m_{Z'}'$ is given in TeV which implies $\Gamma_{Z'}/m_{Z'} = \{0.012, 0.028, 0.050, 0.078, 0.112, 0.152, 0.199\}$ for $m_{Z'}' = \{2, 3, 4, 5, 6, 7, 8\}$ TeV.²³

Event generation and cuts

We generate events in the Les Houches Event format [130] using POWHEG BOX with stable on-shell top quarks and require the underlying Born kinematics to satisfy a cut on the $t\bar{t}$ invariant mass $m_{t\bar{t}} \geq 0.75 m_{Z'}$, in order to enhance the signal over background ratio. We then decay both top quarks leptonically and shower the events using PYTHIA 8.244 [110]. The branching ratio of the leptonic top decay of 10.5% [127] squared is applied, unless stated otherwise. Note

²²Its value is fixed by the condition $\alpha_s(m_Z) = 0.118$.

²³This benchmark point was selected from Figure 1 in [144].

Table 3.1: Total cross sections in LO for top-pair production at $\mathcal{O}(\alpha_s\alpha)$ and $\mathcal{O}(\alpha^2)$ in the SM and SSM at $\sqrt{S} = 14$ TeV. The Z' -boson mass is set to 5 TeV. For all the predictions in this table we use NLO α_s and NLO PDFs.

Contribution	no cuts [fb]	$m_{t\bar{t}}$ cut [fb]	$m_{t\bar{t}}$ & fiducial cuts [%]
$\gamma g + g\gamma \rightarrow t\bar{t}$, $\mathcal{O}(\alpha\alpha_s)$	3700	0.0327	41.6
$qq' \rightarrow W \rightarrow t\bar{t}$, $\mathcal{O}(\alpha^2)$ + interf.	3220	0.0573	3.7
$q\bar{q} \rightarrow g/W \rightarrow t\bar{t}$, $\mathcal{O}(\alpha\alpha_s)$	-1680	0.000703	37.4
$q\bar{q} \rightarrow \gamma/Z \rightarrow t\bar{t}$, $\mathcal{O}(\alpha^2)$	510	0.00614	74.9
$q\bar{q} \rightarrow Z' \rightarrow t\bar{t}$, $\mathcal{O}(\alpha^2)$	0.210	0.114	77.4
$qq' \rightarrow W' \rightarrow t\bar{t}$, $\mathcal{O}(\alpha^2)$ + interf.	0.0025	–	–

that the PYTHIA decays wash out any spin correlations. We use PowhegHooks to veto shower emissions harder than the POWHEG emission and disable QED showers.

We perform further event selection and bin in histograms on-the-fly using Rivet [152, 153]. Events are required to have two or more charged leptons, two or more neutrinos, two or more anti- k_T [154] $R = 0.5$ jets each containing at least one b -parton. All these objects have to fulfil the acceptance cuts $p_T > 25$ GeV and $|y| < 2.5$. Furthermore, we combine charged leptons and neutrinos into W -bosons based on their MC truth PDG id and require each event to feature at least one such W^+ and one such W^- boson.

It is instructive to have a closer look at the size of the various leading order contributions to the EW top-pair production considered in this study, and the effects that the invariant mass and the fiducial cuts have on them. To that effect in Table 3.1, we show integrated cross sections in femtobarn for the centre-of-mass energy $\sqrt{S} = 14$ TeV and the Z' -boson mass, $m_{Z'}$, set to 5 TeV with no cuts in the first column. The cross sections after the invariant mass cut are shown in the second column and after both invariant mass and fiducial cuts in the third column. Note the branching ratio of two leptonic top decays has been stripped from these predictions. We do this because the ratio of the first two columns does not depend on the decay channel and we expect the fiducial cuts, in this study designed for the dileptonic channel, to have a similar impact in all the other decay channels. All the contributions in the table are obtained by multiplying an amplitude by its complex conjugate except for $q\bar{q} \rightarrow g/W \rightarrow t\bar{t}$, which is calculated as $\mathcal{A}(q\bar{q} \rightarrow W \rightarrow t\bar{t})\mathcal{A}^*(q\bar{q} \rightarrow g \rightarrow t\bar{t}) + \text{c.c.}$. The contributions in rows 2 and 6 also contain the interference terms with the contributions in rows 4 and 5 respectively (indicated by “+interf.”).

First we observe that the various SM contributions (rows 1-4) are of similar size, with the resonant production being the smallest. This must be because the Z -boson resonance is

below the $2m_t$ threshold. Furthermore we notice that the “interference term” in the third row is negative, which is not surprising. The invariant mass cut, see the second column, reduces all the SM contributions by roughly 5 orders of magnitude, except for the “interference term” which is reduced even more, by about 7 orders of magnitude.²⁴ The effect of the fiducial cut in the third column is expressed in terms of percentage relative to the second column. It has roughly the same impact on all the SM contributions, except for the non-resonant W -boson production in the second row, in which the bulk of the cross section is in the forward regions outside the acceptance. After both cuts are applied the first two largest contributions are the photon induced and the resonant $t\bar{t}$ productions, both of which were already included in our previous calculation [40].

By design the invariant mass cut has quite a different impact on the resonant Z' production and reduces it only gently, by a factor less than two. As expected the fiducial cut behaves nearly the same for SM and BSM resonant productions. After both cuts are applied the Z' contribution is by far the dominant one. The cuts we designed for this study are thus more than adequate for selecting SSM $Z' \rightarrow t\bar{t}$ production with $m_{Z'} = 5$ TeV at a $\sqrt{S} = 14$ TeV LHC.

The non-resonant W' production is about two orders of magnitude smaller than the resonant one. Moreover we would expect the invariant mass and fiducial cuts to reduce it considerably similarly to the non-resonant W production. This contribution in the SSM and at $\sqrt{S} = 14$ TeV is thus negligible.²⁵ Note that this may not be the case anymore at higher collider energies.

Fiducial cross sections and NLO K -factors

On the upper panels of Figure 3.18 we show fiducial NLO+PS cross sections for the SSM, TFHM and the TC model versus the Z' -boson mass, $m_{Z'}$, at a fixed centre-of-mass energy $\sqrt{S} = 14$ TeV (left) and versus the centre-of-mass energy for fixed mass $m_{Z'} = 3$ TeV (right). In the SSM the W' -boson mass is always set equal to $m_{Z'}$. For comparison we also include the results for the SM²⁶ (grey, dashed line). The event generation setup, the invariant mass and the fiducial cuts are as described above. In all cases, the cross sections fall off with increasing $m_{Z'}$ and grow with increasing \sqrt{S} . The former is also true for the SM in which the cross section only depends on $m_{Z'}$ indirectly through the invariant mass cut.

²⁴The invariant mass cut is a generation cut, so one does not need to worry about the numerical precision in samples without it.

²⁵At the moment, this contribution cannot be calculated independently of the Z' contribution. Because it is much smaller it would require an extremely precise prediction for the Z' contribution. Thus we do not report the numbers after cuts.

²⁶Note that this does not include the QCD contribution.

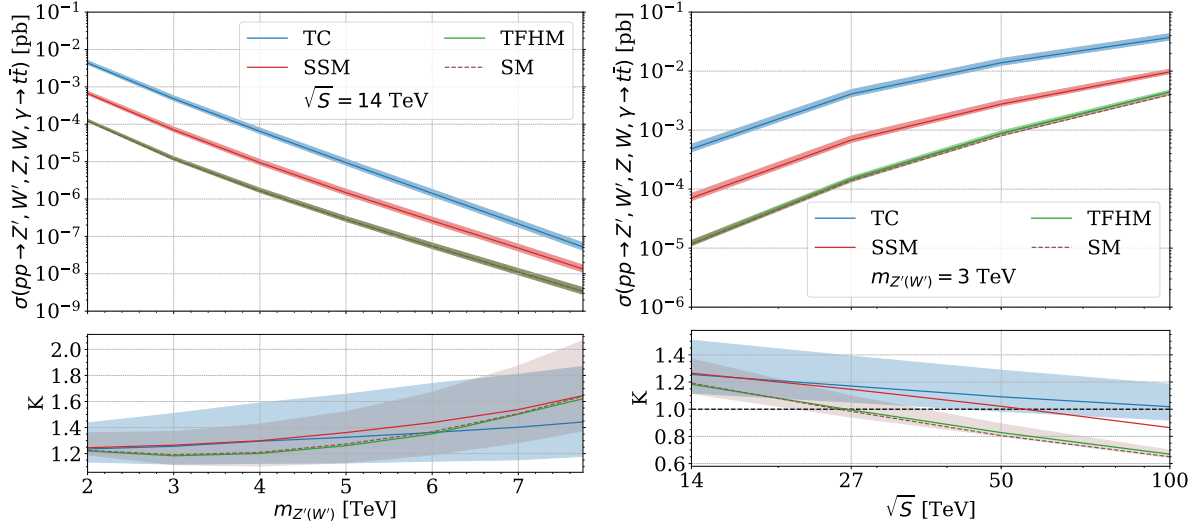


Figure 3.18: Fiducial cross sections for EW $t\bar{t}$ production in the SM, SSM, TC, and TFHM with an invariant mass cut $m_{t\bar{t}} \geq 0.75 m_{Z'}$ and our event selection cuts at NLO+PS (upper panels), and as ratio to LO+PS (lower panels). In the SSM $m_{W'} = m_{Z'}$. The bands represent perturbative uncertainty due to seven-point variation of μ_F and μ_R . Left panel: cross sections at $\sqrt{S} = 14$ TeV as a function of $m_{Z'}$. Right panel: cross sections at $m_{Z'} = 3$ TeV as a function of \sqrt{S} .

The invariant mass cut adequately suppresses the SM background relative to the BSM signal in the SSM and in the TC model. The prediction for the TFHM model, however, can barely be distinguished from the SM background throughout the whole mass range at $\sqrt{S} = 14$ TeV. It only becomes appreciably larger than the SM at higher energies, where its ratio over the SM is roughly 1.13 at $\sqrt{S} = 100$ TeV. Adopting a tighter invariant mass cut would be advised for the TFHM, for example $m_{Z'} - \Gamma_{Z'} < m_{t\bar{t}} < m_{Z'} + \Gamma_{Z'}$.

The NLO+PS over LO+PS K-factors, shown on the lower panels of Figure 3.18, are moderate to large and grow with Z' -boson mass up to $\sim 40\%$ in the TC model and up to $\sim 60\%$ in the SSM. In the absence of BSM effects, this ratio effectively measures the dependence of higher order corrections on the partonic centre-of-mass energy. Between 2 and 4 TeV this ratio is fairly flat but then quickly grows, surpassing 60 % percent at 8 TeV. As expected, the K-factors in the TFHM closely follow those of the SM.

Conversely, the K-factors follow the opposite trend versus \sqrt{S} and eventually almost all drop below one for $m_{Z'} = 3$ TeV. It would be interesting to see whether the higher order corrections for larger Z' masses follow a similar pattern.

Higher order corrections are often included in experimental searches in terms of a constant K-factor. While this is more or less well justified for a range of Z' masses between 2 and 5 TeV, the corrections more than double when this range is extended to 2-8 TeV. It may thus be

desirable to abandon this crude approximation in high luminosity or high energy searches where we expect the reach to extend considerably.

Impact of non-resonant contributions

A new feature of our calculation is that we include non-resonant contributions with t-channel W , W' and Z' exchange. We study their impact here.

In Figure 3.19 we show the ratio of predictions for cross sections for EW $t\bar{t}$ production in the SSM obtained using our new version of PBZp over the old one of Ref. [40]. The left panel shows this ratio as a function of $m_{Z'} = m_{W'}$ at $\sqrt{S} = 14$ TeV, the right panel as a function of \sqrt{S} at $m_{Z'} = m_{W'} = 3$ TeV. The cross sections have been calculated with an invariant mass cut $m_{t\bar{t}} \geq 0.75 m_{Z'}$ and with (red lines) and without (blue lines) fiducial cuts, at NLO+PS (solid lines) and LO+PS (dashed lines).

The ratio of our predictions at $\sqrt{S} = 14$ TeV is roughly between 1.2 and 1.5 when fiducial cuts are not considered. The reason behind it is the new non-resonant contribution, due to the SM $q\bar{q}' \rightarrow W \rightarrow t\bar{t}$ process, not falling off with the invariant mass as fast as the resonant one. This behaviour was already observed in Table 3.1, where this process contributes less than the resonant Z' production after the invariant mass cut but is still roughly of the same order of magnitude. In this respect the $q\bar{q}' \rightarrow W \rightarrow t\bar{t}$ process behaves similarly to the $\gamma g + g\gamma \rightarrow t\bar{t}$ process, which was already included in our old calculation. The situation worsens as the centre-of-mass energy is increased, the value of the ratio reaching almost 5 at $\sqrt{S} = 100$ TeV.

Once the fiducial cuts are switched on, the new contributions are reduced considerably and the ratio of the “new / old” predictions drops down to roughly between 1.0 and 1.05 across the whole mass range at $\sqrt{S} = 14$ TeV and between 1.0 and 1.2 across the whole \sqrt{S} range at fixed mass $m_{Z'} = m_{W'} = 3$. This is simply because the bulk of the high invariant mass cross section for the $q\bar{q}' \rightarrow W \rightarrow t\bar{t}$ process lives in the forward region. In this respect the $q\bar{q}' \rightarrow W \rightarrow t\bar{t}$ process is quite dissimilar to the $\gamma g + g\gamma \rightarrow t\bar{t}$ process.

QCD corrections do not change this picture appreciably, but we note that the corrections to this ratio can be considerable at high centre-of-mass energies, over 50%. Our new calculation thus confirms our previous predictions for the SSM at $\sqrt{S} = 14$ TeV, while at the same time it offers a much more sophisticated description of the interplay of various contributions that enter electroweak top-pair production. This interplay may become very important for Z' 's with weaker couplings and will certainly become important at higher collider energies.

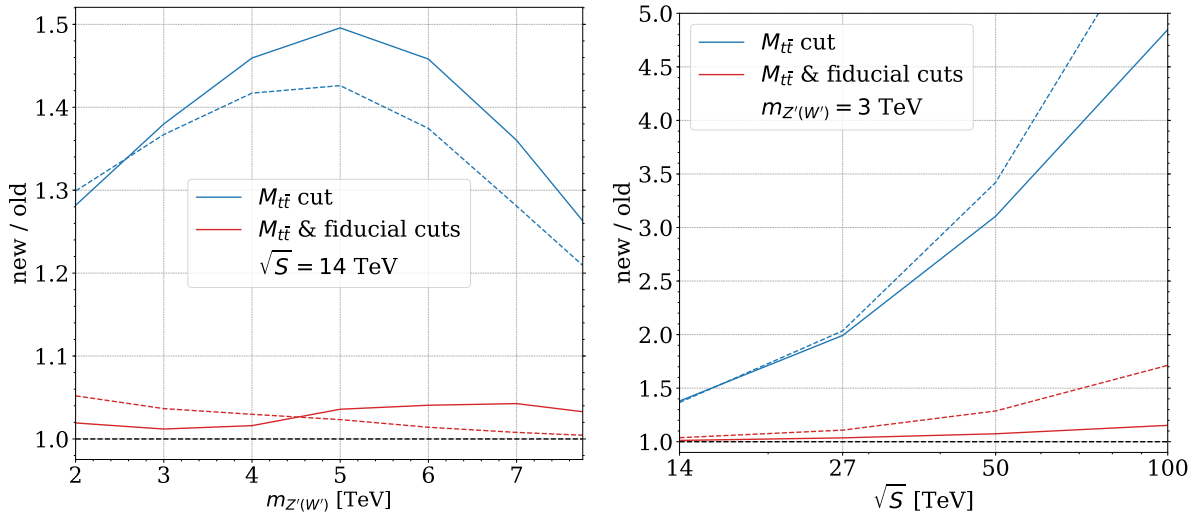


Figure 3.19: The ratio of cross sections for EW $t\bar{t}$ production in the SSM in the new calculation, including t-channel W and W' exchange contributions, over the old calculation, without these contributions, at NLO+PS (solid lines) and LO+PS (dashed lines). The cross sections have been calculated with an invariant mass cut $m_{t\bar{t}} \geq 0.75 m_{Z'}$ and with (red lines) and without (blue lines) fiducial cuts. Left panel: cross section ratio at $\sqrt{S} = 14$ TeV as a function of $m_{Z'} = m_{W'}$. Right panel: cross section ratio at $m_{Z'} = m_{W'} = 3$ TeV as a function of \sqrt{S} .

Signal–background interference

Interferences between the BSM signal and the SM background are routinely neglected even in the most recent experimental searches. The argument is that interferences mostly affect the shapes of resonance bumps, which “bump-hunting” is largely insensitive to. Consequently, experimental analyses work with the SM only and the SM+BSM hypotheses, where the latter is a “naive” sum of the signal and the background.

While interference effects are expected to integrate out in total cross sections, they may no longer be negligible once invariant mass and fiducial cuts are considered. In this section we explore interference effects by studying ratios of the fiducial cross sections for EW $t\bar{t}$ production obtained either using the full process $pp \rightarrow \gamma, Z, Z', W' \rightarrow t\bar{t}$ or by summing the SM background process $pp \rightarrow \gamma, Z \rightarrow t\bar{t}$ and the SSM signal $pp \rightarrow Z', W' \rightarrow t\bar{t}$. Both sets of predictions will include all the contributions to the EW top-pair production considered in our new calculation with one exception: those obtained by summing the SM background and the BSM signal will not include any of the interference terms $\{\gamma, Z, W\} \times \{Z', W'\}$.

This ratio of the cross sections with the interference terms over the ones without them is shown in Figure 3.20 as a function of $m_{Z'}$ on the left and as a function of \sqrt{S} on the right. As in the previous section, the predictions with the invariant mass cut are shown in blue, the

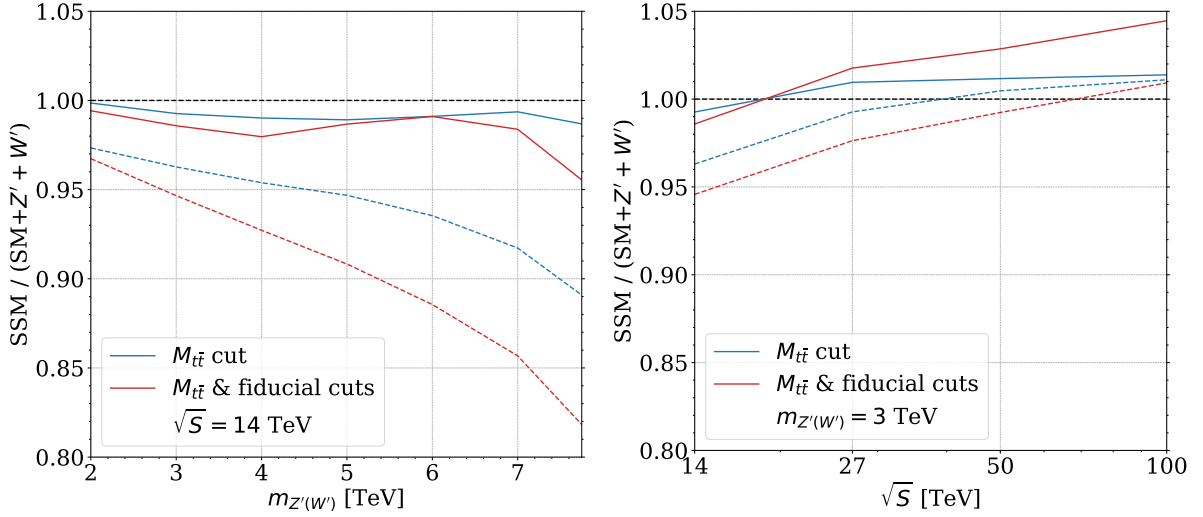


Figure 3.20: The ratio of the cross section for EW $t\bar{t}$ production in the SSM with and without the interference terms between the SM and the Z', W' contributions at NLO+PS (solid) and LO+PS (dashed). The cross sections have been calculated with an invariant mass cut $m_{t\bar{t}} \geq 0.75 m_{Z'}$ and with (red line) and without (blue line) fiducial cuts. Left panel: Cross section ratio at $\sqrt{S} = 14$ TeV as a function of $m_{Z'} = m_{W'}$. Right panel: Cross section ratio at $m_{Z'} = m_{W'} = 3$ TeV as a function of \sqrt{S} .

predictions with both the invariant mass and the fiducial cuts in red; the NLO+PS predictions are plotted with solid lines, while LO+PS ones with dashed lines. We find that the interference reduces the cross section at $\sqrt{S} = 14$ TeV and has a relatively steep profile versus $m_{Z'}$ at LO: a few percent for the light Z' s to well over 20% for the heavy ones. The size of the interference effects seem rather flat as a function of \sqrt{S} for fixed $m_{Z'} = m_{W'} = 3$ TeV in comparison. We also observe that the interference effects tend to be pronounced by the fiducial cuts, while the higher order corrections rather stabilise them.

Note that these conclusions may not generalise, as we expect the interference effects to strongly depend on the BSM scenario and on the position of the invariant mass cut. In view of their potentially large size, however, we advocate they be considered in experimental searches.

Chapter 4

Constraining models with Z' -bosons using LHC fiducial measurements

Working at the interface of theory and experiment in particle physics demands an equilibrium between what we wish to understand regarding the theory under consideration, and what we can achieve using the experimental data. Even though an important number of measurements at the LHC were designed to deal with Standard Model processes, they can still implicitly involve information about possible contributions from BSM physics. The method, “Constraints On New Theories Using Rivet”, Contur [155], uses the fact that unfolded particle level measurements created in fiducial regions of the phase space are highly model-independent. These measurements can thus be exploited to get information about BSM processes implemented in Monte Carlo generators in a very generic way. This approach should not be seen as a discovery procedure, but rather as a method to eliminate inconsistent BSM proposals.

In this chapter we describe the linking between the new PBZp package, explained in the previous chapter, and the Contur tool, in order to test models with extra heavy gauge bosons against the set of corresponding LHC measurements preserved in the Rivet library. We first start by briefly explaining the Contur workflow. We then provide some information on Rivet [153]. Finally, we discuss how we connect PBZp and Contur and give some numerical results.

4.1 The Contur method: workflow and philosophy

The key hypothesis of Contur is that editing the Lagrangian of the Standard Model affects the already well-understood and measured differential cross-sections. Hence, if introducing a new BSM particle modifies a measured distribution beyond its experimental uncertainties, then, we should have detected it already. As a result, if one can foresee how hundreds of differential quantities in existing LHC measurements can be affected according to a specific BSM scenario, then one can compute the exclusion limits of its parameter space without requiring an exclusive search. To this end, Contur designs a workflow that does the following:

- Takes a BSM model point with a set of parameter values.
- Generates simulated particle-level events from it.
- Infer the effect of those events in each bin of the LHC measurements.

- Find the exclusion status at some confidence level for that model point.

Furthermore, it can repeat this procedure over a range of parameter points, to identify the excluded regions of the parameter space.

Contur aims for speed and coverage of new BSM models at the cost of some precision and sensitivity. In order to achieve this, it deals with fiducial, particle-level measurements, that is, observables corrected for detector effects or “unfolded”, but not extrapolated beyond detector acceptance. Another preference of the Contur method is the generation of inclusive events. In this way the model in hand can be tested comprehensively against a wide range of measurements instead of concentrating on some specific signatures.

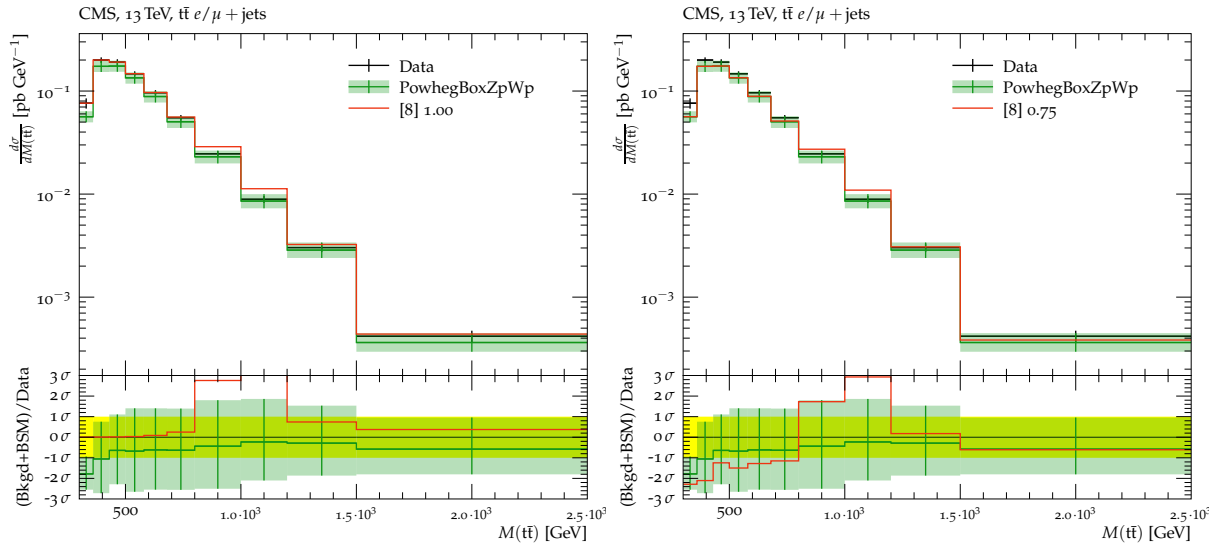


Figure 4.1: A comparison of a leptophobic TC model producing a 1000 GeV Z' resonance in a $t\bar{t}$ mass measurement [156]. An NLO QCD $t\bar{t}$ background prediction is shown in green for comparison. The figure on the left shows the background model generated from data, with the one on the right showing the effect of using the theoretically calculated background model.

Two approaches can be used in order to calculate the exclusion limits with Contur: (i) The most complete one is when the background is defined by the simulated SM predictions and their associated uncertainties. In this case, the BSM signal is added on top of the background. The exclusion is then obtained by comparing the signal + background to the data within uncertainties. (ii) The less complete approach (also known as the null hypothesis of the Contur method) is when the background is assumed to be the data. In this case, the BSM signal is superimposed on top of the data and the uncertainties on the data are considered to define the room that is left for the signal. Both approaches are exemplified in Figure 4.1, where on the left hand side (background = data) the signal (red) is 100% excluded, whereas on the right hand side (background = SM prediction) the BSM signal (red) is excluded at 75% CL. It is important

to note that Contur suffers from some limitations, mainly due to the incomplete information published by the experiments (SM prediction not published, bin-to-bin correlation information for the systematic uncertainties not provided, hidden model-dependent assumptions, ...). For more information about the Contur method and its limitations we refer the reader to [48, 157].

4.2 The Rivet analyses

The Rivet, or Robust Independent Validation of Experiment and Theory, repository is a system where particle-level measurements from the LHC and other colliders are preserved. Each analysis paper has its own Rivet analysis routine, i.e. a C++ code where the measured particle-level cross section is defined. These routines produce histograms which can be compared to the published plots in the corresponding papers. In other words, a Rivet routine chooses the generated events that would go into the fiducial region, and project their properties into histograms that have the same observables and binnings as in the measurement. The format used by Rivet for histograms and associated analysis objects is dubbed YODA.

On the other hand, the digitised record of the measured cross-section values together with their uncertainties is preserved in the HepData library¹ [158]. For every new release, Rivet is synchronised to the up-to-date HepData repository so that the produced SM events can be filtered through the Rivet routines and compared to the corresponding measured data and uncertainties from HepData.

Contur exploits the set of Rivet analysis plugins to set the fiducial cuts on the BSM events instead of the SM ones. For each beam configuration, it is possible to run many (or even all) of the Rivet routines at the same time. Consequently, the produced BSM events can be scanned and filtered using the complete set of routines, which results in a large number of histograms describing if, and where, the BSM signal would have shown in the existing collider measurements. Then, the exclusion limits can be computed following one of the approaches explained in the previous section.

As we have previously seen, Contur superimposes the BSM signal, for each measurement, either directly on top of the data or on top of the corresponding simulated SM theory. Either way, if the signal results in an excess in a measured distribution, there could also be excesses in measurements of similar final states coming from essentially the same events. Since the information about the correlations between different measurements are not provided, one can not take them into account. This would then lead to high exclusion rates due to multiply-counting

¹Occasionally this would also include the best SM theory predictions at the time and/or the breakdown of uncertainties in each bin or other correlation information

what might be the same exclusion against several measurements. In order to avoid such a problem, Contur divide the analysis routines into orthogonal pools in which the measurements are grouped by, crudely, different final states, different experiments, and different centre-of-mass energies.

4.3 Constraints on theories with extra heavy gauge bosons using Contur

There are two ways to study a BSM model with Contur. Regardless of the background choice (data or simulated SM), one can either (i) create a UFO file [82], read it into Herwig, and analyse the generated events with Rivet and Contur, or (ii) Produce fully-final state events in HEPMC format [159, 160] with any MC event generator and analyse them with Rivet and Contur.

We work according to the latter option. Events can be generated in POWHEG in the `.lhe` format using the `pwhg_main` executable together with the `powheg.input` file. These events can then be transformed to the `.hepmc` format and showered using a full-final-state generator such as PYTHIA. The `.hepmc` events can then be passed through Rivet as usual to obtain a YODA file for processing by Contur to get exclusion limits.

Machinery to steer POWHEG using Contur has been created based on the PBZp POWHEG package which produces events at leading and next-to-leading order for electroweak $t\bar{t}$ hadroproduction in models with flavour non-diagonal Z' -boson couplings and W' -bosons [46, 47]. Three BSM models are currently implemented, namely the Sequential Standard Model [24], the Topcolour model [138], and the Third Family Hypercharge Model [71]. In what follows we exemplify this steering chain by explaining how to run jobs on a High Performance Computing (HPC) system to set exclusion limits on the mass of Z' in the TC model.

To run a batch job one needs three executables (`main-pythia.cc`, `pwhg_main`, and `pbzp_input_contur.py`), two files (`param_file.dat` and `powheg.input_template`), and one directory (`RunInfo`), all in one run directory. More details on these are listed below.

- the `main-pythia.cc` script is responsible for the creation of the HEPMC file and of the parton showering.
- The `RunInfo` directory contains the needed analysis steering files (`.ana`). However, if the `.ana` files do not already exist locally, they will be automatically copied by `contur-batch`² to the local `RunInfo` directory.

²A utility for submitting Contur scans to HPC systems.

Listing 4.1: An example Contur configuration file for the SSM.

```

[Run]
generator = "/path/to/setupPBZpWp.sh", "/path/to/setupEnv.sh"
contur = "/path/to/setupContur.sh"

[Parameters]
[[mZp]]
mode = LIN
start = 1000.0
stop = 5000.0
number = 9
[[GZp]]
mode = LIN
start = 30
stop = 150
number = 9
[[model]]
mode = SINGLE
name = TC
[[tsb]]
mode = SINGLE
name = dummy

```

- The `pbzp_input_contur.py` script is used to create and fill the `powheg.input` files based on the model choice in `param_file.dat`, it needs `powheg.input_template` in order to do so.
- The `param_file.dat` file defines a parameter space, as with other generators.

We set the leptophobic TC model such that the only free parameters are the mass (`mZp`) and the total decay width³ (`GZp`) of the Z' -boson, but one also needs to include the name of the model (TC in this example), and the parameters of the other models as dummy⁴. This can be seen from the TC `param_file.dat` file shown in Listing 4.1, where in addition to the parameters we also have `setupPBZpWp.sh` which is a script that sets the environment needed to run `pwg_main`, and `setupEnv.sh` a script which sets up the run-time environment which the batch jobs will use, as a minimum it will need to contain the lines to execute the `rivetenv.sh` and `yodaenv.sh` files. For all the set up files, one should give the full explicit path. The `setupPBZpWp.sh` and the `setupEnv.sh` should be always in the same order as shown in this

³The ratio of the two $U(1)$ coupling constants $\cot\theta_H$ needed to set the couplings is calculated from the mass and the width, see Eq. (6) of [138].

⁴Only the angle θ_{sb} (`tsb`) needed for the TFHMeg, since for now we only include the SSM (`mZp`, `GZp`), the TFHMeg (`mZp`, (`tsb`)) and the TC (`mZp`, `GZp`) models. This is done in order to be able to use the same `powheg.input_template` for all the models.

example, i.e. in generator one first gives the full path to `setupPBZpWp.sh` then the one for `setupEnv.sh`. In addition, one should check that the parameters defined in `params_file.dat` are also defined in `powheg.input_template`, in other words, removing or adding new parameters should be done in both files. The content of `main-pythia.cc`, `pbzp_input_contur.py`, and `powheg.input_template` is shown in Appendix C.1.

To run a test scan over the parameter space defined in `param_file.dat` without submitting it to a batch farm one should run the following command

```
contur-batch -n 1000 -t powheg.input_template -m pbzpw -s
```

where `-n` specifies the number of events (1000 in this particular example), `-m` sets the MC event generator, `-t` indicates the correct template, and the `-s` flag ensure that no jobs will be submitted. This will produce a directory called `myscan##` containing one directory for each beam configuration, each containing however many runpoint directories are indicated by the ranges in the `param_file.dat` (9×9 in our example). One can then have a look at the shell scripts (`runpoint_xxxx.sh`) which have been generated, to check that all is as expected. Moreover, one can manually submit some of the `runpoint_xxxx.sh` files as a test. We should mention that at this stage, i.e. before running the `runpoint_xxxx.sh` files, the `powheg.input` files are not yet created, only after running the `.sh` files, which run the `pbzp_input_contur.py` script, the `powheg.input` files needed by PBZp will be generated and properly filled.

In order to run a batch job one should run the batch submit command without the `-s` flag and specifies the queue on his batch farm using the `-q` flag. Note that `qsub`, `Slurm`, and `Condor` batch systems are all supported in `Contur`. If one has a different submission system one needs to work out how to change the appropriate submission commands in `Contur`. A successful run will produce a directory called `myscan##` as before. When the batch job is complete there should, in every run point directory, be a `runpoint_xxxx.yoda` file and an `output.pbzpw` directory that contains the `.lhe` file.

At this stage we have created a farm of directories, for each beam energy, containing a `.yoda` file for each combination of the mass and the total width of Z' in the TC model. These YODA files can now be scanned and analysed by `Contur` using the following command

```
contur -g myscan##
```

where `-g` specifies the folder with a structured grid of points to analyse, which is the `myscan##` directory in this example. This will create the directory `ANALYSIS` that contains a `.map` file where the `Contur` likelihood analysis for our sampled collection of points is encoded. The

sensitivities calculated by Contur for each grid point can be then expressed as a 2D heatmap showing the overall sensitivity. This will show where our BSM signal can be excluded due to existing LHC measurements available in Rivet and which part of the phase space is still open. The 2D heatmap can be plotted by issuing the command `contu-plot` on the `.map` file while specifying the parameters of the x-axis ($m_{Z'}$) and of the y-axis ($\Gamma_{Z'}$) respectively. The result of our example case is shown in Figure 4.2, where, as specified in `param_file.dat`, the mass of Z' (x-axis) ranges between 1000 and 5000 GeV and its total decay width (y-axis) between 30 and 150 GeV. The exclusion limits are shown in yellow at 95% CL and in green at 68% CL. Here we are using the default null hypothesis approach (background = data). Furthermore, Contur can

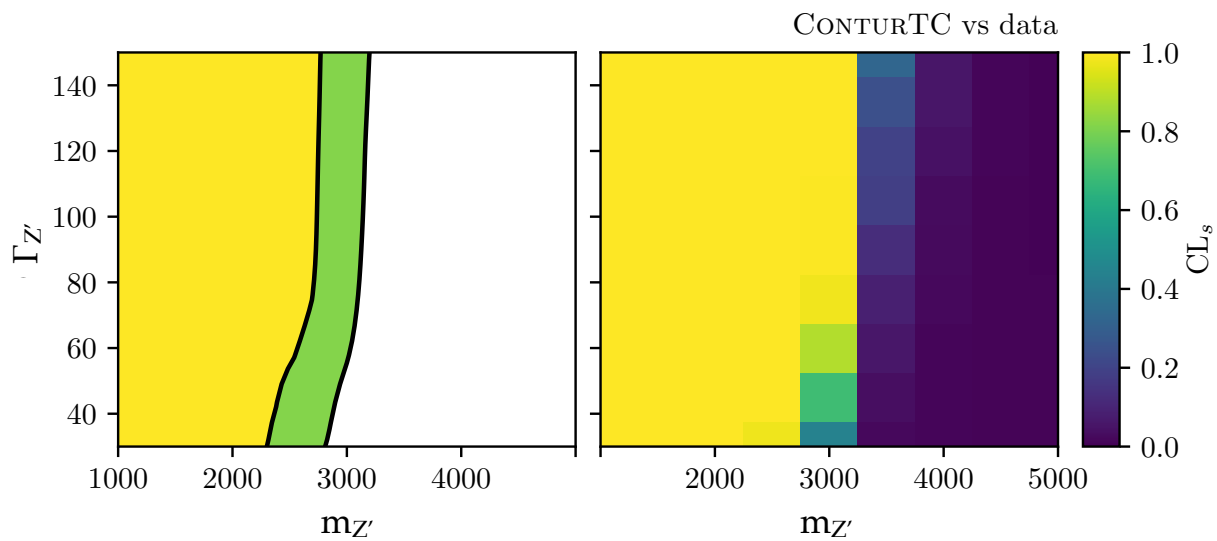


Figure 4.2: Contur 2D heatmap for the leptophobic TC model, in the Z' mass (GeV) versus the Z' total decay width (GeV). The 95% CL (yellow) and 68% CL (green) exclusion limits are superimposed considering the data as background.

plot the heatmap while indicating which analysis pool has the most significant exclusion limit in every scan point. In our case, this can be seen from Figure 4.3 where the region on the left of the white solid (dashed) line is excluded at 95% (68%) CL, and the terms LMETJET; METJET; TTHAD; JETS at the end of each pool name stand for lepton, missing transverse momentum, plus optional jets; missing transverse momentum plus jets; Fully hadronic top events; Inclusive hadronic final states respectively.

In order to test our model using the most complete approach (background = SM predictions) we first simulated the background for all the measurements included in the contributing pools (see Figure 4.3) [156, 161–171] except the ones in ATLAS_13_JETS. We used the hvq POWHEG package [128] to simulate the SM QCD background and our PBZp package for the EW part, and added the two together to obtain an EW+QCD SM background. The scale and PDF variations

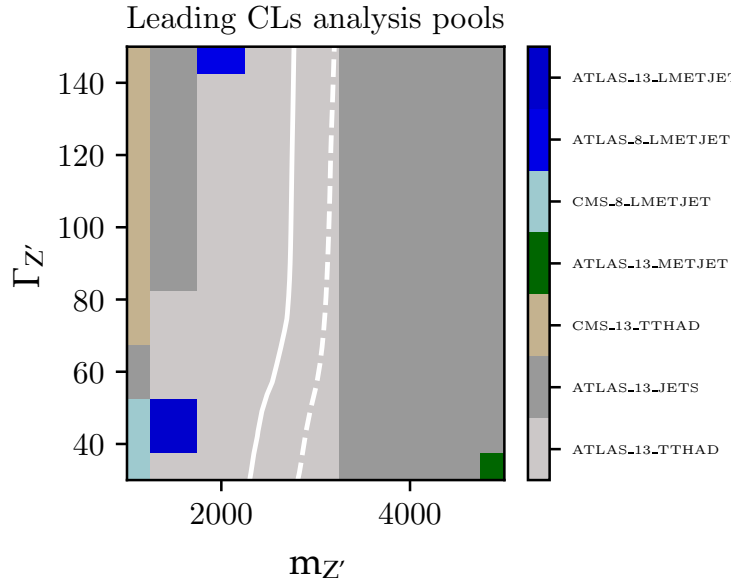


Figure 4.3: The breakdown of Figure 4.2 into the most sensitive analysis pool for each scan point.

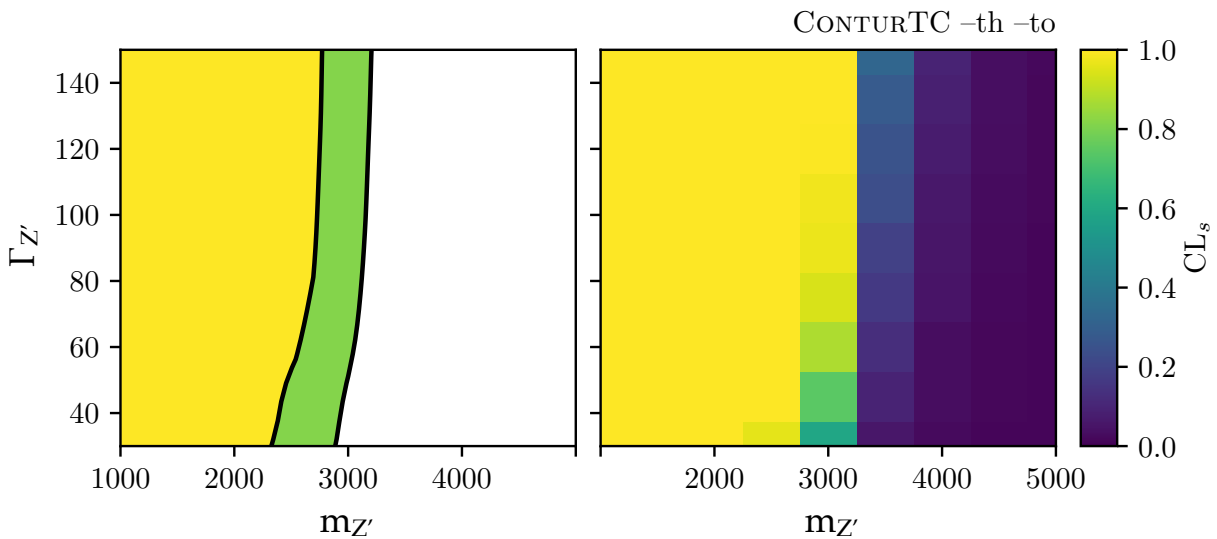


Figure 4.4: Same as Figure 4.2 but using the SM theoretical predictions as background.

were both taken into account. Then, we created the ANALYSIS directory using the command

```
contur -g myscan## --th --to
```

where `-th` tells Contur to use theory as the background if available (fall back to using data otherwise), and `-to` to only use measurements where theory is available (but still use data as the background by default). Thus, to get a `.map` file where we (i) use only measurements where we have a theory prediction and (ii) actually use that prediction, we need both flags together. Finally, the 2D heatmap and the one indicating the contribution of each pool can be generated exactly

as before (using contour-plot). This can be seen in our case in Figs. 4.4 and 4.5 respectively, where the limits we obtain are weaker as compared to the previous case.

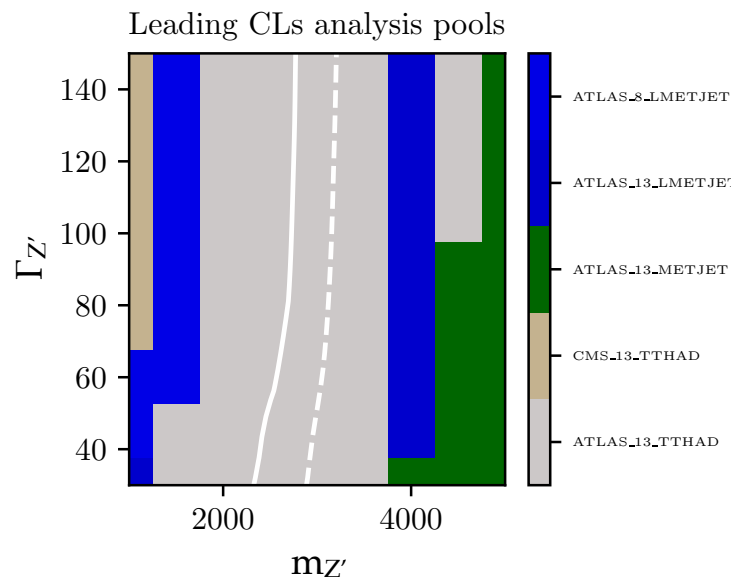


Figure 4.5: The breakdown of Figure 4.4 into the most sensitive analysis pool for each scan point.

Summary and Outlook

New heavy resonances are a common occurrence in BSM theories. In particular, they show up whenever the SM gauge group is extended. In this thesis, we focused on new heavy spin-1 neutral and charged vector bosons denoted as Z' - and W' -bosons respectively.

In Chapter 1 we reviewed such resonances in the context of the G_{221} class. A class that involves models in which the SM gauge group is extended with an additional $SU(2)$ factor. In this perspective, the SM emerges as the low energy limit of theories based on much larger simple gauge groups like $SU(5)$, $SO(10)$ or E_6 . We presented six realisations of this class, namely the Left-Right, Lepto-Phobic, Fermio-Phobic, Hadro-Phobic, Non-Universal and Un-Unified models. We showed how these models differ from each other in their particle content and in the way their $SU(2)_1 \times SU(2)_2 \times U(1)_X$ gauge group is broken. Furthermore, the expressions for the masses and couplings of the new resonances to the SM fermions have also been presented and in some cases calculated.

Chapter 2 was dedicated to higher order predictions for spin-1 resonance searches in two classes of observables, top-quark-pair production and dilepton production at the HL-LHC and the HE-LHC. In the former case, we used the old PBZp code which includes the NLO QCD corrections to the EW production of top-antitop pairs in the presence of a new neutral gauge boson implemented in the parton shower Monte Carlo program POWHEG. The dilepton cross sections were calculated using the NLO+NLL code RESUMMINO which matches a soft-gluon resummation at NLL accuracy to a fixed order NLO calculation. We considered four models: the Un-Unified and the Non-Universal models, a leptophobic Topcolour model, and the Sequential Standard Model.

In Chapter 3 We performed a complete recalculation, including several improvements, of the electroweak top-quark pair hadroproduction in extensions of the Standard Model with extra heavy neutral and charged spin-1 resonances. In particular, we allowed for flavour-non-diagonal Z' couplings in order to accommodate a wider class of heavy resonance models including models which have been brought forward to explain the anomalies currently seen in B decays. We also took into account non-resonant production in the SM and beyond, including the contributions with t-channel W^- , W' - and Z' -bosons. All amplitudes were generated using the RecoLa2 package. Our calculation was one of the first to use RecoLa2 for a BSM calculation. We included NLO QCD corrections and consistently matched them to parton showers with the POWHEG method fully taking into account the interference effects between SM and new physics amplitudes. As a first application, we presented numerical results for $t\bar{t}$ cross sections at hadron colliders with a centre-of-mass energy up to 100 TeV for three models, the Sequential Standard Model, the Topcolour model, as well as the Third Family Hypercharge Model. We discussed the effect of cuts on the signal over background ratio and presented K-factors which turned out to increase considerably as a function of the heavy resonance mass. The impact of the newly included contributions was shown to be modest at 14 TeV if suitable cuts are applied. However, it became sizable when the centre-of-mass energy reached 100 TeV.

Finally, in Chapter 4 we briefly explained the Contur framework where CONTUR stands for “Constraints On New Theories Using Rivet”. This framework exploits the fact that particle-level differential measurements made in fiducial regions of the phase space have a high degree of model-independence and can therefore be used to give information about a wide variety of BSM

physics implemented in Monte Carlo generators, using a broad range of final states. We linked our $t\bar{t}$ calculation to Contur and introduced a steering machinery where the events are produced using PBZp based on a parameter choice defined in Contur. The produced events can then be analysed by Rivet and Contur resulting in a map of exclusion limits. Three models were added to this chain, namely the Sequential Standard Model, the Topcolour model, and the Third Family Hypercharge Model. The machinery was exemplified using the TC model.

The production of single top quarks at the LHC is a powerful means to identify physics beyond the Standard Model. The $t\bar{t}$ study that we performed in Chapter 3 paves the way for a similar upcoming calculation of the NLO QCD corrections to the $pp \rightarrow W/W' \rightarrow t\bar{b}$ process. As before we will use RecoLa2 to calculate the Born, virtual, and real amplitudes. The implementation in POWHEG can then be done as in the case of $t\bar{t}$. Since we understand the different steps in the calculation quite well and many aspects are fairly automatised we expect to finalise the implementation in the near future. The most important task will be to perform an exhaustive precision analysis of W' and single-top production for Run 3 of the LHC, starting in 2021, and to prepare a publication. While models with an additional Z' may explain neutral current B-anomalies, W' -bosons may be a solution for charged current ones. Finally, having both calculations complete, it would be interesting to study the correlations between the observables with different final states (top-antitop, top-bottom) in order to increase the power to discriminate different models. Such a study would be similar in spirit as the one in [30] but at NLO QCD precision.

The experience with Contur/Rivet could be useful to study other BSM models. It would be interesting to address the connection of additional new gauge bosons to dark matter, one of the most important outstanding problems in particle physics. This includes not only studies of the traces of dark photons and other neutral and charged mediators in SM processes, but also possible signals of new physics processes when the new gauge bosons couple to new scalars and fermions. An example for the B-L model can be found in [172]. It could also be interesting to connect Contur/Rivet with global analysis frameworks in the context of effective theories allowing to systematically include LHC constraints in the global analyses.

A. G_{221} models

A.1 Derivation of the second stage SB mass matrices in BP-II

The general Lagrangian that describes the gauge boson masses can be written as

$$\begin{aligned} \mathcal{L}_{mass} = & \frac{1}{2}m_Z^2 \hat{Z}_\mu \hat{Z}^\mu + \frac{1}{2}(m_{Z'}^2 + \Delta m_{Z'}^2) \hat{Z}'_\mu \hat{Z}'^\mu + \delta m_Z^2 (\hat{Z}_\mu \hat{Z}'^\mu + \hat{Z}'_\mu \hat{Z}^\mu) \\ & + m_W^2 \hat{W}_\mu^- \hat{W}^{+\mu} + (m_{W'}^2 + \Delta m_{W'}^2) \hat{W}'_\mu{}^- \hat{W}'^{+\mu} \\ & + \delta m_W^2 (\hat{W}_\mu^- \hat{W}'^{+\mu} + \hat{W}'_\mu{}^- \hat{W}^{+\mu}). \end{aligned} \quad (\text{A.1})$$

The covariant derivative of the second stage SB scalar field reads, see Table 1.3,

$$D_\mu H = \partial_\mu H - ig_2 \frac{1}{2} \vec{\sigma} \cdot \vec{W}_{2\mu} H - i \frac{1}{2} g_X X_\mu H.$$

Below the electroweak scale H acquires its VEV and the covariant derivative takes the following form

$$D_\mu \langle H \rangle = -ig_2 \frac{1}{2} \vec{\sigma} \cdot \vec{W}_{2\mu} \frac{v}{\sqrt{2}} \begin{pmatrix} 0 \\ 1 \end{pmatrix} - i \frac{1}{2} g_X X_\mu \frac{v}{\sqrt{2}} \begin{pmatrix} 0 \\ 1 \end{pmatrix} = -i \frac{v}{2} \begin{pmatrix} \frac{1}{\sqrt{2}} g_2 (W_{2\mu}^1 - iW_{2\mu}^2) \\ \frac{1}{\sqrt{2}} (g_X X_\mu - g_2 W_{2\mu}^3) \end{pmatrix},$$

accordingly, the Hermitian conjugate of the covariant derivative is

$$(D_\mu \langle H \rangle)^\dagger = i \frac{v}{2} \begin{pmatrix} \frac{1}{\sqrt{2}} g_2 (W_{2\mu}^1 + iW_{2\mu}^2) & \frac{1}{\sqrt{2}} (g_X X_\mu - g_2 W_{2\mu}^3) \end{pmatrix}.$$

Multiplying the covariant derivative by its Hermitian conjugate one finds

$$(D_\mu \langle H \rangle)^\dagger (D^\mu \langle H \rangle) = \frac{v^2}{4} g_2^2 W_{2\mu}^- W_2^{+\mu} + \frac{v^2}{8} (g_X X_\mu - g_2 W_{2\mu}^3) (g_X X^\mu - g_2 W_2^{3\mu}). \quad (\text{A.2})$$

Starting from the first component of the right-hand side of Eq. (A.2) and using that $W_{2\mu}^\pm = c_\phi \hat{W}_\mu^\pm - s_\phi \hat{W}'_\mu^\pm$ one obtains

$$\frac{v^2}{4} g_2^2 W_{2\mu}^- W_2^{+\mu} = \frac{1}{4} g_2^2 v^2 (c_\phi^2 \hat{W}_\mu^- \hat{W}^{+\mu} - c_\phi s_\phi \hat{W}_\mu^- \hat{W}'^{+\mu} - c_\phi s_\phi \hat{W}'_\mu{}^- \hat{W}^{+\mu} + s_\phi^2 \hat{W}'_\mu{}^- \hat{W}'^{+\mu}).$$

Thus, by comparing this result to the charged part of the Lagrangian in Eq. (A.1) we obtain the elements of the charged gauge bosons mass matrix:

$$m_{\hat{W}}^2 = \frac{1}{4}g_2^2c_\phi^2v^2, \quad (\text{A.3})$$

$$\delta m_{\hat{W}}^2 = -\frac{1}{4}g_2^2c_\phi s_\phi v^2 = -\frac{1}{4}g_1g_2s_\phi^2v^2, \quad (\text{A.4})$$

$$\Delta m_{\hat{W}'}^2 = \frac{1}{4}g_2^2s_\phi^2v^2. \quad (\text{A.5})$$

On the other hand, rearranging the second component on the right-hand side of Eq. (A.2) using that $X_\mu = \hat{B}_\mu$, $\hat{B}_\mu = c_\theta A_\mu - s_\theta \hat{Z}_\mu$, $W_{2\mu}^3 = c_\phi \hat{W}_\mu^3 - s_\phi \hat{Z}'_\mu$ and $\hat{W}_\mu^3 = c_\theta \hat{Z}_\mu + s_\theta A_\mu$ leads to

$$\begin{aligned} \frac{v^2}{8}(g_X X_\mu - g_2 W_{2\mu}^3)(g_X X^\mu - g_2 W_2^{3\mu}) &= \frac{v^2}{8}[(g_2 c_\phi c_\theta + g_X s_\theta)^2 \hat{Z}_\mu \hat{Z}^\mu - \frac{s_\phi^2}{e} g_1 g_2 g_X \hat{Z}_\mu \hat{Z}'^\mu \\ &\quad - \frac{s_\phi^2}{e} g_1 g_2 g_X \hat{Z}'_\mu \hat{Z}^\mu + g_2^2 s_\phi^2 \hat{Z}'_\mu \hat{Z}'^\mu]. \end{aligned}$$

Hence, by inspecting the neutral part of the Lagrangian in Eq. (A.1), the components of the neutral gauge bosons mass matrix are

$$m_{\hat{Z}}^2 = \frac{1}{4}(g_2 c_\phi c_\theta + g_X s_\theta)^2 v^2, \quad (\text{A.6})$$

$$\delta m_{\hat{Z}}^2 = -\frac{1}{4}g_1 g_2 g_X \frac{s_\phi^2}{e} v^2, \quad (\text{A.7})$$

$$\Delta m_{\hat{Z}'}^2 = \frac{1}{4}g_2^2 s_\phi^2 v^2. \quad (\text{A.8})$$

A.2 Neutral and charged currents in the NU model

In this section we exemplify Eqs. (1.33, 1.34) by the NU model of the G_{221} class. This model is motivated by the strong hierarchy of the fermion mass matrix. The relatively large mass of the third generation fermions may suggest a dynamical behavior different from that of the first two generations. Thus, in the NU model the third generation undergoes a different flavor dynamics from the usual weak interaction proposed in the SM. We assume this flavor dynamics to be associated with the new $SU(2)$ symmetry; no modification to QCD interactions are considered here. This is summarised in Table A.1.

Fields	Components	$SU(2)_1$	$SU(2)_2$	$U(1)_X$
Fermions				
$L_{L(1,2)}$	$\begin{pmatrix} \nu_L \\ e_L \end{pmatrix}_{1^{st}, 2^{nd}}$	2	1	$-\frac{1}{2}$
$L_{L(3)}$	$\begin{pmatrix} \nu_L \\ e_L \end{pmatrix}_{3^{rd}}$	1	2	$-\frac{1}{2}$
E	e_R	1	1	-1
$Q_{L(1,2)}$	$\begin{pmatrix} u_L \\ d_L \end{pmatrix}_{1^{st}, 2^{nd}}$	2	1	$\frac{1}{6}$
$Q_{L(3)}$	$\begin{pmatrix} u_L \\ d_L \end{pmatrix}_{3^{rd}}$	1	2	$\frac{1}{6}$
U	u_R	1	1	$\frac{2}{3}$
D	d_R	1	1	$-\frac{1}{3}$
Gauge Bosons				
W_1	W_1^+, W_1^-, W_1^3	3	1	0
W_2	W_2^+, W_2^-, W_2^3	1	3	0
X	X	1	1	0
Scalars				
Φ	$\begin{pmatrix} \phi^0 + \pi^0 & \sqrt{2}\pi^+ \\ \sqrt{2}\pi^- & \phi^0 - \pi^0 \end{pmatrix}$	2	2	0
H	$\begin{pmatrix} h^+ \\ h^0 \end{pmatrix}$	1	2	$\frac{1}{2}$

Table A.1: The field content of the Non-Universal model [38] and the respective quantum numbers.

Under the symmetry of the G_{221} class, the covariant derivative reads

$$D_\mu \equiv \partial_\mu - ig_1 T_1^i W_{1\mu}^i - ig_2 T_2^j W_{2\mu}^j - ig_X X X_\mu. \quad (\text{A.9})$$

According to the charge assignments in Table A.1, the covariant derivative takes the following forms for each term

$$\begin{aligned} \bar{L}_{L(1,2)} \gamma^\mu D_\mu L_{L(1,2)} &= \bar{L}_{L(1,2)} \gamma^\mu (\partial_\mu - ig_1 T_1^i W_{1\mu}^i - ig_X X X_\mu) L_{L(1,2)}, \\ \bar{L}_{L(3)} \gamma^\mu D_\mu L_{L(3)} &= \bar{L}_{L(3)} \gamma^\mu (\partial_\mu - ig_2 T_2^j W_{2\mu}^j - ig_X X X_\mu) L_{L(3)}, \\ \bar{E} \gamma^\mu D_\mu E &= \bar{E} \gamma^\mu (\partial_\mu - ig_X X X_\mu) E, \end{aligned} \quad (\text{A.10})$$

$$\begin{aligned}
\bar{Q}_{L(1,2)} \gamma^\mu D_\mu Q_{L(1,2)} &= \bar{Q}_{L(1,2)}^\alpha \gamma^\mu [(\partial_\mu - ig_1 T_1^i W_{1\mu}^i - ig_X X X_\mu) \delta_{\alpha\beta} - i \frac{g_s}{2} \lambda_{\alpha\beta}^a \cdot G_\mu^a] Q_{L(1,2)}^\beta, \\
\bar{Q}_{L(3)} \gamma^\mu D_\mu Q_{L(3)} &= \bar{Q}_{L(3)}^\alpha \gamma^\mu [(\partial_\mu - ig_2 T_2^j W_{2\mu}^j - ig_X X X_\mu) \delta_{\alpha\beta} - i \frac{g_s}{2} \lambda_{\alpha\beta}^a \cdot G_\mu^a] Q_{L(3)}^\beta, \\
\bar{U} \gamma^\mu D_\mu U &= \bar{U}^\alpha \gamma^\mu [(\partial_\mu - ig_X X X_\mu) \delta_{\alpha\beta} - i \frac{g_s}{2} \lambda_{\alpha\beta}^a \cdot G_\mu^a] U^\beta, \\
\bar{D} \gamma^\mu D_\mu D &= \bar{D}^\alpha \gamma^\mu [(\partial_\mu - ig_X X X_\mu) \delta_{\alpha\beta} - i \frac{g_s}{2} \lambda_{\alpha\beta}^a \cdot G_\mu^a] D^\beta,
\end{aligned} \tag{A.11}$$

In what follows the strong interactions of fermions and bosons will be neglected. Following Eq. (A.11), the kinetic terms of the first and the second generation left-handed fermions contain the following terms

$$\begin{aligned}
\bar{f}_{L(1,2)} i \gamma^\mu D_\mu f_{L(1,2)} &= \bar{f}_{L(1,2)} i \gamma^\mu (\partial_\mu - ig_1 T_1^i W_{1\mu}^i - ig_X X X_\mu) f_{L(1,2)} \\
&= \bar{f}_{L(1,2)} \gamma^\mu [i \partial_\mu + \frac{g_1}{\sqrt{2}} (W_{1\mu}^+ T_1^+ + W_{1\mu}^- T_1^-) + g_1 W_{1\mu}^3 T_1^3 + g_X X X_\mu] f_{L(1,2)} \\
&\supset \bar{f}_{L(1,2)} \gamma^\mu [\frac{g_1}{\sqrt{2}} (W_{1\mu}^+ T_1^+ + W_{1\mu}^- T_1^-)] P_L f_{L(1,2)} \\
&+ \bar{f}_{L(1,2)} \gamma^\mu [(g_1 s_\phi s_\theta T_1^3 + g_X c_\theta X) A_\mu + (g_1 s_\phi c_\theta T_1^3 - g_X s_\theta X) \hat{Z}_\mu + (g_1 c_\phi T_1^3) \hat{Z}'_\mu] P_L f_{L(1,2)},
\end{aligned} \tag{A.12}$$

where f stands for the quarks and the leptons of the NU model. Furthermore $X_\mu = B_\mu$, $B_\mu = c_\theta A_\mu - s_\theta \hat{Z}_\mu$, $W_{1\mu}^3 = c_\phi \hat{Z}'_\mu + s_\phi \hat{W}_\mu^3$ and $\hat{W}_\mu^3 = c_\theta \hat{Z}_\mu + s_\theta A_\mu$. Similarly and using that $W_{2\mu}^3 = c_\phi \hat{W}_\mu^3 - s_\phi \hat{Z}'_\mu$ the kinetic terms of the third generation left-handed fermions read

$$\begin{aligned}
\bar{f}_{L(3)} i \gamma^\mu D_\mu f_{L(3)} &= \bar{f}_{L(3)} i \gamma^\mu (\partial_\mu - ig_2 T_2^i W_{2\mu}^i - ig_X X X_\mu) f_{L(3)} \\
&= \bar{f}_{L(3)} \gamma^\mu (i \partial_\mu + \frac{g_2}{\sqrt{2}} (W_{2\mu}^+ T_2^+ + W_{2\mu}^- T_2^-) + g_2 W_{2\mu}^3 T_2^3 + g_X X X_\mu) f_{L(3)} \\
&\supset \bar{f}_{L(3)} \gamma^\mu [\frac{g_2}{\sqrt{2}} (W_{2\mu}^+ T_2^+ + W_{2\mu}^- T_2^-)] P_L f_{L(3)} + \bar{f}_{L(3)} \gamma^\mu [(g_2 c_\phi s_\theta T_2^3 + g_X c_\theta X) A_\mu \\
&+ (g_2 c_\phi c_\theta T_2^3 - g_X s_\theta X) \hat{Z}_\mu + (-g_2 s_\phi T_2^3) \hat{Z}'_\mu] P_L f_{L(3)}.
\end{aligned} \tag{A.13}$$

The next step is to rearrange the couplings in the neutral sector of Eqs. (A.12, A.13) in terms of g_L , g_Y and e

$$\begin{aligned}
g_1 s_\phi c_\theta T_1^3 - g_X s_\theta X &= \sqrt{g_L^2 + g_Y^2} (T_1^3 - s_\theta^2 (T_1^3 + X)), \\
g_1 s_\phi s_\theta T_1^3 + g_X c_\theta X &= e (T_1^3 + X),
\end{aligned} \tag{A.14}$$

$$\begin{aligned}
g_2 c_\phi c_\theta T_2^3 - g_X s_\theta X &= \sqrt{g_L^2 + g_Y^2} (T_2^3 - s_\theta^2 (T_2^3 + X)), \\
g_2 c_\phi s_\theta T_2^3 + g_X c_\theta X &= e (T_2^3 + X),
\end{aligned} \tag{A.15}$$

hence using Eqs. (A.14, A.15), the kinetic terms of the left-handed fermions take the following form

$$\begin{aligned}
\bar{f}_{L(1,2)} i \gamma^\mu D_\mu f_{L(1,2)} &\supset \bar{f}_{(1,2)} \gamma^\mu \left[\frac{g_1}{\sqrt{2}} (W_{1\mu}^+ T_1^+ + W_{1\mu}^- T_1^-) \right] P_L f_{(1,2)} \\
&+ \bar{f}_{(1,2)} \gamma^\mu [e (T_1^3 + X) A_\mu + \sqrt{g_L^2 + g_Y^2} (T_1^3 - s_\theta^2 (T_1^3 + X)) \hat{Z}_\mu + (g_1 c_\phi T_1^3) \hat{Z}'_\mu] P_L f_{(1,2)},
\end{aligned} \tag{A.16}$$

and

$$\begin{aligned}
\bar{f}_{L(3)} i \gamma^\mu D_\mu f_{L(3)} &\supset \bar{f}_{(3)} \gamma^\mu \left[\frac{g_2}{\sqrt{2}} (W_{2\mu}^+ T_2^+ + W_{2\mu}^- T_2^-) \right] P_L f_{(3)} \\
&+ \bar{f}_{(3)} \gamma^\mu [e (T_2^3 + X) A_\mu + \sqrt{g_L^2 + g_Y^2} (T_2^3 - s_\theta^2 (T_2^3 + X)) \hat{Z}_\mu + (-g_2 s_\phi T_2^3) \hat{Z}'_\mu] P_L f_{(3)}.
\end{aligned} \tag{A.17}$$

Finally by applying the modified Gell-Mann-Nishijima formula

$$Q(f) = T_1^3(f) + T_2^3(f) + X(f) = T_L^3(f) + Y(f), \tag{A.18}$$

and the fact that $W_{1\mu}^\pm = s_\phi \hat{W}_\mu^\pm + c_\phi \hat{W}'_\mu^\pm$ and that $W_{2\mu}^\pm = c_\phi \hat{W}_\mu^\pm - s_\phi \hat{W}'_\mu^\pm$ one finds

$$\begin{aligned}
\bar{f}_{L(1,2)} i \gamma^\mu D_\mu f_{L(1,2)} &\supset \bar{f}_{(1,2)} \gamma^\mu \left[\frac{g_L}{\sqrt{2}} (\hat{W}_\mu^+ T_L^{+,f} + \hat{W}_\mu^- T_L^{-,f}) + \frac{g_1 c_\phi}{\sqrt{2}} (\hat{W}'_\mu^{+,f} T_L^{+,f} + \hat{W}'_\mu^{-,f} T_L^{-,f}) \right] P_L f_{(1,2)} \\
&+ \bar{f}_{(1,2)} \gamma^\mu [e Q^f A_\mu + \sqrt{g_L^2 + g_Y^2} (T_L^{3,f} - s_\theta^2 Q^f) \hat{Z}_\mu + (g_1 c_\phi T_L^{3,f}) \hat{Z}'_\mu] P_L f_{(1,2)},
\end{aligned} \tag{A.19}$$

and

$$\begin{aligned}
\bar{f}_{L(3)} i \gamma^\mu D_\mu f_{L(3)} &\supset \bar{f}_{(3)} \gamma^\mu \left[\frac{g_L}{\sqrt{2}} (\hat{W}_\mu^+ T_L^{+,f} + \hat{W}_\mu^- T_L^{-,f}) - \frac{g_2 s_\phi}{\sqrt{2}} (\hat{W}'_\mu^{+,f} T_L^{+,f} + \hat{W}'_\mu^{-,f} T_L^{-,f}) \right] P_L f_{(1,2)} \\
&+ \bar{f}_{(3)} \gamma^\mu [e Q^f A_\mu + \sqrt{g_L^2 + g_Y^2} (T_L^{3,f} - s_\theta^2 Q^f) \hat{Z}_\mu + (-g_2 s_\phi T_L^{3,f}) \hat{Z}'_\mu] P_L f_{(3)}.
\end{aligned} \tag{A.20}$$

Accordingly, one can easily find the kinetic terms for the right-handed fermions

$$\begin{aligned}\bar{f}_R i \gamma^\mu D_\mu f_R &= \bar{f}_R i \gamma^\mu (\partial_\mu - i g_X X X_\mu) f_R \\ &\supset \bar{f}_R \gamma^\mu (c_\theta g_X X A_\mu - s_\theta g_X X \hat{Z}_\mu) f_R \\ &= \bar{f} \gamma^\mu (e Q^f A_\mu - \sqrt{g_L^2 + g_Y^2} s_\theta^2 Q^f \hat{Z}_\mu) P_R f.\end{aligned}\quad (\text{A.21})$$

Thus following Eq. (1.31) the fermion kinetic Lagrangian reads

$$\begin{aligned}\mathcal{L}_{fermion} &= \bar{f}_L i \gamma^\mu D_\mu f_L + \bar{f}_R i \gamma^\mu D_\mu f_R \\ &\supset \bar{f} \gamma^\mu [e Q^f A_\mu + \frac{g_L}{\sqrt{2}} (\hat{W}_\mu^+ T_L^{+,f} + \hat{W}_\mu^- T_L^{-,f}) P_L + \sqrt{g_L^2 + g_Y^2} (T_L^{3,f} P_L - s_\theta^2 Q^f) \hat{Z}_\mu] f \\ &+ \bar{f}_{(1,2)} \gamma^\mu [\frac{g_1 c_\phi}{\sqrt{2}} (\hat{W}'_\mu{}^+ T_L^{+,f} + \hat{W}'_\mu{}^- T_L^{-,f}) + g_1 c_\phi (T_L^{3,f}) \hat{Z}'_\mu] P_L f_{(1,2)} \\ &- \bar{f}_{(3)} \gamma^\mu [\frac{g_2 s_\phi}{\sqrt{2}} (\hat{W}'_\mu{}^+ T_L^{+,f} + \hat{W}'_\mu{}^- T_L^{-,f}) + g_2 s_\phi (T_L^{3,f}) \hat{Z}'_\mu] P_L f_{(3)},\end{aligned}\quad (\text{A.22})$$

or in compact form

$$\mathcal{L}_{fermion} = \bar{f}_L i \gamma^\mu D_\mu f_L + \bar{f}_R i \gamma^\mu D_\mu f_R \supset \mathcal{L}_{EM} + \mathcal{L}_{NC} + \mathcal{L}_{CC}, \quad (\text{A.23})$$

where the EM interaction Lagrangian \mathcal{L}_{EM} , the neutral weak interaction Lagrangian \mathcal{L}_{NC} and the charged weak interaction Lagrangian \mathcal{L}_{CC} are defined as follows

$$\begin{aligned}\mathcal{L}_{EM} &= J_\mu A^\mu, \\ \mathcal{L}_{NC} &= J_\mu^0 \hat{Z}^\mu + K_\mu^0 \hat{Z}'^\mu, \\ \mathcal{L}_{CC} &= J_\mu^+ \hat{W}^{+\mu} + J_\mu^- \hat{W}^{-\mu} + K_\mu^+ \hat{W}'^{+\mu} + K_\mu^- \hat{W}'^{-\mu},\end{aligned}\quad (\text{A.24})$$

and the EM current J_μ , the neutral weak currents J_μ^0, K_μ^0 and the charged weak currents J_μ^\pm, K_μ^\pm are defined as follows

$$\begin{aligned}J_\mu &= e \sum_f Q^f \bar{f} \gamma_\mu f, \\ J_\mu^0 &= \sqrt{g_L^2 + g_Y^2} \sum_f [(T_L^{3,f} - s_\theta^2 Q^f) P_L - s_\theta^2 Q^f P_R] \bar{f} \gamma_\mu f, \\ J_\mu^+ &= \frac{g_L}{\sqrt{2}} \sum_f T_L^{+,f} P_L \bar{f} \gamma_\mu f,\end{aligned}\quad (\text{A.25})$$

$$K_\mu^0 = g_1 c_\phi (T_L^{3,f} P_L) \bar{f}_{(1,2)} \gamma_\mu f_{(1,2)} - g_2 s_\phi (T_L^{3,f} P_L) \bar{f}_3 \gamma_\mu f_3, \quad (\text{A.26})$$

$$K^\pm = \frac{g_1 c_\phi}{\sqrt{2}} (T_L^{\pm,f} P_L) \bar{f}_{(1,2)} \gamma_\mu f_{(1,2)} - \frac{g_1 s_\phi}{\sqrt{2}} (T_L^{\pm,f} P_L) \bar{f}_3 \gamma_\mu f_3.$$

Inverting Eqs. (1.14, 1.15) one obtains

$$\hat{Z}_\mu (\hat{W}_\mu^\pm) \equiv Z_\mu (W_\mu^\pm) + \frac{\delta m_{\hat{Z}(\hat{W})}^2}{m_{\hat{Z}'(\hat{W}')}^2} Z'_\mu (W_\mu'^\pm), \quad (\text{A.27})$$

$$\hat{Z}'_\mu (\hat{W}_\mu'^\pm) \equiv -\frac{\delta m_{\hat{Z}(\hat{W})}^2}{m_{\hat{Z}'(\hat{W}')}^2} Z_\mu (W_\mu^\pm) + Z'_\mu (W_\mu'^\pm).$$

Inserting Eq. (A.27) in Eq. (A.22) one obtains for the neutral sector

$$\begin{aligned} & \bar{f} \gamma^\mu [\sqrt{g_L^2 + g_Y^2} (-s_\theta^2 Q^f)] (Z_\mu + \frac{\delta m_{\hat{Z}}^2}{m_{\hat{Z}'}^2} Z'_\mu) P_R f \\ & + \bar{f}_{(1,2)} \gamma^\mu [\sqrt{g_L^2 + g_Y^2} (T_L^{3,f} - s_\theta^2 Q^f)] (Z_\mu + \frac{\delta m_{\hat{Z}}^2}{m_{\hat{Z}'}^2} Z'_\mu) + g_1 c_\phi T_L^{3,f} (-\frac{\delta m_{\hat{Z}}^2}{m_{\hat{Z}'}^2} Z_\mu + Z'_\mu) P_L f_{(1,2)} \\ & + \bar{f}_{(3)} \gamma^\mu [\sqrt{g_L^2 + g_Y^2} (T_L^{3,f} - s_\theta^2 Q^f)] (Z_\mu + \frac{\delta m_{\hat{Z}}^2}{m_{\hat{Z}'}^2} Z'_\mu) - g_2 s_\phi T_L^{3,f} (-\frac{\delta m_{\hat{Z}}^2}{m_{\hat{Z}'}^2} Z_\mu + Z'_\mu) P_L f_{(3)}. \end{aligned}$$

Thus, the new neutral current Lagrangian after the second SB stage, displaying how the SM interactions are modified by the presence of the new neutral resonance, is given by

$$\begin{aligned} \mathcal{L}_{NC}^{Z'} &= [\frac{\delta m_{\hat{Z}}^2}{m_{\hat{Z}'}^2} \sqrt{g_L^2 + g_Y^2} [(T_L^{3,f} - s_\theta^2 Q^f) P_L - s_\theta^2 Q^f P_R] \bar{f} \gamma^\mu f \\ & + g_1 c_\phi (T_L^{3,f} P_L) \bar{f}_{(1,2)} \gamma^\mu f_{(1,2)} - g_2 s_\phi (T_L^{3,f} P_L) \bar{f}_3 \gamma^\mu f_3] Z'_\mu \\ & = [\frac{\delta m_{\hat{Z}}^2}{m_{\hat{Z}'}^2} J^{0\mu} + K^{0\mu}] Z'_\mu. \end{aligned} \quad (\text{A.28})$$

Similarly, for the charged sector in Eq. (A.22)

$$\begin{aligned} & \bar{f}_{(1,2)} \gamma^\mu [\frac{g_L}{\sqrt{2}} (W_\mu^+ + \frac{\delta m_{\hat{W}}^2}{m_{\hat{W}'}^2} W_\mu'^+) T_L^{+,f} + \frac{g_1 c_\phi}{\sqrt{2}} (-\frac{\delta m_{\hat{W}}^2}{m_{\hat{W}'}^2} W_\mu^+ + W_\mu'^+) T_L^{+,f} + (+ \longleftrightarrow -)] P_L f_{(1,2)} \\ & + \bar{f}_{(3)} \gamma^\mu [\frac{g_L}{\sqrt{2}} (W_\mu^+ + \frac{\delta m_{\hat{W}}^2}{m_{\hat{W}'}^2} W_\mu'^+) T_L^{+,f} - \frac{g_2 s_\phi}{\sqrt{2}} (-\frac{\delta m_{\hat{W}}^2}{m_{\hat{W}'}^2} W_\mu^+ + W_\mu'^+) T_L^{+,f} + (+ \longleftrightarrow -)] P_L f_{(3)}. \end{aligned}$$

Hence, the new charged current Lagrangian reads

$$\begin{aligned}
\mathcal{L}_{CC}^{W'} &= \left[\frac{\delta m_{\hat{W}}^2}{m_{\hat{W}'}^2} \frac{g_L}{\sqrt{2}} T_L^{+,f} P_L \bar{f} \gamma_\mu f \right. \\
&\quad \left. + g_1 c_\phi (T_L^{3,f} P_L) \bar{f}_{(1,2)} \gamma_\mu f_{(1,2)} - g_2 s_\phi (T_L^{3,f} P_L) \bar{f}_3 \gamma_\mu f_3 \right] W_\mu'^+ + (+ \longleftrightarrow -) \\
&= \left[\frac{\delta m_{\hat{W}}^2}{m_{\hat{W}'}^2} J^{+\mu} + K^{+\mu} \right] W_\mu'^+ + (+ \longleftrightarrow -). \tag{A.29}
\end{aligned}$$

In order to obtain the couplings of Eq. (2.1) for the NU model, we first solve the equations for the SM-like and the new charged currents:

$$\begin{aligned}
J_\mu^+ &= \frac{g_L}{\sqrt{2}} \sum_f T_L^{+,f} P_L \bar{f} \gamma_\mu f \\
&= \frac{g_L}{\sqrt{2}} (\bar{L}_{(1,2,3)} \gamma_\mu T_L^{+,L} P_L L_{(1,2,3)} + \bar{Q}_{(1,2,3)} \gamma_\mu T_L^{+,Q} P_L Q_{(1,2,3)}) \\
&= \frac{g_L}{\sqrt{2}} (\bar{\nu}_{(1,2,3)} \gamma_\mu P_L e_{(1,2,3)} + \bar{u}_{(1,2,3)} \gamma_\mu P_L d_{(1,2,3)}), \tag{A.30}
\end{aligned}$$

$$\begin{aligned}
K_\mu^+ &= \frac{g_1 c_\phi}{\sqrt{2}} (T_L^{+,f} P_L) \bar{f}_{(1,2)} \gamma_\mu f_{(1,2)} - \frac{g_1 s_\phi}{\sqrt{2}} (T_L^{+,f} P_L) \bar{f}_3 \gamma_\mu f_3 \\
&= \frac{g_1 c_\phi}{\sqrt{2}} (\bar{L}_{(1,2)} \gamma_\mu T_L^{+,L} P_L L_{(1,2)} + \bar{Q}_{(1,2)} \gamma_\mu T_L^{+,Q} P_L Q_{(1,2)}) \\
&\quad - \frac{g_1 s_\phi}{\sqrt{2}} (\bar{L}_{(3)} \gamma_\mu T_L^{+,L} P_L L_{(3)} + \bar{Q}_{(3)} \gamma_\mu T_L^{+,Q} P_L Q_{(3)}) \\
&= \frac{g_1 c_\phi}{\sqrt{2}} (\bar{\nu}_{(1,2)} \gamma_\mu P_L e_{(1,2)} + \bar{u}_{(1,2)} \gamma_\mu P_L d_{(1,2)}) \\
&\quad - \frac{g_1 s_\phi}{\sqrt{2}} (\bar{\nu}_{(3)} \gamma_\mu P_L e_{(3)} + \bar{u}_{(3)} \gamma_\mu P_L d_{(3)}). \tag{A.31}
\end{aligned}$$

Then, inserting the result in Eq. (A.29) leads to

$$\begin{aligned}
 \mathcal{L}_{CC}^{W'} &= \frac{g_L}{2} [\bar{V}_{(1,2)} \gamma^\mu \left(\frac{g_1 c_\phi}{g_L} - \frac{g_1 g_2 s_\phi^2 v^2}{(g_1^2 + g_2^2) u^2} \right) P_L e_{(1,2)} \\
 &\quad + \bar{u}_{(1,2)} \gamma^\mu \left(\frac{g_1 c_\phi}{g_L} - \frac{g_1 g_2 s_\phi^2 v^2}{(g_1^2 + g_2^2) u^2} \right) P_L d_{(1,2)} \\
 &\quad + \bar{V}_{(3)} \gamma^\mu \left(-\frac{g_2 s_\phi}{g_L} - \frac{g_1 g_2 s_\phi^2 v^2}{(g_1^2 + g_2^2) u^2} \right) P_L e_{(3)} \\
 &\quad + \bar{u}_{(3)} \gamma^\mu \left(-\frac{g_2 s_\phi}{g_L} - \frac{g_1 g_2 s_\phi^2 v^2}{(g_1^2 + g_2^2) u^2} \right) P_L d_{(3)},
 \end{aligned} \tag{A.32}$$

where $\frac{\delta m_{\hat{W}}^2}{m_{\hat{W}'}^2} = -\frac{g_1 g_2 s_\phi^2 v^2}{(g_1^2 + g_2^2) u^2}$.

The comparison of Eq. (A.32) with Eq. (1.35) leads to

$$\begin{aligned}
 C_{q^{(\ell)(1,2),L} }^{W'} &= \frac{g_1 c_\phi}{g_L} - \frac{g_1 g_2 s_\phi^2 v^2}{(g_1^2 + g_2^2) u^2}, \\
 C_{q^{(\ell)(1,2),R} }^{W'} &= 0, \\
 C_{q^{(\ell)(3),L} }^{W'} &= -\frac{g_2 s_\phi}{g_L} - \frac{g_1 g_2 s_\phi^2 v^2}{(g_1^2 + g_2^2) u^2}, \\
 C_{q^{(\ell)(3),R} }^{W'} &= 0.
 \end{aligned} \tag{A.33}$$

The last step consists of solving Eq. (1.18) for the VEV u expressed in terms of the resonance mass M and the mixing angle ϕ , which we consequently substitute into Eq. (A.33). This leads to

$$\begin{aligned}
 C_{q^{(\ell)(1,2),L} }^{W'} &= \frac{1}{t_\phi} - c_\theta \mathcal{E}(t_\phi, m), \\
 C_{q^{(\ell)(1,2),R} }^{W'} &= 0, \\
 C_{q^{(\ell)(3),L} }^{W'} &= -t_\phi - c_\theta \mathcal{E}(t_\phi, m), \\
 C_{q^{(\ell)(3),R} }^{W'} &= 0,
 \end{aligned} \tag{A.34}$$

where $\frac{g_1 c_\phi}{g_L} = \frac{1}{t_\phi}$ and $-\frac{g_2 s_\phi}{g_L} = -t_\phi$.

Accordingly, by solving the equations for the SM-like and the new neutral currents and inserting the results in Eq. (A.28) and comparing with Eq. (1.35) we obtain

$$\begin{aligned}
C_{q^{(\ell)}(1,2),L}^{Z'} &= \frac{g_1 c_\phi c_\theta}{g_L} (T_L^{3,q^{(\ell)}}) + \frac{c_\theta g_1 g_2 s_\phi^2 v^2}{g_L (g_1^2 + g_2^2) u^2} \sqrt{g_L^2 + g_Y^2} (T_L^{3,q^{(\ell)}} + Q^{q^{(\ell)}} s_\theta^2), \\
C_{q^{(\ell)}(1,2),R}^{Z'} &= \frac{c_\theta g_1 g_2 s_\phi^2 v^2}{g_L (g_1^2 + g_2^2) u^2} \sqrt{g_L^2 + g_Y^2} (Q^{q^{(\ell)}} s_\theta^2), \\
C_{q^{(\ell)}(3),L}^{Z'} &= -\frac{g_2 s_\phi c_\theta}{g_L} (T_L^{3,q^{(\ell)}}) + \frac{c_\theta g_1 g_2 s_\phi^2 v^2}{g_L (g_1^2 + g_2^2) u^2} \sqrt{g_L^2 + g_Y^2} (T_L^{3,q^{(\ell)}} + Q^{q^{(\ell)}} s_\theta^2), \\
C_{q^{(\ell)}(3),R}^{Z'} &= \frac{c_\theta g_1 g_2 s_\phi^2 v^2}{g_L (g_1^2 + g_2^2) u^2} \sqrt{g_L^2 + g_Y^2} (Q^{q^{(\ell)}} s_\theta^2).
\end{aligned} \tag{A.35}$$

Hence, in a similar way as in Eq. (A.34), the couplings of the Z' to the SM fermions read for the NU model

$$\begin{aligned}
C_{q^{(\ell)}(1,2),L}^{Z'} &= c_\theta \frac{1}{t_\phi} T_L^{3,q^{(\ell)}} + \varepsilon(t_\phi, m) (T_L^{3,q^{(\ell)}} + Q^{q^{(\ell)}} s_\theta^2), \\
C_{q^{(\ell)}(1,2),R}^{Z'} &= \varepsilon(t_\phi, m) Q^{q^{(\ell)}} s_\theta^2, \\
C_{q^{(\ell)}(3),L}^{Z'} &= -c_\theta t_\phi T_L^{3,q^{(\ell)}} + \varepsilon(t_\phi, m) (T_L^{3,q^{(\ell)}} + Q^{q^{(\ell)}} s_\theta^2), \\
C_{q^{(\ell)}(3),R}^{Z'} &= \varepsilon(t_\phi, m) Q^{q^{(\ell)}} s_\theta^2.
\end{aligned} \tag{A.36}$$

B. RecoLa2

B.1 Amplitude structure in RecoLa

RecoLa uses the so-called colour-flow decomposition to evaluate the amplitude of a given process. This method has a physical interpretation in terms of the flow of colour, which makes it ideal for merging the hard-scattering cross section with shower Monte-Carlo programs.

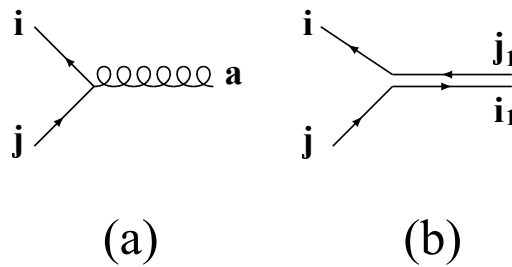


Figure B.1: Quark-gluon vertex in the fundamental representation (a) and in the colour-flow representation where the arrow tracks the flow of colour (b).

Usually the colour index a of the gluon is described in the adjoint representation of $SU(3)$ and can take the values $1, \dots, 8$. However, since the adjoint representation is isomorphic to the tensor product $3 \otimes \bar{3}$ of the fundamental and anti-fundamental representations of $SU(3)$, the gluon's colour coordinate can be replaced by a couple of indices $i, j = 1, 2, 3$. Thus, in the colour-flow representation, each gluon line is replaced by a double line, while quarks sustain the usual colour index $i = 1, 2, 3$ and are represented by a single line, see Figure B.1. Following this decomposition, the amplitude can be written as

$$\mathcal{A} \rightarrow \mathcal{A}_{j_1 \dots j_k}^{i_1 \dots i_k}[h_1, \dots, h_k], \quad (\text{B.1})$$

where k is the number of external particles and h_n ($n = 1, \dots, k$) represents the helicity of the n^{th} external leg. The upper index i transforms under the fundamental representation of $SU(3)$ and can take the values $1, 2, 3$ for gluons, incoming anti-quarks and outgoing quarks, while it vanishes for colourless particles, incoming quarks and outgoing anti-quarks. Furthermore, the lower index j follows the conjugate of the fundamental representation of $SU(3)$ and is absent for colourless particles, incoming anti-quarks and outgoing quarks, while it takes the values $1, 2, 3$ for gluons, incoming quarks and outgoing anti-quarks. The colour flows from the lower index j to the upper index i , as can be seen in Figure B.1 (b). Finally, in order to forbid a $3 \otimes \bar{3}$ gluon

from being in a singlet state¹, the following condition is required

$$\sum_{i_m, j_m} \delta_{j_m}^{i_m} \mathcal{A}_{j_1 \dots j_m \dots j_k}^{i_1 \dots i_m \dots i_k} [h_1, \dots, h_k] = 0, \quad (\text{B.2})$$

where m is a gluon.

In the colour-flow formalism, the colour part in the Feynman rules is described by products of Kronecker δ_s , see Figure 1 of [173]. This means that the colour structure of the amplitude can be expressed as a linear combination of all possible products of Kronecker δ_s carrying the colour indices of the external particles

$$\mathcal{A}_{j_1 \dots j_k}^{i_1 \dots i_k} [h_1, \dots, h_k] = \sum_P \delta_{j_{P(1)}}^{i_1} \delta_{j_{P(2)}}^{i_2} \dots \delta_{j_{P(k)}}^{i_k} \mathcal{A}_{P(1)P(2)\dots P(k)} [h_1, \dots, h_k], \quad (\text{B.3})$$

where $\mathcal{A}_{P(1)P(2)\dots P(k)} [h_1, \dots, h_k]$ are known as the structure-dressed amplitudes, and the sum runs over all possible permutations P of the labels of external gluons, incoming quarks, and outgoing anti-quarks.

To illustrate Eq. (B.3) let us take the process $g\bar{d} \rightarrow t\bar{t}\bar{d}$ as an example. The first element is a gluon and is expressed by an upper index (i_1) and a lower index (j_1). The second component is an incoming anti-quark and will be represented by an upper index (i_2). The third constituent is an outgoing quark which is equivalent to an upper index (i_3). Finally, the fourth and fifth elements of the process are both outgoing anti-quarks and will be both taken into account through two lower indices (j_4) and (j_5) respectively. Thus, since we have 3 lower indices, the number of possible permutations is 3! and the decomposition is given by

$$\begin{aligned} \mathcal{A}_{j_1 j_4 j_5}^{i_1 i_2 i_3} &= \delta_{j_1}^{i_1} \delta_{j_4}^{i_2} \delta_{j_5}^{i_3} \mathcal{A}_{145} + \delta_{j_1}^{i_1} \delta_{j_5}^{i_2} \delta_{j_4}^{i_3} \mathcal{A}_{154} + \delta_{j_4}^{i_1} \delta_{j_1}^{i_2} \delta_{j_5}^{i_3} \mathcal{A}_{415} \\ &+ \delta_{j_4}^{i_1} \delta_{j_5}^{i_2} \delta_{j_1}^{i_3} \mathcal{A}_{451} + \delta_{j_5}^{i_1} \delta_{j_1}^{i_2} \delta_{j_4}^{i_3} \mathcal{A}_{514} + \delta_{j_5}^{i_1} \delta_{j_4}^{i_2} \delta_{j_1}^{i_3} \mathcal{A}_{541}. \end{aligned} \quad (\text{B.4})$$

Using RecoLa the user can calculate the Born and one-loop contributions to the structure-dressed amplitudes $\mathcal{A}^{(\vec{c}, \vec{h})}$ for all the values of the vectors \vec{c} and \vec{h} of the external legs of the process. $\mathcal{A}^{(\vec{c}, \vec{h})}$ is the compressed form of $\mathcal{A}_{P(1)P(2)\dots P(k)} [h_1, \dots, h_k]$ where \vec{c} is a k -dimensional vector with the components c_1, c_2, \dots, c_k are different than zero only if the external particle is a gluon, an incoming anti-quark or an outgoing quark, and \vec{h} is the helicity vector representing the h_1, \dots, h_k components. Moreover, RecoLa can also compute the squared amplitudes at the

¹The colour singlet state is $(1\bar{1} + 2\bar{2} + 3\bar{3})/\sqrt{3}$. QCD is based on the $SU(3)$ colour symmetry which has 8 generators and therefore 8 (not 9) gauge field quanta: there is no room for a singlet gluon in an $SU(3)$ gauge theory.

Born and the one-loop level, summed over helicities and colours of the outgoing particles and averaged over helicities and colours of the incoming ones.

B.2 Input parameters of SMWZp

The complete set of the external input parameters of the SMWZp is shown Table B.1, where, in addition to the parameters described in Section 3.3.1, we have k_G that allows to disable the contributions from the non-diagonal goldstone bosons G'_0 and G'^{\pm} . By default it is set to 1 and should never have any value other than 0 or 1. The couplings of these new goldstone bosons to quarks and leptons need to be in accordance with the corresponding Z' and W' couplings to leptons and quarks, which is guaranteed by construction (i.e. they get scaled by the same k_Z and k_W factors). α_W and α_S are the EW and strong coupling constants respectively. The rest of the parameters are the masses and the widths of the particles of the SMWZp model.

In order to change the value of any of the previous parameters using the Fortran programming language one needs to call the subroutine `set_parameter_rcl(param, value)`, where `param` is of type `character` and can be any of the parameters of Table B.1 and `value` is of type `complex(dp)`. An imaginary part of `value` can lead to undefined behaviour, and `value` should be real even though it is of type `complex(dp)`. For instance, to set the α_S parameter to 0.118 one needs to call `set_parameter_rcl(aS, cplx(0.118d0, 0d0, dp))`.

B.3 The anatomy of the SMWZp amplitudes within RecoLa2

Here we describe in more details the anatomy of the squared amplitudes of the SMWZp. As discussed in Section 3.3.2, they are computed in RecoLa2 based on the powers in $\sqrt{\alpha_S}$ and $\sqrt{\alpha_W}$, or in RecoLa2's syntax on the powers in "QCD QED WZP".

At the Born level the squared amplitude will have exactly 4 vertices in our calculation. Since we do EW top-pair production, no QCD vertices are allowed, meaning that we will have either "0 QCD 4 QED 0 WZP" or "0 QCD 4 QED 2 WZP" or "0 QCD 4 QED 4 WZP" (again, 4 QED 4 WZP do not mean 8 vertices, but 4 EW vertices of which 4 are of BSM nature) as can be seen in Figure B.2. However, as discussed previously, since we include t-channel diagrams mediated by W , W' , or Z' , and since these diagrams would interfere with QCD diagrams, we could also have squared amplitudes with "2 QCD 2 QED 0 WZP" and "2 QCD 2 QED 2 WZP", see Figure B.3.

Parameters	RecoLa identifier
$k_{W,+}, k_{W,-}$	kWR, kWL
$k_{Z,+}, k_{Z,-}$	kZR, kZL
$C_{W,+}^l$	CWlR1x1, CWlR1x2, CWlR1x3, CWlR2x1, ..., CWlR3x2, CWlR3x3
$C_{W,-}^l$	CWlL1x1, CWlL1x2, CWlL1x3, CWlL2x1, ..., CWlL3x2, CWlL3x3
$C_{W,+}^q$	CWqR1x1, CWqR1x2, CWqR1x3, CWqR2x1, ..., CWqR3x2, CWqR3x3
$C_{W,-}^q$	CWqL1x1, CWqL1x2, CWqL1x3, CWqL2x1, ..., CWqL3x2, CWqL3x3
$C_{Z,+}^l$	CZlR1x1, CZlR1x2, CZlR1x3, CZlR2x1, ..., CZlR3x2, CZlR3x3
$C_{Z,-}^l$	CZlL1x1, CZlL1x2, CZlL1x3, CZlL2x1, ..., CZlL3x2, CZlL3x3
$C_{Z,+}^u$	CZuR1x1, CZuR1x2, CZuR1x3, CZuR2x1, ..., CZuR3x2, CZuR3x3
$C_{Z,-}^u$	CZuL1x1, CZuL1x2, CZuL1x3, CZuL2x1, ..., CZuL3x2, CZuL3x3
$C_{Z,+}^d$	CZdR1x1, CZdR1x2, CZdR1x3, CZdR2x1, ..., CZdR3x2, CZdR3x3
$C_{Z,-}^d$	CZdL1x1, CZdL1x2, CZdL1x3, CZdL2x1, ..., CZdL3x2, CZdL3x3
k_G	kG
α_W	aEW
α_S	aS
m_H, Γ_H	MH, WH
$m_{W'}, \Gamma_{W'}$	MWp, WWp
$m_{Z'}, \Gamma_{Z'}$	MZp, WZp
m_e	ME
m_μ, Γ_μ	MM, WM
m_τ, Γ_τ	MTA, WTA
m_u	MU
m_c, Γ_c	MC, WC
m_t, Γ_t	MT, WT
m_d	MD
m_s	MS
m_b, Γ_b	MB, WB
m_W, Γ_W	MW, WW
m_Z, Γ_Z	MZ, WZ

Table B.1: The external input parameters of the SMWZp model file and their identifier in RecoLa.

In Figure B.2 we show the pure EW squared Born amplitudes that enter in our calculation. The first block contains the pure SM diagrams and is labeled as 040 meaning “ 0 QCD 0 QED 0 WZP”. The first line involves 2 s-channel γ or Z mediated diagrams, in this case the initial state quarks should be of the same type (no flavour-mixing). The second line has 2 t-channel

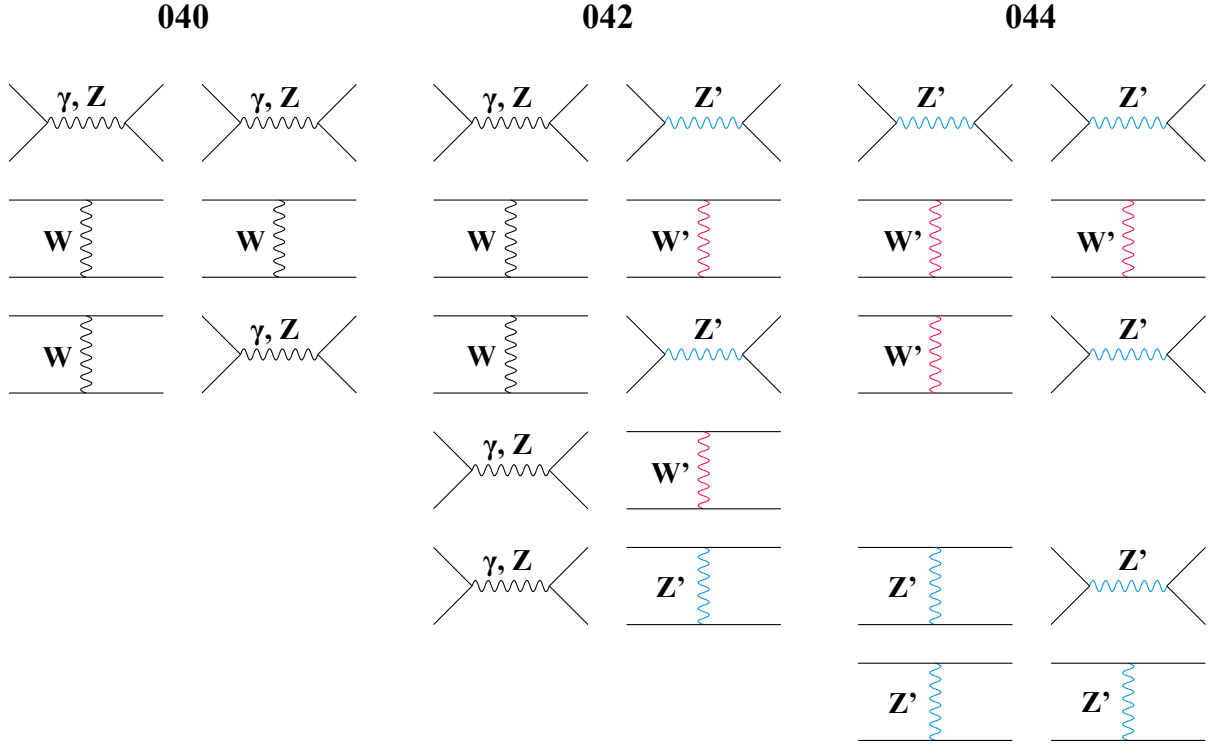


Figure B.2: The pure EW diagrams that interfere at the Born level in our calculation.

W mediated diagrams, where in this case the initial state quarks can be of different nature but should be of down type. The third line has 1 t-channel W mediated diagram and 1 s-channel γ or Z mediated diagram, here no flavour-mixing is allowed because of the latter diagram and only down type quarks are authorised due to the first diagram. The second block shows the squared amplitudes that involve 1 SM diagram and 1 BSM diagram (042). The first line shows the interference between a s-channel γ or Z mediated diagram and a s-channel Z' mediated diagram, here due to the first diagram, the Z' has to be diagonal. The second line has two t-channel diagrams one of which is mediated by a W and the other one by W' , as in the 040 case the initial state quarks can only be of down type and flavour-mixing is allowed. The third line involve a t-channel W diagram interfering with a s-channel Z' diagram, and as in the previous line, the initial state quarks can have flavour-mixing only within the down family. The fourth line consists of one s-channel γ or Z mediated diagram and one t-channel W' mediated diagram where no flavour-mixing is allowed and only down type quarks are authorised. The last line of the second block has again a s-channel diagram with either a photon or a Z -boson propagator and a t-channel Z' mediated diagram this time, here $q'\bar{q}$ can only be of up type and no flavour-mixing is accepted. Finally the last block (044) involves pure BSM diagrams. The first line has 2 s-channel Z' diagrams where mixing and any type of quarks is allowed. The second line has 2 t-channel W' diagrams allowing for flavour-mixing within the down family. The third line contains one t-channel W' diagram and one s-channel Z' diagram, $q'\bar{q} \in \{d\bar{d}, s\bar{s}, b\bar{b}\}$.

The penultimate line involve one t-channel and one s-channel Z' and final line 2 t-channel Z' diagrams where in both cases the initial state quarks can only be of up type but flavour-mixing is accepted.

In Figure B.3 we show the squared amplitudes with one QCD and one EW diagrams that we consider in our calculation at the Born level. The first block (220) has only one squared amplitude with one s-channel gluon mediated diagram and one t-channel W diagram where the initial state should be diagonal and only down type quarks are allowed. the second block (222) consists of 2 squared amplitudes. The first one has, in addition to the s-channel QCD diagram, a t-channel W' diagram and thus only allow, as in 220, for down type diagonal initial state whereas the second amplitude has t-channel Z' diagram and only up type diagonal quarks are accepted in the initial state. In what follows, we show the squared amplitudes that could be calculated by

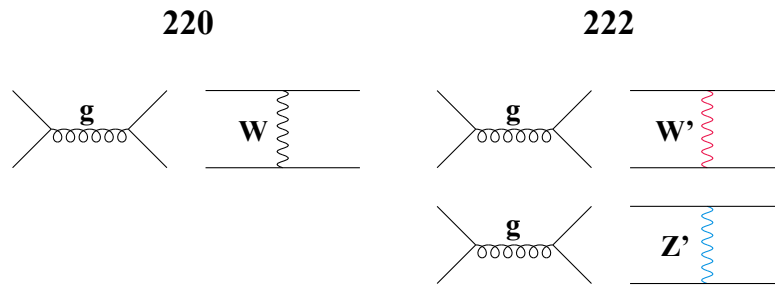


Figure B.3: Born level squared amplitudes including QCD and EW interference that we include in our calculation.

RecoLa2 within SMWZp for the 13 $q'\bar{q}$ ($2 \rightarrow 2$) sub-processes (we don't show $\gamma g \rightarrow t\bar{t}$ here even though, as discussed before, we take this contribution into account) that enter our calculation at LO and NLO. In particular, we show this for different contributions by including gradually the different mediators (γ , Z , W , Z' , and W'). This is visualised in 16 different tables where the first column consists of the initial state quark combinations for each set of mediators, the second column contains the possible LO squared amplitudes for each initial state based on the chosen propagators, and the third column involves also the squared amplitudes but at NLO. Whenever it appears in any of the tables, the term “does not exist” means that we can not ask RecoLa2 to compute the squared amplitude for this specific initial state where a particular mediators are chosen, for instance, one can not calculate a non-diagonal $t\bar{t}$ production when the Z -boson is the mediator as seen in Table B.2. Amplitudes in red indicate that we do not include these contribution in our calculation but RecoLa2 can calculate them. The bold font means that the contribution is negligible. Finally, n - Z' and d - Z' stand for a non-diagonal and a diagonal Z' -boson respectively.

γ, Z	LO			NLO	
$d\bar{b}$	does not exist			does not exist	
$d\bar{s}$	does not exist			does not exist	
$d\bar{d}$	040	220	400	240	420
$u\bar{c}$	does not exist			does not exist	
$u\bar{u}$	040	220	400	240	420
$s\bar{b}$	does not exist			does not exist	
$s\bar{s}$	040	220	400	240	420
$s\bar{d}$	does not exist			does not exist	
$c\bar{c}$	040	220	400	240	420
$c\bar{u}$	does not exist			does not exist	
$b\bar{b}$	040	220	400	240	420
$b\bar{s}$	does not exist			does not exist	
$b\bar{d}$	does not exist			does not exist	

Table B.2: Squared amplitudes that can be calculated with RecoLa2 for 13 $q'\bar{q}$ ($2 \rightarrow 2$) sub-processes mediated by γ or Z -boson.

γ, Z, W	LO			NLO	
$d\bar{b}$	040			240	
$d\bar{s}$	040			240	
$d\bar{d}$	040	220	400	240	420
$u\bar{c}$					440
$u\bar{u}$	040	220	400	240	420
$s\bar{b}$	040			240	
$s\bar{s}$	040	220	400	240	420
$s\bar{d}$	040			240	
$c\bar{c}$	040	220	400	240	420
$c\bar{u}$					440
$b\bar{b}$	040	220	400	240	420
$b\bar{s}$	040			240	
$b\bar{d}$	040			240	

Table B.3: Same as Table B.2 but for sub-processes possibly mediated by $\gamma, Z,$ or W .

γ, Z, W'	LO	NLO
$d\bar{b}$	044	244
$d\bar{s}$	044	244
$d\bar{d}$	040 042 044 220 222 400	240 242 244 420 422
$u\bar{c}$		444
$u\bar{u}$	040 220 400	240 242 420 422
$s\bar{b}$	044	244
$s\bar{s}$	040 042 044 220 222 400	240 242 244 420 422
$s\bar{d}$	044	244
$c\bar{c}$	040 220 400	240 242 420 422
$c\bar{u}$		444
$b\bar{b}$	040 042 044 220 222 400	240 242 244 420 422
$b\bar{s}$	044	244
$b\bar{d}$	044	244

Table B.4: Same as Table B.2 but for sub-processes possibly mediated by $\gamma, Z,$ or W' .

$\gamma, Z, d-Z'$	LO	NLO
$d\bar{b}$	does not exist	does not exist
$d\bar{s}$	does not exist	does not exist
$d\bar{d}$	040 042 044 220 222 400	240 242 244 420 422
$u\bar{c}$	does not exist	does not exist
$u\bar{u}$	040 042 044 220 222 400	240 242 244 420 422
$s\bar{b}$	does not exist	does not exist
$s\bar{s}$	040 042 044 220 222 400	240 242 244 420 422
$s\bar{d}$	does not exist	does not exist
$c\bar{c}$	040 042 044 220 222 400	240 242 244 420 422
$c\bar{u}$	does not exist	does not exist
$b\bar{b}$	040 042 044 220 222 400	240 242 244 420 422
$b\bar{s}$	does not exist	does not exist
$b\bar{d}$	does not exist	does not exist

Table B.5: Same as Table B.2 but for sub-processes possibly mediated by $\gamma, Z,$ or a diagonal Z' .

$\gamma, Z, n-Z'$	<i>LO</i>	<i>NLO</i>
$d\bar{b}$		444
$d\bar{s}$		444
$d\bar{d}$	040 220 400	240 242 420 422
$u\bar{c}$	044	244
$u\bar{u}$	040 042 044 220 222 400	240 242 244 420 422
$s\bar{b}$		444
$s\bar{s}$	040 220 400	240 242 420 422
$s\bar{d}$		444
$c\bar{c}$	040 042 044 220 222 400	240 242 244 420 422
$c\bar{u}$	044	244
$b\bar{b}$	040 220 400	240 242 420 422
$b\bar{s}$		444
$b\bar{d}$		444

Table B.6: Same as Table B.2 but for sub-processes possibly mediated by γ , Z , or a non-diagonal Z' .

γ, Z, W, W'	<i>LO</i>	<i>NLO</i>
$d\bar{b}$	040 042 044	240 242 244
$d\bar{s}$	040 042 044	240 242 244
$d\bar{d}$	040 042 044 220 222 400	240 242 244 420 422
$u\bar{c}$		440 442 444
$u\bar{u}$	040 220 400	240 242 420 422
$s\bar{b}$	040 042 044	240 242 244
$s\bar{s}$	040 042 044 220 222 400	240 242 244 420 422
$s\bar{d}$	040 042 044	240 242 244
$c\bar{c}$	040 220 400	240 242 420 422
$c\bar{u}$		440 442 444
$b\bar{b}$	040 042 044 220 222 400	240 242 244 420 422
$b\bar{s}$	040 042 044	240 242 244
$b\bar{d}$	040 042 044	240 242 244

Table B.7: Same as Table B.2 but for sub-processes possibly mediated by γ , Z , W , or W' .

$\gamma, Z, n\text{-}Z',$ $d\text{-}Z'$	<i>LO</i>	<i>NLO</i>
$d\bar{b}$	044	244
$d\bar{s}$	044	244
$d\bar{d}$	040 042 044 220 222 400	240 242 244 420 422
$u\bar{c}$	044	244
$u\bar{u}$	040 042 044 220 222 400	240 242 244 420 422
$s\bar{b}$	044	244
$s\bar{s}$	040 042 044 220 222 400	240 242 244 420 422
$s\bar{d}$	044	244
$c\bar{c}$	040 042 044 220 222 400	240 242 244 420 422
$c\bar{u}$	044	244
$b\bar{b}$	040 042 044 220 222 400	240 242 244 420 422
$b\bar{s}$	044	244
$b\bar{d}$	044	244

Table B.8: Same as Table B.2 but for sub-processes possibly mediated by γ , Z , non-diagonal Z' , or a diagonal Z' .

$\gamma, Z, W,$ $d\text{-}Z'$	<i>LO</i>	<i>NLO</i>
$d\bar{b}$	040	240
$d\bar{s}$	040	240
$d\bar{d}$	040 042 044 220 222 400	240 242 244 420 422
$u\bar{c}$		440
$u\bar{u}$	040 042 044 220 222 400	240 242 244 420 422
$s\bar{b}$	040	240
$s\bar{s}$	040 042 044 220 222 400	240 242 244 420 422
$s\bar{d}$	040	240
$c\bar{c}$	040 042 044 220 222 400	240 242 244 420 422
$c\bar{u}$		440
$b\bar{b}$	040 042 044 220 222 400	240 242 244 420 422
$b\bar{s}$	040	240
$b\bar{d}$	040	240

Table B.9: Same as Table B.2 but for sub-processes possibly mediated by γ , Z , W , or a diagonal Z' .

$\gamma, Z, W, n-Z'$	<i>LO</i>	<i>NLO</i>
$d\bar{b}$	040	240 242
$d\bar{s}$	040	240 242
$d\bar{d}$	040 220 400	240 242 420 422
$u\bar{c}$	044	242 244
$u\bar{u}$	040 042 044 220 222 400	240 242 244 420 422
$s\bar{b}$	040	240 242
$s\bar{s}$	040 220 400	240 242 420 422
$s\bar{d}$	040	240 242
$c\bar{c}$	040 042 044 220 222 400	240 242 244 420 422
$c\bar{u}$	044	242 244
$b\bar{b}$	040 220 400	240 242 420 422
$b\bar{s}$	040	240 242
$b\bar{d}$	040	240 242

Table B.10: Same as Table B.2 but for sub-processes possibly mediated by γ, Z, W , or a non-diagonal Z' .

$\gamma, Z, W', d-Z'$	<i>LO</i>	<i>NLO</i>
$d\bar{b}$	044	244
$d\bar{s}$	044	244
$d\bar{d}$	040 042 044 220 222 400	240 242 244 420 422
$u\bar{c}$		444
$u\bar{u}$	040 042 044 220 222 400	240 242 244 420 422
$s\bar{b}$	044	244
$s\bar{s}$	040 042 044 220 222 400	240 242 244 420 422
$s\bar{d}$	044	244
$c\bar{c}$	040 042 044 220 222 400	240 242 244 420 422
$c\bar{u}$		444
$b\bar{b}$	040 042 044 220 222 400	240 242 244 420 422
$b\bar{s}$	044	244
$b\bar{d}$	044	244

Table B.11: Same as Table B.2 but for sub-processes possibly mediated by γ, Z, W' , or a diagonal Z' .

$\gamma, Z, W',$ $n-Z'$	<i>LO</i>	<i>NLO</i>
$d\bar{b}$	044	244
$d\bar{s}$	044	244
$d\bar{d}$	040 042 044 220 222 400	240 242 244 420 422
$u\bar{c}$	044	244
$u\bar{u}$	040 042 044 220 222 400	240 242 244 420 422
$s\bar{b}$	044	244
$s\bar{s}$	040 042 044 220 222 400	240 242 244 420 422
$s\bar{d}$	044	244
$c\bar{c}$	040 042 044 220 222 400	240 242 244 420 422
$c\bar{u}$	044	244
$b\bar{b}$	040 042 044 220 222 400	240 242 244 420 422
$b\bar{s}$	044	244
$b\bar{d}$	044	244

Table B.12: Same as Table B.2 but for sub-processes possibly mediated by $\gamma, Z, W',$ or a non-diagonal Z' .

$\gamma, Z, W,$ $n-Z', d-Z'$	<i>LO</i>	<i>NLO</i>
$d\bar{b}$	040 042 044	240 242 244
$d\bar{s}$	040 042 044	240 242 244
$d\bar{d}$	040 042 044 220 222 400	240 242 244 420 422
$u\bar{c}$	044	242 244
$u\bar{u}$	040 042 044 220 222 400	240 242 244 420 422
$s\bar{b}$	040 042 044	240 242 244
$s\bar{s}$	040 042 044 220 222 400	240 242 244 420 422
$s\bar{d}$	040 042 044	240 242 244
$c\bar{c}$	040 042 044 220 222 400	240 242 244 420 422
$c\bar{u}$	044	242 244
$b\bar{b}$	040 042 044 220 222 400	240 242 244 420 422
$b\bar{s}$	040 042 044	240 242 244
$b\bar{d}$	040 042 044	240 242 244

Table B.13: Same as Table B.2 but for sub-processes possibly mediated by $\gamma, Z, W,$ non-diagonal Z' , or a diagonal Z' .

$\gamma, Z, W',$ $n-Z', d-Z'$	<i>LO</i>	<i>NLO</i>
$d\bar{b}$	044	244
$d\bar{s}$	044	244
$d\bar{d}$	040 042 044 220 222 400	240 242 244 420 422
$u\bar{c}$	044	244
$u\bar{u}$	040 042 044 220 222 400	240 242 244 420 422
$s\bar{b}$	044	244
$s\bar{s}$	040 042 044 220 222 400	240 242 244 420 422
$s\bar{d}$	044	244
$c\bar{c}$	040 042 044 220 222 400	240 242 244 420 422
$c\bar{u}$	044	244
$b\bar{b}$	040 042 044 220 222 400	240 242 244 420 422
$b\bar{s}$	044	244
$b\bar{d}$	044	244

Table B.14: Same as Table B.2 but for sub-processes possibly mediated by γ, Z, W' , non-diagonal Z' , or a diagonal Z' .

$\gamma, Z, W,$ $d-Z', W'$	<i>LO</i>	<i>NLO</i>
$d\bar{b}$	040 042 044	240 242 244
$d\bar{s}$	040 042 044	240 242 244
$d\bar{d}$	040 042 044 220 222 400	240 242 244 420 422
$u\bar{c}$		440 442 444
$u\bar{u}$	040 042 044 220 222 400	240 242 244 420 422
$s\bar{b}$	040 042 044	240 242 244
$s\bar{s}$	040 042 044 220 222 400	240 242 244 420 422
$s\bar{d}$	040 042 044	240 242 244
$c\bar{c}$	040 042 044 220 222 400	240 242 244 420 422
$c\bar{u}$		440 442 444
$b\bar{b}$	040 042 044 220 222 400	240 242 244 420 422
$b\bar{s}$	040 042 044	240 242 244
$b\bar{d}$	040 042 044	240 242 244

Table B.15: Same as Table B.2 but for sub-processes possibly mediated by γ, Z, W , diagonal Z' , or W' .

$\gamma, Z, W,$ $n-Z', W'$	<i>LO</i>	<i>NLO</i>
$d\bar{b}$	040 042 044	240 242 244
$d\bar{s}$	040 042 044	240 242 244
$d\bar{d}$	040 042 044 220 222 400	240 242 244 420 422
$u\bar{c}$	044	242 244
$u\bar{u}$	040 042 044 220 222 400	240 242 244 420 422
$s\bar{b}$	040 042 044	240 242 244
$s\bar{s}$	040 042 044 220 222 400	240 242 244 420 422
$s\bar{d}$	040 042 044	240 242 244
$c\bar{c}$	040 042 044 220 222 400	240 242 244 420 422
$c\bar{u}$	044	242 244
$b\bar{b}$	040 042 044 220 222 400	240 242 244 420 422
$b\bar{s}$	040 042 044	240 242 244
$b\bar{d}$	040 042 044	240 242 244

Table B.16: Same as Table B.2 but for sub-processes possibly mediated by γ, Z, W , non-diagonal Z' , or W' .

$\gamma, Z, W,$ $n-Z', d-Z', W'$	<i>LO</i>	<i>NLO</i>
$d\bar{b}$	040 042 044	240 242 244
$d\bar{s}$	040 042 044	240 242 244
$d\bar{d}$	040 042 044 220 222 400	240 242 244 420 422
$u\bar{c}$	044	242 244
$u\bar{u}$	040 042 044 220 222 400	240 242 244 420 422
$s\bar{b}$	040 042 044	240 242 244
$s\bar{s}$	040 042 044 220 222 400	240 242 244 420 422
$s\bar{d}$	040 042 044	240 242 244
$c\bar{c}$	040 042 044 220 222 400	240 242 244 420 422
$c\bar{u}$	044	242 244
$b\bar{b}$	040 042 044 220 222 400	240 242 244 420 422
$b\bar{s}$	040 042 044	240 242 244
$b\bar{d}$	040 042 044	240 242 244

Table B.17: Same as Table B.2 but for sub-processes possibly mediated by γ, Z, W , non-diagonal Z' , diagonal Z' , or W' .

B.4 Couplings in RecoLa2 vs couplings in old PBZp

While, as can be seen from Eq. (3.7), RecoLa2 uses the left-right (LR) notation for the couplings between the gauge bosons and the fermions, the old PBZp package uses the axial-vector (AV) notation [174]

$$\mathcal{L}_{Z'} = \frac{g_W}{4c_W} Z'_\mu \left(C_V - C_A \gamma^5 \right) \bar{f} \gamma^\mu f, \quad (\text{B.5})$$

where $g_W = \frac{e}{s_W}$ is the $SU(2)_L$ gauge coupling. To exemplify the transition between the two notations we will use the Lagrangian that describes the diagonal interaction between Z' -boson and $\bar{d}d$. In RecoLa2 this can be derived from Eq. (3.7)

$$\mathcal{L}_{Z' d\bar{d}} = k_{Z,+} \frac{e}{s_W c_W} Z'_\mu \left(C_{Z,+}^d w^+ \right) \bar{d} \gamma^\mu d + k_{Z,-} \frac{e}{s_W c_W} Z'_\mu \left(C_{Z,-}^d w^- \right) \bar{d} \gamma^\mu d, \quad (\text{B.6})$$

using the fact that $w_\pm = (1 \pm \gamma^5)/2$ Eq. (B.6) can be rearranged as follows

$$\mathcal{L}_{Z' d\bar{d}} = \frac{e}{2s_W c_W} Z'_\mu \left(\left(k_{Z,+} C_{Z,+}^d + k_{Z,-} C_{Z,-}^d \right) + \gamma^5 \left(k_{Z,+} C_{Z,+}^d - k_{Z,-} C_{Z,-}^d \right) \right) \bar{d} \gamma^\mu d \quad (\text{B.7})$$

Thus, by comparing Eq. (B.5) and Eq. (B.7) one can find $C_{V(A)}$ in terms of $C_{Z,\pm}^d$ and vice-versa

$$C_V = 2 \left(k_{Z,-} C_{Z,-}^d + k_{Z,+} C_{Z,+}^d \right) \quad (\text{B.8})$$

$$C_A = 2 \left(k_{Z,-} C_{Z,-}^d - k_{Z,+} C_{Z,+}^d \right) \quad (\text{B.9})$$

$$C_{Z,-}^d = \frac{1}{4k_{Z,-}} \left(C_V + C_A \right) \quad (\text{B.10})$$

$$C_{Z,+}^d = \frac{1}{4k_{Z,+}} \left(C_V - C_A \right) \quad (\text{B.11})$$

B.5 Snippet codes to call an amplitude in Madgraph and in RecoLa2

Here we show how to call an amplitude for one phase space point in RecoLa2 and in Madgraph using the Python programming language.

Listing B.1: A python script example to call the matrix element in Recola.

```
# Import the Recola library (pyrecola) as follows:
from pyrecola import *

# set model parameters
set_parameter_rcl("MZp", 800.)
set_parameter_rcl("WZp", 23.)
set_parameter_rcl("MZ", 9.118800e+01)
set_parameter_rcl("WZ", 2.4414039999999 )
set_parameter_rcl("MW", 80.419002445756163)
set_parameter_rcl("WW", 2.085000e+00)
set_parameter_rcl("aEW", 0.0075467711139788835)
set_parameter_rcl("kWL", 0.0)
set_parameter_rcl("kWR", 0.0)
set_parameter_rcl("kZL", 1.4142135623730951)
set_parameter_rcl("kZR", 1.4142135623730951)
set_parameter_rcl("CZdL1x1", -0.301169)
set_parameter_rcl("CZdL1x2", 0.0)
set_parameter_rcl("CZdL1x3", 0.0)
set_parameter_rcl("CZdL2x1", 0.0)
set_parameter_rcl("CZdL2x2", -0.301169)
set_parameter_rcl("CZdL2x3", 0.0)
set_parameter_rcl("CZdL3x1", 0.0)
set_parameter_rcl("CZdL3x2", 0.0)
set_parameter_rcl("CZdL3x3", -0.301169)
set_parameter_rcl("CZuR1x1", -0.104768)
set_parameter_rcl("CZuR1x2", 0.0)
set_parameter_rcl("CZuR1x3", 0.0)
set_parameter_rcl("CZuR2x1", 0.0)
set_parameter_rcl("CZuR2x2", -0.104768)
set_parameter_rcl("CZuR2x3", 0.0)
set_parameter_rcl("CZuR3x1", 0.0)
set_parameter_rcl("CZuR3x2", 0.0)
set_parameter_rcl("CZuR3x3", -0.104768)
set_parameter_rcl("CZdR1x1", 0.052384)
set_parameter_rcl("CZdR1x2", 0.0)
set_parameter_rcl("CZdR1x3", 0.0)
set_parameter_rcl("CZdR2x1", 0.0)
```

```
set_parameter_rcl("CZdR2x2", 0.052384)
set_parameter_rcl("CZdR2x3", 0.0)
set_parameter_rcl("CZdR3x1", 0.0)
set_parameter_rcl("CZdR3x2", 0.0)
set_parameter_rcl("CZdR3x3", 0.052384)
set_parameter_rcl("CZuL1x1", 0.248785)
set_parameter_rcl("CZuL1x2", 0.0)
set_parameter_rcl("CZuL1x3", 0.0)
set_parameter_rcl("CZuL2x1", 0.0)
set_parameter_rcl("CZuL2x2", 0.248785)
set_parameter_rcl("CZuL2x3", 0.0)
set_parameter_rcl("CZuL3x1", 0.0)
set_parameter_rcl("CZuL3x2", 0.0)
set_parameter_rcl("CZuL3x3", 0.248785)

#define the process
define_process_rcl(1, "d_d~_~>_t_t~", "L0")

#generate the process
generate_processes_rcl()

p1 = [500., 0., 0., 500.]
p2 = [500., 0., 0., -500.]

# generate a sample PSP using RAMBO
p = set_outgoing_momenta_rcl(1, [p1, p2])

# compute tree squared amplitude
compute_process_rcl(1, p, 'L0')

# get a specific contributions
get_squared_amplitude_rcl(1, 'L0', pow=[0, 4, 4])
```

Listing B.2: A python script example to call the matrix element in MG5.

```

import matrix2py

def invert_momenta(p):
    """ fortran/C-python do not order table in the same order """
    new_p = []
    for i in range(len(p[0])): new_p.append([0]*len(p))
    for i, onep in enumerate(p):
        for j, x in enumerate(onep):
            new_p[j][i] = x
    return new_p

matrix2py.initialisemodel("/path/to/Cards/param_card.dat")
p = [[ 500., 0., 0., 500.],
      [ 500., 0., 0., 500.],
      [ 500, 110.9243, 444.8308, -199.5529],
      [ 500, -110.9243, -444.8308, 199.5529]]

P =invert_momenta(p)
alphas = 0.118 # strong coupling constant
nhel = -1 # sum over helicity

me2 = matrix2py.get_value(P, alphas, nhel)

```

Listing B.3: Some parameters needed to set the loop matrix element in RecoLa.

```

set_delta_ir_rcl(0.,pi**2/6.)
set_mu_ms_rcl(100.)
set_mu_ir_rcl(100.)

```

B.6 The powheg.input file

Her we show an example of the file powheg.input for a NLO calculation of the total cross section for BSM+SM $t\bar{t}$ hadroproduction at 13 TeV.

Listing B.4: An example of powheg.input in the SSM.

```

! q + qbar -> gamma/Z/W/Z'/W' -> t + tbar inputs
! GENERAL POWHEG PARAMETERS

numevts 100000 ! number of events to be generated
ih1 1 ! hadron 1 (1 for protons, -1 for antiprotons)

```

```

ih2 1 ! hadron 2 (1 for protons, -1 for antiprotons)
ebeam1 6500d0 ! energy of beam 1
ebeam2 6500d0 ! energy of beam 2

! To be set only if using LHA pdfs
lhans1 324900 ! pdf set for hadron 1 (LHA numbering)
lhans2 324900 ! pdf set for hadron 2 (LHA numbering)

! Parameters to allow or not the use of stored data
use-old-grid 1 ! if 1 use old grid if file pwggrids.dat is
                ! present (<> 1 regenerate)
use-old-ubound 1 ! if 1 use norm of upper bounding function stored in
                ! pwgubound.dat, if present; <> 1 regenerate

! Integration precision related settings
ncall1 50000 ! number of calls for initializing the integration grid
itmx1 1 ! number of iterations for initializing the integration grid
ncall1rm 1000000 ! number of calls for initializing the integration grid
itmx1rm 1 ! number of iterations for initializing the integration grid
ncall2 100000 ! number of calls for computing the integral and finding
                ! upper bound
itmx2 5 ! number of iterations for computing the integral and finding
                ! upper bound
foldcsi 2 ! number of folds on csi integration
foldy 5 ! number of folds on y integration
foldphi 1 ! number of folds on phi integration
nubound 50000 ! number of calls to setup upper bounds for radiation
icsimax 1 ! <= 100, number of csi subdivision when computing the upper bounds
iymax 5 ! <= 100, number of y subdivision when computing the upper bounds
xupbound 2d0 ! increase upper bound for radiation generation

! Calculate with remnants
withdamp 1 ! (default 0, do not use) use Born-zero damping factor

! PROCESS SPECIFIC PARAMETERS

! scale settings
scale 1 ! 0...muf=mur=sqrt(pt^2+m^2), 1...muf=mur=sqrt(shat),
        ! otherwise...muf=muF, mur=muR

```

```
! optional production parameters
! (defaults defined in init_couplings.f)
alphaem_inv 126.89 ! 1/alphaem (at 2*mt=2*172.5 according to pythia)
topmass 172.5 ! top mass (ATLAS tbar search)
! Z
zmass 91.1876 !PDG 2016
zwidth 2.4952 !PDG 2016
! W
wmass 80.385 !PDG 2016
wwidth 2.085 !PDG 2016
! W CKM couplings
CKM1x1 0.0
CKM1x2 0.0
CKM1x3 0.0
CKM2x1 0.0
CKM2x2 0.0
CKM2x3 0.0
CKM3x1 0.0
CKM3x2 0.0
CKM3x3 0.0
!sthw2 = 1 - MW**2/MZ**2
kG 1
! Z'
zpmass 2000.0
zewidth 60.0
kZL 1.41421356
kZR 1.41421356
! Z' diagonal couplings
lzpu1x1 0.245189276376
rzpu1x1 -0.108364112362
lzpd1x1 -0.299282945137
rzpd1x1 0.0542704445273
lzpu2x2 0.245189276376
rzpu2x2 -0.108364112362
lzpd2x2 -0.299282945137
rzpd2x2 0.0542704445273
lzpu3x3 0.245189276376
rzpu3x3 -0.108364112362
lzpd3x3 -0.299282945137
rzpd3x3 0.0542704445273
```


!Z' non-diagonal couplings

lzpu1x2 0.0
rzpu1x2 0.0
lzpd1x2 0.0
rzpd1x2 0.0
lzpu1x3 0.0
rzpu1x3 0.0
lzpd1x3 0.0
rzpd1x3 0.0
lzpu2x1 0.0
rzpu2x1 0.0
lzpd2x1 0.0
rzpd2x1 0.0
lzpu2x3 0.0
rzpu2x3 0.0
lzpd2x3 0.0
rzpd2x3 0.0
lzpu3x1 0.0
rzpu3x1 0.0
lzpd3x1 0.0
rzpd3x1 0.0
lzpu3x2 0.0
rzpu3x2 0.0
lzpd3x2 0.0
rzpd3x2 0.0

!W'

wpmass 2000.0
wpwidth 66.0

!W' couplings

lwpq1x1 0.0
rwpq1x1 0.0
lwpq1x2 0.0
rwpq1x2 0.0
lwpq1x3 0.0
rwpq1x3 0.0
lwpq2x1 0.0
rwpq2x1 0.0
lwpq2x2 0.0
rwpq2x2 0.0
lwpq2x3 0.0

```
rwpq2x3 0.0
lwpq3x1 0.0
rwpq3x1 0.0
lwpq3x2 0.0
rwpq3x2 0.0
lwpq3x3 0.0
rwpq3x3 0.0
```

! which subset of corrections to calculate?

! channel: 3 — Z'/W'; 4 — photon/Z/W; 7 — photon/Z/W/Z'/W'

```
channel 7
```

```
bornonly 0 ! calculate the cross sections at NLO
```

```
gaswitch 1 ! include photon induced diagrams
```

```
LRscheme 1 ! use the LR format for the couplings
```

```
micut 1500.0 ! set a generation cut on the top pair invariant mass
```

```
useRecolaBorn 1 ! use Recola to calculate the Born amplitudes
```

! (if 0 use old PBZp routines)

```
useRecolaReal 1 ! use Recola to calculate the real amplitudes
```

! (if 0 use old PBZp routines)

```
useRecolaVirtual 1 ! use Recola to calculate the virtual amplitudes
```

! (if 0 use old PBZp routines)

C. Contur

C.1 Steering files

Here we show the content of three files needed by Contur when steering PBZp and running jobs on a high performance computing system.

Listing C.1: mainpythia.cc.

```
#include "Pythia8/Pythia.h"
#include "Pythia8Plugins/HepMC2.h"
#include "Pythia8Plugins/PowhegHooks.h"
using namespace Pythia8;

int main(int argc, char* argv[]) {

    // Check that correct number of command-line arguments
    if (argc != 4) {
        cerr << "Unexpected number of command-line arguments.\nYou are"
             << " expected to provide one input and one output file name.\n"
             << "Program stopped!" << endl;
        return 1;
    }

    // Confirm that external files will be used for input and output.
    cout << "\n>>> The lh events will be read from file" << argv[2]
         << " <<<\n>>> The Number of events is" << argv[3]
         << " <<<\n>>> HepMC events will be written to file"
         << argv[1] << " <<<\n" << endl;

    // Interface for conversion from Pythia8::Event to HepMC event.
    HepMC::Pythia8ToHepMC ToHepMC;

    // Specify file where HepMC events will be stored.
    HepMC::IO_GenEvent ascii_io(argv[1], std::ios::out);

    // Generator.
    Pythia pythia;
```

```

// the input file, events will be read from the .lhe file
pythia.readString("Beams:frameType=_4"); // Choice of frame for the two colliding particles.
    For options 4 the beam identities are obtained by the Les Houches information.
pythia.readString("Beams:LHEF_="+std::string(argv[2]));

// allow top and anti-top decay
pythia.readString("6:mayDecay=_on");
pythia.readString("-6:mayDecay=_on");
pythia.readString("6:m0=_172.5"); // top mass
pythia.readString("23:m0=_91.1876"); // Z mass
pythia.readString("23:mWidth=_2.4952"); // Z width
pythia.readString("23:doForceWidth=_on");
pythia.readString("24:m0=_80.385"); // W mass
pythia.readString("24:mWidth=_2.085"); // W width
pythia.readString("24:doForceWidth=_on");
pythia.readString("SigmaProcess:alphaEMorder=_-1"); // fixed value of  $\alpha_{EM}$  at the MZ
pythia.readString("StandardModel:alphaEMmZ=_0.00788084168"); // it's value at the MZ
// Weinberg angle  $1 - MW^2/MZ^2$ 
//pythia.readString("StandardModel:sin2thetaW = 0.228686755");
//pythia.readString("StandardModel:sin2thetaWbar = 0.228686755");
pythia.readString("StandardModel:sin2thetaW=_0.23116");
pythia.readString("StandardModel:sin2thetaWbar=_0.23116");
// we leave the Z boson couplings unchanged, pythia manual mentions that
// they are calculated from the sin2thetaWbar value, in which case
// they should be correct, albeit inconsistent, if the user sets them to
// outrageous values

// switch off QED radiation
pythia.readString("SpaceShower:QEDshowerByQ=_on"); // From quarks
pythia.readString("SpaceShower:QEDshowerByL=_on"); // From Leptons
pythia.readString("TimeShower:QEDshowerByQ=_on"); // From quarks
pythia.readString("TimeShower:QEDshowerByL=_on"); // From Leptons
cout << "pythia_init:_QEDshower_on" << endl;

// SpaceShower(TimeShower):pTmaxMatch — pT veto setting for ISR(FSR)
// 0 ... the default Pythia setting
// 1 ... Pythia will use scalup to limit radiation
// 2 ... Pythia will use a UserHook to veto
// PowhegHook related settings
PowhegHooks *powhegHooks = NULL;

```

```
int veto = 1; // see PowhegHook settings above
int vetoCount = 3; // see above
int pThard = 0; // see above
int pTdef = 1; // see above
int pTemt = 0; // see above
int emitted = 0; // see above
int nFinal = 2; // number of final state particles at Born level

// use UserHooks for ISR and FSR
pythia.readString("SpaceShower:pTmaxMatch=_2");
pythia.readString("TimeShower:pTmaxMatch=_2");
// set up user hooks
pythia.readString("POWHEG:nFinal=_ " + std::to_string(nFinal));
pythia.readString("POWHEG:veto=_ " + std::to_string(veto));
pythia.readString("POWHEG:vetoCount=_ " + std::to_string(vetoCount));
pythia.readString("POWHEG:pThard=_ " + std::to_string(pThard));
pythia.readString("POWHEG:pTemt=_ " + std::to_string(pTemt));
pythia.readString("POWHEG:emitted=_ " + std::to_string(emitted));
pythia.readString("POWHEG:pTdef=_ " + std::to_string(pTdef));
powhegHooks = new PowhegHooks();
pythia.setUserHooksPtr((UserHooks *) powhegHooks);

// switch on matrix element corrections (this is the default I believe)
pythia.readString("TimeShower:MEcorrections=_on");
pythia.readString("SpaceShower:MEcorrections=_on");
// underlying event
pythia.readString("Tune:preferLHAPDF=0"); // using pythia built-in PDF
pythia.readString("Tune:pp=14"); // Monash 2013 tune

// switch off multiparton interaction
pythia.readString("PartonLevel:MPI=_on");
// switch off hadronization
pythia.readString("HadronLevel:all=_on");

// show x event records
pythia.readString("Next:numberShowEvent=_1");

// Extract settings to be used in the main program.
int nEvent = atoi(argv[3]);
int nAbort = 3;
```

```
// Initialization.
pythia.init();

// Begin event loop.
int iAbort = 0;
for (int iEvent = 0; iEvent < nEvent; ++iEvent) {

    // Generate event.
    if (!pythia.next()) {

        // If failure because reached end of file then exit event loop.
        if (pythia.info.atEndOfFile()) {
            cout << "_Aborted_since_reached_end_of_Les_Houches_Event_File\n";
            break;
        }
        // First few failures write off as "acceptable" errors, then quit.
        if (++iAbort < nAbort) continue;
        cout << "_Event_generation_aborted_prematurely,_owing_to_error!\n";
        break;
    }

    // Construct new empty HepMC event and fill it.
    // Units will be as chosen for HepMC build, but can be changed
    // by arguments, e.g. GenEvt( HepMC::Units::GEV, HepMC::Units::MM)
    HepMC::GenEvent* hepmcevt = new HepMC::GenEvent();
    ToHepMC.fill_next_event( pythia, hepmcevt );

    // Write the HepMC event to file. Done with it.
    ascii_io << hepmcevt;
    delete hepmcevt;

    // End of event loop. Statistics.
}
pythia.stat();

// Done.
return 0;
}
```

Listing C.2: pbzp_input_contur.py.

```
#!/usr/bin/env python
from math import *
from sympy import *
import numpy as np

def matrixform(data):
    """
    Translates an Array or nested list, or anything that behaves
    similarly, into a structure of nested matrices.
    """
    try:
        A = data.tolist()
    except AttributeError:
        A = data
    try:
        M = Matrix(A)
        return M.applyfunc(matrixform)
    except TypeError:
        return A

# The default model is the SSM
model = 'SSM'

# Read the name of the model and the values of its parameters from "params.dat"
path_to_params = 'params.dat'
f = open(path_to_params)
for line in f:
    if 'model' in line:
        model = str(line.split()[2])

## TFHMeg
if model in ['TFHMeg', 'tfhmeg', 'Tfhmeg']:
    f = open(path_to_params)
    for line in f:
        if 'tsb' in line:
            tsb = float(line.split()[2]) # angle theta_{sb} see Fig. 1 (right) in
            1905.06073
        if 'mZp' in line:
            MZp = float(line.split()[2])
```

```

## TC
elif model in ['TC', 'tc', 'Tc', 'tC']:
    f = open(path_to_params)
    for line in f:
        if 'GZp' in line:
            GZp = float(line.split()[2])
        if 'mZp' in line:
            MZp = float(line.split()[2])
## SSM
else:
    checkGZp = False
    f = open(path_to_params)
    for line in f:
        if 'GZp' in line:
            GZp = float(line.split()[2])
            checkGZp = True
        if 'mZp' in line:
            MZp = float(line.split()[2])
# Third Family Hypercharge Model example
if model in ['TFHMeg', 'tfhmeg', 'Tfhmeg']:
    ## Read alpha_em, mass of Z, and mass of W from "powheg.input_template"
    path_to_template = 'powheg.input_template'
    f = open(path_to_template)
    for line in f:
        if 'zmass' in line:
            MZ = float(line.split()[1])
        if 'wmass' in line:
            MW = float(line.split()[1])
        if 'alphaem_inv' in line:
            alphaem_inv = float(line.split()[1])

    ## Input for the TFHMeg
    s2w = 1 - MW**2/MZ**2
    sw = sqrt(s2w)
    cw = sqrt(1 - s2w)
    aEM = 1/alphaem_inv
    ee = 2.*sqrt(np.pi)*sqrt(aEM) # in Recola src/class_particles.f90
    const = (sqrt(2.)*ee)/(cw*sw) # Recola factor for Z' couplings
    gF = (MZp/36000.)*(sqrt((24.*1.06)/sin(2*tsb))) # Eq. 2.16 in 1904.10954, 36000
    since MZ' in GeV

```



```

ssb = sin(tsb) # sin of theta_sb
csb = cos(tsb) # cos of theta_sb

## VCKM matrix: Eq. 12.27 PDG Review 2018
VCKM = Matrix([[0.97446,0.22452,0.00365],
[0.22438,0.97359,0.04214],[0.00896,0.04133,0.999105]])

## arxiv : 1809.01158
xi = Matrix([[0.,0.,0.],[0.,0.,0.],[0.,0.,1.]]) # Eq. 2.12
VdR = Identity(3)
VuR = Identity(3)
VdL = Matrix([[1.,0.,0.],[0.,csb,-ssb],[0.,ssb,csb]]) # Eq. 2.13 (Eq. 1 in
1905.06073)
VuL = VdL*VCKM.H # page 8 first paragraph
LamdR = VdR.T*xi*VdR # Eq. 2.11
LamuR = VuR.T*xi*VuR # Eq. 2.11
LamdL = VdL.H*xi*VdL # Eq. 2.11
LamuL = VCKM*LamdL*VCKM.H # page 9 first sentence

```

Leptophobic TopColour model

```
elif model in ['TC', 'tc', 'Tc', 'tC']:
```

```
## Read alpha_em, mass of top, mass of Z, and mass of W from "powheg.input_template"
```

```
path_to_template = 'powheg.input_template'
```

```
f = open(path_to_template)
```

```
for line in f:
```

```
    if 'topmass' in line:
```

```
        Mtop = float(line.split()[1])
```

```
    if 'zmass' in line:
```

```
        MZ = float(line.split()[1])
```

```
    if 'wmass' in line:
```

```
        MW = float(line.split()[1])
```

```
    if 'alphaem_inv' in line:
```

```
        alphaem_inv = float(line.split()[1])
```

```
## Input for the TC
```

```
s2w = 1 - MW**2/MZ**2
```

```
sw = sqrt(s2w)
```

```
cw = sqrt(1 - s2w)
```

```
aEM = 1/alphaem_inv
```

```
ee = 2.*sqrt(np.pi)*sqrt(aEM) # in Recola src/class_particles.f90
```

```

g1 = ee/cw
const = (sqrt(2.)*ee)/(cw*sw) #Recola factor for Z' couplings
fac = sqrt(1 - ((4 * Mtop**2) / (MZp**2))) * (2 + 4 * (Mtop**2/MZp**2)) +
      4 # see eq. 6 in 1112.4928v3
cotH2 = (GZp * 8 * cw**2) / (aEM * MZp * fac) # see eq. 6 in 1112.4928v3
cotH = sqrt(cotH2)

```

Set the couplings

TFHMeg

if model in ['TFHMeg', 'tfhmeg', 'Tfhmeg']:

Write the TFHMeg couplings into Recola's L-R form

float(): convert couplings from sympy.core.numbers.Float to float numbers

```

lzpu1x1=float((1./const)*(-1./6.)*LamuL[0,0]*(gF))
lzpu1x2=float((1./const)*(-1./6.)*LamuL[0,1]*(gF))
lzpu1x3=float((1./const)*(-1./6.)*LamuL[0,2]*(gF))
lzpu2x1=float((1./const)*(-1./6.)*LamuL[1,0]*(gF))
lzpu2x2=float((1./const)*(-1./6.)*LamuL[1,1]*(gF))
lzpu2x3=float((1./const)*(-1./6.)*LamuL[1,2]*(gF))
lzpu3x1=float((1./const)*(-1./6.)*LamuL[2,0]*(gF))
lzpu3x2=float((1./const)*(-1./6.)*LamuL[2,1]*(gF))
lzpu3x3=float((1./const)*(-1./6.)*LamuL[2,2]*(gF))
rzpu1x1=float((1./const)*(-2./3.)*LamuR[0,0]*(gF))
rzpu1x2=float((1./const)*(-2./3.)*LamuR[0,1]*(gF))
rzpu1x3=float((1./const)*(-2./3.)*LamuR[0,2]*(gF))
rzpu2x1=float((1./const)*(-2./3.)*LamuR[1,0]*(gF))
rzpu2x2=float((1./const)*(-2./3.)*LamuR[1,1]*(gF))
rzpu2x3=float((1./const)*(-2./3.)*LamuR[1,2]*(gF))
rzpu3x1=float((1./const)*(-2./3.)*LamuR[2,0]*(gF))
rzpu3x2=float((1./const)*(-2./3.)*LamuR[2,1]*(gF))
rzpu3x3=float((1./const)*(-2./3.)*LamuR[2,2]*(gF))
lzpd1x1=float((1./const)*(-1./6.)*LamdL[0,0]*(gF))
lzpd1x2=float((1./const)*(-1./6.)*LamdL[0,1]*(gF))
lzpd1x3=float((1./const)*(-1./6.)*LamdL[0,2]*(gF))
lzpd2x1=float((1./const)*(-1./6.)*LamdL[1,0]*(gF))
lzpd2x2=float((1./const)*(-1./6.)*LamdL[1,1]*(gF))
lzpd2x3=float((1./const)*(-1./6.)*LamdL[1,2]*(gF))
lzpd3x1=float((1./const)*(-1./6.)*LamdL[2,0]*(gF))
lzpd3x2=float((1./const)*(-1./6.)*LamdL[2,1]*(gF))

```

```

lzpd3x3=float((1./const)*(-1./6.)*LamdL[2,2]*(gF))
rzpd1x1=float((1./const)*(1./3.)*LamdR[0,0]*(gF))
rzpd1x2=float((1./const)*(1./3.)*LamdR[0,1]*(gF))
rzpd1x3=float((1./const)*(1./3.)*LamdR[0,2]*(gF))
rzpd2x1=float((1./const)*(1./3.)*LamdR[1,0]*(gF))
rzpd2x2=float((1./const)*(1./3.)*LamdR[1,1]*(gF))
rzpd2x3=float((1./const)*(1./3.)*LamdR[1,2]*(gF))
rzpd3x1=float((1./const)*(1./3.)*LamdR[2,0]*(gF))
rzpd3x2=float((1./const)*(1./3.)*LamdR[2,1]*(gF))
rzpd3x3=float((1./const)*(1./3.)*LamdR[2,2]*(gF))
lwpq1x1=0.0
lwpq1x2=0.0
lwpq1x3=0.0
lwpq2x1=0.0
lwpq2x2=0.0
lwpq2x3=0.0
lwpq3x1=0.0
lwpq3x2=0.0
lwpq3x3=0.0
rwpq1x1=0.0
rwpq1x2=0.0
rwpq1x3=0.0
rwpq2x1=0.0
rwpq2x2=0.0
rwpq2x3=0.0
rwpq3x1=0.0
rwpq3x2=0.0
rwpq3x3=0.0

```

TC

`elif model in ['TC', 'tc', 'Tc', 'tC']:`

Write the TC couplings into Recola's L-R form

```

lzpu1x1=- (1./const)*0.5*(g1)*coth
lzpu1x2=0.0
lzpu1x3=0.0
lzpu2x1=0.0
lzpu2x2=0.0
lzpu2x3=0.0
lzpu3x1=0.0
lzpu3x2=0.0

```

```
lzpu3x3=(1./const)*0.5*(g1)*cotH
rzpu1x1=- (1./const)*0.5*(g1)*cotH
rzpu1x2=0.0
rzpu1x3=0.0
rzpu2x1=0.0
rzpu2x2=0.0
rzpu2x3=0.0
rzpu3x1=0.0
rzpu3x2=0.0
rzpu3x3=(1./const)*0.5*(g1)*cotH
lzd1x1=- (1./const)*0.5*(g1)*cotH
lzd1x2=0.0
lzd1x3=0.0
lzd2x1=0.0
lzd2x2=0.0
lzd2x3=0.0
lzd3x1=0.0
lzd3x2=0.0
lzd3x3=(1./const)*0.5*(g1)*cotH
rzpd1x1=0.0
rzpd1x2=0.0
rzpd1x3=0.0
rzpd2x1=0.0
rzpd2x2=0.0
rzpd2x3=0.0
rzpd3x1=0.0
rzpd3x2=0.0
rzpd3x3=0.0
lwpq1x1=0.0
lwpq1x2=0.0
lwpq1x3=0.0
lwpq2x1=0.0
lwpq2x2=0.0
lwpq2x3=0.0
lwpq3x1=0.0
lwpq3x2=0.0
lwpq3x3=0.0
rwpq1x1=0.0
rwpq1x2=0.0
rwpq1x3=0.0
```

```
rwq2x1=0.0
rwq2x2=0.0
rwq2x3=0.0
rwq3x1=0.0
rwq3x2=0.0
rwq3x3=0.0
```

```
## SSM
```

```
else:
```

```
## The SSM Z' couplings in Recola's LR format
```

```
lzpu1x1=0.245189276376
lzpu1x2=0.0
lzpu1x3=0.0
lzpu2x1=0.0
lzpu2x2=0.245189276376
lzpu2x3=0.0
lzpu3x1=0.0
lzpu3x2=0.0
lzpu3x3=0.245189276376
rzpu1x1=-0.108364112362
rzpu1x2=0.0
rzpu1x3=0.0
rzpu2x1=0.0
rzpu2x2=-0.108364112362
rzpu2x3=0.0
rzpu3x1=0.0
rzpu3x2=0.0
rzpu3x3=-0.108364112362
lzpd1x1=-0.299282945137
lzpd1x2=0.0
lzpd1x3=0.0
lzpd2x1=0.0
lzpd2x2=-0.299282945137
lzpd2x3=0.0
lzpd3x1=0.0
lzpd3x2=0.0
lzpd3x3=-0.299282945137
rzpd1x1=0.0542704445273
rzpd1x2=0.0
rzpd1x3=0.0
rzpd2x1=0.0
```

```

rzpd2x2=0.0542704445273
rzpd2x3=0.0
rzpd3x1=0.0
rzpd3x2=0.0
rzpd3x3=0.0542704445273
lwpq1x1=0.0
lwpq1x2=0.0
lwpq1x3=0.0
lwpq2x1=0.0
lwpq2x2=0.0
lwpq2x3=0.0
lwpq3x1=0.0
lwpq3x2=0.0
lwpq3x3=0.0
rwpq1x1=0.0
rwpq1x2=0.0
rwpq1x3=0.0
rwpq2x1=0.0
rwpq2x2=0.0
rwpq2x3=0.0
rwpq3x1=0.0
rwpq3x2=0.0
rwpq3x3=0.0

# Set the width of Z'
## TFHMeg
if model in ['TFHMeg', 'tfhmeg', 'Tfhmeg']:
    GZp = float((5.*MZp*gF**2)/(36*np.pi))
## SSM Z' width, in case not given as a parameter
elif model in ['SSM', 'ssm', 'Ssm']:
    if checkGZp == False:
        GZp = float(0.03*MZp)

# Read the powheg.input_template file
lines = file('powheg.input_template','r').readlines()

# Edit the content
for ill,ll in enumerate(lines):
    ## TFHMeg

```

```

if model in ['TFHMeg', 'tfhmeg', 'Tfhmeg']:
    if 'This_is_the_TFHMeg' in ll:
        lines[ill] = lines[ill].replace("This_is_the_TFHMeg", str("
            This_is_the_TFHMeg,_see_arxiv:_1809.01158"))
## TC
elif model in ['TC', 'tc', 'Tc', 'tC']:
    if 'This_is_the_TC' in ll:
        lines[ill] = lines[ill].replace("This_is_the_TC", str("This_is
            _the_Leptophobic_TC_model,_see_arxiv:_1112.4928v3"))
    if 'The_theta_sb' in ll:
        lines[ill] = lines[ill].replace("!_The_theta_sb_parameter_is_
            equal_to_dummy", str("_"))
## SSM
else:
    if 'This_is_the_SSM' in ll:
        lines[ill] = lines[ill].replace("This_is_the_SSM", str("This_
            is_the_SSM,_a_toy_model"))
    if 'The_theta_sb' in ll:
        lines[ill] = lines[ill].replace("!_The_theta_sb_parameter_is_
            equal_to_dummy", str("_"))
## All the models
if '{GZp}' in ll:
    lines[ill] = lines[ill].replace("{GZp}", "{0:.8e}".format(GZp))
if '#lzpu1x1' in ll:
    lines[ill] = lines[ill].replace("#lzpu1x1", "{0:.8e}".format(lzpu1x1)
        )
if '#rzpu1x1' in ll:
    lines[ill] = lines[ill].replace("#rzpu1x1", "{0:.8e}".format(rzpu1x1)
        )
if '#lzpu2x2' in ll:
    lines[ill] = lines[ill].replace("#lzpu2x2", "{0:.8e}".format(lzpu2x2)
        )
if '#rzpu2x2' in ll:
    lines[ill] = lines[ill].replace("#rzpu2x2", "{0:.8e}".format(rzpu2x2)
        )
if '#lzpu3x3' in ll:
    lines[ill] = lines[ill].replace("#lzpu3x3", "{0:.8e}".format(lzpu3x3)
        )
if '#rzpu3x3' in ll:

```

```
        lines[ill] = lines[ill].replace("#rzpu3x3", "{0:.8e}".format(rzpu3x3)
        )
    if '#lzpd1x1' in ll:
        lines[ill] = lines[ill].replace("#lzpd1x1", "{0:.8e}".format(lzpd1x1)
        )
    if '#rzpd1x1' in ll:
        lines[ill] = lines[ill].replace("#rzpd1x1", "{0:.8e}".format(rzpd1x1)
        )
    if '#lzpd2x2' in ll:
        lines[ill] = lines[ill].replace("#lzpd2x2", "{0:.8e}".format(lzpd2x2)
        )
    if '#rzpd2x2' in ll:
        lines[ill] = lines[ill].replace("#rzpd2x2", "{0:.8e}".format(rzpd2x2)
        )
    if '#lzpd3x3' in ll:
        lines[ill] = lines[ill].replace("#lzpd3x3", "{0:.8e}".format(lzpd3x3)
        )
    if '#rzpd3x3' in ll:
        lines[ill] = lines[ill].replace("#rzpd3x3", "{0:.8e}".format(rzpd3x3)
        )
    if '#lzpu1x2' in ll:
        lines[ill] = lines[ill].replace("#lzpu1x2", "{0:.8e}".format(lzpu1x2)
        )
    if '#rzpu1x2' in ll:
        lines[ill] = lines[ill].replace("#rzpu1x2", "{0:.8e}".format(rzpu1x2)
        )
    if '#lzpu1x3' in ll:
        lines[ill] = lines[ill].replace("#lzpu1x3", "{0:.8e}".format(lzpu1x3)
        )
    if '#rzpu1x3' in ll:
        lines[ill] = lines[ill].replace("#rzpu1x3", "{0:.8e}".format(rzpu1x3)
        )
    if '#lzpu2x1' in ll:
        lines[ill] = lines[ill].replace("#lzpu2x1", "{0:.8e}".format(lzpu2x1)
        )
    if '#rzpu2x1' in ll:
        lines[ill] = lines[ill].replace("#rzpu2x1", "{0:.8e}".format(rzpu2x1)
        )
    if '#lzpd1x2' in ll:
```



```
        lines[ill] = lines[ill].replace("#lzpd1x2", "{0:.8e}".format(lzpd1x2)
        )
    if '#rzpd1x2' in ll:
        lines[ill] = lines[ill].replace("#rzpd1x2", "{0:.8e}".format(rzpd1x2)
        )
    if '#lzpd1x3' in ll:
        lines[ill] = lines[ill].replace("#lzpd1x3", "{0:.8e}".format(lzpd1x3)
        )
    if '#rzpd1x3' in ll:
        lines[ill] = lines[ill].replace("#rzpd1x3", "{0:.8e}".format(rzpd1x3)
        )
    if '#lzpd2x1' in ll:
        lines[ill] = lines[ill].replace("#lzpd2x1", "{0:.8e}".format(lzpd2x1)
        )
    if '#rzpd2x1' in ll:
        lines[ill] = lines[ill].replace("#rzpd2x1", "{0:.8e}".format(rzpd2x1)
        )
    if '#lzpu2x3' in ll:
        lines[ill] = lines[ill].replace("#lzpu2x3", "{0:.8e}".format(lzpu2x3)
        )
    if '#rzpu2x3' in ll:
        lines[ill] = lines[ill].replace("#rzpu2x3", "{0:.8e}".format(rzpu2x3)
        )
    if '#lzpu3x1' in ll:
        lines[ill] = lines[ill].replace("#lzpu3x1", "{0:.8e}".format(lzpu3x1)
        )
    if '#rzpu3x1' in ll:
        lines[ill] = lines[ill].replace("#rzpu3x1", "{0:.8e}".format(rzpu3x1)
        )
    if '#lzpu3x2' in ll:
        lines[ill] = lines[ill].replace("#lzpu3x2", "{0:.8e}".format(lzpu3x2)
        )
    if '#rzpu3x2' in ll:
        lines[ill] = lines[ill].replace("#rzpu3x2", "{0:.8e}".format(rzpu3x2)
        )
    if '#lzpd2x3' in ll:
        lines[ill] = lines[ill].replace("#lzpd2x3", "{0:.8e}".format(lzpd2x3)
        )
    if '#rzpd2x3' in ll:
```

```
        lines[ill] = lines[ill].replace("#rzpd2x3", "{0:.8e}".format(rzpd2x3)
        )
if '#lzpd3x1' in ll:
    lines[ill] = lines[ill].replace("#lzpd3x1", "{0:.8e}".format(lzpd3x1)
    )
if '#rzpd3x1' in ll:
    lines[ill] = lines[ill].replace("#rzpd3x1", "{0:.8e}".format(rzpd3x1)
    )
if '#lzpd3x2' in ll:
    lines[ill] = lines[ill].replace("#lzpd3x2", "{0:.8e}".format(lzpd3x2)
    )
if '#rzpd3x2' in ll:
    lines[ill] = lines[ill].replace("#rzpd3x2", "{0:.8e}".format(rzpd3x2)
    )
if '#lwpq1x1' in ll:
    lines[ill] = lines[ill].replace("#lwpq1x1", "{0:.8e}".format(lwpq1x1)
    )
if '#lwpq1x2' in ll:
    lines[ill] = lines[ill].replace("#lwpq1x2", "{0:.8e}".format(lwpq1x2)
    )
if '#lwpq1x3' in ll:
    lines[ill] = lines[ill].replace("#lwpq1x3", "{0:.8e}".format(lwpq1x3)
    )
if '#lwpq2x1' in ll:
    lines[ill] = lines[ill].replace("#lwpq2x1", "{0:.8e}".format(lwpq2x1)
    )
if '#lwpq2x2' in ll:
    lines[ill] = lines[ill].replace("#lwpq2x2", "{0:.8e}".format(lwpq2x2)
    )
if '#lwpq2x3' in ll:
    lines[ill] = lines[ill].replace("#lwpq2x3", "{0:.8e}".format(lwpq2x3)
    )
if '#lwpq3x1' in ll:
    lines[ill] = lines[ill].replace("#lwpq3x1", "{0:.8e}".format(lwpq3x1)
    )
if '#lwpq3x2' in ll:
    lines[ill] = lines[ill].replace("#lwpq3x2", "{0:.8e}".format(lwpq3x2)
    )
if '#lwpq3x3' in ll:
```

```
        lines[ill] = lines[ill].replace("#lwpq3x3", "{0:.8e}".format(lwpq3x3)
        )
    if '#rwpq1x1' in ll:
        lines[ill] = lines[ill].replace("#rwpq1x1", "{0:.8e}".format(rwpq1x1)
        )
    if '#rwpq1x2' in ll:
        lines[ill] = lines[ill].replace("#rwpq1x2", "{0:.8e}".format(rwpq1x2)
        )
    if '#rwpq1x3' in ll:
        lines[ill] = lines[ill].replace("#rwpq1x3", "{0:.8e}".format(rwpq1x3)
        )
    if '#rwpq2x1' in ll:
        lines[ill] = lines[ill].replace("#rwpq2x1", "{0:.8e}".format(rwpq2x1)
        )
    if '#rwpq2x2' in ll:
        lines[ill] = lines[ill].replace("#rwpq2x2", "{0:.8e}".format(rwpq2x2)
        )
    if '#rwpq2x3' in ll:
        lines[ill] = lines[ill].replace("#rwpq2x3", "{0:.8e}".format(rwpq2x3)
        )
    if '#rwpq3x1' in ll:
        lines[ill] = lines[ill].replace("#rwpq3x1", "{0:.8e}".format(rwpq3x1)
        )
    if '#rwpq3x2' in ll:
        lines[ill] = lines[ill].replace("#rwpq3x2", "{0:.8e}".format(rwpq3x2)
        )
    if '#rwpq3x3' in ll:
        lines[ill] = lines[ill].replace("#rwpq3x3", "{0:.8e}".format(rwpq3x3)
        )
```

Create a powheg.input file and write the edited content to it

```
f= open('powheg.input', 'w')
f.write('').join(lines)
f.close()
```

Delete the Single variables from params.dat to be able to make a HeatMap at a later stage

```
with open(path_to_params, "r") as f:
    lines = f.readlines()
with open(path_to_params, "w") as f:
    for line in lines:
```

```

        if "model" not in line.strip("\n"):
            f.write(line)
with open(path_to_params, "r") as f:
    lines = f.readlines()
with open(path_to_params, "w") as f:
    for line in lines:
        if "dummy" not in line.strip("\n"):
            f.write(line)
if model in ['TFHMeg', 'tfhmeg', 'Tfhmeg']:
    with open(path_to_params, "r") as f:
        lines = f.readlines()
    with open(path_to_params, "w") as f:
        for line in lines:
            if "GZp" not in line.strip("\n"):
                f.write(line)

```

Listing C.3: powheg.input_template.

```

! q + qbar -> Z' -> t + tbar inputs

! This is the {model}
! The theta_sb parameter is equal to {tsb}

! GENERAL POWHEG PARAMETERS

numevts 10000 ! The number of events
ih1 1
ih2 1
ebeam1 6500 ! The energy of beam one
ebeam2 6500 ! The energy of beam two

lhans1 324900
lhans2 324900

! Parameters to allow or not the use of stored data
use-old-grid 1
use-old-ubound 1
ncall1 5000
itmx1 1

```

```
ncall2 5000
itmx2 2
foldcsi 1
foldy 1
foldphi 1
nubound 10000
icsimax 1
iymax 5
xupbound 2d0
withdamp 0

!PROCESS SPECIFIC PARAMETERS

!scale settings
scale 1

!optional production parameters
!(defaults defined in init_couplings.f)

alphaem_inv 126.889999998
!sthw2 = 1 - MW**2/MZ**2

topmass 172.5

!Z
zmass 91.1876 !PDG 2016
zwidth 2.4952 !PDG 2016

!W
wmass 80.385 !PDG 2016
wwidth 2.085 !PDG 2016

!Z'
zpmass {mZp} ! The mass of Z'
zpwidht {GZp} ! The width of Z'

!Z' diagonal couplings
lzpu1x1 #lzpu1x1
rzpu1x1 #rzpu1x1
lzpd1x1 #lzpd1x1
```

```
rzpd1x1 #rzpd1x1
lzpu2x2 #lzpu2x2
rzpu2x2 #rzpu2x2
lzpd2x2 #lzpd2x2
rzpd2x2 #rzpd2x2
lzpu3x3 #lzpu3x3
rzpu3x3 #rzpu3x3
lzpd3x3 #lzpd3x3
rzpd3x3 #rzpd3x3
```

!Z' non-diagonal couplings

```
lzpu1x2 #lzpu1x2
rzpu1x2 #rzpu1x2
lzpd1x2 #lzpd1x2
rzpd1x2 #rzpd1x2
lzpu1x3 #lzpu1x3
rzpu1x3 #rzpu1x3
lzpd1x3 #lzpd1x3
rzpd1x3 #rzpd1x3
lzpu2x1 #lzpu2x1
rzpu2x1 #rzpu2x1
lzpd2x1 #lzpd2x1
rzpd2x1 #rzpd2x1
lzpu2x3 #lzpu2x3
rzpu2x3 #rzpu2x3
lzpd2x3 #lzpd2x3
rzpd2x3 #rzpd2x3
lzpu3x1 #lzpu3x1
rzpu3x1 #rzpu3x1
lzpd3x1 #lzpd3x1
rzpd3x1 #rzpd3x1
lzpu3x2 #lzpu3x2
rzpu3x2 #rzpu3x2
lzpd3x2 #lzpd3x2
rzpd3x2 #rzpd3x2
```

!W'

```
wpmass 5500.0
wpwidth 181.5
```

!W' couplings

```
lwpq1x1 #lwpq1x1
rwpq1x1 #rwpq1x1
lwpq1x2 #lwpq1x2
rwpq1x2 #rwpq1x2
lwpq1x3 #lwpq1x3
rwpq1x3 #rwpq1x3
lwpq2x1 #lwpq2x1
rwpq2x1 #rwpq2x1
lwpq2x2 #lwpq2x2
rwpq2x2 #rwpq2x2
lwpq2x3 #lwpq2x3
rwpq2x3 #rwpq2x3
lwpq3x1 #lwpq3x1
rwpq3x1 #rwpq3x1
lwpq3x2 #lwpq3x2
rwpq3x2 #rwpq3x2
lwpq3x3 #lwpq3x3
rwpq3x3 #rwpq3x3
```

! OTHER OPTIONAL PARAMETERS

! which subset of corrections to calculate?

! channel: 3 — Z'; 4 — photon/Z/W; 7 — photon/Z/W/Z'/W'

```
channel 3
```

```
bornonly 0
```

```
!LOevents 1
```

```
gaswitch 0
```

```
LRscheme 1
```

```
useRecolaBorn 1
```

```
useRecolaReal 1
```

```
useRecolaVirtual 1
```


Bibliography

- [1] S. L. Glashow, “Partial Symmetries of Weak Interactions,” *Nucl. Phys.* **22** (1961) 579–588.
- [2] A. Salam and J. C. Ward, “Electromagnetic and weak interactions,” *Phys. Lett.* **13** (1964) 168–171.
- [3] S. Weinberg, “A model of leptons,” *Phys. Rev. Lett.* **19** (1967) 1264–1266.
- [4] S. L. Glashow, J. Iliopoulos, and L. Maiani, “Weak interactions with lepton - hadron symmetry,” *Phys. Rev.* **D2** (1970) 1285–1292.
- [5] S. Weinberg, “Mixing angle in renormalizable theories of weak and electromagnetic interactions,” *Phys. Rev. D* **5** (1972) 1962–1967.
- [6] D. J. Gross and F. Wilczek, “Asymptotically free gauge theories. i,” *Phys. Rev. D* **8** (Nov, 1973) 3633–3652. <https://link.aps.org/doi/10.1103/PhysRevD.8.3633>.
- [7] M. Kobayashi and T. Maskawa, “CP-Violation in the Renormalizable Theory of Weak Interaction,” *Progress of Theoretical Physics* **49** no. 2, (02, 1973) 652–657, <https://academic.oup.com/ptp/article-pdf/49/2/652/5257692/49-2-652.pdf>. <https://doi.org/10.1143/PTP.49.652>.
- [8] D. J. Gross and F. Wilczek, “Asymptotically free gauge theories. ii,” *Phys. Rev. D* **9** (Feb, 1974) 980–993. <https://link.aps.org/doi/10.1103/PhysRevD.9.980>.
- [9] H. D. Politzer, “Asymptotic Freedom: An Approach to Strong Interactions,” *Phys. Rept.* **14** (1974) 129–180.
- [10] C. Rovelli, “Notes for a brief history of quantum gravity,” in *9th Marcel Grossmann Meeting on Recent Developments in Theoretical and Experimental General Relativity, Gravitation and Relativistic Field Theories (MG 9)*, pp. 742–768. 6, 2000. [arXiv:gr-qc/0006061](https://arxiv.org/abs/gr-qc/0006061).
- [11] G. Bertone, D. Hooper, and J. Silk, “Particle dark matter: Evidence, candidates and constraints,” *Phys. Rept.* **405** (2005) 279–390, [arXiv:hep-ph/0404175](https://arxiv.org/abs/hep-ph/0404175).
- [12] G. R. Farrar and M. E. Shaposhnikov, “Baryon asymmetry of the universe in the standard electroweak theory,” *Phys. Rev. D* **50** (1994) 774, [arXiv:hep-ph/9305275](https://arxiv.org/abs/hep-ph/9305275).
- [13] M. B. Gavela, M. Lozano, J. Orloff, and O. Pene, “Standard model CP violation and baryon asymmetry. Part 1: Zero temperature,” *Nucl. Phys. B* **430** (1994) 345–381, [arXiv:hep-ph/9406288](https://arxiv.org/abs/hep-ph/9406288).

- [14] P. Huet and E. Sather, “Electroweak baryogenesis and standard model CP violation,” *Phys. Rev. D* **51** (1995) 379–394, [arXiv:hep-ph/9404302](#).
- [15] **Super-Kamiokande** Collaboration, Y. Fukuda *et al.*, “Evidence for oscillation of atmospheric neutrinos,” *Phys. Rev. Lett.* **81** (1998) 1562–1567, [arXiv:hep-ex/9807003](#).
- [16] **SNO** Collaboration, Q. R. Ahmad *et al.*, “Measurement of the rate of $\nu_e + d \rightarrow p + p + e^-$ interactions produced by ^8B solar neutrinos at the Sudbury Neutrino Observatory,” *Phys. Rev. Lett.* **87** (2001) 071301, [arXiv:nucl-ex/0106015](#).
- [17] **SNO** Collaboration, Q. R. Ahmad *et al.*, “Direct evidence for neutrino flavor transformation from neutral current interactions in the Sudbury Neutrino Observatory,” *Phys. Rev. Lett.* **89** (2002) 011301, [arXiv:nucl-ex/0204008](#).
- [18] U. Baur, D. Schildknecht, and K. H. G. Schwarzer, “EXCITED WEAK VECTOR BOSONS,” *Phys. Rev. D* **35** (1987) 297.
- [19] A. Datta, P. J. O’Donnell, Z. H. Lin, X. Zhang, and T. Huang, “Effects of Kaluza-Klein excited W on single top quark production at Tevatron,” *Phys. Lett. B* **483** (2000) 203–209, [arXiv:hep-ph/0001059](#).
- [20] H. Georgi and S. L. Glashow, “Unity of All Elementary Particle Forces,” *Phys. Rev. Lett.* **32** (1974) 438–441.
- [21] J. C. Pati and A. Salam, “Lepton Number as the Fourth Color,” *Phys. Rev. D* **10** (1974) 275–289. [Erratum: *Phys.Rev.D* 11, 703–703 (1975)].
- [22] H. Fritzsch and P. Minkowski, “Unified Interactions of Leptons and Hadrons,” *Annals Phys.* **93** (1975) 193–266.
- [23] H. Georgi, “The State of the Art—Gauge Theories,” *AIP Conf. Proc.* **23** (1975) 575–582.
- [24] G. Altarelli, B. Mele, and M. Ruiz-Altaba, “Searching for new heavy vector bosons in $p\bar{p}$ colliders,” *Z. Phys.* **C45** (1989) 109. Erratum-*ibid.* **C47**, 676 (1990).
- [25] R. Martinez and F. Ochoa, “Constraints on 3-3-1 models with electroweak Z pole observables and Z’ search at the LHC,” *Phys. Rev. D* **90** no. 1, (2014) 015028, [arXiv:1405.4566 \[hep-ph\]](#).
- [26] J. de Blas, J. M. Lizana, and M. Perez-Victoria, “Combining searches of Z’ and W’ bosons,” *JHEP* **01** (2013) 166, [arXiv:1211.2229 \[hep-ph\]](#).
- [27] C. Grojean, E. Salvioni, and R. Torre, “A weakly constrained W’ at the early LHC,”

- JHEP* **07** (2011) 002, [arXiv:1103.2761 \[hep-ph\]](#).
- [28] E. Salvioni, A. Strumia, G. Villadoro, and F. Zwirner, “Non-universal minimal Z' models: present bounds and early LHC reach,” *JHEP* **03** (2010) 010, [arXiv:0911.1450 \[hep-ph\]](#).
- [29] E. Salvioni, G. Villadoro, and F. Zwirner, “Minimal Z' -prime models: Present bounds and early LHC reach,” *JHEP* **11** (2009) 068, [arXiv:0909.1320 \[hep-ph\]](#).
- [30] T. Ježo, M. Klasen, and I. Schienbein, “LHC phenomenology of general $SU(2) \times SU(2) \times U(1)$ models,” *Physical Review D* **86** no. 3, (2012) 035005.
- [31] Q.-H. Cao, Z. Li, J.-H. Yu, and C. P. Yuan, “Discovery and Identification of W' and Z' in $SU(2) \times SU(2) \times U(1)$ Models at the LHC,” *Phys. Rev. D* **86** (2012) 095010, [arXiv:1205.3769 \[hep-ph\]](#).
- [32] R. N. Mohapatra and J. C. Pati, ““ natural” left-right symmetry,” *Physical Review D* **11** no. 9, (1975) 2558.
- [33] R. N. Mohapatra and J. C. Pati, “Left-right gauge symmetry and an “isoconjugate” model of CP violation,” *Phys. Rev. D* **11** (Feb, 1975) 566–571. <https://link.aps.org/doi/10.1103/PhysRevD.11.566>.
- [34] V. Barger, W.-Y. Keung, and E. Ma, “Gauge model with light W and Z bosons,” *Physical Review D* **22** no. 3, (1980) 727.
- [35] V. Barger, W.-Y. Keung, and E. Ma, “Doubling of weak gauge bosons in an extension of the standard model,” *Physical Review Letters* **44** no. 18, (1980) 1169.
- [36] H. Georgi, E. E. Jenkins, and E. H. Simmons, “The un-unified standard model,” *Nuclear Physics B* **331** no. 3, (1990) 541–555.
- [37] H. Georgi, E. E. Jenkins, and E. H. Simmons, “Ununifying the standard model,” *Physical Review Letters* **62** no. 24, (1989) 2789.
- [38] E. Malkawi, T. Tait, and C.-P. Yuan, “A model of strong flavor dynamics for the top quark,” *Physics Letters B* **385** no. 1-4, (1996) 304–310.
- [39] X.-y. Li and E. Ma, “Gauge model of generation nonuniversality,” *Phys. Rev. Lett.* **47** (Dec, 1981) 1788–1791. <https://link.aps.org/doi/10.1103/PhysRevLett.47.1788>.
- [40] R. Bonciani, T. Jezo, M. Klasen, F. Lyonnet, and I. Schienbein, “Electroweak top-quark pair production at the LHC with Z' bosons to NLO QCD in POWHEG,” *JHEP* **02** (2016)

- 141, [arXiv:1511.08185 \[hep-ph\]](#).
- [41] B. Fuks, M. Klasen, D. R. Lamprea, and M. Rothering, “Precision predictions for electroweak superpartner production at hadron colliders with Resummino,” *Eur. Phys. J. C* **73** (2013) 2480, [arXiv:1304.0790 \[hep-ph\]](#).
- [42] S. Frixione, P. Nason, and C. Oleari, “Matching NLO QCD computations with Parton Shower simulations: the POWHEG method,” *JHEP* **11** (2007) 070, [arXiv:0709.2092 \[hep-ph\]](#).
- [43] A. Denner, J.-N. Lang, and S. Uccirati, “Recola2: REcursive Computation of One-Loop Amplitudes 2,” *Comput. Phys. Commun.* **224** (2018) 346–361, [arXiv:1711.07388 \[hep-ph\]](#).
- [44] S. Alioli, P. Nason, C. Oleari, and E. Re, “A general framework for implementing NLO calculations in shower Monte Carlo programs: the POWHEG BOX,” *JHEP* **06** (2010) 043, [arXiv:1002.2581 \[hep-ph\]](#).
- [45] X. Cid Vidal *et al.*, “Report from Working Group 3: Beyond the Standard Model physics at the HL-LHC and HE-LHC,” [arXiv:1812.07831 \[hep-ph\]](#).
- [46] M. M. Altakach, T. Ježo, M. Klasen, J.-N. Lang, and I. Schienbein, “Electroweak $t\bar{t}$ hadroproduction in the presence of heavy Z' and W' bosons at NLO QCD in POWHEG,” [arXiv:2012.14855 \[hep-ph\]](#).
- [47] M. M. Altakach, T. Ježo, M. Klasen, J. N. Lang, and I. Schienbein, “Precise predictions for electroweak $t\bar{t}$ production at the LHC in models with flavour non-diagonal Z' boson couplings and W' bosons,” [arXiv:2012.15092 \[hep-ph\]](#).
- [48] A. Buckley *et al.*, “Testing new-physics models with global comparisons to collider measurements: the Contur toolkit,” [arXiv:2102.04377 \[hep-ph\]](#).
- [49] M. M. Altakach, J. M. Butterworth, T. Ježo, M. Klasen, and I. Schienbein, “New constraints on TopColour models,” [arXiv:21xx.xxxx \[hep-ph\]](#).
- [50] P. Langacker, “The physics of heavy Z' gauge bosons,” *Reviews of Modern Physics* **81** no. 3, (2009) 1199.
- [51] F. Del Aguila, “The physics of Z' bosons,” *arXiv preprint hep-ph/9404323* (1994) .
- [52] K. Hsieh, K. Schmitz, J.-H. Yu, and C.-P. Yuan, “Global analysis of general $SU(2) \times SU(2) \times U(1)$ models with precision data,” *Physical Review D* **82** no. 3, (2010) 035011.
- [53] T. Jezo, Z' and W' gauge bosons in $SU(2) \times SU(2) \times U(1)$ models : Collider phenomenology

- at LO and NLO QCD*. Theses, Université de Grenoble, Sept., 2013.
<https://tel.archives-ouvertes.fr/tel-01492965>.
- [54] T. Jezo, M. Klasen, D. R. Lamprea, F. Lyonnet, and I. Schienbein, “NLO+NLL limits on Z' and W' gauge boson masses in general extensions of the Standard Model,” *JHEP* **12** (2014) 092, [arXiv:1410.4692](https://arxiv.org/abs/1410.4692) [hep-ph].
- [55] ATLAS Collaboration, G. Aad *et al.*, “Observation of a new particle in the search for the Standard Model Higgs boson with the ATLAS detector at the LHC,” *Phys. Lett.* **B716** (2012) 1–29, [arXiv:1207.7214](https://arxiv.org/abs/1207.7214) [hep-ex].
- [56] CMS Collaboration, S. Chatrchyan *et al.*, “Observation of a New Boson at a Mass of 125 GeV with the CMS Experiment at the LHC,” *Phys. Lett.* **B716** (2012) 30–61, [arXiv:1207.7235](https://arxiv.org/abs/1207.7235) [hep-ex].
- [57] O. Brüning and L. Rossi, “The high-luminosity large hadron collider,” *Nature Reviews Physics* **1** no. 4, (2019) 241–243. <https://doi.org/10.1038/s42254-019-0050-6>.
- [58] CDF Collaboration, F. Abe, H. Akimoto, *et al.*, “Observation of top quark production in $\bar{p}p$ collisions with the collider detector at fermilab,” *Phys. Rev. Lett.* **74** (Apr, 1995) 2626–2631. <https://link.aps.org/doi/10.1103/PhysRevLett.74.2626>.
- [59] D0 Collaboration, S. Abachi, B. Abbott, *et al.*, “Observation of the top quark,” *Phys. Rev. Lett.* **74** (Apr, 1995) 2632–2637. <https://link.aps.org/doi/10.1103/PhysRevLett.74.2632>.
- [60] P. Nason, “A New method for combining NLO QCD with shower Monte Carlo algorithms,” *JHEP* **11** (2004) 040, [arXiv:hep-ph/0409146](https://arxiv.org/abs/hep-ph/0409146) [hep-ph].
- [61] Particle Data Group Collaboration, K. Olive *et al.*, “Review of Particle Physics,” *Chin. Phys. C* **38** (2014) 090001.
- [62] T. Sjostrand, S. Mrenna, and P. Z. Skands, “PYTHIA 6.4 Physics and Manual,” *JHEP* **05** (2006) 026, [arXiv:hep-ph/0603175](https://arxiv.org/abs/hep-ph/0603175) [hep-ph].
- [63] S. Dulat, T.-J. Hou, J. Gao, M. Guzzi, J. Huston, P. Nadolsky, J. Pumplin, C. Schmidt, D. Stump, and C. P. Yuan, “New parton distribution functions from a global analysis of quantum chromodynamics,” *Phys. Rev.* **D93** no. 3, (2016) 033006, [arXiv:1506.07443](https://arxiv.org/abs/1506.07443) [hep-ph].
- [64] J. Pumplin, D. R. Stump, and W. K. Tung, “Multivariate fitting and the error matrix in global analysis of data,” *Phys. Rev. D* **65** (2001) 014011, [arXiv:hep-ph/0008191](https://arxiv.org/abs/hep-ph/0008191).

- [65] J. Pumplin, D. Stump, R. Brock, D. Casey, J. Huston, J. Kalk, H. L. Lai, and W. K. Tung, “Uncertainties of predictions from parton distribution functions. 2. The Hessian method,” *Phys. Rev. D* **65** (2001) 014013, [arXiv:hep-ph/0101032](#).
- [66] J. Pumplin, D. R. Stump, J. Huston, H. L. Lai, P. M. Nadolsky, and W. K. Tung, “New generation of parton distributions with uncertainties from global QCD analysis,” *JHEP* **07** (2002) 012, [arXiv:hep-ph/0201195](#) [hep-ph].
- [67] G. Bozzi, B. Fuks, and M. Klasen, “Threshold Resummation for Slepton-Pair Production at Hadron Colliders,” *Nucl. Phys.* **B777** (2007) 157–181, [arXiv:hep-ph/0701202](#) [hep-ph].
- [68] J. Debove, B. Fuks, and M. Klasen, “Threshold resummation for gaugino pair production at hadron colliders,” *Nucl. Phys.* **B842** (2011) 51–85, [arXiv:1005.2909](#) [hep-ph].
- [69] G. Bozzi, B. Fuks, and M. Klasen, “Transverse-momentum resummation for slepton-pair production at the CERN LHC,” *Phys. Rev.* **D74** (2006) 015001, [arXiv:hep-ph/0603074](#) [hep-ph].
- [70] J. Debove, B. Fuks, and M. Klasen, “Transverse-momentum resummation for gaugino-pair production at hadron colliders,” *Phys. Lett.* **B688** (2010) 208–211, [arXiv:0907.1105](#) [hep-ph].
- [71] B. Allanach and J. Davighi, “Third family hypercharge model for $R_{K^{(*)}}$ and aspects of the fermion mass problem,” *JHEP* **12** (2018) 075, [arXiv:1809.01158](#) [hep-ph].
- [72] B. Allanach and J. Davighi, “Naturalising the third family hypercharge model for neutral current B -anomalies,” *Eur. Phys. J. C* **79** no. 11, (2019) 908, [arXiv:1905.10327](#) [hep-ph].
- [73] **LHCb** Collaboration, R. Aaij *et al.*, “Test of lepton universality with $B^0 \rightarrow K^{*0} \ell^+ \ell^-$ decays,” *JHEP* **08** (2017) 055, [arXiv:1705.05802](#) [hep-ex].
- [74] **LHCb** Collaboration, R. Aaij *et al.*, “Angular analysis of the $B^0 \rightarrow K^{*0} \mu^+ \mu^-$ decay using 3 fb^{-1} of integrated luminosity,” *JHEP* **02** (2016) 104, [arXiv:1512.04442](#) [hep-ex].
- [75] **LHCb** Collaboration, R. Aaij *et al.*, “Measurement of Form-Factor-Independent Observables in the Decay $B^0 \rightarrow K^{*0} \mu^+ \mu^-$,” *Phys. Rev. Lett.* **111** (2013) 191801, [arXiv:1308.1707](#) [hep-ex].
- [76] **LHCb** Collaboration, R. Aaij *et al.*, “Measurement of the $B_s^0 \rightarrow \mu^+ \mu^-$ branching fraction and effective lifetime and search for $B^0 \rightarrow \mu^+ \mu^-$ decays,” *Phys. Rev. Lett.* **118**

- no. 19, (2017) 191801, [arXiv:1703.05747 \[hep-ex\]](#).
- [77] **ATLAS** Collaboration, M. Aaboud *et al.*, “Study of the rare decays of B_s^0 and B^0 mesons into muon pairs using data collected during 2015 and 2016 with the ATLAS detector,” *JHEP* **04** (2019) 098, [arXiv:1812.03017 \[hep-ex\]](#).
- [78] **CMS, LHCb** Collaboration, V. Khachatryan *et al.*, “Observation of the rare $B_s^0 \rightarrow \mu^+ \mu^-$ decay from the combined analysis of CMS and LHCb data,” *Nature* **522** (2015) 68–72, [arXiv:1411.4413 \[hep-ex\]](#).
- [79] **CMS** Collaboration, S. Chatrchyan *et al.*, “Measurement of the $B_s^0 \rightarrow \mu^+ \mu^-$ Branching Fraction and Search for $B^0 \rightarrow \mu^+ \mu^-$ with the CMS Experiment,” *Phys. Rev. Lett.* **111** (2013) 101804, [arXiv:1307.5025 \[hep-ex\]](#).
- [80] C. Bobeth, M. Chrzaszcz, D. van Dyk, and J. Virto, “Long-distance effects in $B \rightarrow K^* \ell \ell$ from analyticity,” *Eur. Phys. J. C* **78** no. 6, (2018) 451, [arXiv:1707.07305 \[hep-ph\]](#).
- [81] **CMS** Collaboration, V. Khachatryan *et al.*, “Angular analysis of the decay $B^0 \rightarrow K^{*0} \mu^+ \mu^-$ from pp collisions at $\sqrt{s} = 8$ TeV,” *Phys. Lett. B* **753** (2016) 424–448, [arXiv:1507.08126 \[hep-ex\]](#).
- [82] C. Degrande, C. Duhr, B. Fuks, D. Grellscheid, O. Mattelaer, and T. Reiter, “UFO - The Universal FeynRules Output,” *Comput. Phys. Commun.* **183** (2012) 1201–1214, [arXiv:1108.2040 \[hep-ph\]](#).
- [83] J. C. Collins, D. E. Soper, and G. F. Sterman, “Factorization of Hard Processes in QCD,” *Adv. Ser. Direct. High Energy Phys.* **5** (1989) 1–91, [arXiv:hep-ph/0409313](#).
- [84] P. Nason, S. Dawson, and R. Ellis, “The Total Cross-Section for the Production of Heavy Quarks in Hadronic Collisions,” *Nucl. Phys. B* **303** (1988) 607–633.
- [85] P. Nason, S. Dawson, and R. Ellis, “The One Particle Inclusive Differential Cross-Section for Heavy Quark Production in Hadronic Collisions,” *Nucl. Phys. B* **327** (1989) 49–92. [Erratum: *Nucl.Phys.B* 335, 260–260 (1990)].
- [86] W. Beenakker, H. Kuijf, W. van Neerven, and J. Smith, “QCD Corrections to Heavy Quark Production in p anti-p Collisions,” *Phys. Rev. D* **40** (1989) 54–82.
- [87] W. Beenakker, W. van Neerven, R. Meng, G. Schuler, and J. Smith, “QCD corrections to heavy quark production in hadron hadron collisions,” *Nucl. Phys. B* **351** (1991) 507–560.
- [88] M. L. Mangano, P. Nason, and G. Ridolfi, “Heavy quark correlations in hadron collisions at next-to-leading order,” *Nucl. Phys. B* **373** (1992) 295–345.

- [89] W. Bernreuther, A. Brandenburg, Z. Si, and P. Uwer, “Top quark spin correlations at hadron colliders: Predictions at next-to-leading order QCD,” *Phys. Rev. Lett.* **87** (2001) 242002, [arXiv:hep-ph/0107086](#).
- [90] W. Bernreuther, A. Brandenburg, Z. Si, and P. Uwer, “Top quark pair production and decay at hadron colliders,” *Nucl. Phys. B* **690** (2004) 81–137, [arXiv:hep-ph/0403035](#).
- [91] W. Beenakker, A. Denner, W. Hollik, R. Mertig, T. Sack, and D. Wackerroth, “Electroweak one loop contributions to top pair production in hadron colliders,” *Nucl. Phys. B* **411** (1994) 343–380.
- [92] C. Kao and D. Wackerroth, “Parity violating asymmetries in top pair production at hadron colliders,” *Phys. Rev. D* **61** (2000) 055009, [arXiv:hep-ph/9902202](#).
- [93] J. H. Kuhn, A. Scharf, and P. Uwer, “Electroweak corrections to top-quark pair production in quark-antiquark annihilation,” *Eur. Phys. J. C* **45** (2006) 139–150, [arXiv:hep-ph/0508092](#).
- [94] S. Moretti, M. Nolten, and D. Ross, “Weak corrections to gluon-induced top-antitop hadro-production,” *Phys. Lett. B* **639** (2006) 513–519, [arXiv:hep-ph/0603083](#). [Erratum: *Phys.Lett.B* 660, 607–609 (2008)].
- [95] W. Bernreuther, M. Fückler, and Z. Si, “Mixed QCD and weak corrections to top quark pair production at hadron colliders,” *Phys. Lett. B* **633** (2006) 54–60, [arXiv:hep-ph/0508091](#). [Erratum: *Phys.Lett.B* 644, 386–386 (2007)].
- [96] W. Bernreuther, M. Fuecker, and Z.-G. Si, “Weak interaction corrections to hadronic top quark pair production,” *Phys. Rev. D* **74** (2006) 113005, [arXiv:hep-ph/0610334](#).
- [97] W. Hollik and M. Kollar, “NLO QED contributions to top-pair production at hadron collider,” *Phys. Rev. D* **77** (2008) 014008, [arXiv:0708.1697 \[hep-ph\]](#).
- [98] D. Pagani, I. Tsinikos, and M. Zaro, “The impact of the photon PDF and electroweak corrections on $t\bar{t}$ distributions,” *Eur. Phys. J. C* **76** no. 9, (2016) 479, [arXiv:1606.01915 \[hep-ph\]](#).
- [99] C. Gütschow, J. M. Lindert, and M. Schönherr, “Multi-jet merged top-pair production including electroweak corrections,” *Eur. Phys. J. C* **78** no. 4, (2018) 317, [arXiv:1803.00950 \[hep-ph\]](#).
- [100] A. Denner, G. Weiglein, and S. Dittmaier, “Application of the background field method to the electroweak standard model,” *Nucl. Phys. B* **440** (1995) 95, [arXiv:hep-ph/9410338](#).

- [101] A. Denner, J.-N. Lang, and S. Uccirati, “NLO electroweak corrections in extended Higgs Sectors with RECOLA2,” *JHEP* **07** (2017) 087, [arXiv:1705.06053 \[hep-ph\]](#).
- [102] S. Frixione, Z. Kunszt, and A. Signer, “Three jet cross-sections to next-to-leading order,” *Nucl. Phys. B* **467** (1996) 399–442, [arXiv:hep-ph/9512328](#).
- [103] S. Frixione, “A General approach to jet cross-sections in QCD,” *Nucl. Phys. B* **507** (1997) 295–314, [arXiv:hep-ph/9706545](#).
- [104] S. Actis, A. Denner, L. Hofer, J.-N. Lang, A. Scharf, and S. Uccirati, “RECOLA: REcursive Computation of One-Loop Amplitudes,” *Comput. Phys. Commun.* **214** (2017) 140–173, [arXiv:1605.01090 \[hep-ph\]](#).
- [105] A. Denner, S. Dittmaier, and L. Hofer, “Collier: a fortran-based Complex One-Loop Library in Extended Regularizations,” *Comput. Phys. Commun.* **212** (2017) 220–238, [arXiv:1604.06792 \[hep-ph\]](#).
- [106] G. Ossola, C. G. Papadopoulos, and R. Pittau, “On the Rational Terms of the one-loop amplitudes,” *JHEP* **05** (2008) 004, [arXiv:0802.1876 \[hep-ph\]](#).
- [107] A. Alloul, N. D. Christensen, C. Degrande, C. Duhr, and B. Fuks, “FeynRules 2.0 - A complete toolbox for tree-level phenomenology,” *Comput. Phys. Commun.* **185** (2014) 2250–2300, [arXiv:1310.1921 \[hep-ph\]](#).
- [108] A. Denner and S. Dittmaier, “Electroweak Radiative Corrections for Collider Physics,” *Phys. Rept.* **864** (2020) 1–163, [arXiv:1912.06823 \[hep-ph\]](#).
- [109] A. Denner, “Techniques for calculation of electroweak radiative corrections at the one loop level and results for W physics at LEP-200,” *Fortsch. Phys.* **41** (1993) 307–420, [arXiv:0709.1075 \[hep-ph\]](#).
- [110] T. Sjostrand, S. Mrenna, and P. Z. Skands, “A Brief Introduction to PYTHIA 8.1,” *Comput. Phys. Commun.* **178** (2008) 852–867, [arXiv:0710.3820 \[hep-ph\]](#).
- [111] G. Corcella, I. G. Knowles, G. Marchesini, S. Moretti, K. Odagiri, P. Richardson, M. H. Seymour, and B. R. Webber, “HERWIG 6.5 release note,” [arXiv:hep-ph/0210213](#).
- [112] S. Ovin, X. Rouby, and V. Lemaitre, “DELPHES, a framework for fast simulation of a generic collider experiment,” [arXiv:0903.2225 \[hep-ph\]](#).
- [113] S. Hoeche, F. Krauss, N. Lavesson, L. Lonnblad, M. Mangano, A. Schalicke, and S. Schumann, “Matching parton showers and matrix elements,” in *HERA and the LHC: A Workshop on the Implications of HERA for LHC Physics: CERN - DESY Workshop*

- 2004/2005 (Midterm Meeting, CERN, 11-13 October 2004; Final Meeting, DESY, 17-21 January 2005), pp. 288–289. 2005. [arXiv:hep-ph/0602031](#).
- [114] S. Catani, F. Krauss, R. Kuhn, and B. R. Webber, “QCD matrix elements + parton showers,” *JHEP* **11** (2001) 063, [arXiv:hep-ph/0109231](#).
- [115] F. Krauss, “Matrix elements and parton showers in hadronic interactions,” *JHEP* **08** (2002) 015, [arXiv:hep-ph/0205283](#).
- [116] S. Weinzierl, “Introduction to Monte Carlo methods,” [arXiv:hep-ph/0006269](#).
- [117] G. P. Lepage, “A New Algorithm for Adaptive Multidimensional Integration,” *J. Comput. Phys.* **27** (1978) 192.
- [118] G. P. Lepage, “VEGAS: AN ADAPTIVE MULTIDIMENSIONAL INTEGRATION PROGRAM,”.
- [119] R. Frederix, S. Frixione, F. Maltoni, and T. Stelzer, “Automation of next-to-leading order computations in QCD: The FKS subtraction,” *JHEP* **10** (2009) 003, [arXiv:0908.4272 \[hep-ph\]](#).
- [120] S. Alioli, *Matching next-to-leading-order QCD calculations with shower Monte Carlo Simulations: single vector boson and higgs boson productions in powheg*. Theses, Università degli Studi di Milano-Bicocca, 2009. <http://hdl.handle.net/10281/7381>.
- [121] S. Alioli, P. Nason, C. Oleari, and E. Re, “NLO single-top production matched with shower in POWHEG: s- and t-channel contributions,” *JHEP* **09** (2009) 111, [arXiv:0907.4076 \[hep-ph\]](#). [Erratum: *JHEP* **02**, 011 (2010)].
- [122] E. Re, “Single-top Wt-channel production matched with parton showers using the POWHEG method,” *Eur. Phys. J. C* **71** (2011) 1547, [arXiv:1009.2450 \[hep-ph\]](#).
- [123] S. Alioli, P. Nason, C. Oleari, and E. Re, “NLO Higgs boson production via gluon fusion matched with shower in POWHEG,” *JHEP* **04** (2009) 002, [arXiv:0812.0578 \[hep-ph\]](#).
- [124] S. Alioli, S.-O. Moch, and P. Uwer, “Hadronic top-quark pair-production with one jet and parton showering,” *JHEP* **01** (2012) 137, [arXiv:1110.5251 \[hep-ph\]](#).
- [125] S. Alioli, V. Cirigliano, W. Dekens, J. de Vries, and E. Mereghetti, “Right-handed charged currents in the era of the Large Hadron Collider,” *JHEP* **05** (2017) 086, [arXiv:1703.04751 \[hep-ph\]](#).

- [126] F. F. Cordero, M. Kraus, and L. Reina, “Top-quark pair production in association with a W^\pm gauge boson in the POWHEG-BOX,” [arXiv:2101.11808 \[hep-ph\]](#).
- [127] **Particle Data Group** Collaboration, P. Zyla *et al.*, “Review of Particle Physics,” *PTEP* **2020** no. 8, (2020) 083C01.
- [128] S. Frixione, P. Nason, and G. Ridolfi, “A Positive-weight next-to-leading-order Monte Carlo for heavy flavour hadroproduction,” *JHEP* **09** (2007) 126, [arXiv:0707.3088 \[hep-ph\]](#).
- [129] S. Alioli, P. Nason, C. Oleari, and E. Re, *The POWHEG BOX user manual: common features*, March, 2011. <http://th-www.if.uj.edu.pl/~erichter/POWHEG-BOX-V2/Docs/manual-BOX.pdf>.
- [130] J. Alwall *et al.*, “A Standard format for Les Houches event files,” *Comput. Phys. Commun.* **176** (2007) 300–304, [arXiv:hep-ph/0609017](#).
- [131] **ATLAS** Collaboration, G. Aad *et al.*, “Search for high-mass dilepton resonances using 139 fb^{-1} of pp collision data collected at $\sqrt{s} = 13 \text{ TeV}$ with the ATLAS detector,” *Phys. Lett.* **B796** (2019) 68–87, [arXiv:1903.06248 \[hep-ex\]](#).
- [132] **CMS** Collaboration, C. Collaboration, “Search for a narrow resonance in high-mass dilepton final states in proton-proton collisions using 140 fb^{-1} of data at $\sqrt{s} = 13 \text{ TeV}$,” CMS-PAS-EXO-19-019.
- [133] **ATLAS** Collaboration, G. Aad *et al.*, “Search for a heavy charged boson in events with a charged lepton and missing transverse momentum from pp collisions at $\sqrt{s} = 13 \text{ TeV}$ with the ATLAS detector,” *Phys. Rev.* **D100** no. 5, (2019) 052013, [arXiv:1906.05609 \[hep-ex\]](#).
- [134] **CMS** Collaboration, A. M. Sirunyan *et al.*, “Search for high-mass resonances in final states with a lepton and missing transverse momentum at $\sqrt{s} = 13 \text{ TeV}$,” *JHEP* **06** (2018) 128, [arXiv:1803.11133 \[hep-ex\]](#).
- [135] C. T. Hill, “Topcolor: top quark condensation in a gauge extension of the standard model,” *Physics Letters B* **266** no. 3, (1991) 419 – 424. <http://www.sciencedirect.com/science/article/pii/037026939191061Y>.
- [136] C. T. Hill, “Topcolor assisted technicolor,” *Phys. Lett. B* **345** (1995) 483–489, [arXiv:hep-ph/9411426](#).
- [137] R. M. Harris, C. T. Hill, and S. J. Parke, “Cross-Section for Topcolor Z'_t Decaying to $t\bar{t}$,” [arXiv:hep-ph/9911288](#).

- [138] R. M. Harris and S. Jain, “Cross Sections for Leptophobic Topcolor Z' Decaying to Top-Antitop,” *Eur. Phys. J. C* **72** (2012) 2072, [arXiv:1112.4928 \[hep-ph\]](#).
- [139] **ATLAS** Collaboration, G. Aad *et al.*, “Search for $t\bar{t}$ resonances in fully hadronic final states in pp collisions at $\sqrt{s} = 13$ TeV with the ATLAS detector,” *JHEP* **10** (2020) 061, [arXiv:2005.05138 \[hep-ex\]](#).
- [140] **CMS** Collaboration, A. M. Sirunyan *et al.*, “Search for resonant $t\bar{t}$ production in proton-proton collisions at $\sqrt{s} = 13$ TeV,” *JHEP* **04** (2019) 031, [arXiv:1810.05905 \[hep-ex\]](#).
- [141] **LHCb** Collaboration, R. Aaij *et al.*, “Search for lepton-universality violation in $B^+ \rightarrow K^+ \ell^+ \ell^-$ decays,” *Phys. Rev. Lett.* **122** no. 19, (2019) 191801, [arXiv:1903.09252 \[hep-ex\]](#).
- [142] **ATLAS** Collaboration, T. A. collaboration, “Angular analysis of $B_d^0 \rightarrow K^* \mu^+ \mu^-$ decays in pp collisions at $\sqrt{s} = 8$ TeV with the ATLAS detector,”.
- [143] **CMS** Collaboration, C. Collaboration, “Measurement of the P_1 and P_5' angular parameters of the decay $B^0 \rightarrow K^{*0} \mu^+ \mu^-$ in proton-proton collisions at $\sqrt{s} = 8$ TeV,”.
- [144] J. Davighi, “Connecting neutral current B anomalies with the heaviness of the third family,” in *54th Rencontres de Moriond on QCD and High Energy Interactions (Moriond QCD 2019) La Thuile, Italy, March 23-30, 2019*. 2019. [arXiv:1905.06073 \[hep-ph\]](#).
- [145] B. C. Allanach, J. M. Butterworth, and T. Corbett, “Collider constraints on Z' models for neutral current B-anomalies,” *JHEP* **08** (2019) 106, [arXiv:1904.10954 \[hep-ph\]](#).
- [146] **Particle Data Group** Collaboration, C. Patrignani *et al.*, “Review of Particle Physics,” *Chin. Phys. C* **40** no. 10, (2016) 100001.
- [147] **NNPDF** Collaboration, V. Bertone, S. Carrazza, N. P. Hartland, and J. Rojo, “Illuminating the photon content of the proton within a global PDF analysis,” *SciPost Phys.* **5** no. 1, (2018) 008, [arXiv:1712.07053 \[hep-ph\]](#).
- [148] A. Manohar, P. Nason, G. P. Salam, and G. Zanderighi, “How bright is the proton? A precise determination of the photon parton distribution function,” *Phys. Rev. Lett.* **117** no. 24, (2016) 242002, [arXiv:1607.04266 \[hep-ph\]](#).
- [149] A. V. Manohar, P. Nason, G. P. Salam, and G. Zanderighi, “The Photon Content of the Proton,” *JHEP* **12** (2017) 046, [arXiv:1708.01256 \[hep-ph\]](#).
- [150] A. Buckley, J. Ferrando, S. Lloyd, K. Nordström, B. Page, M. Rufenacht, M. Schönherr,

- and G. Watt, “LHAPDF6: parton density access in the LHC precision era,” *Eur. Phys. J. C* **75** (2015) 132, [arXiv:1412.7420 \[hep-ph\]](https://arxiv.org/abs/1412.7420). URL: <https://lhpdf.hepforge.org/>.
- [151] J. Andersen *et al.*, “Les Houches 2013: Physics at TeV Colliders: Standard Model Working Group Report,” [arXiv:1405.1067 \[hep-ph\]](https://arxiv.org/abs/1405.1067).
- [152] A. Buckley, J. Butterworth, L. Lonnblad, D. Grellscheid, H. Hoeth, J. Monk, H. Schulz, and F. Siegert, “Rivet user manual,” *Comput. Phys. Commun.* **184** (2013) 2803–2819, [arXiv:1003.0694 \[hep-ph\]](https://arxiv.org/abs/1003.0694).
- [153] C. Bierlich *et al.*, “Robust Independent Validation of Experiment and Theory: Rivet version 3,” *SciPost Phys.* **8** (2020) 026, [arXiv:1912.05451 \[hep-ph\]](https://arxiv.org/abs/1912.05451).
- [154] M. Cacciari, G. P. Salam, and G. Soyez, “The anti- k_t jet clustering algorithm,” *JHEP* **04** (2008) 063, [arXiv:0802.1189 \[hep-ph\]](https://arxiv.org/abs/0802.1189).
- [155] J. M. Butterworth, D. Grellscheid, M. Krämer, B. Sarrazin, and D. Yallup, “Constraining new physics with collider measurements of Standard Model signatures,” *JHEP* **03** (2017) 078, [arXiv:1606.05296 \[hep-ph\]](https://arxiv.org/abs/1606.05296).
- [156] CMS Collaboration, A. M. Sirunyan *et al.*, “Measurement of differential cross sections for the production of top quark pairs and of additional jets in lepton+jets events from pp collisions at $\sqrt{s} = 13$ TeV,” *Phys. Rev. D* **97** no. 11, (2018) 112003, [arXiv:1803.08856 \[hep-ex\]](https://arxiv.org/abs/1803.08856).
- [157] D. Yallup, *Constraining new physics with fiducial measurements at the LHC*. Theses, Università degli Studi di Milano-Bicocca, 2020.
<https://discovery.ucl.ac.uk/id/eprint/10095492>.
- [158] E. Maguire, L. Heinrich, and G. Watt, “HEPData: a repository for high energy physics data,” *J. Phys. Conf. Ser.* **898** no. 10, (2017) 102006, [arXiv:1704.05473 \[hep-ex\]](https://arxiv.org/abs/1704.05473).
- [159] M. Dobbs *et al.*, “The hepmc c++ monte carlo event record for high energy physics,” *Computer Physics Communications* **134** no. 1, (2001) 41–46.
<https://www.sciencedirect.com/science/article/pii/S0010465500001892>.
- [160] A. Buckley *et al.*, “The hepmc3 event record library for monte carlo event generators,” *Computer Physics Communications* **260** (2021) 107310.
<https://www.sciencedirect.com/science/article/pii/S0010465520301181>.
- [161] ATLAS Collaboration, G. Aad *et al.*, “Measurement of the differential cross-section of highly boosted top quarks as a function of their transverse momentum in $\sqrt{s} = 8$ TeV proton-proton collisions using the ATLAS detector,” *Phys. Rev. D* **93** no. 3, (2016)

- 032009, [arXiv:1510.03818](#) [hep-ex].
- [162] **ATLAS** Collaboration, G. Aad *et al.*, “Measurements of top-quark pair differential cross-sections in the lepton+jets channel in pp collisions at $\sqrt{s} = 8$ TeV using the ATLAS detector,” *Eur. Phys. J. C* **76** no. 10, (2016) 538, [arXiv:1511.04716](#) [hep-ex].
- [163] **CMS** Collaboration, A. M. Sirunyan *et al.*, “Measurement of the jet mass in highly boosted $t\bar{t}$ events from pp collisions at $\sqrt{s} = 8$ TeV,” *Eur. Phys. J. C* **77** no. 7, (2017) 467, [arXiv:1703.06330](#) [hep-ex].
- [164] **CMS** Collaboration, A. M. Sirunyan *et al.*, “Measurement of the Jet Mass Distribution and Top Quark Mass in Hadronic Decays of Boosted Top Quarks in pp Collisions at $\sqrt{s} = 8$ TeV,” *Phys. Rev. Lett.* **124** no. 20, (2020) 202001, [arXiv:1911.03800](#) [hep-ex].
- [165] **ATLAS** Collaboration, G. Aad *et al.*, “Measurement of the $t\bar{t}$ production cross-section and lepton differential distributions in $e\mu$ dilepton events from pp collisions at $\sqrt{s} = 13$ TeV with the ATLAS detector,” *Eur. Phys. J. C* **80** no. 6, (2020) 528, [arXiv:1910.08819](#) [hep-ex].
- [166] **ATLAS** Collaboration, G. Aad *et al.*, “Measurements of top-quark pair differential and double-differential cross-sections in the ℓ +jets channel with pp collisions at $\sqrt{s} = 13$ TeV using the ATLAS detector,” *Eur. Phys. J. C* **79** no. 12, (2019) 1028, [arXiv:1908.07305](#) [hep-ex]. [Erratum: *Eur.Phys.J.C* 80, 1092 (2020)].
- [167] **ATLAS** Collaboration, M. Aaboud *et al.*, “Measurements of top-quark pair differential cross-sections in the lepton+jets channel in pp collisions at $\sqrt{s} = 13$ TeV using the ATLAS detector,” *JHEP* **11** (2017) 191, [arXiv:1708.00727](#) [hep-ex].
- [168] **ATLAS** Collaboration, M. Aaboud *et al.*, “Measurements of differential cross sections of top quark pair production in association with jets in pp collisions at $\sqrt{s} = 13$ TeV using the ATLAS detector,” *JHEP* **10** (2018) 159, [arXiv:1802.06572](#) [hep-ex].
- [169] **CMS** Collaboration, A. M. Sirunyan *et al.*, “Measurements of differential cross sections of top quark pair production as a function of kinematic event variables in proton-proton collisions at $\sqrt{s} = 13$ TeV,” *JHEP* **06** (2018) 002, [arXiv:1803.03991](#) [hep-ex].
- [170] **ATLAS** Collaboration, M. Aaboud *et al.*, “Measurements of $t\bar{t}$ differential cross-sections of highly boosted top quarks decaying to all-hadronic final states in pp collisions at $\sqrt{s} = 13$ TeV using the ATLAS detector,” *Phys. Rev. D* **98** no. 1, (2018) 012003, [arXiv:1801.02052](#) [hep-ex].

- [171] CMS Collaboration, V. Khachatryan *et al.*, “Measurement of differential cross sections for top quark pair production using the lepton+jets final state in proton-proton collisions at 13 TeV,” *Phys. Rev. D* **95** no. 9, (2017) 092001, [arXiv:1610.04191](https://arxiv.org/abs/1610.04191) [hep-ex].
- [172] M. Klasen, F. Lyonnet, and F. S. Queiroz, “NLO+NLL collider bounds, Dirac fermion and scalar dark matter in the B–L model,” *The European Physical Journal C* **77** no. 5, (May, 2017) . <http://dx.doi.org/10.1140/epjc/s10052-017-4904-8>.
- [173] F. Maltoni, K. Paul, T. Stelzer, and S. Willenbrock, “Color Flow Decomposition of QCD Amplitudes,” *Phys. Rev. D* **67** (2003) 014026, [arXiv:hep-ph/0209271](https://arxiv.org/abs/hep-ph/0209271).
- [174] CDF Collaboration, C. Ciobanu, T. Junk, G. Veramendi, J. Lee, G. De Lentdecker, K. S. McFarland, and K. Maeshima, “Z’ generation with PYTHIA,”.